A Search for Ultra-High Energy Neutrinos and Cosmic Rays with ANITA-3

Ben Strutt

A dissertation submitted in partial fulfillment

of the requirements for the degree of

Doctor of Philosophy

of

University College London.

Department of Physics and Astronomy

University College London

January 21, 2017

I, Ben Strutt, confirm that the work presented in this thesis is my own. Where information has been derived from other sources, I confirm that this has been indicated in the work.

Abstract

The Antarctic Impulsive Transient Antenna (ANITA) is a balloon borne radio interferometer, designed to detect the impulsive Askaryan radiation created by ultra-high energy neutrinos interacting in the ice sheets of Antarctica. Previous flights of the experiment have demonstrated an unexpected sensitivity to cosmic rays, detecting the radio emission from geo-magnetically induced transverse currents in extended air showers. The third flight of ANITA (ANITA-3) took place during the austral summer of 2014-15.

In this thesis I present two contributions to the ANITA-3 experiment, the timing calibration of the digitizer electronics, and my implementation of a real-time interferometric event prioritizer using a GPU flown with the experiment.

Finally, I present a search for neutrinos and cosmic rays in the ANITA-3 data set. No evidence of neutrino interactions is observed, with zero candidate events discovered on a background of 0.11 ± 0.07 leading to the world's best limit on the ultra-high energy neutrino flux in the energy range $10^{19}\,\mathrm{eV}$ to $10^{21}\,\mathrm{eV}$. Four isolated, predominantly horizontally polarised events are found in the data. Further work is required to confirm these events have all the properties consistent with radio emission induced by cosmic ray air showers.

Acknowledgements

Firstly, I would like thank my supervisor Ryan Nichol for the opportunity to work on ANITA, for his guidance, enthusiasm, and seemingly inexhaustible patience.

The ANITA collaboration are a wonderful cohort. I would like to thank the Hawaii group for making me feel so welcome from day one. In particular, Peter Gorham, Christian Miki, Brian Hill, Harm Schoorlemmer, Jarred Roberts, and Ben Rotter made my work visits to Oahu a real pleasure. Thanks to David Saltzberg, Abby Vieregg, Andres Romero-Wolf for many insightful and fun conversations whenever we met. I have learned a lot from you all. Specific thanks to Amy Connolly for digging out her flux limit plotting macro and sending me a copy. Special thanks go to Stephanie Wissel for her advice and friendship, and Katie Mulrey with whom I learnt the ropes.

Linda Cremonesi and Cosmin Deaconu have been fantastic to work with in this final period of my PhD. Their tireless production of Monte Carlo neutrinos and diligent cross-checking of angular resolutions made my work go much more smoothly.

Thank you to all the members of the UCL HEP group past and present, for all the evenings I've lost in the Jeremy Bentham. Particular thanks go to my office mates in C17, Andy Edmonds, Andy Perch, Becca Falla, and Sally Shaw for afternoon coffee breaks, cryptic crosswords, and for listening to me talk about my Emacs configuration in an incredibly self indulgent manner.

Away from physics I would like to thank my brothers for their friendship and for helping me to keep everything in perspective. No words I write here could thank my parents enough for their constant encouragement over decades, for engaging

with my interest in science from a young age, and for believing in me. Without you both I could never have come this far.

Finally, thank you to my fiancee Amy. You've been with me through every step of this journey. Here's to our next big adventure.

Contents

List of Figures

List of Tables

Chapter 1

Introduction

There is a horizon in our current view of the Universe. Cosmic rays, the charged particles that crash into the Earth's atmosphere from space, have reached our planet with enormous energies, $E \sim 10^{20}\,\mathrm{eV}$, from sources unknown [16]. Information about their origin is blocked from traditional astrophysical messengers by a sea of background photons. High energy photons suffer horizon effects when they reach energies sufficient to pair produce electrons on the infrared and cosmic microwave background. High energy protons scatter on the cosmic microwave background when their energies exceed $5 \times 10^{19}\,\mathrm{eV}$, producing a spray of short lived π-mesons [17]. Surviving protons have reduced energy and their trajectories are bent by weak extra-galactic magnetic fields obscuring their direction of origin. New detection technologies are required to see into the highest energy processes in the distant Universe.

A flux of ultra-high energy cosmogenic neutrinos is expected from the decay of charged π-mesons created by the highest energy protons scattering on the cosmic microwave background [18]. Detecting these neutrinos is a challenge because the expected flux is low and neutrinos do not interact readily with ordinary matter. However, the rewards would be great. Neutrinos do not suffer from the horizon effects that plague protons and photons and they travel through space undeflected by the weak extra-galactic magnetic fields. A measurement of the properties of a statistically significant sample would also allow new tests of fundamental physics as their energies are orders of magnitude greater than what can be produced on Earth

with current technology. Their detection would illuminate the Universe in a new light at the longest distances and highest energies.

ANITA is an innovative experiment designed to search for cosmogenic neutrinos. Neutrino interactions are expected to produce a sizeable radio impulse. By hanging radio detectors from a balloon suspended above the ice sheets of Antarctica it views 1 million km^3 scanning for impulsive radio signals that are the telltale sign of an ultra-high energy neutrino interaction. Previous flights have set the world's best limit on the flux of ultra-high energy neutrinos arriving at the Earth [19, 20, 21].

The fourth iteration[1] of the ANITA experiment, ANITA-3, was flown in the 2014-15 austral summer. This thesis describes the various aspects of my work over the last four years on ANITA-3. Chapter 2 gives a brief introduction to neutrino physics. Chapter 3 gives a brief introduction to cosmic rays up to the GZK cutoff at 5×10^{19} eV and discusses the motivation to look for a cosmogenic flux of ultra-high energy neutrinos. Chapter 4 motivates the use of radio to look for energetic particle showers, with particular focus of ultra-high energy neutrino detection in ice. In Chapter 5, I introduce the ANITA instrument. In Chapter 6, I describe my work in doing the timing calibration of the digitizers and signal chain. In Chapter 7, I give a brief summary of the ANITA-3 flight during the 2014-15 austral summer. Chapter 8 describes my implementation of the event reconstruction. Chapter 9 contains a summary of my work to produce an GPU based interferometric event prioritizer for instrument telemetry. In Chapter 10, I describe my analysis for evidence of ultra-high energy neutrinos and cosmic rays in the ANITA-3 data set. Finally, in Chapter 11 I summarise my results and comment on the outlook for the ANITA-4 flight, which is taking place at the end of this year.

[1] Including the prototype ANITA-lite flight.

Chapter 2

The Standard Model and Neutrino Physics

2.1 The Standard Model

The Standard Model of Particle Physics is a spectacularly successful theory that describes the interaction of fundamental particles. The theory describes three of the four known fundamental forces: electromagnetism, the strong nuclear force, and the weak nuclear force.

The standard model is an $SU(3) \times SU(2) \times U(1)$ gauge theory of quantum fields. Matter is made of particles called fermions with intrinsic angular momentum, spin-$\frac{1}{2}$, and forces are carried by vector bosons with spin-1. Each force couples to a different type of charge. For each particle there is an anti-particle which carries an opposite unit of each type of charge.

2.1.1 The Bosons

The three forces in the Standard Model are mediated by one or more bosons. The properties of the bosons determine the macroscopic features of the forces.

The electromagnetic (EM) force is mediated by a single boson, the photon. The photon couples to electric charge, and the EM forces extends over an infinite range because the photon is massless.

The Weak force is mediated by the electrically charged $W^{\pm}$ bosons and the neutral Z^0 boson, with masses 80.36 GeV and 91.19 GeV, respectively. These large

masses mean the Weak nuclear force can only act over a short distance, making it appear weak compared to electromagnetic forces. The $W^{\pm}, Z^0$ bosons couple to weak isospin, the only type of charge carried by all fermions in the standard model.

The Strong force is mediated by eight gluons, g, and couples to a type of charge called colour. There are three colour charges red (r), blue (b), and green (g) and anti-charges $\bar{r}$, $\bar{g}$, $\bar{b}$. Gluons carry one colour and one anti-colour charge. The theory describing the interaction of particles carrying colour charge is called quantum chromodynamics (QCD). In QCD the attractive force between colour charges does not diminish with distance, but particles carrying colour are asymptotically free at very short distances and high energies. The gluons have zero mass but because they carry colour charge they are never found in isolation, but always with other colour charged particles (see Section 2.1.2.1).

2.1.2 The Fermions

The fermions are divided into two groups, quarks and leptons. There are six types of quark and six types of lepton.

2.1.2.1 Quarks

The six quarks flavours are: up u, down d, charm c, strange s, top t, and bottom, b. The quarks, q, carry one of three colour charges, r, g, b and anti-quarks, $\bar{q}$, carry the corresponding anti-charges, $\bar{r}$, $\bar{g}$, $\bar{b}$. Quarks and gluons are confined into colour-neutral or "colourless" particle states called hadrons. Hadrons composed of either three quarks with colour states rgb (baryons) or a quark anti-quark pair with colour states $r\bar{r}$, $g\bar{g}$, or $b\bar{b}$ (mesons). The only stable baryon is the proton (uud). The Neutron (udd) is only stable when inside an atomic nucleus. All mesons are unstable, however particles like the charged pions $\pi^{\pm}(u\bar{d})(d\bar{u})$ and neutral pion, $\pi^0(\frac{1}{\sqrt{2}}(u\bar{u}-d\bar{d})$ are commonly produced in nuclear scattering.

Other than colour, the quarks also carry weak isospin and electric charge. The u, c, t have $\frac{+2e}{3}$, and d, s, b have $\frac{-e}{3}$. The quarks are grouped in three generations of

weak isospin doublets, as shown in (2.1).

$$\begin{pmatrix} u \\ d \end{pmatrix} \begin{pmatrix} c \\ s \end{pmatrix} \begin{pmatrix} t \\ b \end{pmatrix} \tag{2.1}$$

The u,c,t and b,s,d quarks are identical in every respect except for their mass, which increases in each generation.

2.1.2.2 Leptons

Like the quarks there are six lepton flavours. Only three carry electric charge. These are the electron (e), muon (μ), and tau (τ), all with electric charge $-e$. For each charged lepton there is a corresponding neutral lepton, the electron neutrino (ν_e), muon neutrino (ν_μ), and tau neutrino, ν_τ. Like the quarks the leptons are grouped into three generations (2.2) of weak isospin doublets with identical properties except for their mass.

$$\begin{pmatrix} \nu_e \\ e \end{pmatrix} \begin{pmatrix} \nu_\mu \\ \mu \end{pmatrix} \begin{pmatrix} \nu_\tau \\ \tau \end{pmatrix} \tag{2.2}$$

The charged leptons interact via the EM and Weak forces, but the electrically neutral, colour free neutrinos only interact via the Weak nuclear force. In the original formulation of the Standard Model, the neutrinos were massless, however experimental observations over the last couple of decades require non-zero neutrino masses.

2.2 Neutrinos Physics

The neutrino, meaning "little neutral one", was originally proposed by Wolfgang Pauli [22] in 1930 as a light, electrically neutral particle produced in β-decay (2.3), to account for the missing energy and momentum in the electron and nuclear recoil.

$$n \rightarrow p^+ + e^- + \overline{\nu_e} \tag{2.3}$$

Its existence was experimentally confirmed in 1953 with the Cowan-Reines experiment [23], which measured the change in rate of inverse β-decay (2.4) in the pres-

ence of an active nuclear reactor, which is a source of $\overline{\nu_e}$

$$p^+ + \overline{\nu_e} \rightarrow n + e^+ \tag{2.4}$$

The existence of different flavours of neutrino was confirmed with the discovery of the ν_μ by a team of researchers at Brookhaven National Laboratory in 1962 using a beam of neutrinos produced by a particle accelerator, when they observed neutrinos that produced muons rather than electrons [24].

2.2.1 The Solar Neutrino Problem

Neutrinos are detected when they exchange a $W^\pm$ or Z^0 with electrons or quarks inside atomic nuclei. When a $W^\pm$ is exchanged, the incident neutrino flavour is determined by the flavour of the charged lepton. This is a Charged Current (CC) interaction. When a Z^0 is exchanged it is not possible to determine the flavour state of the incident neutrino. This is a Neutral Current (NC) interaction. Feynman diagrams from these interactions are shown in Figure 2.1.

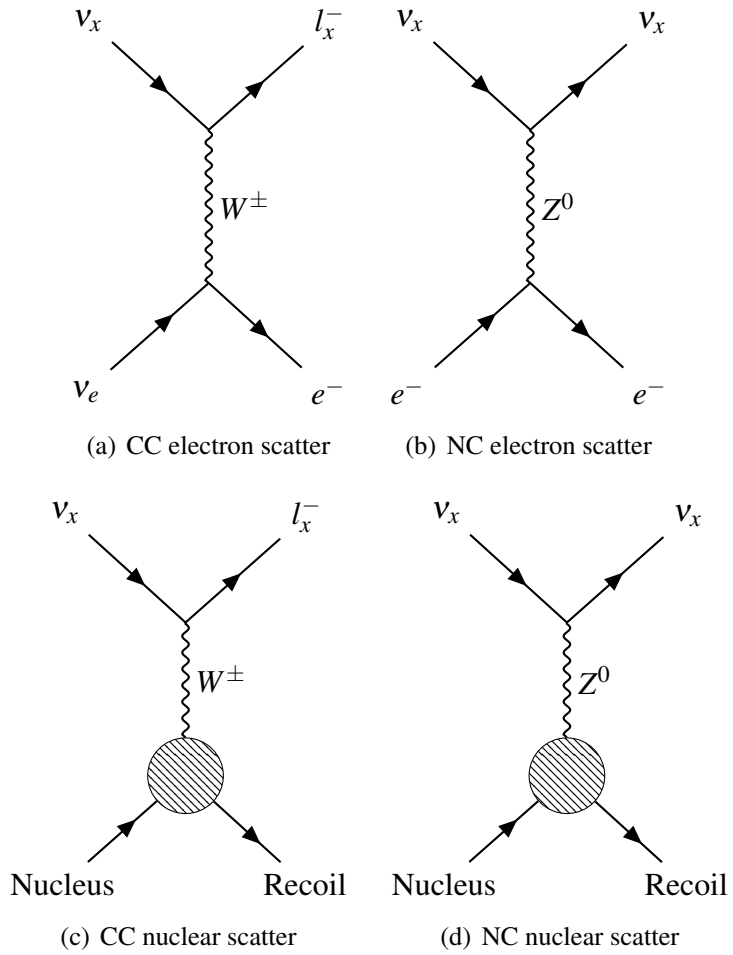

(a) CC electron scatter (b) NC electron scatter

(c) CC nuclear scatter (d) NC nuclear scatter

Figure 2.1: Feynman diagrams showing the CC and NC neutrino interactions with electrons and quarks inside the nucleus.

From the early 1970s, solar neutrino detection experiments, such as the Homestake Mine Experiment [25], measured a lower flux of ν_e arriving at the Earth than expected based on models of nuclear reactions in the sun's core. This "solar neutrino problem" was not solved until the early 2000s, when the Sudbury Neutrino Observatory (SNO) measured the total neutrino flux ($\nu_e + \nu_\mu + \nu_\tau$) from the sun [26]. Previous measurements, such as the one made by Super-Kamiokande [27], were only sensitive to ν_e interaction. The total neutrino flux measured by SNO agreed with models of the sun's nuclear reactions, but the distribution of flavours did not.

2.2.2 Neutrino Oscillation

The phenomenon of neutrino changing flavour is explained most conservatively by two changes to the Standard Model. Firstly, the neutrino weak flavour eigenstates ν_e, ν_μ, ν_τ are not identical to the mass eigenstates ν_1, ν_2, ν_3 (with masses m_1, m_2, m_3). Secondly, at least two of the mass eigenstates must be non-zero.

In this framework, the flavour eigenstates are a linear superposition of the mass eigenstates, with the coefficients $U_{\alpha i}$, given by the elements of the Pontecorvo-Maki-Nakagawa-Sakata (PMNS) matrix [28, 29], U.

$$\begin{pmatrix} \nu_e \\ \nu_\mu \\ \nu_\tau \end{pmatrix} = \begin{pmatrix} U_{e1} & U_{\mu 2} & U_{\tau 3} \\ U_{e1} & U_{\mu 2} & U_{\tau 3} \\ U_{e1} & U_{\mu 2} & U_{\tau 3} \end{pmatrix} \begin{pmatrix} \nu_1 \\ \nu_2 \\ \nu_3 \end{pmatrix} \tag{2.5}$$

The PMNS matrix is commonly represented as the product of three matrices with four free parameters,

$$U = \begin{pmatrix} 1 & 0 & 0 \\ 0 & c_{23} & s_{23} \\ 0 & -s_{23} & c_{23} \end{pmatrix} \begin{pmatrix} c_{13} & 0 & -s_{13}e^{-i\delta_{CP}} \\ 0 & 1 & 0 \\ s_{13}e^{i\delta_{CP}} & 1 & c_{13} \end{pmatrix} \begin{pmatrix} c_{12} & s_{12} & 0 \\ -s_{12} & c_{12} & 0 \\ 0 & 0 & 1 \end{pmatrix} \tag{2.6}$$

where

$$s_{ij} = \sin(\theta_{ij}) \text{ and } c_{ij} = \cos(\theta_{ij}) \tag{2.7}$$

and θ_{ij} is the mixing angle between the flavour state i and mass state j and δ_{CP} is a *CP* violating phase.

In this framework the probability of finding a neutrino in a different flavour state will oscillate with distance. To see how this follows, consider the simpler case of two neutrino flavours, ν_α, ν_β. In this scheme the PMNS matrix is replaced by a two dimensional rotation matrix, with mixing angle θ.

$$\begin{pmatrix} \nu_\alpha \\ \nu_\beta \end{pmatrix} = \begin{pmatrix} \cos(\theta) & \sin(\theta) \\ -\sin(\theta) & \cos(\theta) \end{pmatrix} \begin{pmatrix} \nu_1 \\ \nu_2 \end{pmatrix} \tag{2.8}$$

Neutrinos are created with a definite flavour state ν_e and momentum state p at a time $t = 0$.

$$|\nu_\alpha(0)\rangle = \cos(\theta)\,|\nu 1\rangle + \sin(\theta)\,|\nu_2\rangle \tag{2.9}$$

This state then propagates for a time, t. An exact treatment of the propagating neutrino states requires describing them as spatially extended wave packets [30]. However, the broad features of the phenomenon emerge from treating them as completely localised, evolving each mass state $|\nu_i\rangle$ to $e^{iE_i t}\,|\nu_i\rangle$.

$$\begin{aligned}
|\nu_\alpha(t)\rangle &= \cos(\theta)e^{iE_1 t}\,|\nu_1\rangle + \sin(\theta)e^{iE_2 t}\,|\nu_2\rangle \\
&= \cos(\theta)e^{iE_1 t}\left(\cos(\theta)\,|\nu_\alpha\rangle - \sin(\theta)\left|\nu_\beta\right\rangle\right) + \sin(\theta)e^{iE_2 t}\left(\sin(\theta)\,|\nu_\alpha\rangle + \cos(\theta)\left|\nu_\beta\right\rangle\right) \\
&= \left(\cos^2(\theta)e^{iE_1 t} + \sin^2(\theta)e^{iE_2 t}\right)|\nu_\alpha\rangle + \sin(\theta)\cos\theta\left(e^{iE_2 t} - e^{iE_1 t}\right)\left|\nu_\beta\right\rangle
\end{aligned} \tag{2.10}$$

where from the last line in Equation (2.10) the $\left|\nu_\beta\right\rangle$ state amplitude is non-zero if $\theta \neq 0$ or π, and $E_1 \neq E_2$. The probability of finding the neutrino in flavour state $\left|\nu_\beta\right\rangle$ is then

$$\begin{aligned}
P(\nu_\alpha \to \nu_\beta) &= \left\langle \nu_\beta \middle| \nu_\alpha \right\rangle \\
&= (\sin(\theta)\cos(\theta)(e^{iE_2 t} - e^{iE_1 t}))^* \quad (\sin(\theta)\cos\theta(e^{iE_2 t} - e^{iE_1 t})) \\
&= \sin^2(\theta)\cos^2(\theta)(2 - (e^{i(E_2 - E_1)t} - e^{-i(E_2 - E_1)t})) \\
&= \sin^2(2\theta)\sin^2\left(\frac{(E_2 - E_1)t}{2}\right)
\end{aligned} \tag{2.11}$$

In the limit that $m_i \ll E_i$,

$$E_i = \sqrt{p^2 + m_i^2} = p^2 + \frac{m_i^2}{2p} \tag{2.12}$$

$$(E_2 - E_1)t = \frac{(m_2^2 - m_1^2)L}{2p} \tag{2.13}$$

where the neutrinos have travelled a distance $L = t$ in natural units and when not considering the differences between energies $p = E$, we can rewrite equation (2.11)

as

$$P(\nu_\alpha \to \nu_\beta) = \sin^2(2\theta)\sin^2\left(\frac{\Delta m^2_{21}}{4}\frac{L}{E}\right) \tag{2.14}$$

From equation (2.14) we see that the oscillation probability depends the mixing angle θ, the difference between the squares of the masses, Δm^2_{12}. Equation (2.14) also implies that experimenters can maximise the effects of neutrino oscillations by choosing neutrino energy E and travel distance L such that $\sin^2\left(\frac{\Delta m_{12}}{4}\frac{L}{E}\right)$ is maximal.

2.2.3 Neutrino Oscillation Measurements

Over the last couple of decades there have been a suite of experiments at different L/E designed to measure the neutrino mixing angles θ_{ij} and squared mass differences Δm^2_{ij}.

The Sudbury Neutrino Observatory (SNO) [31], and Super-Kamiokande [32] have measured the disappearance of solar ν_e between the Earth and Sun. Super-Kamiokande [33] (and more recently IceCube [34]) has also measured the disappearance of atmospheric $\nu_\mu, \overline{\nu_\mu}$, produced by the decays of pions and kaons created by cosmic ray showers in the upper atmosphere. Reactor neutrino experiments, such as KamLAND [35], Daya Bay [36], and RENO [37] have measured the disappearance of $\overline{\nu_e}$ produced in nuclear reactors.

Long-baseline accelerator experiments are in control of their primary neutrino flux and as such can finely control their energy and distance baseline. Neutrinos are produced with particle accelerators beam and sent through a near and far detector. Experiments such as MINOS [38, 39], T2K [40] have confirmed the disappearance of ν_μ and saw evidence of the appearance of ν_e. OPERA [41] has reported disappearance of ν_μ and appearance of ν_τ.

The best-fit to the oscillation parameters using data from all experiments is shown in table 2.1.

Table 2.1: Best fit values of the three neutrino mixing oscillation parameters reproduced from [4].

Parameter	Value $\pm 1\sigma$
Δm^2_{21}	$7.54^{+0.26}_{-0.22} \times 10^5\,\mathrm{eV}^2$
Δm^2	$2.43 \pm 0.06 \times 10^3\,\mathrm{eV}^2$
$\sin^2(\theta_{21})$	0.308 ± 0.017
$\sin^2(\theta_{32})(\Delta m^2_{32} > 0)$	$0.437^{+0.033}_{-0.023}$
$\sin^2(\theta_{23})(\Delta m^2_{32} < 0)$	$0.455^{+0.039}_{-0.031}$
$\sin^2(\theta_{13})(\Delta m^2_{32} > 0)$	$0.0234^{+0.0020}_{-0.0019}$
$\sin^2(\theta_{13})(\Delta m^2_{32} < 0)$	$0.0240^{+0.0019}_{-0.0022}$
δ/π (2σ range quoted)	$1.39^{+0.38}_{-0.27}(1.31^{+0.29}_{-0.33})$

As indicated in Table 2.1, the ordering of the neutrino mass states is currently unknown. Depending on the sign of Δm^2_{32}, the neutrino mass states could be ordered $m_1 < m_2 < m_3$ (normal hierarchy), or $m_3 < m_1 < m_2$ (inverted hierarchy).

2.3 Ultra-High Energy Neutrinos and Beyond the Standard Model Physics

Despite the successes of the Standard Model it is not a complete description of nature. Most glaringly, it does not describe gravity, which is 10^{32} times weaker than electro-weak forces. This enormous difference in strength between the forces is known as the hierarchy problem.

Models of large extra dimensions are designed to address the hierarchy problem by making gravity propagate in the extra dimensions but confining the three Standard Model forces to our regular 3 dimensions. With Plank masses $M_D \sim 1\,\mathrm{TeV}$ the interaction cross-sections of neutrino-nucleon scattering would be larger than Standard Model predictions at ultra-high energies. Figure 2.2 shows the enhancement of such cross-sections with gravitons and microscopic black holes for a variety of M_D from [1].

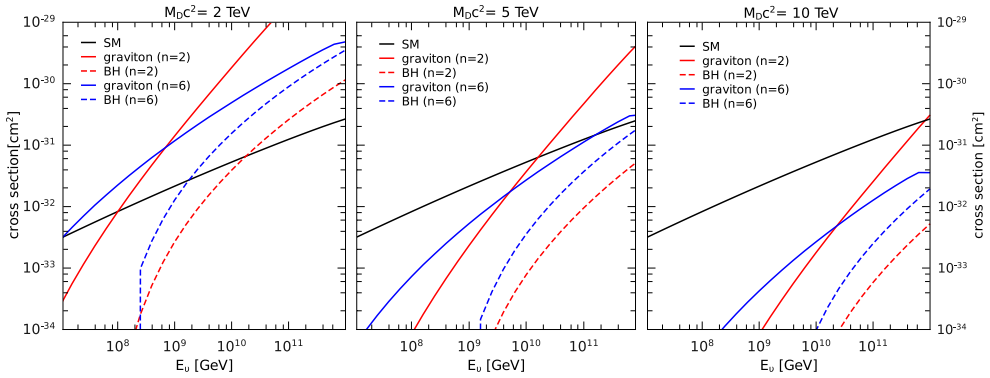

Figure 2.2: Enhancement of neutrino nucleon interaction cross-section with large extra dimensions. Figure from [1].

The energies required to observe these effects are well beyond the limits of current accelerators technologies. However, if one were to make a measurement establishing the existence of ultra-high energy neutrinos produced by cosmic sources, the Earth could be used as a shield to make cross-section measurements. The possible existence of such a flux is discussed in Chapter 3.

Chapter 3

Ultra-High Energy Astroparticle Physics

3.1 The Cosmic Ray Spectrum

Cosmic rays are protons and heavier atomic nuclei that bombard the atmosphere from space. They were discovered in 1912 when Victor Hess made a series of balloon flights with a detector and found that above 1km the intensity of ionising radiation increased with altitude [42].

Over the following century enormous progress was made in understanding the composition, sources and acceleration mechanisms of all but the highest energy cosmic rays. The discovery of Extended Air Showers by Pierre Auger [43], implied that primary cosmic rays, which create showers of secondary cosmic rays in the atmosphere, had energies at least as high as 10^{15} eV. Figure 3.1 shows the flux of cosmic rays detected at the Earth as a function of primary cosmic ray energy. The spectrum follows a power law over nearly ten decades of energy, with only slight variations in steepness.

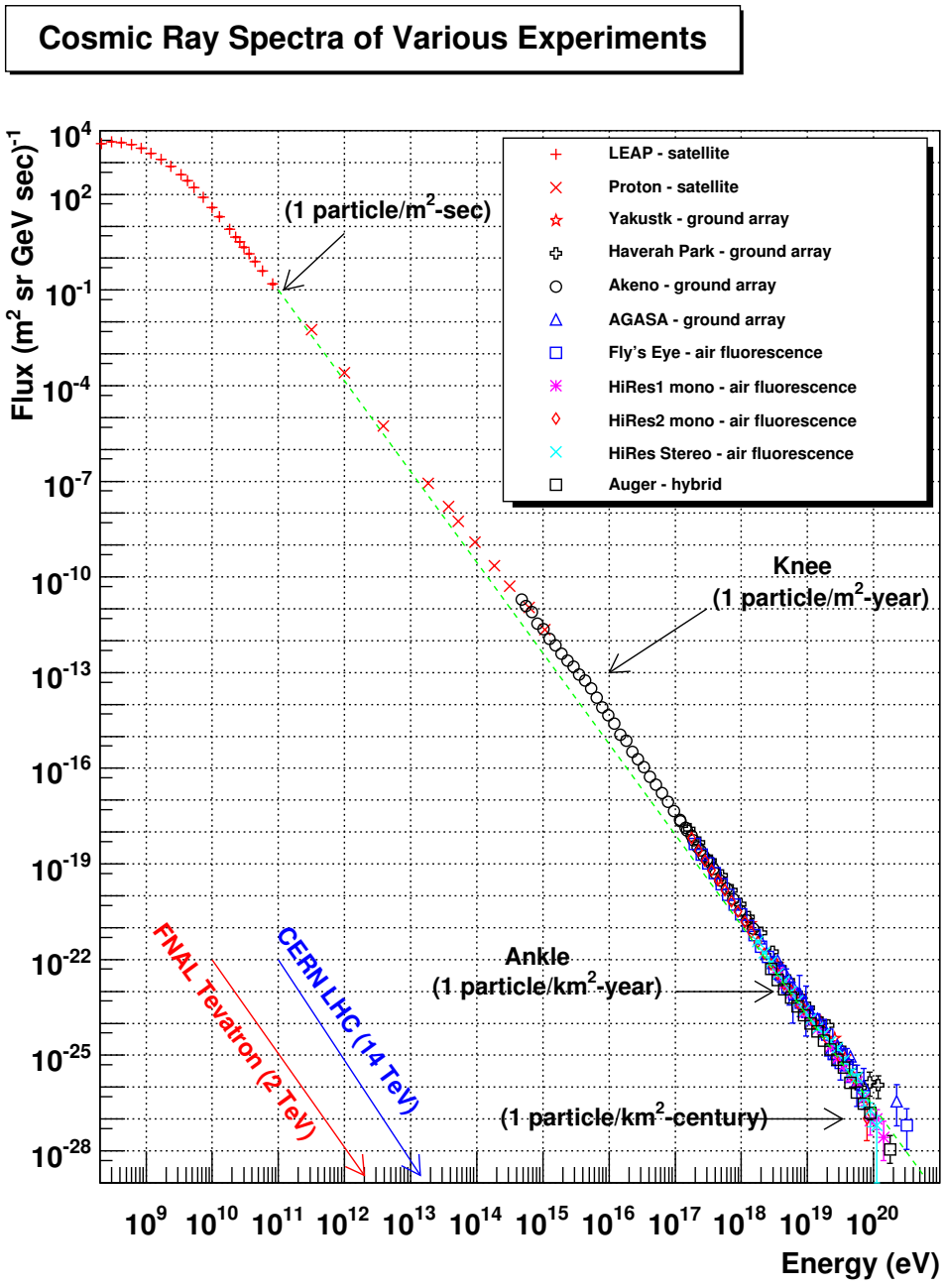

Figure 3.1: The cosmic ray energy spectrum over eleven orders of magnitude in energy. This is a reproduction of the plot by S. Swordy [2] made by W. Hanlon [3].

To a good approximation the primary nucleon intensity I_N is given by

$$I_N \propto \left(\frac{E}{1\,\mathrm{GeV}}\right)^{-\gamma} \frac{\text{nucleons}}{\mathrm{m^2\,sr\,GeV}} \quad , \tag{3.1}$$

where E is the energy of the cosmic ray and γ is the spectral index, I_N is the num-

ber of nucleons per unit area, per unit time, per unit of sky solid angle, per unit energy [4]. From 10^{10} eV to "the knee" in the spectrum at 3×10^{15} eV, Equation (10.26) models the flux well with $\gamma = 2.7$. Above the knee the spectrum becomes slightly steeper, $\gamma \approx 3$ until "the ankle" at 3×10^{18} eV where it briefly becomes shallower again, $\gamma \approx 2.6$ [5].

It is generally accepted that first order Fermi acceleration in supernova remnants in the milky way is the mechanism of cosmic ray acceleration up to the knee, perhaps as far as the ankle [44]. In this process, protons with energy E are magnetically scattered back and forth across the shock front in a supernova, gaining energy ΔE with each transition (3.2).

$$\frac{\Delta E}{E} \propto \beta \quad , \tag{3.2}$$

where $\beta = \frac{U}{c}$, U is the shock velocity and c is the speed of light. Supernova remnants populate the galaxy and generate cosmic rays with a spectral distribution index $\gamma \approx 2$. The cosmic rays propagate through the weak galactic magnetic field we measure a spectral index $\gamma = 2.7$ at the Earth. There are two theories for the steepening spectral slope at the knee.

The first interpretation is that the weak galactic magnetic fields no longer confine the cosmic rays inside our galaxy. The radius of curvature of a charged particle in a constant magnetic field, r_L (the Larmor radius), is given by equation (3.3).

$$r_L = \frac{p_\perp}{|q|B} \quad , \tag{3.3}$$

where $p_\perp$ is the particle's momentum perpendicular to the magnetic field, B, and q is the charge of the particle. In a population of relativistic particles with energy, $E = pc$, those with the lowest charge, q, have the largest Larmor radius. At some point the magnetic fields in the vicinity of the milky way, $r_{mw} = 10^{21}$ m, will no longer be able to confine the cosmic rays. The galactic population of cosmic rays will leak into the intergalactic medium, lightest elements first, lowering the chance of detection at the Earth, and steepening the cosmic ray spectrum.

The second interpretation for the steepening spectral index at the knee, is that

the astrophysical shock fronts in our galaxy cannot accelerate cosmic rays beyond a certain energy. The magnetic fields around the shock front must be strong enough to steer cosmic rays back and forth repeatedly. The Larmor radius must be smaller than the radius of the astrophysical accelerator, R. This is the Hillas criterion [45],

$$E_{\max} = \frac{|q|BR}{c} \quad , \tag{3.4}$$

where $E_{\max}$ is the maximum energy, q is the cosmic ray charge, B is the local magnetic field of astrophysical object with radius R, and c is the speed of light. This interpretation also implies a transition to heavier primaries since $E_{\max} \propto q$.

Heavier primaries beyond the knee have been measured by The KASCADE experiment [46] and the upgraded KASCADE-Grande experiment [47].

3.2 The GZK Effect

Cosmic rays with $E > 3 \times 10^{18}\,\text{eV}$ are known as ultra-high energy cosmic rays (UHECRs). The UHECR regime begins at the ankle, where the spectral index flattens. This is commonly interpreted as the presence of an extra-galactic flux of cosmic rays beginning to dominate over the galactic flux. At the tail of the cosmic ray spectrum, around $5 \times 10^{19}\,\text{eV}$, the UHECR flux drops off quickly. Figure 3.2 shows the cosmic ray spectrum beyond the knee, multiplied by $E^{2.6}$ to emphasise the knee, ankle and cutoff.

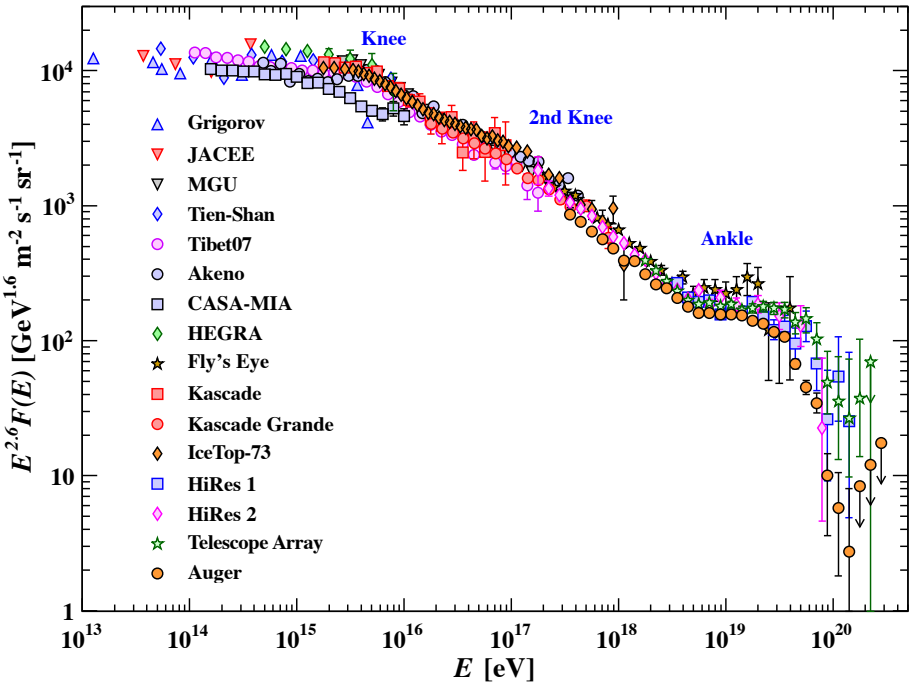

Figure 3.2: The high energy tail of the cosmic ray spectrum, multiplied by $E^{2.6}$ to emphasise the changes in spectral slope. Figure from [4].

The UHECR flux drop off at 5×10^{19} eV was independently predicted by Greisen [17], and Zatsepin and Kuzmin [48] in 1966 after the discovery of the Cosmic Microwave Background (CMB) in 1965 by Penzias and Wilson [49]. Greisen, Zatsepin and Kuzmin argued that a 5×10^{19} eV proton will interact with the 2.7 K photons, with a centre-of-mass energy that reaches the Δ^+ resonance at 1232 MeV. This leads to pion, $\pi^{+/0}$, production as shown in Equations (3.5) and (3.6).

$$p^+ + \gamma_{\text{CMB}} \rightarrow \Delta^+ \rightarrow \pi^0 + p^+ \tag{3.5}$$

$$p^+ + \gamma_{\text{CMB}} \rightarrow \Delta^+ \rightarrow \pi^+ + n \tag{3.6}$$

The incident protons are either converted to unstable neutrons, or emerge from the interaction with less energy. This attenuation by the CMB means that protons with $E_{p^+} > 5 \times 10^{19}$ eV cannot propagate beyond ~ 50 Mpc, causing the reduced flux at the Earth. This mechanism is known as the GZK effect after Greisen, Zatsepin and Kuzmin.

At the tail of the cosmic ray spectrum particles with energies $E > 10^{20}\,\text{eV}$ have been observed. Determining the source of the highest energy cosmic rays is difficult because the flux is very low and the cosmic rays are deflected by weak extra-galactic magnetic fields during propagation. Equation (3.4) places limits on the radius, R, and local magnetic field, on the type of astrophysical object that can accelerate a cosmic ray to such energies. Figure 3.3 is a Hillas Plot [45] of classes of astrophysical object as a function of B and R. The area above the solid lines indicate regions allowed for acceleration by the Hillas Criterion. Supernova remnants are excluded as sources of 10^{20} eV cosmic rays.

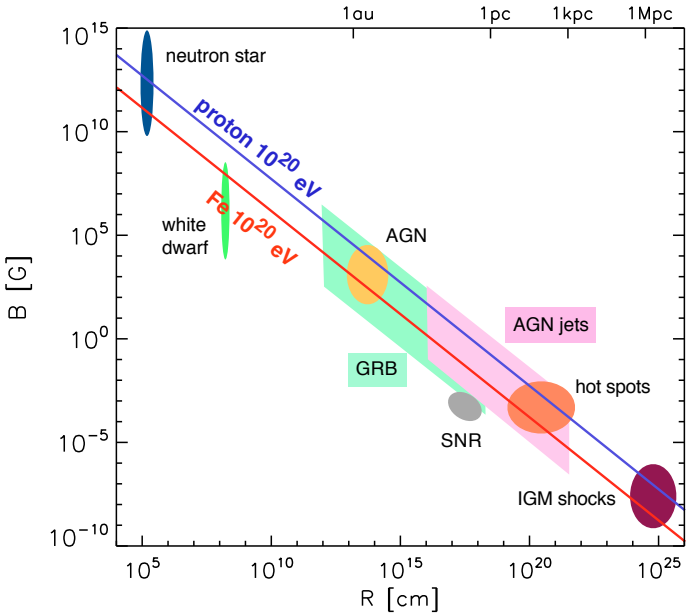

Figure 3.3: A Hillas Plot of candidate UHECR sources taken from [5]. Various astrophysical objects are plotted as a function of local magnetic field, B, and radius, R. The area above the red line indicates the allowed region for iron acceleration. The area above the blue line indicates allowed regions for proton acceleration.

In 2015, the Pierre Auger Observatory reported no significant anisotropy in the arrival direction of cosmic rays with energies above the GZK cutoff [50]. If this trend continues, then determining the sources of the highest energy cosmic rays by their arrival direction will not be possible.

3.3 Cosmogenic Neutrinos

In 1969 Beresinsky and Zatsepin noted that the universe is transparent to neutrinos up to 10^{25} eV [18]. The processes that produce horizon effects for photons, protons, and heavier nuclei do not affect neutrinos because they do not interact electromagnetically or via the strong nuclear force. Neutrinos also travel to the Earth without being deflected by the weak magnetic fields between the their source and the Earth. Figure 3.4 shows the horizon of protons and photons as a function of energy.

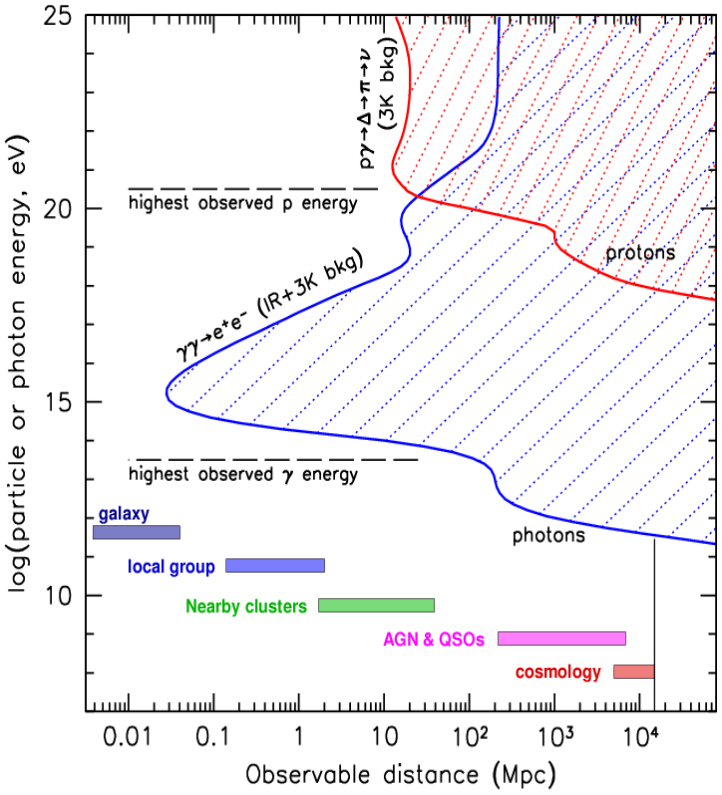

Figure 3.4: Horizon of protons and photons at different energy scales. Shaded blue region is not observable with photons, shaded red region is not observable with protons. The universe is transparent to neutrinos throughout the plotted parameter space. Plot by Peter Gorham.

Beresinsky and Zatsepin also noted that a flux of ultra-high energy neutrinos (UHEN) would be produced by the decay of charged pions from the GZK effect, Equation (3.5). Equation (3.7) shows the production processes for cosmogenic neu-

trinos.

$$\begin{aligned} \pi^+ &\rightarrow \mu^+ + \nu_\mu \\ &\downarrow \\ \mu^+ &\rightarrow \overline{\nu_\mu} + e^+ + \nu_e \quad , \end{aligned} \tag{3.7}$$

where the μ^+ also decays to produce more neutrinos. A few percent of the incident proton energy is carried by each neutrino, producing several UHEN with $E \sim 10^{18}$ eV. Figure 3.5 shows the ultra-high energy neutrino flux from a particular source model assuming a pure proton spectrum.

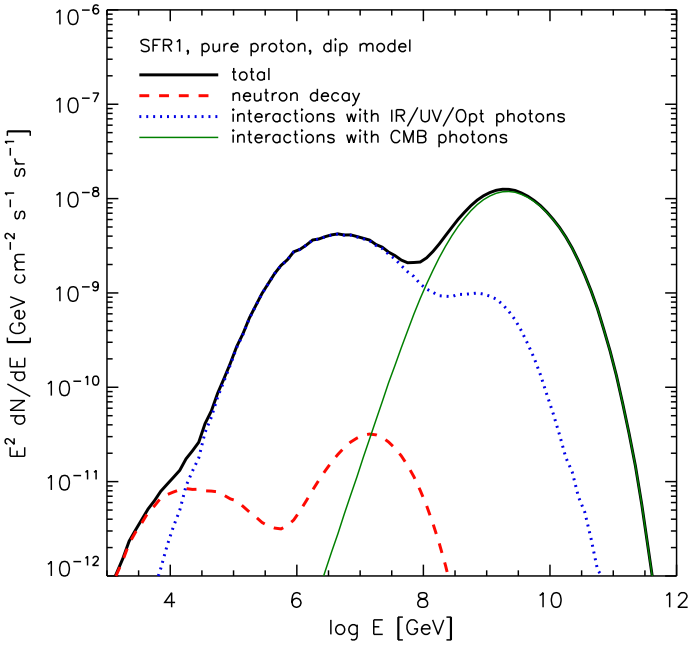

Figure 3.5: Contribution to the UHEN flux from different decay mechanisms in with a pure proton cosmic ray flux. Figure from [6].

Uncertainties in the chemical composition of the cosmic rays, source energy spectrum and maximum energy, and source evolution history all play a role in determining the expected flux of neutrinos arriving at the Earth [5]. The primary attenuation process for cosmic ray primaries heavier than protons is not the GZK mechanism. Instead, CMB and Extra-galactic Background Light (EBL) photons

cause disintegration of the nuclei (Equation 3.8).

$$A + \gamma_{\text{CMB, EBL}} \rightarrow (A - nN) + nN \quad , \tag{3.8}$$

reducing the atomic number of the primary to from A to $A - nN$, where the primary cosmic ray with A nucleons has ejected n of them. In this scenario UHEN can still be produced by photon scattering of the ejected nucleons, as long as the cosmic ray energy per nucleon is above the pion production threshold. Since the energy per nucleon is smaller for heavier primaries, the UHEN flux is significantly suppressed in models where an iron rich cosmic rays composition is combined with low maximum energies. Figure 3.6 shows four models from 10^{14} eV to 10^{21} eV. The ultra-high energy neutrino flux varies by orders of magnitude at the highest energies.

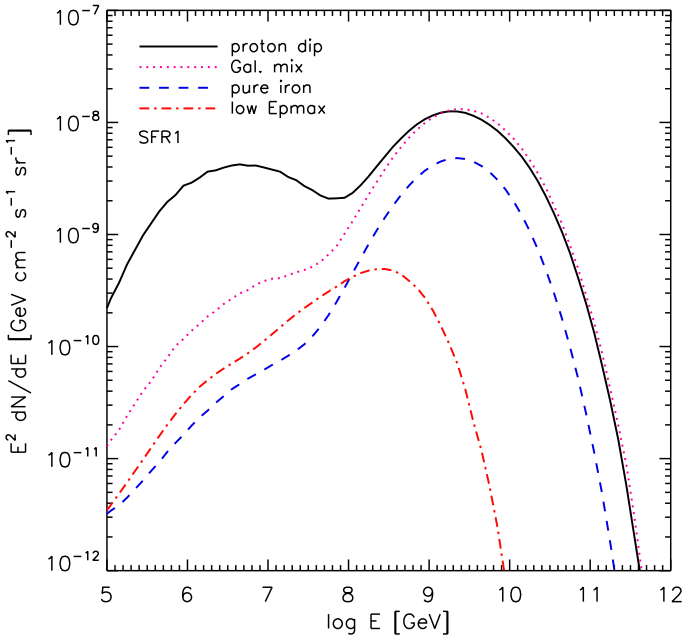

Figure 3.6: Four different models of UHEN from [6]. The black line indicates a pure proton spectrum. The pink dotted line is a proton dominated mixed composition. The blue dashed line is a pure iron spectrum. The red dash-dotted line is an iron rich spectrum with low accelerator maximum energy.

3.4 Summary

Ultra-high energy neutrinos have a lot of potential as astrophysical messengers. Measuring the flux at the Earth will constrain the parameter space of cosmic ray acceleration. Since they travel to the Earth without magnetic deflection, their arrival direction indicate the sources of the highest energy particles in the Universe.

Chapter 4

Radio Emission in Ultra-High Energy Particle Showers

Large detection volumes are required to measure the low flux of cosmogenic neutrinos. Radio detection using ice as a detection volume is a promising avenue for cosmogenic neutrino searches because radio has an attenuation length $O(1\,\mathrm{km})$ in ice [51]. This allows large detection volumes to be instrumented relatively sparsely, making experiments cost effective. Several experiments, such as ARA [52], ARIANNA [53], and of course ANITA [19], aim to use this technique to search for ultra-high energy neutrinos. ANITA also has some sensitivity to the radio emission from cosmic ray induced air showers, which is discussed at the end of this chapter.

4.1 Cherenkov Radiation

Cherenkov radiation is produced when a charged particle travels through a dielectric medium faster than the speed of light in that medium. To detect a neutrino interaction, a detection volume like ice or water is populated with photo-multiplier tubes (PMTs). Charged particles created by the neutrino interaction travel through the volume faster than light. A cone of light is emitted at an angle θ_c to the particle track,

$$\cos(\theta_c) = \frac{1}{n\beta} \quad , \tag{4.1}$$

where $\beta = \frac{u}{c}$ is the particle speed as a fraction of the speed of light and n is the refractive index of the medium. The process is illustrated in Figure 4.1

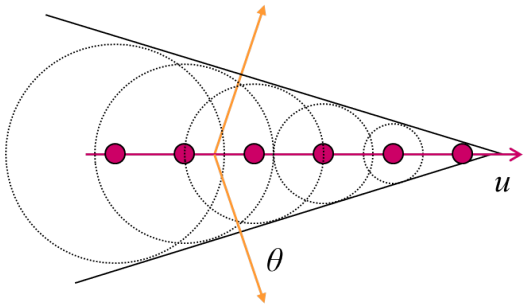

Figure 4.1: Cherenkov radiation is emitted at an angle θ_c when a particle travels through a dielectric medium faster than the speed of light in that medium. Figure from [7].

The Cherenkov radiation energy, E, per unit length, x, per unit frequency, ω, is given by Frank-Tamm formula, Equation (4.2).

$$\frac{dE}{dx\,d\omega} = \frac{q^2}{4\pi}\mu(\omega)\omega\left(1 - \frac{1}{\beta^2 n^2(\omega)}\right) \quad , \tag{4.2}$$

where q is the charge of the particle, $\mu(\omega)$ is the frequency dependent dielectric magnetic permeability, and $n(\omega)$ is the refractive index. The magnetic permeability, $\mu(\omega)$, characterises the magnitude of an auxiliary magnetic field, $\mathbf{H}$, created inside a medium when a megnetic field $\mathbf{B}$, is applied such that $\mathbf{H} = \mu\mathbf{B}$.

4.2 Askaryan Radiation

The idea to use radio to register energetic particle showers was first considered in the 1960s by Gurgen Askaryan [54]. He noted that a negative charge excess would develop in an electromagnetic shower in a dielectric medium. Electron-positron pairs are created as the shower develops, but positrons are removed by annihilation with the atomic electrons, which are also Compton scattered into the shower. This creates a $\sim 20\%$ negative charge excess at the shower maximum. The negative charge excess travels faster than the speed of light in the medium, producing Cherenkov radiation at an angle θ_c to the shower axis.

Examining Equation (4.2) one would naively expect that the power emitted in the radio frequency portion of electromagnetic spectrum would be many orders of magnitude lower than that of visible light. However, for wavelengths larger than

the transverse size of the shower, the Cherenkov radiation from all particles in the shower interferes constructively to produce a significant radio frequency (RF) pulse, called Askaryan radiation.

At the shower maximum, the number particles, N, and therefore the charge excess, q, are directly proportional to the energy of the initial particle. Equation 4.2 implies that the coherent power in an Askaryan pulse scales with the square of the incident particle energy, making the technique particularly attractive for high energy particle showers.

Askaryan radiation also benefits from a dense dielectric medium. The use of dense materials contains the shower in a smaller volume, so shorter wavelengths (higher frequencies) contribute to the Askaryan pulse. Integrating equation (4.2) over frequency, ω, (assuming constant $n(\omega), \mu(\omega)$) the power quadruples if the radial extent of the shower is halved.

Experimental measurements of the Askaryan effect have been made in silica sand [55], rock salt [8], and ice [9], confirming their suitability as materials for the radio detection of ultra-high energy neutrinos. An example of a pulse induced by the Askaryan effect is shown in Figure 4.2.

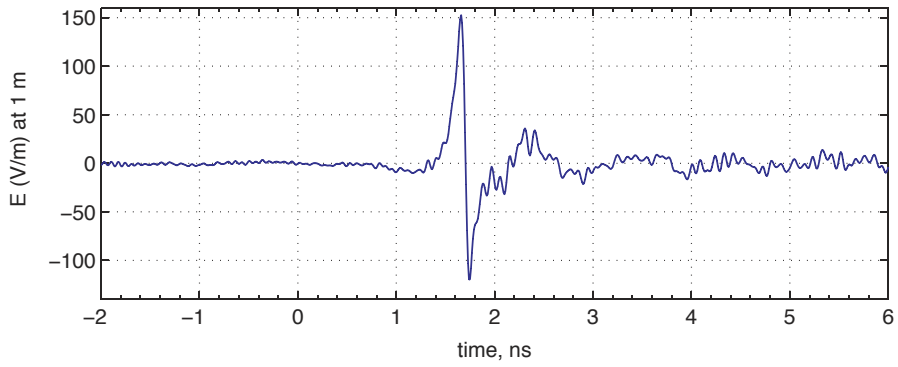

Figure 4.2: Example of an Askaryan pulse from a particle shower in rock salt. The ringing behind the pulse is a deconvolution effect. Figure taken from [8].

Figure 4.3 shows another experimental observation of the Askaryan effect. The power scales with the square of the shower energy.

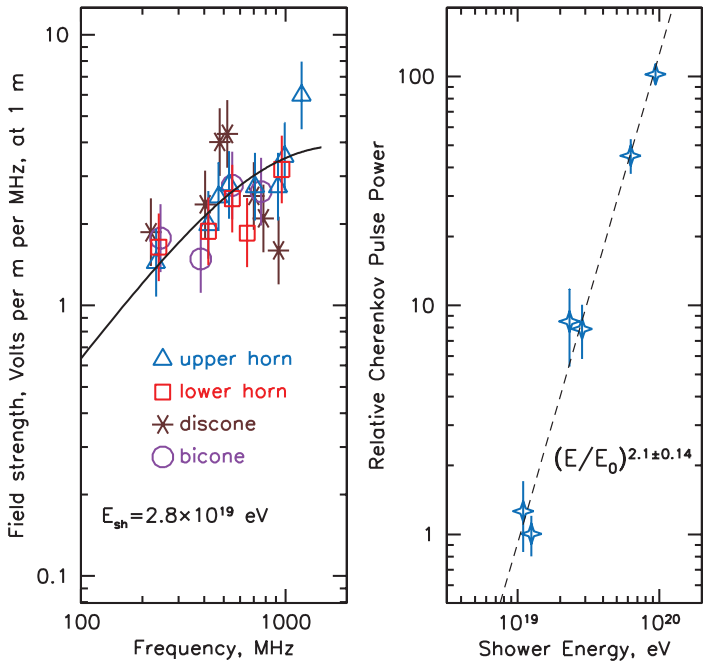

Figure 4.3: The left plot shows electric field strength as a function of frequency. The right plot shows the relative Cherenkov power scaling with the square of the shower energy. Plots from [9].

4.3 Radio Detection of Cosmic Rays

It has been known for over half a century that Extended Air Showers (EAS) also give rise to a radio emission [56]. Electron-positron pairs are created in an Extended Air Shower and curve in the Earth's magnetic field, emitting synchrotron radiation ("geo-synchrotron radiation"). (Cherenkov radiation and Askaryan radiation are present, but play a sub-dominant role.) The electrons and positrons are accelerated by the Lorentz force, $\mathbf{F} = q(\mathbf{v} \times \mathbf{B})$ in the Earth's magnetic field. Around the Earth's poles, the magnetic field direction is approximately vertical. The charged particles radiate perpendicular to $\mathbf{B}$ and particles in the shower. Around the south pole this produces predominantly horizontally polarised signals. In the frequency range from a few MHz to 100 MHz, emission from the entire shower interfere constructively and the radio emission from air showers is well described by the empirically deter-

mined Allan formula [57],

$$\varepsilon_\nu = 20\,\mu\mathrm{V\,m^{-1}\,MHz^{-1}} \left(\frac{E_p}{10^{17}\,\mathrm{eV}}\right) \sin(\alpha)\cos(\theta)\exp\left(\frac{-R}{R_0(\nu,\theta)}\right) \quad , \qquad (4.3)$$

where ε_ν is the amplitude of the electric field vector divided by the bandwidth, E_p is energy of the primary cosmic ray, α is the angle of the shower axis relative to the geomagnetic axis, θ is the zenith angle of the primary cosmic ray, R is the perpendicular distance from the shower axis, and R_0 is a frequency and angle dependent normalisation. In this simple picture, maximum power is detected when the observer is close to the shower axis.

Modern simulations include the effects of refractive index, which alters the lateral radiation profile. The geo-synchroton radiation travels through air slower than the electron-positron shower itself. This creates a Cherenkov-like effect and an instantaneous peak in received power at the Cherenkov angle, θ_c relative to the shower maximum. At the Cherenkov angle, radio emission along the length of the shower arrive with the minimum possible separation in time.

For frequencies above $\sim 100\,\mathrm{MHz}$, the emission along the shower profile does not interfere constructively along its length, meaning the optimum position for detection lies at the Cherenkov angle with respect to the shower axis. Models of the frequency content of the radio emission predict significant power emitted up to 3 GHz [58].

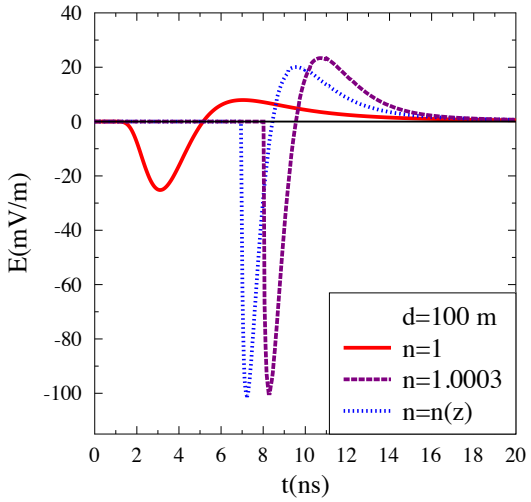

(a) Simulated enhancement to geo-magnetic pulses when including refractive index effects. Figure from [59].

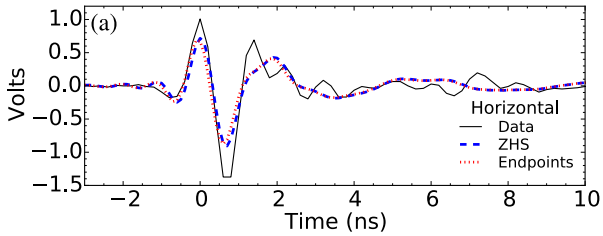

(b) Data and simulation of a magnetically induced radio pulse in a particle shower during the T-510 experiment [60].

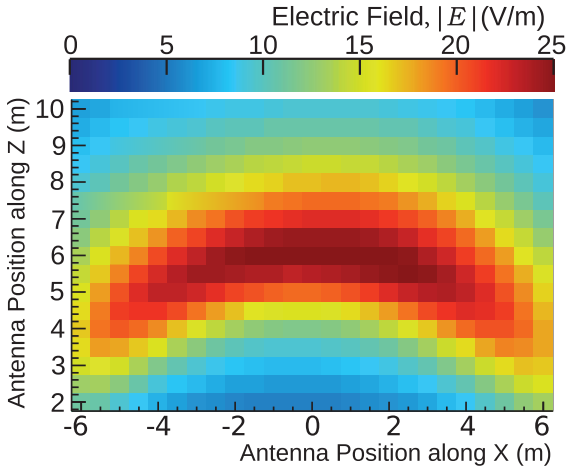

(c) Endpoints simulation of the cone shape of radio emission at T-510. Figure from [60].

Figure 4.4: Collection of plots illustrating geo-magnetic emission from cosmic ray air showers.

Figure 4.4a shows the enhancement of radio pulse in amplitude for an off-axis observer, when considering the effects of refractive index.

The validity of modern theoretical models of radio emission from air showers have been confirmed by a recent experiment at the Stanford Linear Accelerator (SLAC) by the T-510 experiment [60]. An electron beam was used to create particle cascades inside in a polyethylene target over a set of magnetic coils. Figure 4.4b shows the high frequency radio pulse induced perpendicularly to the magnetic field. A simulation of the radiation shows a Cherenkov-like cone shown in Figure 4.4c, which was confirmed by the experiment.

Chapter 5

The Antarctic Impulsive Transient Antenna

5.1 Introduction

The Antarctic Impulsive Transient Antenna (ANITA) is designed to search for ultra-high energy neutrinos. Its strategy is to measure the Askaryan radio emission generated by energetic particle showers in ice. Unlike experiments such as ARA [52] and ARIANNA [61], which aim to sparsely instrument $O(100)$ km^3 volumes of ice over several years to get sensitivity to the ultra-high energy neutrino flux, ANITA takes advantage of radio propagation in air by hanging its radio sensors from a helium balloon high above the ice, rather than inside it. At an altitude of 37 km ANITA's field of view encompasses a detection volume $O(10^6)$ km^3 of ice[1]. This larger detection volume offsets the relatively short flight time $O($a few weeks$)$ in exposure to the ultra-high energy neutrino flux [62] and has allowed previous flights to set world's best limits at the highest energies [19, 20, 21].

[1] Assuming an ice depth of 1 km

5.2 Layout

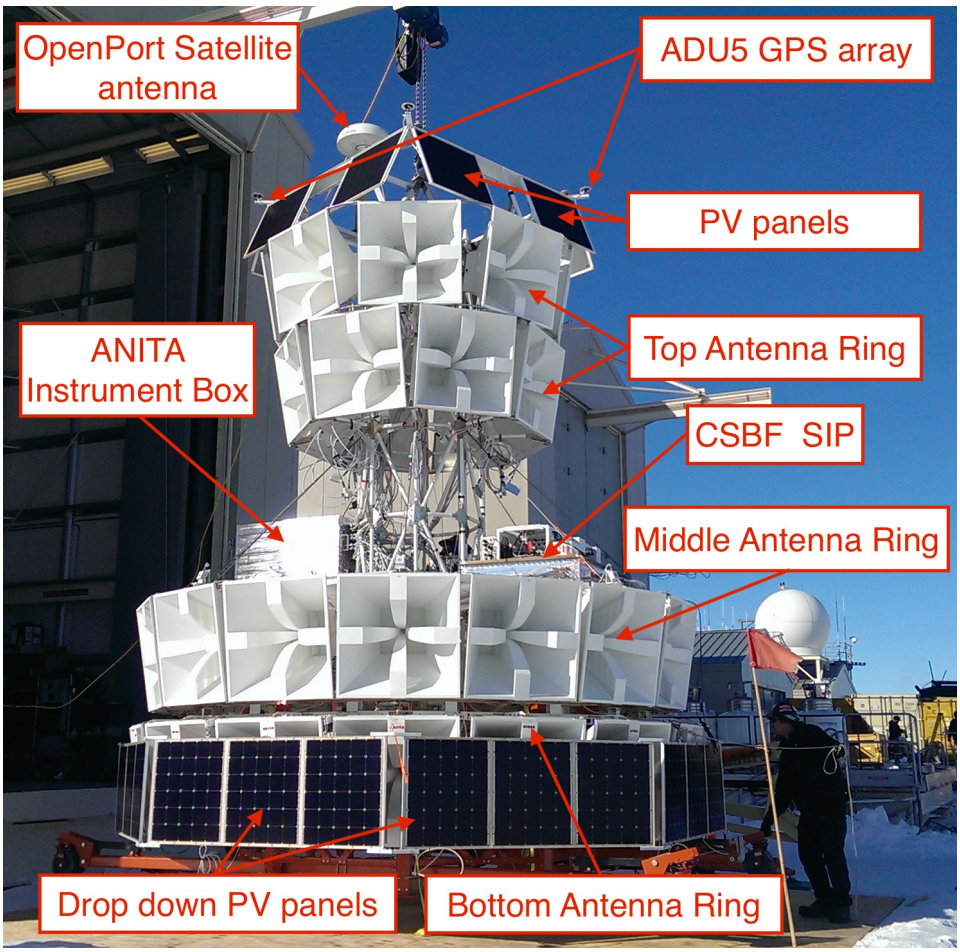

Figure 5.1: The ANITA payload hanging on a crane outside the Long Duration Balloon hangar in Antarctica. My photo from the 5th December 2014.

Figure 5.1 is a photo of ANITA-3 hanging from a crane outside the Long Duration Balloon (LDB) hangar in Antarctica. Many of the components necessary for such an experiment are visible and labelled. The black photo-voltaic (PV) panels are described in Section 5.12. The white horn antennas give ANITA 360° coverage in azimuth as it hangs from the balloon, they are described in Section 5.3. The antennas are angled 10° down for sensitivity to signals coming from ice near the horizon. The vertical size and radial profile of the ANITA payload are constrained by the size of the launch vehicle. This is why the top antenna ring is staggered into two narrow sub-rings, and why the bottom ring of PV panels drops down to reveal the bottom antenna ring after launch (see Figure 5.2).

The ANITA instrument box contains the majority of the electronics used to operate the experiment. It is housed in a Faraday cage in order to reduce electromagnetic interference (EMI) in the ANITA frequency range, much of this chapter content is dedicated to describing the electronics inside this box. The OpenPort satellite antenna is described in Section 5.11. The GPS antennas are described in Section 5.8. ANITA's science mission is supported by the Columbia Scientific Balloon Facility (CSBF) division of NASA, the CSBF Support Instrument Package (SIP) is described in Section 5.10.

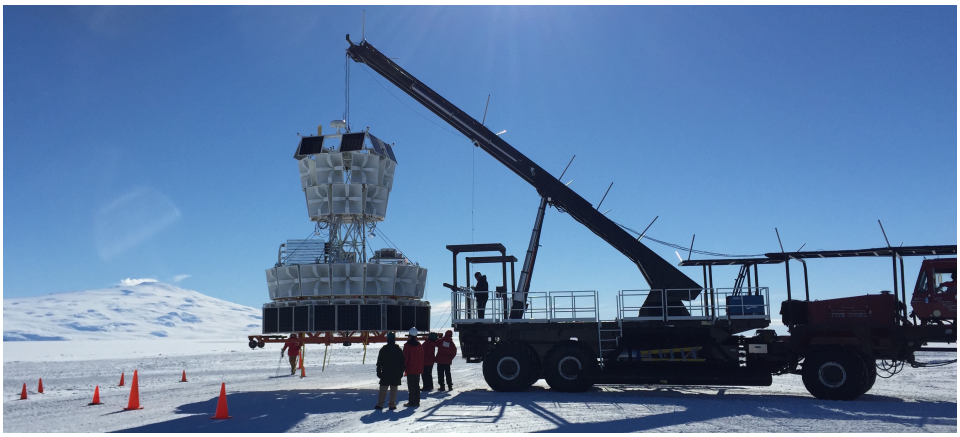

Figure 5.2: The ANITA payload hanging from the launch vehicle, "The Boss". ANITA pushes the vertical and radial envelope that the launch vehicle can accommodate, necessitating the drop down PVs and narrow top antenna ring.

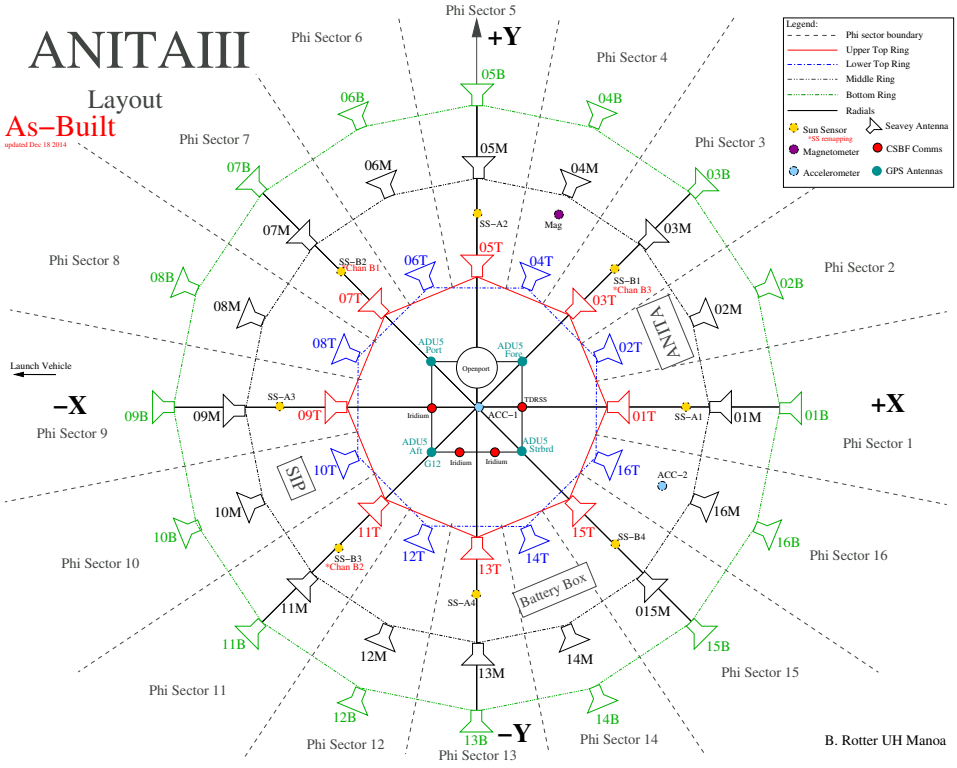

Figure 5.3: A schematic diagram of ANITA, as built. Figure produced by Ben Rotter.

Figure 5.3 is a schematic diagram of ANITA-3 from above. Some components not visible in figure 5.1, such as additional satellite antennas, sensors, and the battery box, are shown here. The antennas in each ring are vertically aligned to create 16 Φ-sectors.

5.3 The Seavey Antennas

ANITA uses broadband, quad-ridge horn antennas manufactured by Seavey Instruments. The antennas contain two perpendicular feeds to allow detection of vertically polarised (VPol) and horizontally polarised (HPol) signals.

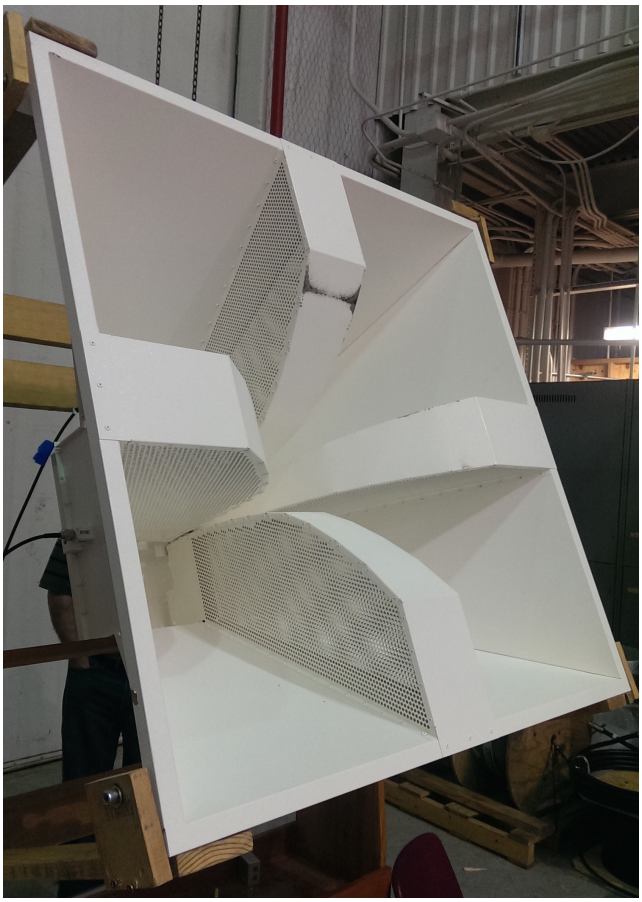

Figure 5.4: One of the Seavey antennas used for ANITA-3 being tested during the hardware integration period in Palestine, 2014.

Figure 5.5 shows the on-boresight gain of the antennas for both polarisations over a range of frequencies slightly wider than the ANITA band (200 MHz to 1200 MHz). The y-axis shows the gain in dBi, defined as the gain in dB relative to an isotropic transmitter or receiver (at 0 dB).

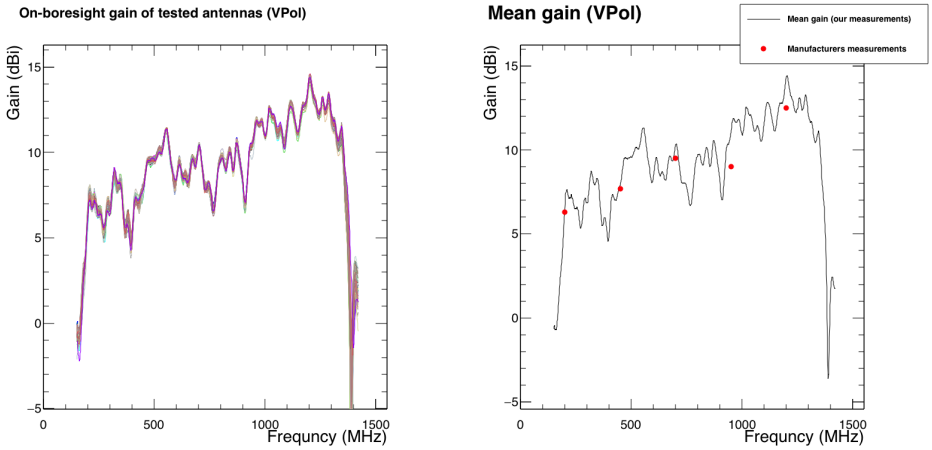

(a) VPol channels

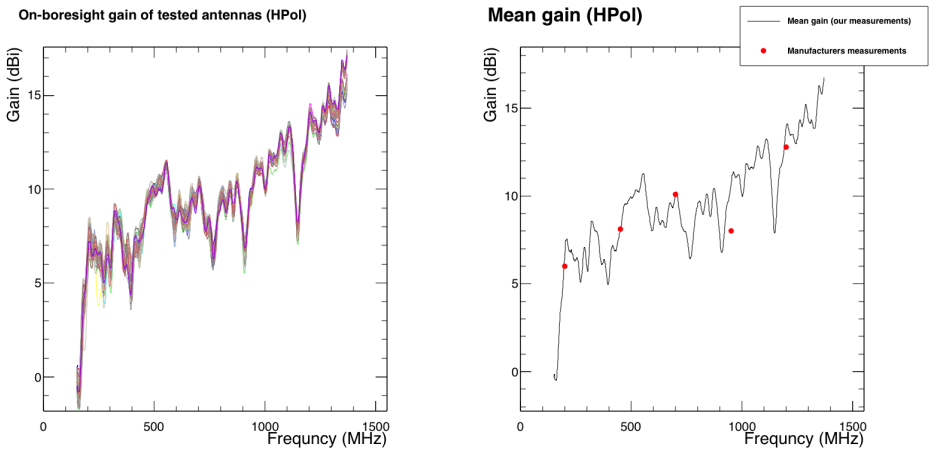

(b) HPol channels

Figure 5.5: The left plot is on-boresight gain (dBi) for 51 tested antennas. The black line on the right plots shows the mean of those 51 antennas for each polarisation and red dots show the manufacturers' measurements.

In both figures the left sub-plot shows the gain of each of 51 antennas tested during the hardware integration period in Palestine, 2014. Within the same polarisation the antennas are very consistent, with approximately 1dB variation within the tested group. The right sub-plots in figure 5.5 show the mean of the 51 measurements plotted against 4 data points provided by Seavey. The agreement is good as the curves measured by the ANITA collaboration pick out the points from the manufacturer's measurement.

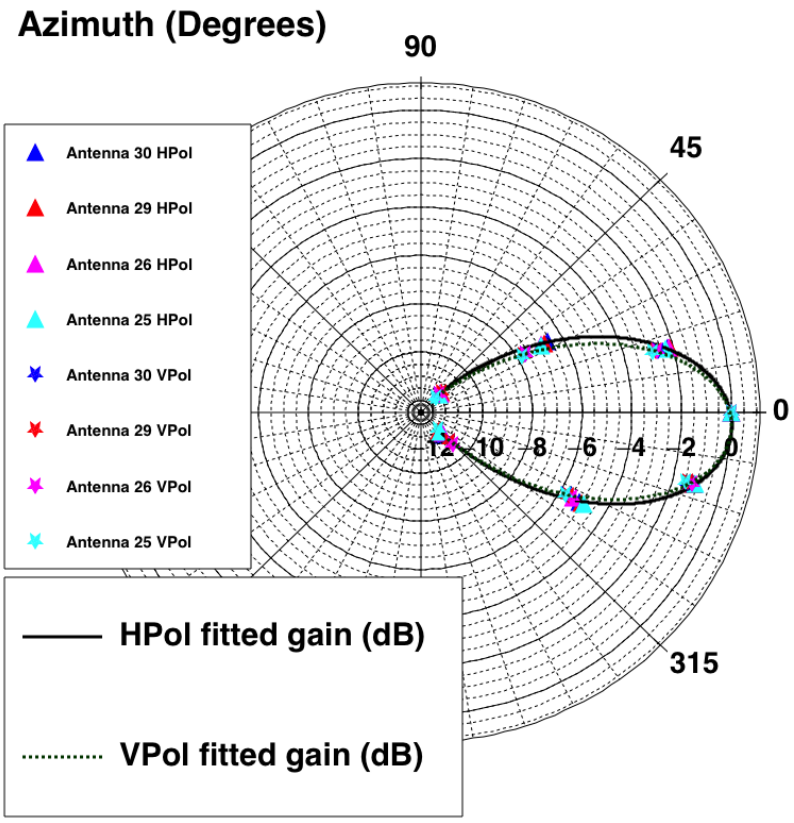

(a) Azimuth

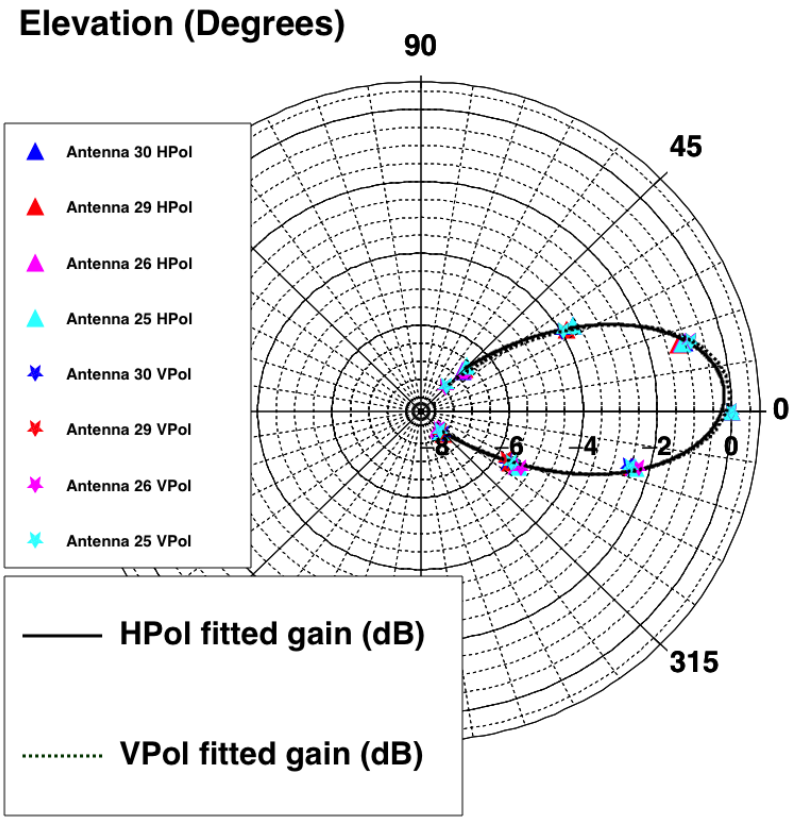

(b) Elevation

Figure 5.6: The off-axis gain relative to boresight across the ANITA band for HPol and VPol for four tested antennas. The fits are fourth order polynomials to the data points from all tested antennas.

The off-axis response was measured for a subset of the antennas. The mean gain across the ANITA band relative to the boresight is plotted in Figure 5.6. There is good consistency between the antennas, with the midpoint of the fit a few degrees off-axis for the azimuth and elevation fits. The -3dB point at approximately 20° from the midpoint in azimuth and 25° from the midpoint in elevation. Since each ring has an antenna every 22.5°, ANITA has good sensitivity over the entire 360° range in azimuth.

5.4 Front End Amplification

The amount of amplification required to make ANITA work is determined by the expected electric field of an Askaryan impulse at the payload, the gain of the antennas, and the dynamic range of the digitizer. Figure 4.2 (in Section 4.2) shows an Askaryan pulse induced by an ultra-high energy particle shower with peak electric field strength of $|E_0| \approx 150\,\mathrm{V\,m^{-1}}$ at 1 m from the shower. Assuming it travels one attenuation length, L_{atten} through the ice $L_1 = L_{\mathrm{atten}} = 1\,\mathrm{km}$, and a further distance to ANITA, $L_2 = 500\,\mathrm{km}$, with $1/R$ free space loss in field strength,

$$|E_{\mathrm{ANITA}}| \approx \frac{|E_0| e^{L_1/L_{\mathrm{atten}}}}{(L_1+L_2)/1\,\mathrm{m}} \tag{5.1}$$

$$= \frac{150\,\mathrm{V\,m^{-1}} \times e^{-1}}{5\times 10^5\,\mathrm{m}/1\,\mathrm{m}} \approx 1.1\times 10^{-4}\,\mathrm{V\,m^{-1}} \tag{5.2}$$

The magnitude of the Poynting vector, $|S|$, in free space at the antenna is given by

$$|S| = \frac{|E^2|}{2\eta} \approx \frac{(1.1\times 10^{-4}\,\mathrm{V\,m^{-1}})^2}{2\times 377\,\Omega} \approx 1.6\times 10^{-11}\,\mathrm{W\,m^{-2}} \quad , \tag{5.3}$$

where $\eta = 377\,\Omega$ is the impedance of free space.

The power received by the Seavey antennas depends on the antenna gain, G, which is related to the effective area, A_{eff}, by

$$A_{\mathrm{eff}} = \frac{G\lambda^2}{4\pi} \tag{5.4}$$

Assuming an on boresight pulse with 5dBi gain (Section 5.3) and choosing

300 MHz, which is conservative as it is at the low end of the ANITA band (and has the simplifying property that the wavelength, $\lambda = 1\,\mathrm{m}$), the power received, P_r by the Seaveys is approximately

$$P_r = |S|A_{\mathrm{eff}} \approx \frac{3.16}{4\pi}\mathrm{m}^2 1.6\times10^{-12}\,\mathrm{W\,m^{-2}} \approx 4.1\times10^{-12}\,\mathrm{W} \tag{5.5}$$

This is comparable to power at the payload from thermal noise alone. The ANITA frequency range is 200 MHz to 1200 MHz, and the average temperature of the field of view is $T = 150\,\mathrm{K}$, (approximately 50% ice at 300 K and sky at 3 K). The thermal power, P_{thermal}, received at ANITA is given by

$$P_{\mathrm{thermal}} = k_B T \Delta f = 1.38\times10^{-23}\,\mathrm{J\,K^{-1}}\times150\,\mathrm{K}\times1\,\mathrm{GHz} = 2\times10^{-12}\,\mathrm{W} \tag{5.6}$$

where k_B is Boltzmann's constant, T is the temperature in Kelvin and Δf is the ANITA bandwidth. This means that smaller Askaryan pulses are rapidly drowned in a sea of thermal noise fluctuations.

To see what amplification is required to see the Askaryan pulse in the digitizers, the power behind the antennas, P, must be converted to voltage V, with $P = V^2/R$, where the signal chain is $50\,\Omega$ terminated

$$V = \sqrt{PR} = (4.1\times10^{-12}\,\mathrm{W}\times50\,\Omega)^{\frac{1}{2}} \approx 1.4\times10^{-5}\,\mathrm{V} = 14\,\mu\mathrm{V} \quad . \tag{5.7}$$

To get a pulse of O(10 mV), which is visible in the ANITA digitizers, the voltage must be boosted by a factor of ≈ 3000.

$$\mathrm{Gain(dB)} = 10\log\left(\frac{P_{\mathrm{out}}}{P_{\mathrm{in}}}\right) = 20\log\left(\frac{V_{\mathrm{out}}}{V_{\mathrm{in}}}\right) \quad , \tag{5.8}$$

which implies the ANITA signal chain needs approximately 70 dB of gain.

To account for splitters in signal chain, ANITA adds 80 dB of amplification, over the course of the RF front end of the experiment. Figure 5.7 shows the components a signal travels through inside the ANITA instrument.

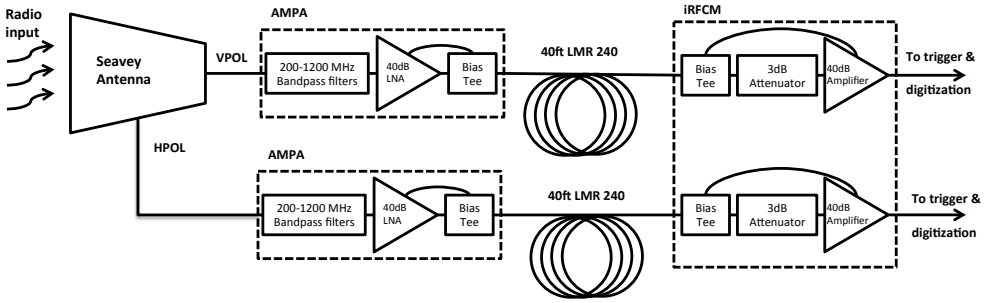

Figure 5.7: Diagram showing the RF front end of the ANITA-3 instrument for a VPol and HPol channel coming from a single Seavey antenna. The dashed lines represent Faraday housing.

Custom built front end amplifiers, called AMPAs, are connected directly behind the antenna HPol and VPol outputs. Each AMPA contains a high pass filter (200MHz) and a low pass filter (1200MHz), followed by a 40 dB Low Noise Amplifier (LNA), followed by a bias tee. Placing the filters in front of the amplifier ensures that any power outside the ANITA band is suppressed before the signal is boosted. Amplifying the signal requires power. Direct current (DC) flows down the cable from the instrument crate and is extracted by the bias tee to power the amplifier. The bias tee connects the amplifiers alternating current (AC) output to the mixed AD/DC line.

The thermal noise background means that it is important that the amplification have a low noise temperature (which adds noise power into the signal via equation (5.6)). The gains and noise temperatures of the two types front end amplifiers are plotted in figures 5.8, 5.9. The data plotted here were collected by a team of testers during the hardware integration in Palestine, 2014.

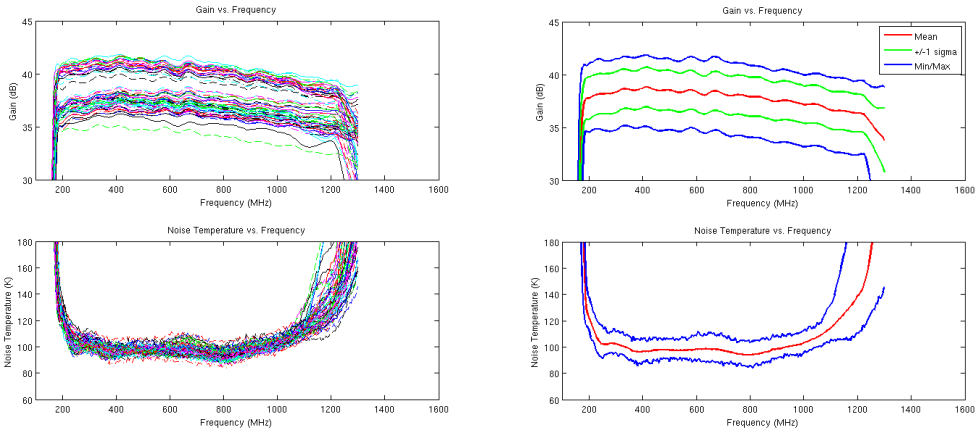

(a) AMPA gain and noise measurements (b) AMPA summary

Figure 5.8: Gain and noise figure plots for the individual regular AMPAs.

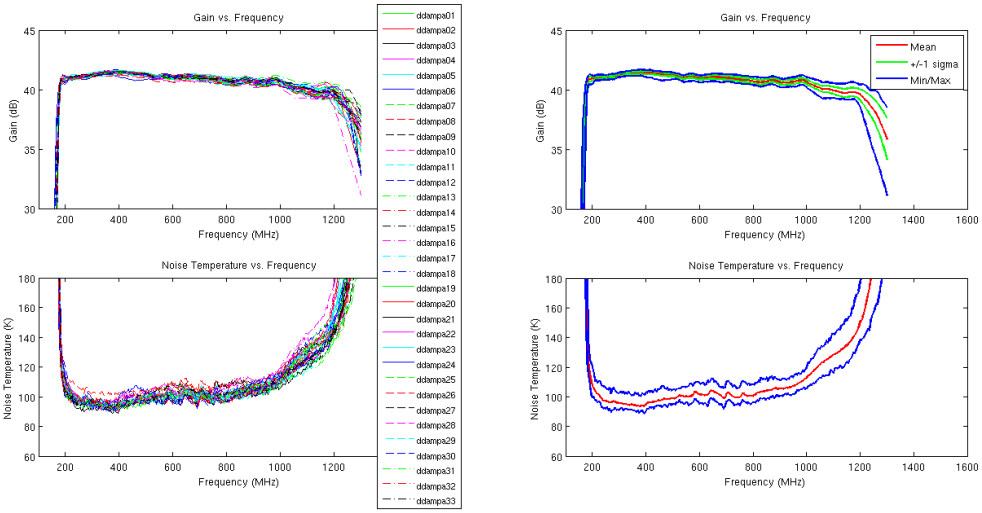

(a) DDAMPA gain and noise measurements (b) DDAMPA summary

Figure 5.9: Gain and noise figure plots for the individual DDAMPAs.

Given that neutrino induced radio impulses are expected to be primarily vertically polarised (see Section 5.15), the AMPAs with the lowest gains and highest noise temperatures were used for the HPol channels.

Once the signal leaves the AMPA it travels through approximately 40ft of LMR240 cable, which takes it to the instrument crate. Inside the crate, the signal immediately passes through a second stage of amplification. There are four

boxes called iRFCMs (internal Radio Frequency Control Modules), each with 24 input channels.

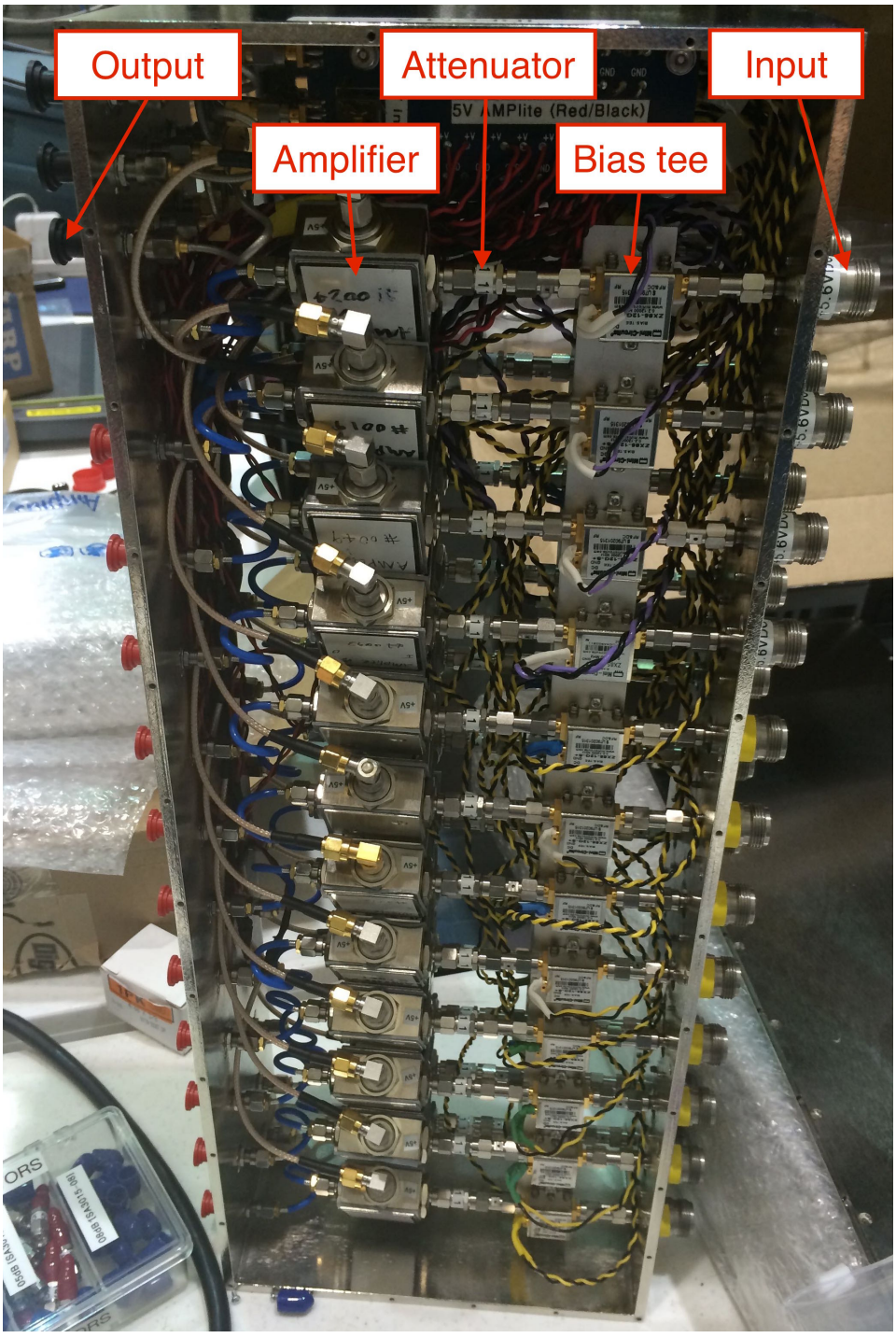

Figure 5.10: An iRFCM. 12 of the 24 channels are visible. The input connection, bias tee, attenuator and amplifier are labelled for one of the channels.

Each channel has a bias tee, followed by an attenuator, followed by a Low

Noise Amplifier. The bias tee couples DC to the LMR240 to power the AMPA at the other end of the cable. Behind the bias tee, the RF signal goes through an attenuator and 40 dB amplifier. The attenuator is placed in front of the amplifier to dampen any reflected power from travelling backwards up the signal chain. The attenuators, 1 dB to 3 dB, were chosen to try and balance the channel-to-channel variation in AMPA and iRFCM gains.

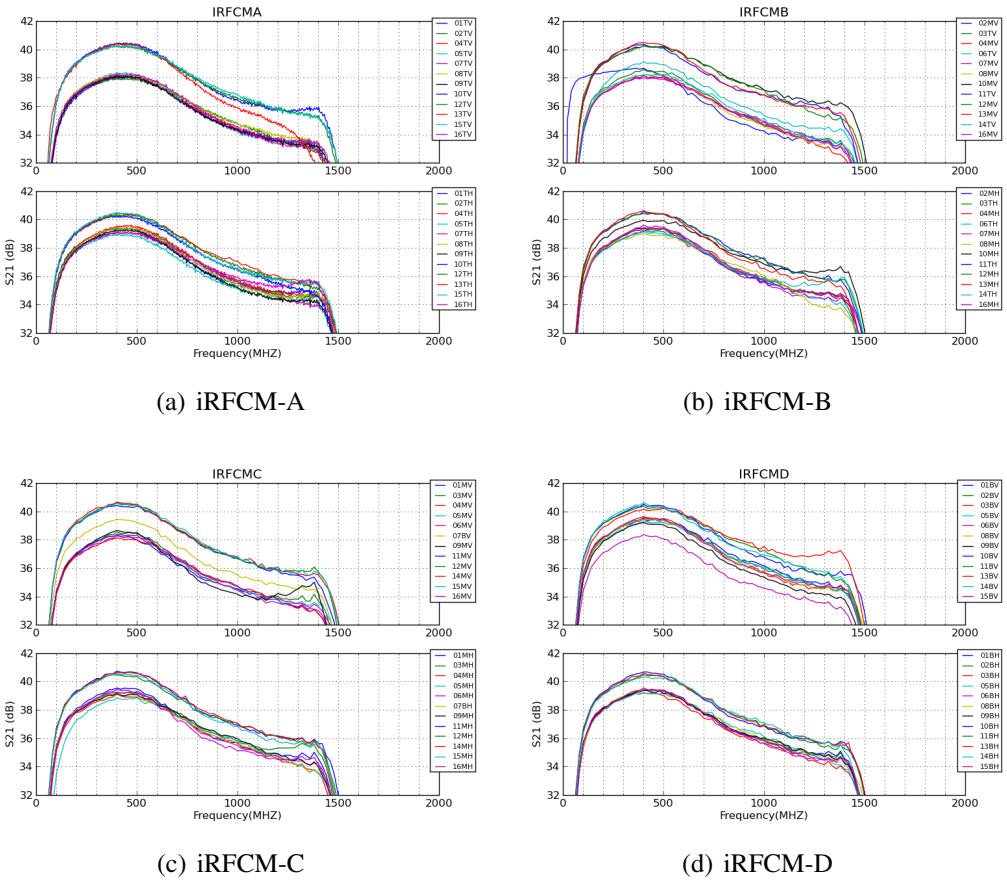

(a) iRFCM-A (b) iRFCM-B

(c) iRFCM-C (d) iRFCM-D

Figure 5.11: Gain plots for all 4 iRFCMs.

Figure 5.11 show the gain of the iRFCMs for each channel. The data plotted here were taken by Jarred Roberts, Ben Rotter and Sam Stafford during the Palestine integration period. Once the signal has passed through the iRFCM it travels though a short length of coaxial cable before passing through a series of 200 MHz to 1200 MHz Lark filters. At this point the signal travels through a 3 dB splitter, sending a copy of the signal to the trigger and digitiser paths.

5.5 Digitiser path

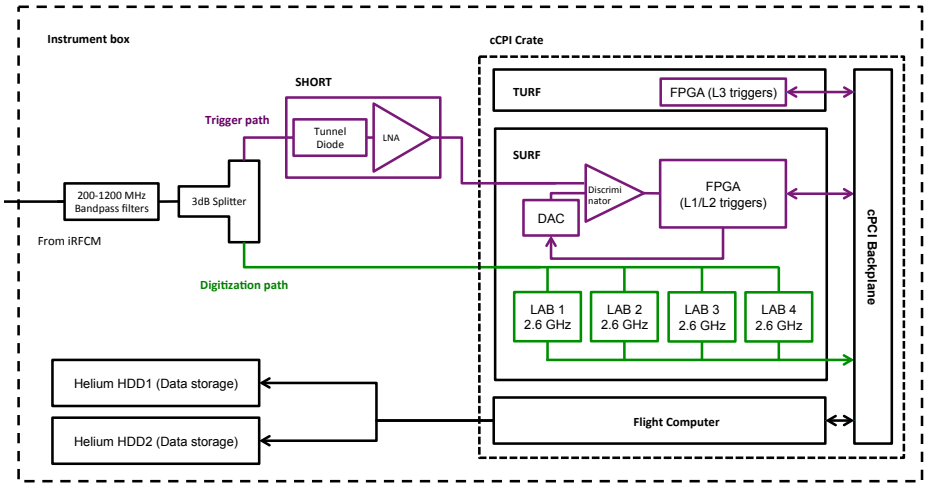

Figure 5.12: Signal chain for a single channel inside the ANITA instrument box. Only a single SURF is shown. All SURF/TURF/CPU communication is via the cPCI back plane.

The cable on the digitiser side of each splitter connects to one of twelve Sampling Units for Radio Frequencies (SURFs). The SURFs are circuit boards which live in the ANITA Compact Peripheral Component Interface (cPCI) crate. (This crate also contains the ANITA single board flight computer, described in Section 5.14.) One of the two primary functions of each SURF is to digitise its 8 of the RF input channels. To do this each SURF houses four custom built ASICs (Application Specific Integrated Circuits) called LABRADORs (Large Analogue Bandwidth Recorder And Digitiser with Ordered Readout), or LABs for short. ANITA-3 uses the third generation of LAB chips which, due to the lower power requirements of the experiment, were designed specifically for ANITA [12]. As the RF signal enters the SURF it undergoes a four way split, as the input gets piped to the four LABs. This generates a -6dB insertion loss.

The LABs have a Switched Capacitor Array (SCA) with 9×260 cells to record incoming signals. The SCA has a nominal sampling rate of 2.6 GHz so that at any given moment the charge stored in each row of successive capacitors represents a 100 ns record of the channel voltage. The last act of the amplified RF signal in analogue form is to transfer charge into or out of successive capacitors in the SCA.

When the LAB receives an instruction to do so, the sampling is stopped and the charge in each capacitor is measured by a 12 bit Wilkinson Analogue-to-Digital Converter (ADC). The flight computer subsequently reads out the event data over the CPCI back plane.

In addition to the 8 RF channels, each LAB also digitises a 33 MHz square wave clock, common to all the SURFs. The clock is generated by the cPCI crate. This is done because each LAB has its own 250 MHz clock driving the state of its logic. This creates a delay of up to 4 ns in acting on an instruction. By making each LAB record 100 ns of the same 33 MHz clock, this uncontrollable delay is measured by the relative phase of the digitised 33 MHz clocks.

A LAB must stop sampling for some time ($\leq 50\,\mu$s see [12]) as its cells are read out and digitised. In order to reduce experimental dead time, each SURF holds fours LABs to allow events to be buffered. Ideally, as one LAB stops sampling the next is ready for triggering. This is only the case when the time between four successive events is greater than the LAB readout time. When the trigger rate exceeds this the experiment live time is reduced.

5.6 Trigger Path

Power and bandwidth both limit the rate at which ANITA can record events. Continually recording waveforms would consume $O(10\,\mathrm{W})$ per channel, too much considering ANITA's power budget (Section 5.12), however the constant digitisation with readout on triggering consumes $O(1\,\mathrm{W})$ per channel. Additionally, recording a 100 ns event with ANITA generates a certain number of bits: 12 SURFs $\times$ 9 channels per SURF $\times$ 260 samples per channel $\times$ 12 bits per sample. If ANITA were to record continuously, for all 10^7 100 ns snapshots per second, the data rate would be

$$12 \times 9 \times 260 \times 12\,\mathrm{bit} \times 10^7\,\mathrm{s}^{-1} = 3.3696 \times 10^{12}\,\mathrm{bit\,s}^{-1} \quad , \tag{5.9}$$

which is about $0.4\,\mathrm{TB\,s^{-1}}$. Recording at this rate[2]is not possible due to many bandwidth bottlenecks inside the ANITA Data Acquisition (DAQ) chain. Both these constraints mean that ANITA must decide which 100 ns snapshots to record on the fly. This job is done by the trigger system.

On the trigger side of the 3 dB splitter separating the trigger and digitiser paths, the RF signal from the antenna travels to a box called the SURF High Occupancy RF Trigger (SHORT). Each SHORT takes in 4 channels. The RF signal in a SHORT channel passes through a tunnel diode and an amplifier. This functions as power detector, outputting a signal approximately proportional to the square of the voltage of the RF signal.

In addition to handling the digitization the SURFs also handle the individual channel triggering in ANITA. After travelling through the SHORT, the squared RF signal is routed to a SURF trigger input. Every SURF has 12 trigger channels so the trigger channels are only used on eight SURFs. Once in a SURF's trigger channel, the squared signal enters a discriminator where its voltage is compared to the output of a software controlled[3] Digital-to-Analogue Converter (DAC). As the squared RF signal voltage surpasses the threshold set by the discriminator, it sends a signal to a trigger dedicated Field Programmable Gate Array (FPGA) for further processing, as shown in Figure 5.12. This is the end of the analogue signal in the trigger path.

5.7 RF Trigger Logic

Thermal noise is uncorrelated between channels whereas an Askaryan pulse should be seen in many channels as it passes the payload. Therefore the key principle of ANITA's trigger logic is coherence between neighbouring antennas. The first level of triggering occurs when the trigger channel voltage surpasses the SURF DAC voltage, this is an L1 (channel level) trigger. The L1 triggers are fed to an FPGA on the SURF. Channels with the same polarisation in each Φ-sector go to the same SURF. This allows the FPGA to look for timing coincidences in L1 triggers of the

[2]This does not take compression into account, which reduces the size of the pedestal subtracted RF data to $\sim 40\%$ of the uncompressed size [62]

[3]See section 5.14.2

same polarisation in a Φ-sector.

The ANITA-3 L2 trigger is a two of three coincidence trigger. Each L1 trigger opens a timing window. If another L1 trigger in the same polarisation and ϕ-sector occurs within the window, then an L2 trigger is formed. The window lengths are different in each ring:

- An L1 trigger in the bottom ring opens a 16 ns window.
- An L1 trigger in the middle ring opens a 12 ns window.
- An L1 trigger in the top ring opens a 4 ns window.

This feature was designed to preferentially trigger on RF signals coming up from the ice and not trigger on any down going signals. Two examples of this is shown in Figure 5.13.

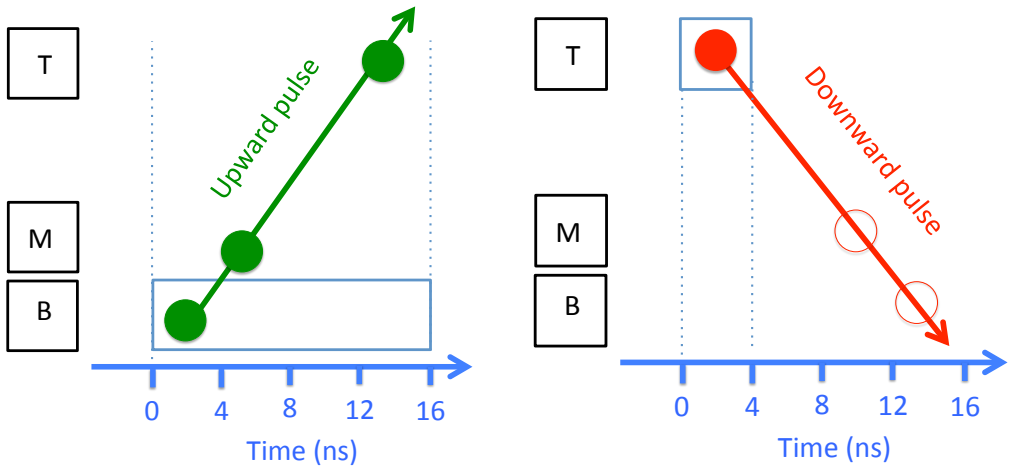

(a) An L1 trigger in the bottom ring opens a 16 ns window, in which time the pulse can travel to the middle and top rings.

(b) An L1 trigger in the top ring opens a 4 ns window, which is too short a time for the pulse to travel either the middle or bottom rings.

Figure 5.13: Schematic diagrams of the L2 trigger system in ANITA-3.

L2 triggers are passed from the SURFs to a dedicated board which handles triggering, called the Triggering Unit for Radio Frequencies (TURF). The TURF also has an FPGA that looks for L2 triggers of same polarisation between two adjacent Φ-sectors. If there are two such triggers in an 8 ns window then an L3 trigger is formed. An example of the L1 and L2 triggers required for an L3 trigger is shown

in Figure 5.14. When this condition is met, the TURF sends an instruction to the SURFs to stop sampling and digitise the voltages recorded in the active LABs. In addition to the event data from the SURFs, the flight computer also records meta-data from the TURF about which combination of L1 and L2 triggers formed the L3 trigger.

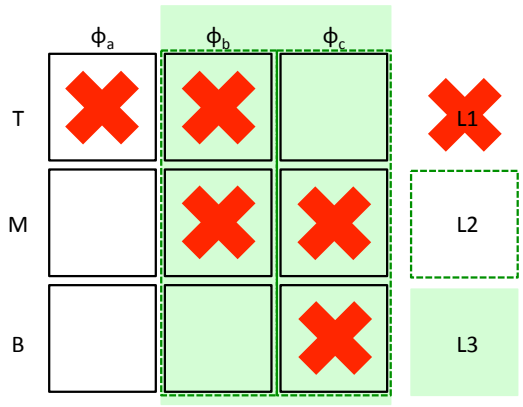

Figure 5.14: Example of the trigger logic. Φ_a has only one L1 trigger in the top ring and no further trigger states are generated. Φ_b and Φ_c both have 2/3 L1 triggers and so form an L2 trigger. Because Φ_b and Φ_c are neighbouring Φ-sectors, they form an L3 trigger so an event is recorded.

5.8 The GPS Antennas

Determining the source of any RF signals detected by ANITA requires accurate knowledge of the payload position and orientation. For this reason ANITA has three independent GPS systems on board. It has two sets of ADU5 GPS antennas, manufactured by Ashtech called ADU5A and ADU5B. These are visible in the Figure 5.1 photograph and are shown in the Figure 5.3 diagram. Both ADU5s are arrays of 4 antennas and give independent measurements of altitude, latitude, longitude, heading, pitch, roll, and the Universal Time Coordinated (UTC). The third GPS system is a G12 GPS, also manufactured by Ashtech. The G12 gives position, velocity and UTC. The GPS data is sent via serial port to a serial port to universal serial bus (USB) converter, manufactured by Future Technologies Devices International Ltd. (FTDI). The FTDI converter connects to a USB port on the flight computer, where the GPS data are recorded every second.

In addition to the flight computer, the GPS units also talk to the TURF (described in Section 5.7) via an extension board for managing external inputs called the TURFIO (Trigger Unit for RF Input/Output). The GPS units are used to issue Pulse Per Second (PPS) triggers as described in Section 5.8.1.

5.8.1 Minimum Bias Triggering

The DAC thresholds described in Section 5.7 mean that momentary increases in RF power across neighbouring channels are likely to trigger the instrument. This creates a bias in the distribution of events that ANITA records. Data analysts need an unbiased picture of the experiment environment to understand how likely it is that a thermal fluctuation or man-made signal could produce an event that looks like a neutrino. In order to get this, ANITA records a certain number of minimum bias (MB) events.

MB triggers are issued at regular intervals so that ANITA records an event regardless of the state of the L1, L2 or L3 triggers. Several devices are responsible for issuing MB trigger commands, which are sent to the TURF via the TURFIO. The ADU5 issues a Pulse Per Second (PPS) trigger to the TURF via the PPS1 connector on the TURFIO. The G12 has a configurable PPS rate and is connected to the PPS2 connector on the TURFIO. The flight computer also issues software triggers at a configurable rate based on the computer clock.

Software triggers were set to 1 Hz and the ADU5 (PPS1) trigger was enabled for the entire ANITA-3 flight. (The RF triggered event rate was typically between 20 Hz-80 Hz). The G12 (PPS2) trigger was set to 5 Hz for a short time after launch, but then disabled for the rest of the flight.

5.8.2 RF power monitor

At the digitiser input of each SURF, a 13dB coupler splits a small fraction of the signal away from the input to the LABs. This small fraction of the signal is routed to an RF logarithmic amplifier on the SURF, which outputs a voltage proportional to the RF power. A single 12 bit ADC on each SURF digitises the RF power from each channel in turn, every 30 ms. The digitised values are put into SURF memory

and are available as part of the SURF housekeeping data. The RF power measures power over longer timescales than the individual ANITA events, and is not derived from the digitised events so is unbiased by short-timescale fluctuations in power. This is useful in understanding the environment during flight as sources of power will appear to move between Φ-sectors as the payload rotates. However, these data are not used in neutrino or cosmic ray searches as they cannot provide.

5.9 Housekeeping Sensors

In addition to the Seavey antennas ANITA has a suite of housekeeping sensors which monitor the environment and the status of the instrument. Multiple temperature sensors are used to monitor the condition of the experiment and are placed inside the instrument box and around the gondola. While the temperature data is not used directly in analysis, the sampling rate of the LABRADOR digitizers is known to vary with temperature [12], so these sensors provide a useful cross-check to any derived calibration corrections.

A set of sun sensors, accelerometers and a magnetometer are also installed on the payload deck, these are shown in figure 5.3. These sensors give the possibility of an alternative method of determining payload attitude should the GPS fail[4]. In order to interface with the computers via the cPCI crate, these sensors were plugged into an FPGA express-PCI Mezzanine Card (XMC) manufactured by Acromag. Since the GPS sensors did not fail during any portion of the ANITA-3 flight, the quantities recorded by the housekeeping sensors are not directly used in neutrino and cosmic ray searches.

5.10 Support Instrument Package

ANITA is a Long Duration Balloon (LDB) mission, supported by the Columbia Scientific Balloon Facility (CSBF). LDB missions carry a standard Support Instrument Package (SIP), created and controlled by CSBF. The SIP is labelled in Figure 5.1, on the ANITA deck in a Faraday cage to reduce EMI.

[4]This was the case for a small portion of the ANITA-2 flight, when the sun sensors were used to fill in the payload attitude during periods when the GPS sensors failed [63].

The SIP controls the balloon ascent with servos that release ballast and controls the descent of the payload by cutting the balloon away, deploying a parachute at the end of the flight. These functions are controlled by CSBF from the ground. There are three lines of communication from the ground to the SIP. When ANITA is near the LDB facility, a line-of-sight (LOS) antenna allows direct communication with the payload. When ANITA is over the horizon, there are two satellite networks that the SIP uses for communication. These are the Tracking and Data Relay Satellite System (TDRSS) and the Iridium satellite network. The TDRSS and Iridium antennas are mounted on top of gondola, shown in the schematic figure 5.3. The SIP also sends data about the instrument status to the ground, such as battery status, power usage and temperatures. The SIP has its own array of associated GPS antennas, which are used to relay the balloon position and altitude to the ground for tracking.

5.11 The OpenPort Antenna

In addition to the TDRSS, Iridium and LOS connections (see Section 5.10) ANITA-3 made use of an OpenPort antenna for satellite communication. This can be seen in the white casing, visible at the top of the payload in figure 5.1. It contains an array of smaller antennas allowing for a higher bandwidth connection to the Iridium satellite network. This is an upgrade to ANITA-3, that was not present in ANITA-2. Event data and housekeeping data are sent back over this connection (see Section 5.14.7). The bandwidth even allows remote login to the flight computer during flight using the Secure Shell (SSH) protocol, although this was not used after launch.

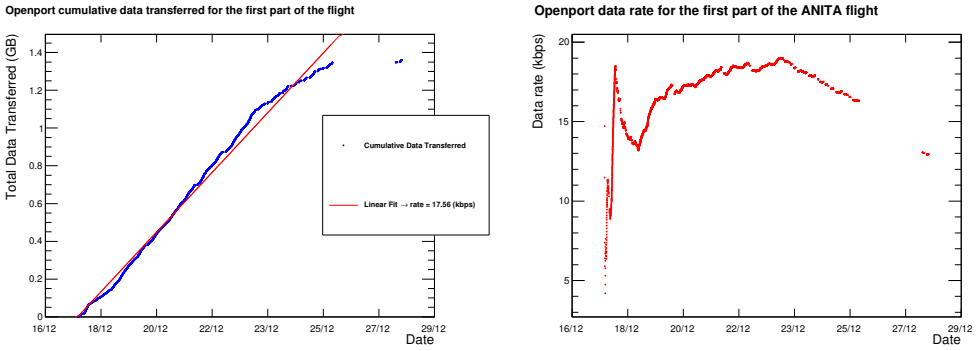

(a) OpenPort cumulative data transferred (b) OpenPort data rate

Figure 5.15: OpenPort data transfer statistics for the first part of the ANITA-3 flight

Figure 5.15 shows the cumulative data transferred over the OpenPort satellite connection and its derivative. The plots indicate the typical OpenPort data rate to be in the range of 15-20kbps. This compares favourably with the TDRSS data rate, which is typically around 6kbps [10].

5.12 Power System

ANITA has unusual power constraints for a neutrino detection experiment because it is balloon mounted. ANITA-3 requires around 450W to power all the electronics and sensors on the payload, all of which must be generated by an array of PV panels. ANITA uses 720 C60 solar cells manufactured by SunPower. These cells are arranged in eight 90-cell strings, laid out in an octagon around the bottom of the payload. These eight strings are remotely instructed to drop down by the SIP, which fires a servo to lower them below the bottom ring of antennas after launch. The undeployed PVs are visible in Figure 5.1 at the bottom of the gondola. The other set of PVs at the top of the gondola are managed by CSBF and used to power the SIP.

Although it is constantly daylight in the Antarctic summer, the amount of power the solar panels produce changes in line with the sun's elevation during each 24 hour period. In order to handle the diurnal variation in sun's position, ANITA-3 has 6 pairs of Panasonic LC-X1220P (Pb-acid) batteries. Each is a 20 A h 12 V battery, so the set of 12 together can store can store 2880 W h of power. These are

contained the battery box, labelled in the schematic diagram Figure 5.3.

5.13 The ANITA Low Frequency Antenna

An additional, non-Seavey antenna was added to ANITA-3 to detect low frequency radio emission associated with cosmic ray air showers. Like the drop down PVs, the ANITA Low Frequency Antenna (ALFA) is designed to deploy below the main payload after launch.

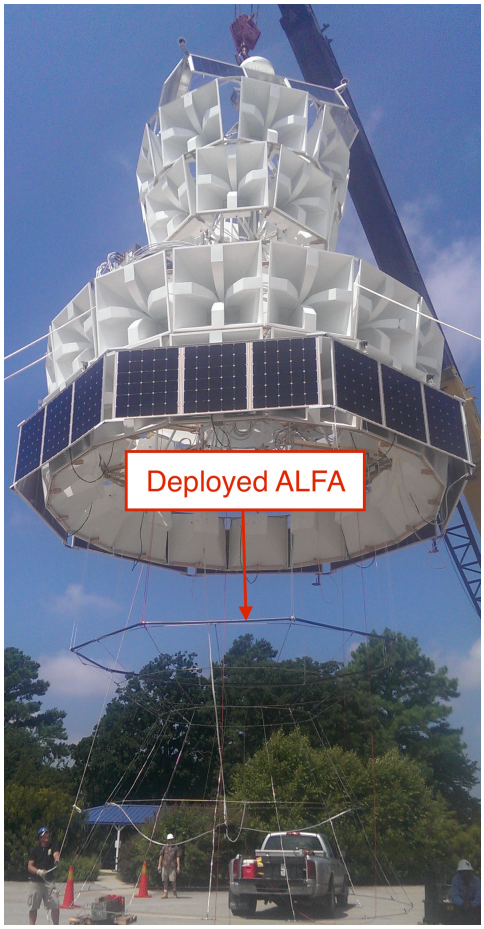

Figure 5.16: The ALFA antenna deployed below ANITA during the ANITA-3 hang test in Palestine, 2014.

The ALFA is designed to measure the frequency range 25 MHz to 80 MHz, which is below the ANITA band. As there are no spare channels for digitization, the ALFA signal chain contains a mixer with a Local Oscillator (LO) at 790 MHz. The combined ALFA+LO signal forms a double peak at $f_{\mathrm{LO}} - f_{\mathrm{ALFA}}$ and $f_{\mathrm{LO}} + f_{\mathrm{ALFA}}$. This creates an approximate range 710 MHz to 870 MHz, which is at the upper

end of the ANITA band. The combined output of the ALFA and mixer signal was coupled into channel 5TH.

5.14 Flight Computer

The ANITA flight computer is an XCR14 single board computer, manufactured by GE Intelligent Platforms, running the Red Hat Enterprise Linux (RHEL). It is house inside the cPCI crate alongside the SURFs, TURF, TURFIO and Acromag boards. Its ruggedized design makes it suitable for operations in extreme environments, such as the near vacuum atmospheric pressure at 37 km altitude.

5.14.1 Software Overview

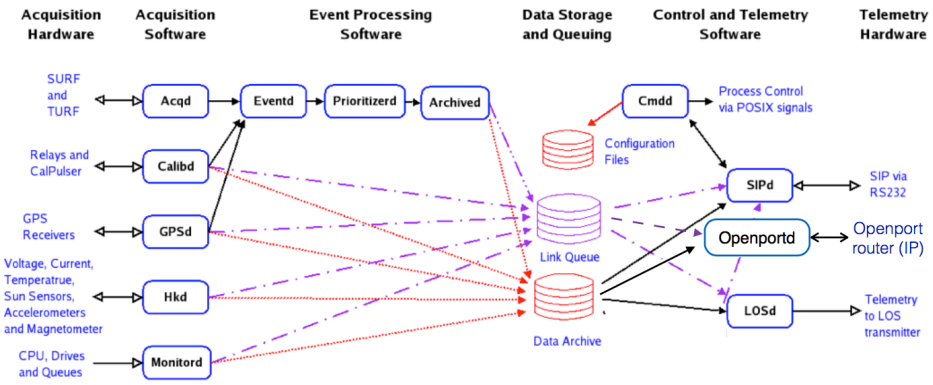

Figure 5.17: The ANITA-3 software moves data between various sources and destinations. Figure by Ryan Nichol.

The flight computer is the brain of the ANITA experiment. It has to autonomously coordinate the multiple tasks, that when done together make the ANITA experiment work. Its jobs are to gather data from all the instruments and sensors, write all the data to the hard disks, send some fraction of event and housekeeping data back to the ground. It also needs to listen for and execute commands sent by the experimenters on the ground and item change the state of the instrument in response to the changes in the environment.

These jobs are divided among a set of programs which run on the flight computer. They are listed in Tables 5.1 with a very brief description of their function. These functions are expanded upon in the sections listed in the table.

Table 5.1: A list of the programs running on the ANITA flight computer and a brief description of their function.

Name	Function	Related sections
Acqd	Read SURFs/TURF data to RAM disk. Change L1 thresholds. Φ-sector/channel masking.	Section 5.14.2
Archived	Read RAM disk event data. Write to hard disks.	Section 5.14.3
Calibd	Control instrument power relays.	Section 5.14.4
Cmdd	Executes instructions from other processes.	Section 5.14.4
Eventd	Merge event & gps data for Prioritizerd.	Section 5.14.8
GPSd	Read GPS data Write to hard disks & telem queues.	Section 5.14.6
Hkd	Read Acromag sensor data. Write to hard disks & telemetry queues.	Section 5.14.6
LOSd	Read LOS telemetry queue data Write to LOS board.	Section 5.11
LogWatchd	Read syslogs and config file data Write to hard disks & telemetry queues.	Section 5.14.4
Monitord	Keep daemons running. Read RAM & hard disks stats, queue stats. Write to hard disks & telemetry queues.	Section 5.14.5
Openportd	Read OpenPort telemetry queue data. Write to OpenPort router.	Section 5.14.7
Playbackd	Read hard disk event data. Write to telemetry queues.	Section 5.14.7
Prioritizerd	Assign event priority for telemetry queues.	Section 5.14.8
SIPd	Read telemetry queue data. Write to SIP. Listen to SIP for commands.	Section 5.14.7

5.14.2 Acqd

Acqd (acquisition daemon) is the program that interacts with the SURFs and TURF. In terms of data transfer, the majority of this work is reading the event data from the SURF and the triggering information from the TURF. This data is copied to the flight computer RAM disk, which is used to buffer event data once it reaches the flight computer. Other software daemons are responsible for handling the event data once it reaches the RAM disk.

In addition to the event data from the LABs and the TURF triggering information, Acqd also records some housekeeping data from the SURFs. This includes the

currently set DAC thresholds, the number of L1 triggers in the last second, and the RF power (see Section 5.8.2). These values are stored as SURF housekeeping data.

Acqd also writes to the memory on the SURFs and TURF. This allows it to set the SURF L1 channel thresholds dynamically or mask channels to switch them off completely. ANITA rotates around as it dangles from its helium balloon. As this happens sources of power (e.g. the sun or galactic centre) will enter and leave each channel's field of view. Acqd computes a Proportional-Integral-Derivative (PID) loop and can set the thresholds of the L1 triggers in response to the changing conditions seen by each channel. Equation 5.10 describes generic a PID loop. A control variable, $u(t)$, is changed in response to an error value, $e(t)$, the difference between the current state and a desired state. In ANITA's case, $u(t)$ is the L1 threshold and $e(t)$ is the difference in the L1 rate from the desired rate.

$$u(t) = K_p e(t) + K_i \int_0^t e(\tau) d\tau + K_d \frac{de(t)}{dt} \quad , \tag{5.10}$$

where the coefficients K_p, K_i, K_d control the relative weights of the current error value, the integral of the error value, and the rate of change of the error value. The desired L1 trigger rates (PID goals) and the coefficients K_p, K_i, K_d are set in configuration files.

Typically the ANITA-3 L1 trigger rate goal is set to 450 kHz in the Acqd configuration file. The L1 trigger rates are read out by Acqd at a rate of 1Hz. After eight seconds of data collection, the L1 rates are fed into the PID loop, and the updated DAC thresholds are sent to the SURFs.

A simpler method of stopping the in event rate of a channel from getting too high is to switch it off completely for a short time. Acqd can mask individual channels or entire Φ-sectors dynamically in response to the changing event rate. There are four parameters required for this masking, which are also set in the Acqd configuration file. The masking is switched on if the event rate is above a high threshold, r_{hi} for a specified length of time, t_{hi}. The masking is switched off after the event rate is below a low threshold, r_{lo}, for a different, specified length of time, t_{lo}.

Due to changes in firmware the masking was partially broken in ANITA-3. The masking only works if the L1 triggers are counted even though they are not allowed to participate in an L2 trigger. This was not the case in ANITA-3 as the L1 triggers were not recorded in the SURFs when the masking was on. This meant that Acqd saw the event rate, r_{lo} drop to zero, no matter the conditions experienced by the masked channel. The masking would always be switched off after the time t_{lo} had passed, exposing ANITA to whatever caused the event rate to increase initially.

5.14.3 Permanent Data Storage

All the experimental data is permanently stored. The primary storage devices are a pair of HGST UltraStar He^6 disks, each with 6TB capacity. These two Helium drives contain identical copies of the data for redundancy in case of a drive failure.

A program called Archived (archive daemon) is responsible for copying all event data from the RAM disk to the hard disks. Other than Acqd, programs reading data from external hardware write their own data directly to the hard disks.

Secondary data storage is provided by an array of 6 $\times$ 1TB SSDs. These are controlled by an independent single board computer, which connects to the flight computer via an ethernet switch. The secondary SBC copies data from the Helium drives onto the array of SSDs. As one SSD fills up, the copy destination is switched to the next empty SSD.

5.14.4 Commanding ANITA

ANITA needs to be almost autonomous. The scientists on the ground can send certain instructions to the payload via the SIP (see Sections 5.10). A dedicated program on the flight computer, SIPd (SIP daemon), listens to a connection to the SIP for instructions sent over these links. Some commands, such as stopping various software daemons or rebooting, are executed directly by SIPd. Otherwise the SIPd passes these instructions along to another program, Cmdd.

The Cmdd (command daemon) carries out the majority of the instructions experimenters on the ground can send. Most instructions involve changing the state of a variable in software. Each ANITA flight software daemon has a configuration

file (e.g. Acqd.config) which is read when each program starts. Cmdd changes the state of the software by changing the variable value in a configuration file. All of the ANITA flight software programs run as daemons, meaning the operating system (OS) should restart them if they stop running for some reason. Cmdd can execute commands to kill other processes, although they should be restarted by the OS. Cmdd can also start the programs as daemons. Other commands not executed in this fashion are forwarded to other programs. After executing or forwarding each command Cmdd sends a special packet (a command echo) to the ground to notify the experimenters that the command was received.

The Calibd (calibration daemon[5]) controls relays which send power to various components requiring power in the signal chain. This includes the AMPAs, SHORT boards, and iRFCM amplifiers. The relay states are set in the Calibd configuration file. ANITA is launched with the amplification switched off and as the payload ascends the components are gradually switched on with remote commanding.

LogWatchd (the log watching daemon) monitors the system logs of the flight computer and the state of the program configuration files, which control many aspects of the flight software. At the beginning of each run the configuration files are sent to the ground. Cmdd also forwards a request for the last N lines of the flight computer system logs (journalctrl) to Logwatchd, which pipes the log data into telemetry queues.

5.14.5 Flight Computer Monitoring

The flight computer is a critical part of the DAQ chain and so data relating to its status is sent to the ground during flight. Monitord (the Monitoring daemon) tracks the state of the various telemetry queues on the RAM disk, the hard disk space, and the state of the ANITA software daemons. In the case that the RAM disk is too full then the Acqd daemon is stopped (preventing the OS from automatically restarting it). The RAM disk could get too full because events are being read by Acqd faster than Archived can write them to disk. In this instance Monitord stops

[5]In previous flights Calibd controlled a relay to a calibration pulser on the payload, hence the name. This pulser was not present on ANITA-3.

the Acqd daemon and restarts it when the RAM disk is sufficiently empty. (This condition was not reached during the ANITA-3 flight). Monitord will also send an instruction to Cmdd to restart any of the software daemons if it fails to find them running. Cmdd is an exception to this, which Monitord will try to start itself, since if Cmdd isn't running, it cannot execute any commands.

5.14.6 GPS and Housekeeping Data

GPSd (GPS daemon) reads out data from all three GPS sensors, the ADU5A, ADU5B, and G12 (see Section 5.8). The GPSd reads the data as fast as the GPS units provide it and writes the data to the hard disk. A configurable fraction of the GPS data is written to the telemetry queues for payload monitoring purposes.

Hkd (Housekeeping daemon) reads out the Acromag data (see Section 5.9) over the cPCI back plane. During the ANITA-3 flight the housekeeping sensors were read out at a rate of 10Hz. The data is written directly to the hard disk, with a configurable fraction written to telemetry queues. Acqd also produces SURF housekeeping data, which encompasses the non-event Data recorded by the SURFs (see Section 5.14.2). The SURF housekeeping data is written to disk at a configurable rate, with a configurable fraction of that data written to telemetry queues.

Monitord (see Section 5.14.5) also writes its housekeeping data to the hard disk and telemetry queues at a configurable rate.

5.14.7 Data Telemetry

Outgoing telemetry streams are managed by separate programs, piping data to the appropriate device. The two satellite connections via the SIP are managed by SIPd, which sends data to the SIP, which forwards it over the TDRSS and Iridium satellite connections. The Openportd sends the data to the Openport router. The LOSd wraps the LOS telemetry queue data correctly for the LOS antenna protocol, forwards it to the LOS board, which forwards it (via the SIP) to the LOS antenna for transmission.

Under normal conditions events can be telemetered while they are on the RAM disk before Archived writes them to the hard disks. Playbackd is designed for the case when ANITA enters LOS communication with the LDB facility after one cir-

cuit of Antarctica. Playbackd reads back data from the hard disk to the RAM disk, adding old events to telemetry queues. Data taken near LDB, when we have LOS contact is full of man made background, so it is likely the events already written to disk are of more scientific interest.

5.14.8 Event Prioritization

The signal discovery nature of ANITA's science mission mean that most events recorded will be background rather than signal. The bandwidth of the data connections relative to the ANITA event rate mean that only $\sim 0.1\%$ of events can be sent to the ground during flight. The flight computer does some data analysis on the fly in order to maximize the chance of transmitting a scientifically interesting event. Prioritizerd assigns a priority value from 1 to 9 to each event, which maps to a set of telemetry queues on the flight computer. Each priority is assigned a configurable bandwidth, which determines how often the SIPd, LOSd and Openportd programs read and transmit an event from that queue to the ground. Typically, priority 1 is reserved for the most signal-like events and increasing priority numbers are determined to be more like thermal noise or other sources of background. The ANITA-3 Prioritizer was my responsibility and its design and performance is fully described in Chapter 9.

5.15 Detection Of UHENs With ANITA

Extrapolations of the standard model neutrino interaction cross sections predict that the Earth is opaque to neutrinos. The attenuation length of the neutrinos is $O(100\,\mathrm{km})$ in materials such as water or ice [64]. This creates a geometrical constraint on the arrival direction of the particles. To detect such particles they must be Earth skimming, travelling $\sim 100\,\mathrm{km}$ through the Earth just below the surface before interacting. If the particle shower happens within the $\sim 1\,\mathrm{km}$ of the surface, then the Cherenkov cone will meet the surface. Since Cherenkov radiation is radially polarised, the edge of the cone reaching the top of the ice will be predominantly vertically polarised. The top of the cone will refract through the surface, travel through the air, and arrive at the ANITA payload. For geometrical reasons

the volume of ice subtended per unit angle is greatest at the horizon. The expected signatures of UHEN interactions are isolated, vertically polarised Askaryan pulses that reconstruct at the horizon. A sketch of the ANITA observation method is shown in Figure 5.18.

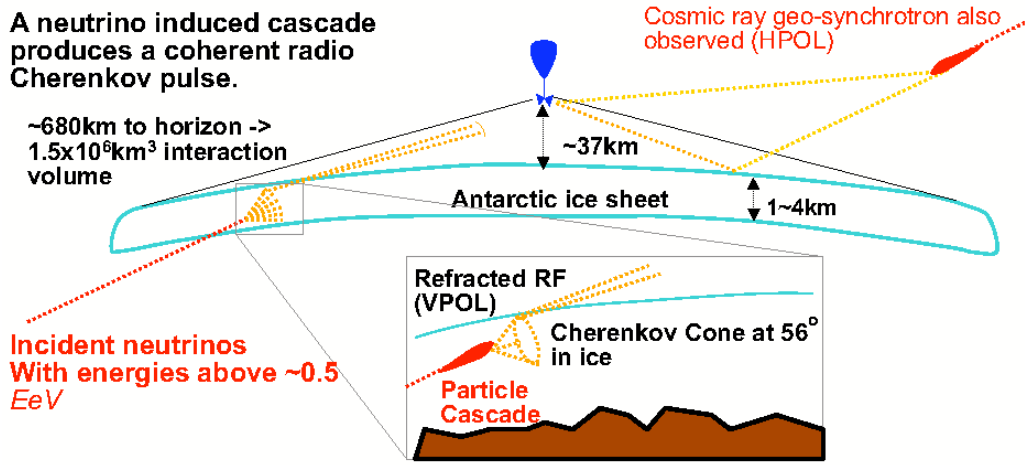

Figure 5.18: Sketch of the ANITA detection strategy for ultra-high energy neutrinos and ultra-high energy cosmic rays. Figure by Matt Mottram from [10].

5.16 Detection Of UHECRs With ANITA

ANITA-1 detected 16 isolated primarily horizontally polarised signals [20]. It took several years, until after the flight of ANITA-2, to understand that these were the radio emission from extended air showers. In Antarctica the geomagnetic field is aligned vertically, so the air shower radio is emission is primarily horizontally polarised. The polarisation angle of the 16 events aligned very well with the projected magnetic field angle (Figure 5.19a). There were 2 events that reconstructed above the horizon and had inverted polarity relative to the other 14, which reconstructed to the surface of the Earth (Figure 5.19b).

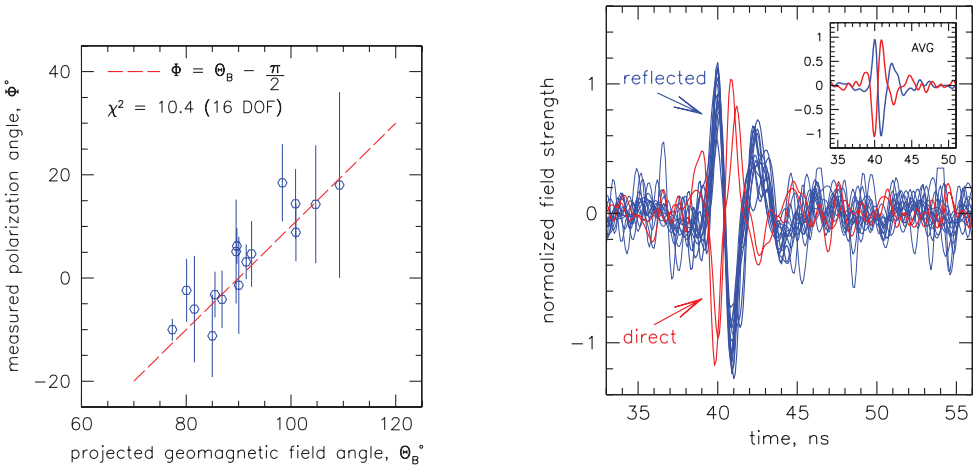

(a) Geo-magnetic field angle vs. event polarisation.

(b) Polarity of direct and reflected events.

Figure 5.19: Summary plots of the 14 reflected and 2 direct ANITA-1 UHECR events.

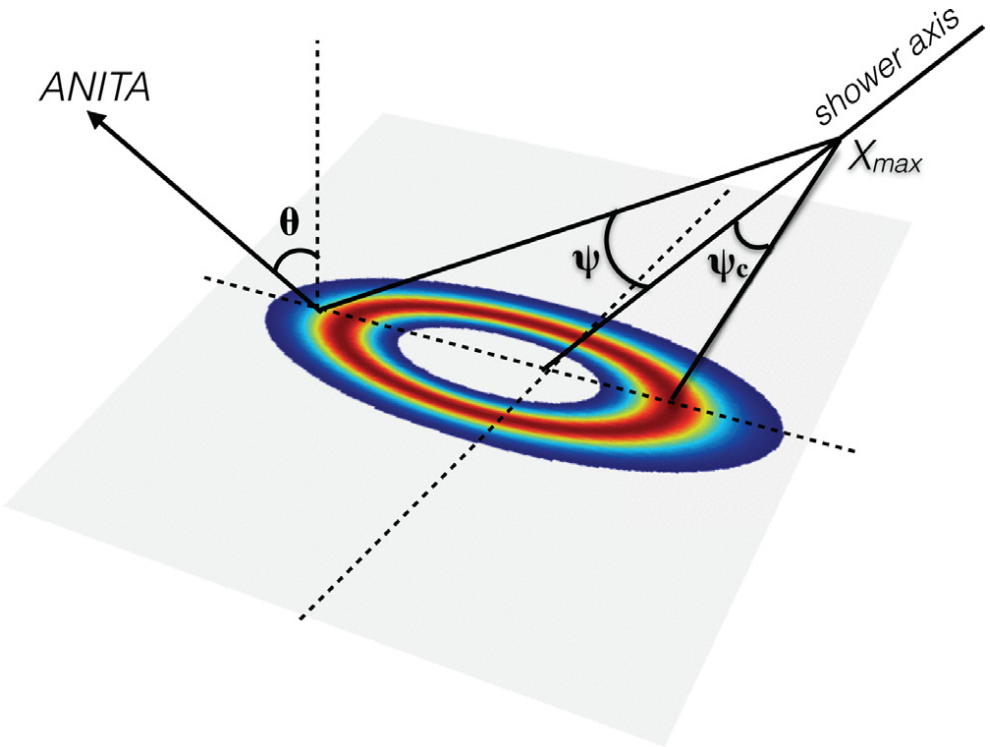

Figure 5.20: Reflected cosmic ray air shower detection with ANITA. Figure from [11].

This was interpreted as the 14 same polarity events being reflections from the Antarctic ice of down going geo-synchrotron radiation as shown in figure 5.20.

ANITA-2 disabled the HPol trigger to create a more sensitive multi-band VPol trigger and so only detected 4 isolated events and one non-isolated event [10].

A recent re-analysis [11] of the frequency content of the ANITA-1 cosmic ray events led to an improved energy estimate than the original paper [20]. The updated analysis of the 14 direct events gave a mean energy of 2.9×10^{18} eV, around a factor of 4 lower than the previous estimate, but still within the ultra-high energy regime.

Chapter 6

Timing Calibration of ANITA-3

When ANITA-3 records an event, the signal that triggered the instrument appears at different times in different channels because of the physical separation of the antennas. During analysis, the time offsets of a signal between nearby channels are combined and used to determine the signal's direction of origin.

Figure 6.1 shows how a timing misalignment for a single pair of antennas (δt) would change the apparent direction of origin of the signal. For simplicity I show the elevation shift ($\delta\theta$) for three vertically aligned antenna pairs in a single ϕ-sector, and the azimuth shift ($\delta\phi$) for horizontally aligned antenna pairs in a single ring.

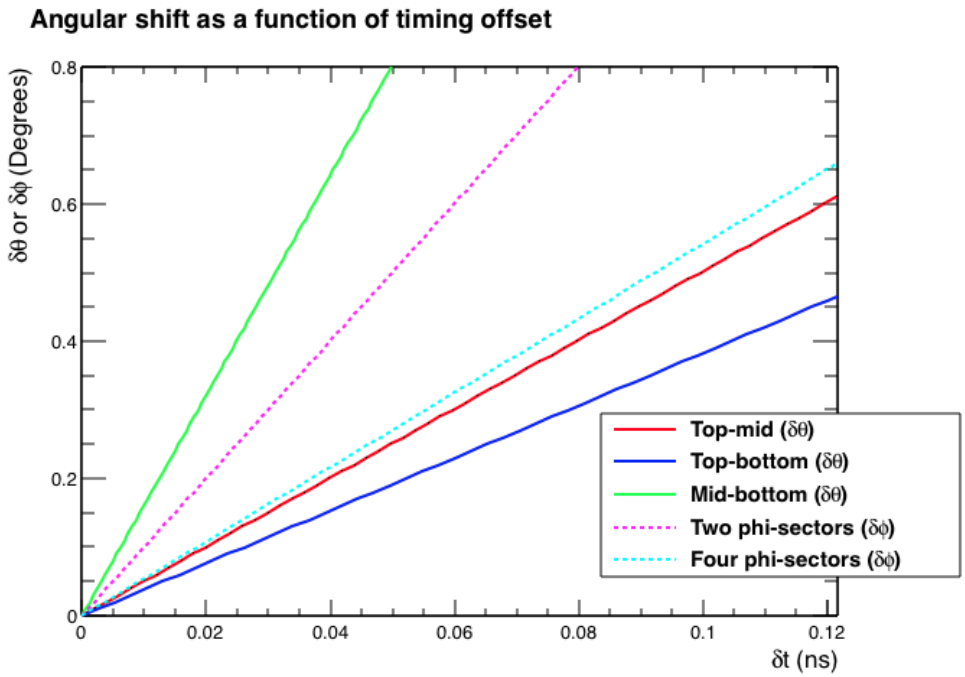

Figure 6.1: Angular offset as a function of signal misalignment in 5 antenna pairs. The dotted lines show the azmimuthal shift, $\delta\phi$, for horizontally aligned antennas in the same ring. The dotted lines show the elevation shift, $\delta\theta$, for vertically aligned antennas in the same ϕ-sector. The difference in gradients of the different antenna pairs is caused by the larger and smaller separations of the two antennas under consideration.

The ANITA analysis must reject impulsive signals that originate from human activity on the continent, and this is done by recording its direction of origin. Optimal angular resolution requires an accurate timing calibration of all the channels in the instrument. In this chapter I present my timing calibration of the ANITA-3 digitizers. To obtain the best possible timing resolution, the following quantities were calibrated:

- The uneven time base of the digitizers (sample-to-sample δts).
- The wrap around time of the electronic write pointer (ε_0 and ε_1).
- A temperature correction factor for each individual digitizer.
- cPCI Clock alignment algorithm.
- Relative cable delays from the antennas to the digitizers.

These are all presented in this chapter with a final summary of the timing resolution as a function of Signal-to-Noise ratio (SNR).

6.1 LABRADOR Architecture

The ANITA-3 digitizers, the Large Analogue Bandwidth Recorders And Digitizers with Ordered Readout (LABRADORs or LABs for short), were used to record the 96 channels of voltage-time information that comprise an ANITA-3 event. LAB chips are groups into sets of four on larger boards called Sampling Unit for Radio Frequency (SURF) boards.

The LABs used a ring oscillator as a timing control to successively connect and disconnect an input voltage line to cells in a Switched Capacitor Array (SCA) with 9 rows $\times$ 260 columns. The ring oscillator worked by connecting an odd number of voltage inverters together in a loop so that a transition propagated around it, successively from high-to-low then low-to-high. This moving transition, called the Ripple Carry Out (RCO), controlled the timing of all 9 rows of the capacitor array. A diagram showing the layout of the LAB is shown in Figure 6.3.

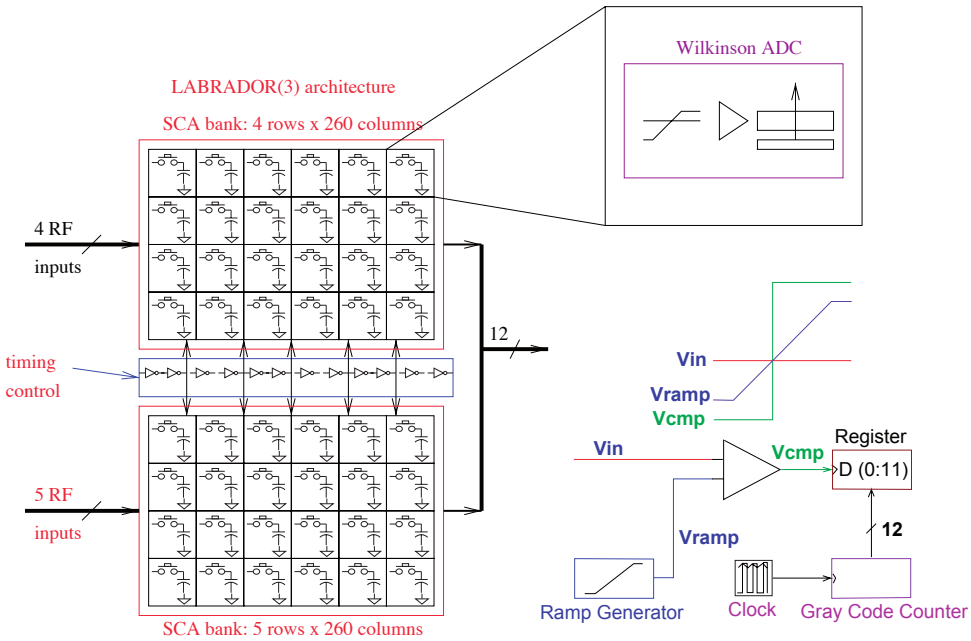

Figure 6.2: Schematic of the LAB-3 Architecture, taken from [12]. An inverter chain is used as a timing control for all 9 rows of the SCA.

For 4-6 columns in front of the RCO, some look ahead circuitry connected the capacitor rows to their respective input voltage line. Once connected, the changing input voltages moved charge to or from the capacitors. A short time later the RCO reached the switch for the SCA column and disconnected the capacitors from the RF input lines. This fixed the charge in the capacitors. This mechanism meant that the RCO functioned as electronic write pointer, recording the input voltage as function of time in successive SCA cells as it disconnected them from the RF input. The write pointer looped around the SCA until a trigger signal was received, at which point the write pointer was stopped. Each cell had a dedicated Wilkinson Analogue-to-Digital Converter (ADC) to measure the voltage generated by each capacitor. The digitized ADC values are then read out by the ANITA flight computer.

6.2 Intra-SURF Calibration

The uneven time base δt, write pointer wrap around time (ε), and temperature correction factors all calibrate the time between samples within an individual LAB. These are the intra-SURF calibrations.

The time for the write pointer to propagate between successive samples, δt, is determined by the sum of the inverter gate delays between the SCA column switches. The gate delay of an inverter is the time taken for the inverter's output voltage to change in once the input voltage is switched. Inverter gate delays are phase dependent, δt(low-to-high) $\neq$ δt(high-to-low), and were different for each inverter. The odd number of inverters required to make the RCO propagate meant that the RCO phase alternated with every loop. The write pointer circuit split and looped back to the beginning of the SCA after 256 samples, with 4 samples behind the split to fill in the gap in the time record. The time taken for the write pointer to loop back around to the start of the SCA after the 256th sample is called the wrap around time, ε. The relationship between the RCO phase, δts and εs is illustrated in Figure 6.3.

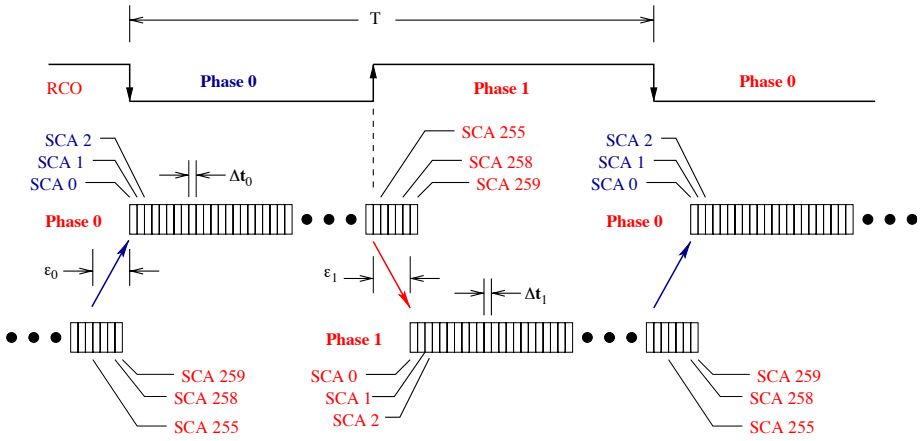

Figure 6.3: Schematic of the relationship between the LAB-3 timing constants to be determined, taken from [12]. The phase of the individual δts changes with each loop of the write pointer. The gap created by the wrap around time, ε, is covered by 4 additional samples at the back of the SCA.

The timing calibration constants within a LAB chip were determined with a single data set. A sine wave generator and splitter were used to feed a 432.1 MHz sine wave into one channel per SURF. One of the remaining splitter outputs was connected to a spectrum analyser to accurately measure the generated sine wave frequency. Figure 6.4 shows a diagram of the data taking setup.

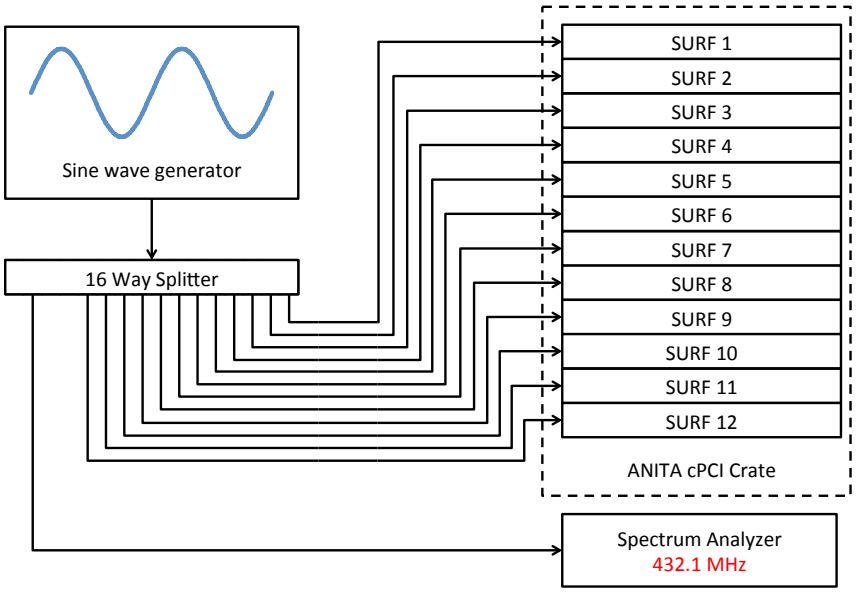

Figure 6.4: Sine wave injection setup for the inter-SURF calibration. 13 of the 16 splitter outputs are used to send the sine wave into the 12 SURFs and a spectrum analyser.

ANITA was set to trigger at a forced rate of 1 Hz and left overnight to record a large number of events. One event is shown in Figure 6.5, as rendered in the ANITA data viewing software `MagicDisplay`. The sine wave was injected into channel 2 or 4 depending on the SURF. Low channel numbers were chosen to minimise the effect of channel-to-channel cross talk from the clock in channel 9. The particular channels that were used were determined by ease of access inside the instrument box. No voltage or timing calibration is applied to the pedestal subtracted data in Figure 6.5. The y-axis of each graph is ADC counts and the x-axis is capacitor number.

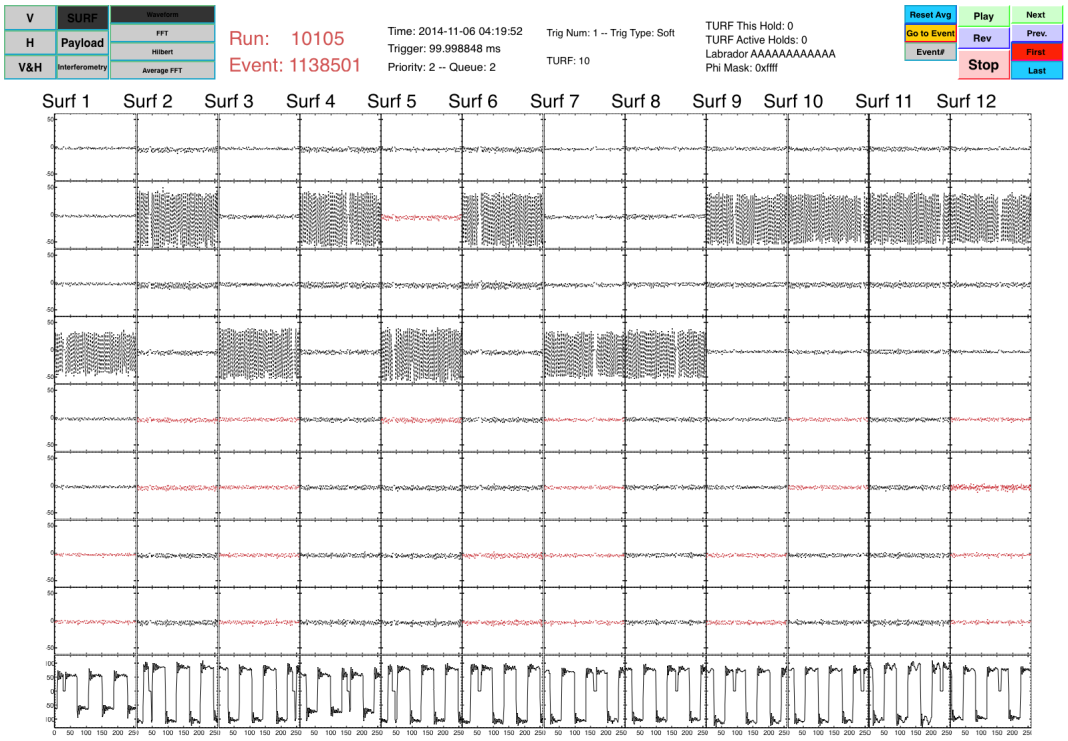

Figure 6.5: An event from the injected sine wave run shown in `MagicDisplay` with no calibrations applied. The channels are arranged with SURF number increasing from left-to-right and channel number increasing from top-to-bottom. The channels selected for sine wave injection are far from the clock.

In each event there were a group of successive samples with exactly zero ADC counts in the same position of each channel on a SURF. This can be seen most easily in the sine wave and clock channels in Figure 6.5 as the other channels only contain digitizer noise. This region is called the `HitBus`. The `HitBus` was typically 8-10 samples long and contained the 4-6 capacitors connected to the RF input in front of the write pointer when recording was stopped (see Section 6.1). Its location changed with every event because the external triggers were not in phase with the write pointer. Figure 6.6 shows a close up of SURF 1 channel 4 with the `HitBus` labelled.

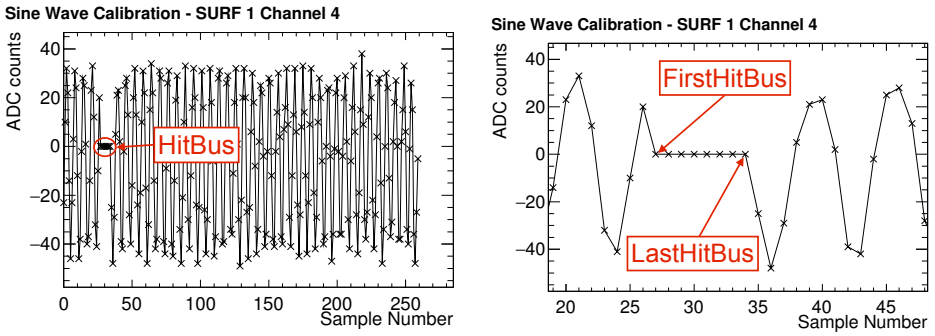

(a) Sine wave event. The `HitBus` region is labelled.

(b) Close up of SURF 1 Channel 4 from the sine wave event displayed in Figure 6.5.

Figure 6.6: Position of `FirstHitBus` and `LastHitBus`.

The `HitBus` position was recorded with an used bit in the ADC. To time order the digitized waveform, it must be unwrapped. The sample directly after the `LastHitBus` is the earliest sample. The sample just before the `FirstHitBus` is the latest sample. They are labelled in Figure 6.6. During readout, the Data Acquisition (DAQ) software overwrites the `HitBus` with zeros before saving the event to disk.

6.2.1 Sample-to-sample δts

The sample-to-sample δts were determined using the calibration data set. Digitising many sine waves of random phase, the probability of the sine wave crossing zero between two samples is directly proportional to the time between them. For a sufficiently large number of events the sample-to-sample δt_i is given by equation (6.1).

$$\delta t_i = \frac{N_i^{zc}}{2N_i f} \quad , \tag{6.1}$$

where δt_i is the time between sample i and sample $i+1$, N_i^{zc} is the number of zero crossings between i and $i+1$, N_i is the number of events that ith sample was not in the `HitBus`, f is the sine wave frequency 432.1 MHz, and the factor of 2 accounts for the two sine wave zero crossings in a period.

The N_i and N_i^{zc} as derived from the sine wave calibration data set for one particular LAB chip are shown in Figures 6.7 and 6.8 respectively.

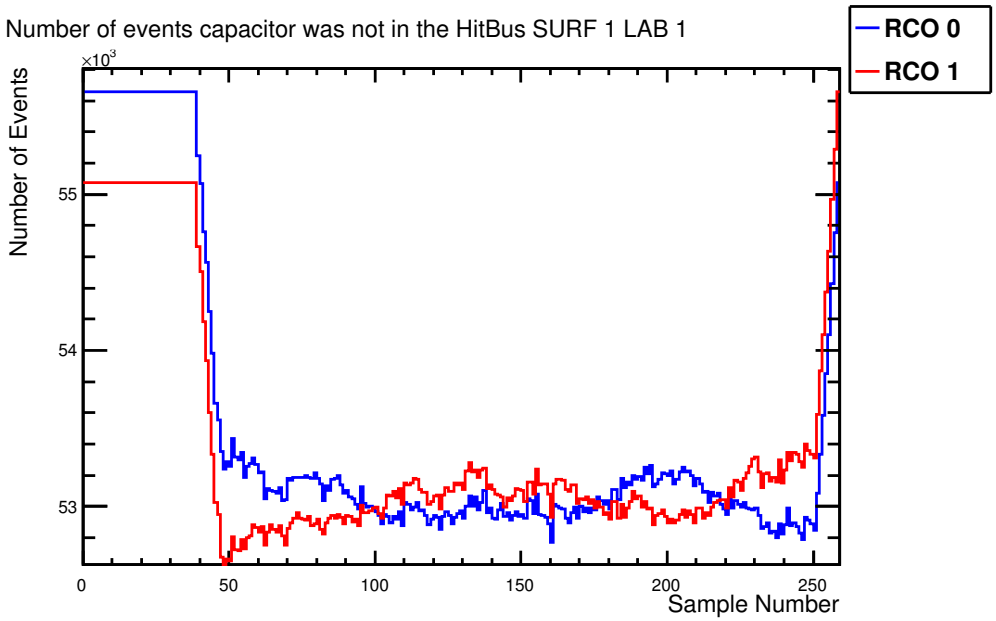

Figure 6.7: The number of times the samples of SURF 1 LAB 1 were not in the `HitBus` region during the sine wave calibration run, N_i. Some cuts on `HitBus` position have been applied to allow the RCO phases to be selected (see text for details). The zero is suppressed on the y-axis.

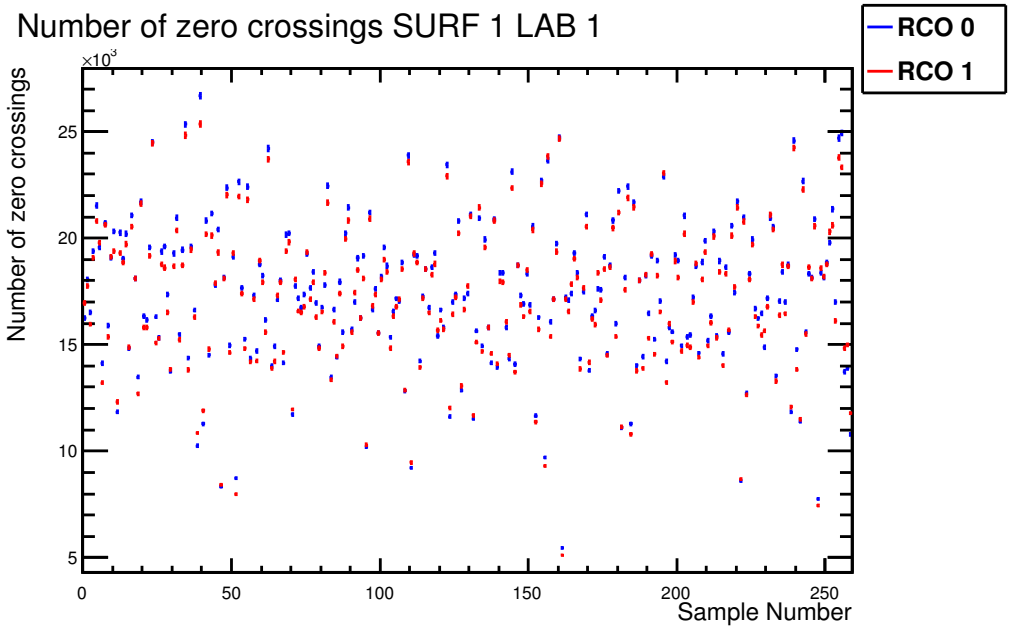

Figure 6.8: The number of times the sine waved crossed zero between successive samples for SURF 1 LAB 1 for both RCO phases, N_i^{zc}.

To explain the cuts on the `HitBus` location, a short digression into RCO phase determination is required. ANITA-2 and ANITA-3 both used the same generation

of LAB digitizers. For ANITA-2, the RCO phase of each LAB was determined in analysis software. For ANITA-3, a firmware update to the SURFs allowed the RCO phase to be read out when the event was digitised. The ANITA-2 software worked out the RCO phase by applying both possible sets of δts to the clock channel, and then and compared the clock period as measured in both RCO phases to the to the true clock period. With the wrong RCO phase applied all the clock periods would be too long or too short. The updated firmware was tested by comparing the RCO phase determined by software to the value reported by firmware. The test and its results of the test are fully described in an ANITA internal note that I co-authored with Harm Schoorlemmer [13].

The results in [13] showed a delay in the RCO phase being latched in the LAB register. Figures 6.9 and 6.10 are two plots from the note [13]. Figure 6.9 shows the effect of the RCO latch delay. Once a few ns have passed after the write pointer has started along the SCA, the software and firmware value agree. Prior to this time (26 samples for the example shown) they disagree. I have selected a plot with few outliers to best illustrate the effect, however there are a couple of disagreements between software and firmware reported RCO. This is due to the fact that an old, incorrect set of δts are applied to the clock to measure its period and determine the RCO phase. The algorithm still worked most of the time because the difference in the δts between RCO phases is close to the true RCO phase δt differences when averaged over the clock period. However there are possible clock phase and `HitBus` positions that cause the algorithm to give the wrong result.

Figure 6.10 shows the derived delay in terms of `FirstHitBus` value for the first 10 SURFs. ANITA-2 had fewer channels and so only used 10 SURFs. When the study was done, the old ANITA-2 calibrated δts were still in the software framework for the first 10 SURFs. The new SURFs had identical $\delta t = (1/2.6)$ ns for both RCO phases. This meant that the clock period looked identical when unwrapped in both RCO phases and the algorithm could not distinguish them so they are not included in Figure 6.10.

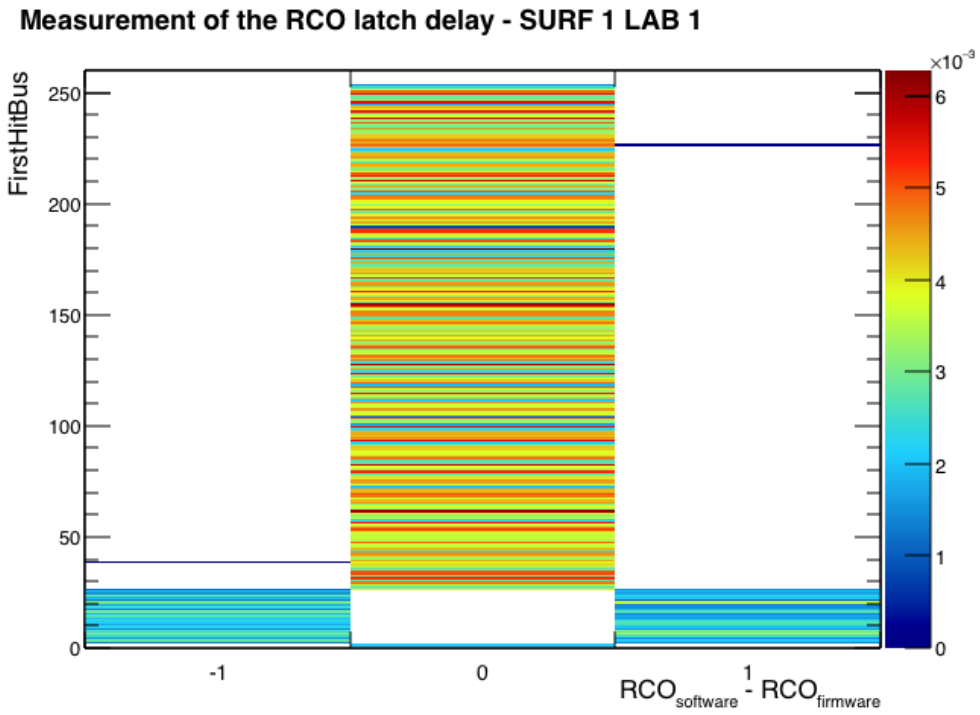

Figure 6.9: The difference between the firmware and software RCO values in SURF 1 LAB 1 as a function of `HitBus` location. The switch to both values agreeing occurs around `FirstHitBus` = 26. The software algorithm used an outdated set of δts but still generated the correct result (mostly) for reasons explained in the text. Similar plots for all SURFs and LABs are contained in [13].

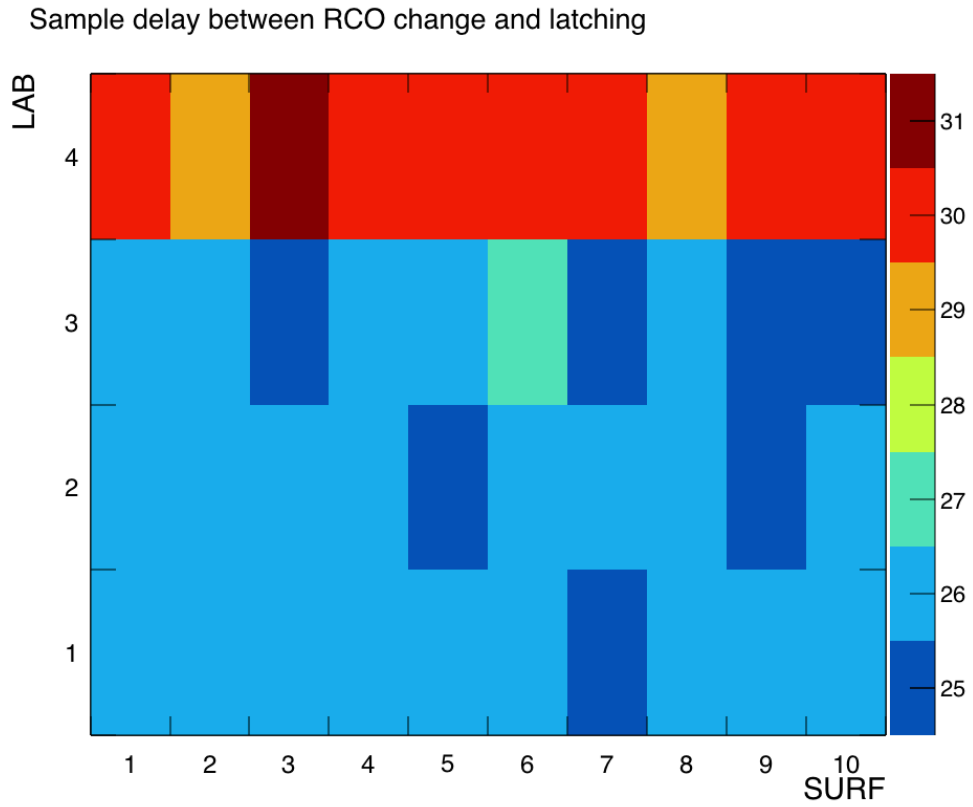

Figure 6.10: The delay in RCO phase latching in SURF firmware, measured using an outdated δt calibration. Plots from an internal ANITA note [13].

For the δt stage of the ANITA-3 intra-SURF timing calibration a conservative cut, `FirstHitBus` $>= 40$ was applied. It was sensible to be conservative because it was noted after initial tests that subsequent reprogramming of the SURF firmware altered the RCO latch delay time slightly. This cut is responsible for the flat region of Figure 6.7 for low values of `FirstHitBus`. The values are largest in this region because those samples are always in the zero crossing event sample. An additional cut on the value of `LastHitBus` < 258 was applied to ensure that there are at least two samples in the region of the waveform behind the `HitBus`. (These cuts also remove a possible `HitBus` configuration from the data set called the wrapped `HitBus`, where the `HitBus` region straddles the wrap around and the entire waveform is in one RCO phase.)

After taking the ratio of Figures 6.8, 6.7 and applying the conversion factor $1/2f$, the resulting δts and their distribution for SURF 1, LAB 1 are shown in Fig-

ures 6.11 and 6.12. The errors on the individual δts are propagated from the sum of the squared weights of the N_i^{zc}. The uncertainty on each sample δt is approximately 3.3 ps.

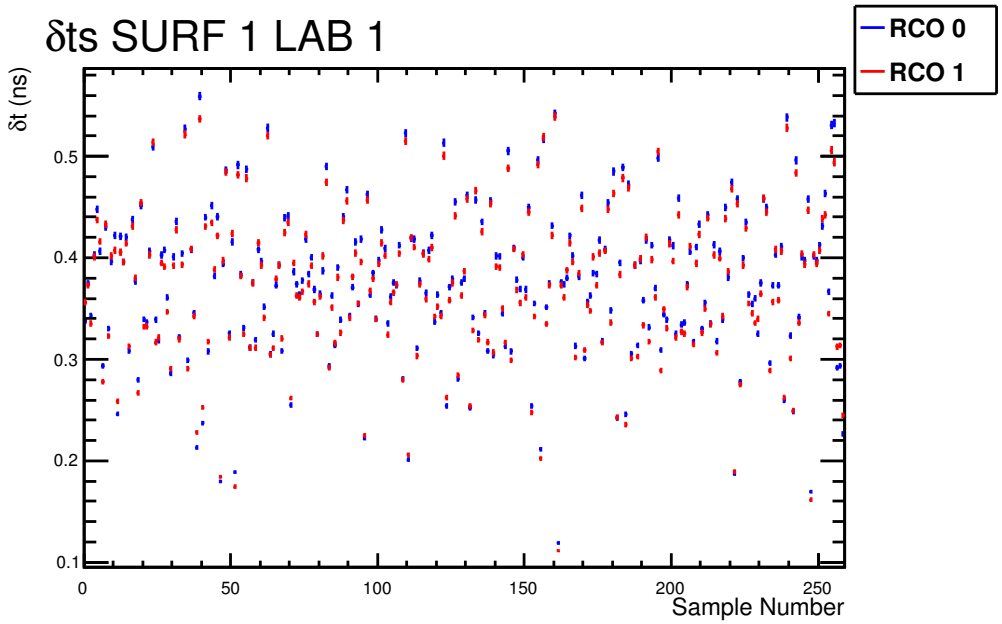

Figure 6.11: The values of δt for SURF 1 LAB 1. The sample-to-sample differences are large compared to the differences between the RCO phases.

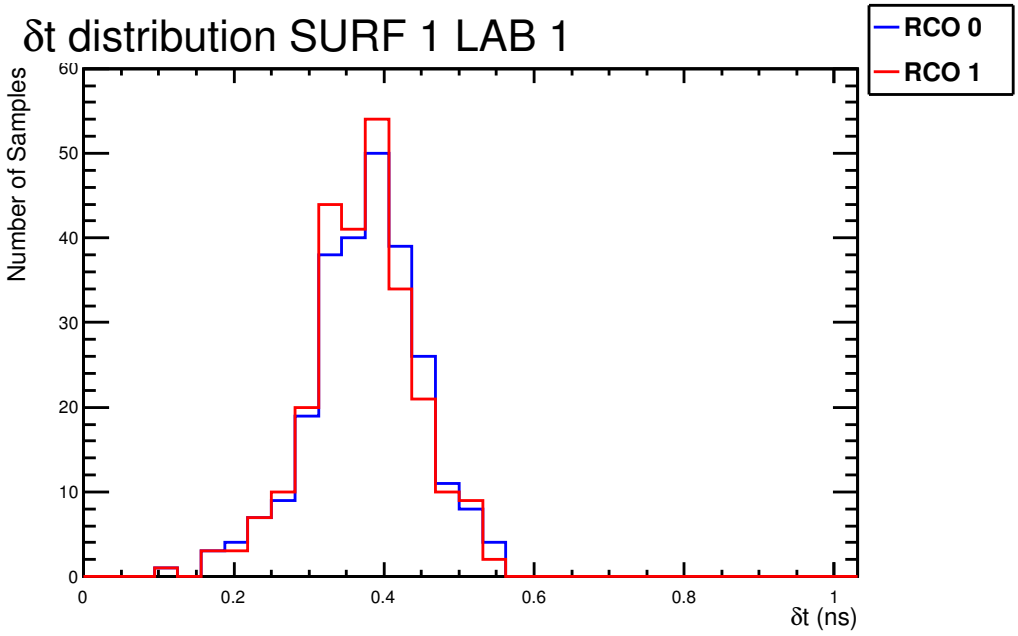

Figure 6.12: The distribution of δts for both RCO phases for SURF 1 LAB 1.

Each sample has a different δt in the two RCO phases, which gives $259 \times 2 = 518$ δts per channel. There are 4 LAB chips per SURF and 12 SURFs so the number of δts, $N_{\delta t}$, is

$$N_{\delta t} = 259 \times 2 \times 4 \times 12 = 24864 \quad . \tag{6.2}$$

The δt distribution for all the LABs is shown in Figure 6.13. For both RCO phases the sample-to-sample variation is $\approx 23\%$ of the distribution mean. The mean difference in δts between the RCO phases is shown in Figure 6.14.

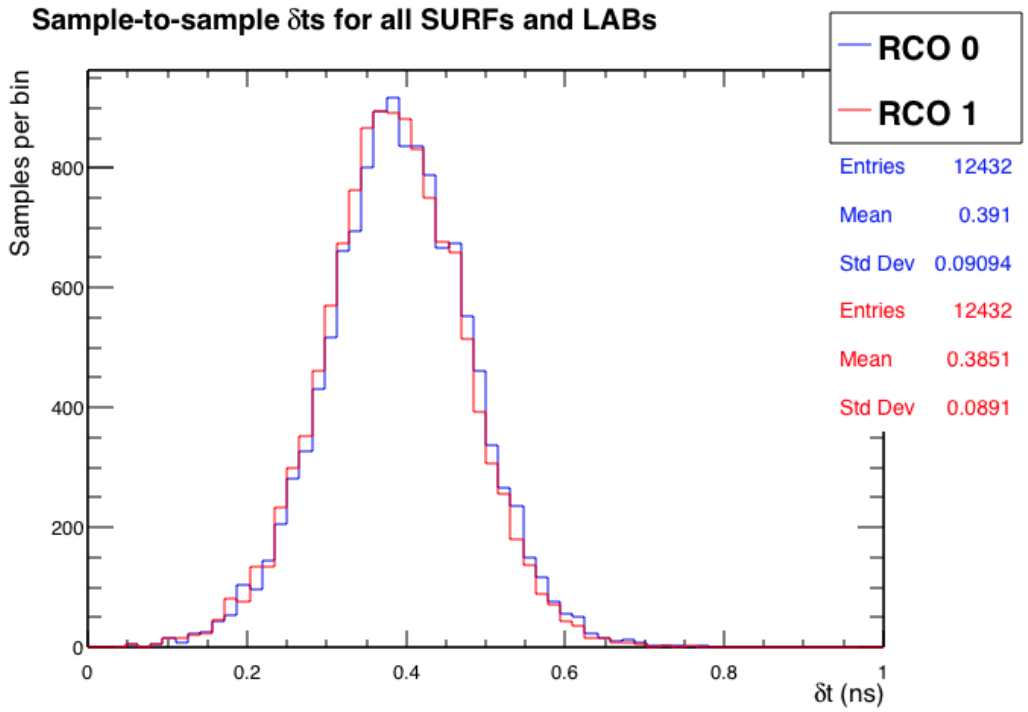

Figure 6.13: Distribution of δts for both RCO phases for all LABs.

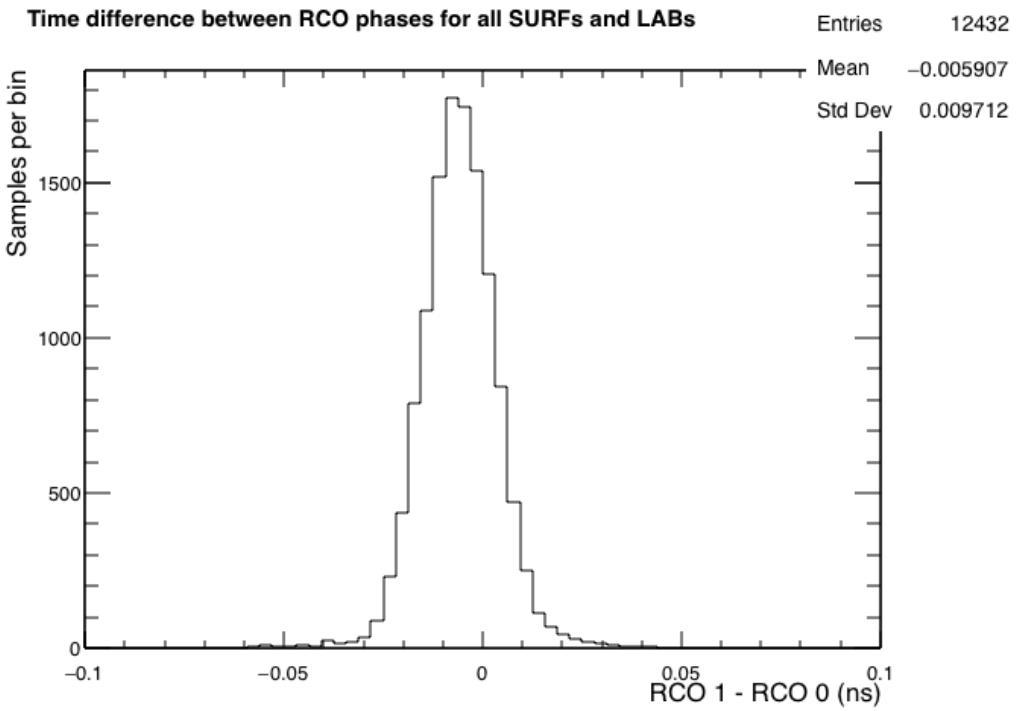

Figure 6.14: Distribution $\delta t_1 - \delta t_0$ for all LABs.

6.2.2 RCO wrap around time, ε

Once the write pointer passed the 256th sample it looped back to the 1st sample as illustrated in Figure 6.15. The time difference between the 256th sample and the 1st sample is called the wrap around time, ε. It was also be measured using the same sine wave data set.

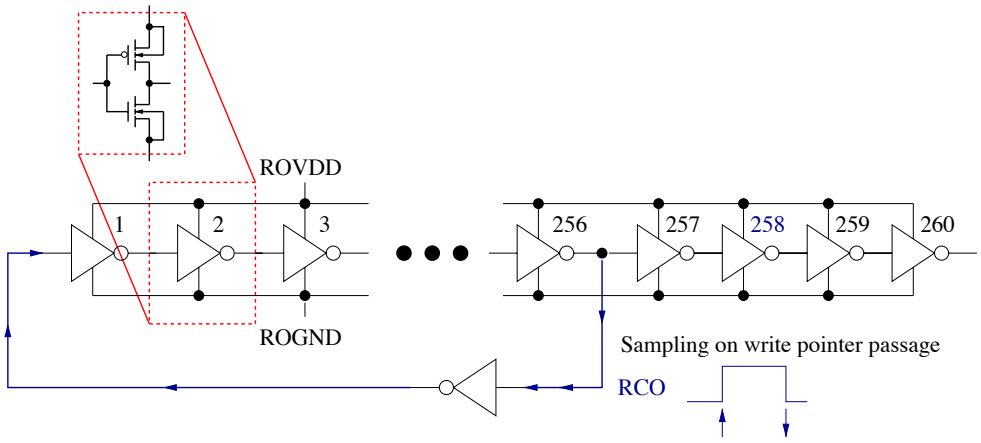

Figure 6.15: Diagram illustrating the write pointer looping back to the beginning of the SCA after the 256th sample. Figure from [12].

Calibrating the sine wave events with the sample-to-sample δts applied before and after the `HitBus` allowed a sine wave to be fitted to those regions.

The value of ε can be inferred using the phase of fitted sine wave at sample 255, Φ_{255}, and sample 0, Φ_0, as shown in Equation (6.3).

$$\varepsilon = \frac{1}{2\pi f}(\Phi_0 - \Phi_{255}) \quad , \tag{6.3}$$

where $f = 432.1\,\text{MHz} \pm 200\,\text{Hz}$ and, if necessary, 2π is added to Φ_0 to ensure

$$0 \leq \Phi_0 - \Phi_{255} < 2\pi \quad . \tag{6.4}$$

A cut was applied so fits were only made to events with 40 samples before and after the `HitBus` to ensure the phase is well constrained. The results of the fits of the two regions (a, b) require, $\chi_a^2/n_a + \chi_b^2/n_b < 25$, to reject events where the fitter failed to converge. The results of the fit for all LABs on SURF 1 are shown in Figure 6.16.

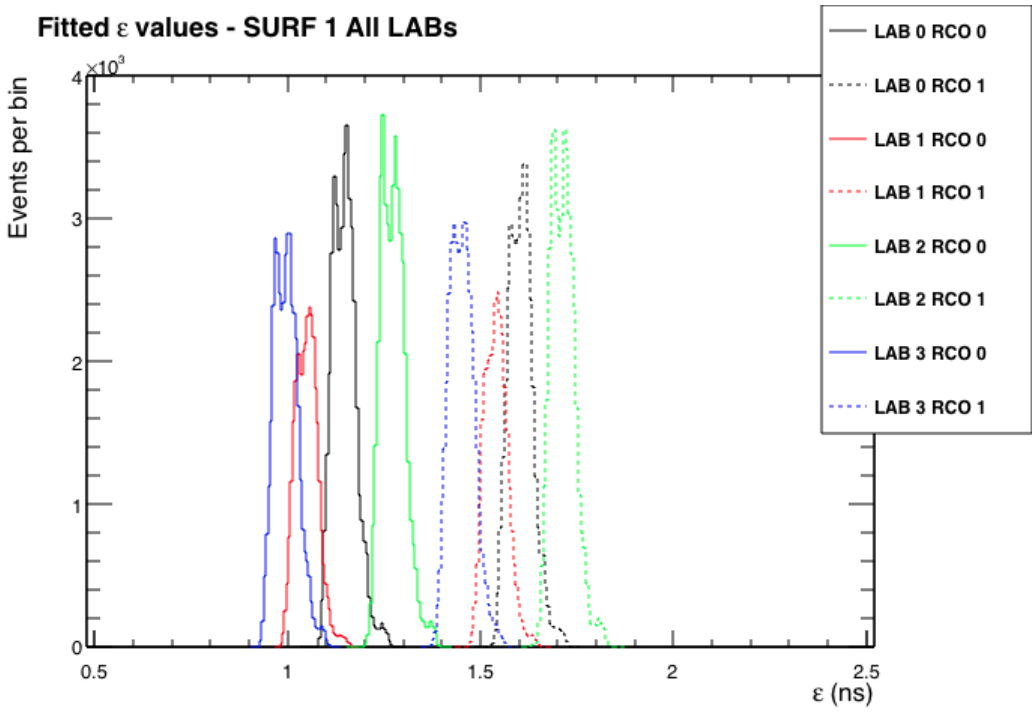

Figure 6.16: Fitted ε results for SURF 1. Each LAB is a different colour, with solid lines for RCO 0 and dashed lines for RCO 1. The phase used to label the wrap around is the RCO phase of the region before the wrap around (from `LastHitBus` to the end of the SCA).

The results for the other SURFs show identical features. There is a significant difference between RCO phase with the two phases separated by ~ 0.45 ns, which is a percentage change around $35-45\%$.

6.2.3 Temperature correction

The dual peak structure in Figure 6.16 is visible in both RCO phases for all channels. Figure 6.17 is a plot of ε as a function of event number for a couple of LABs.

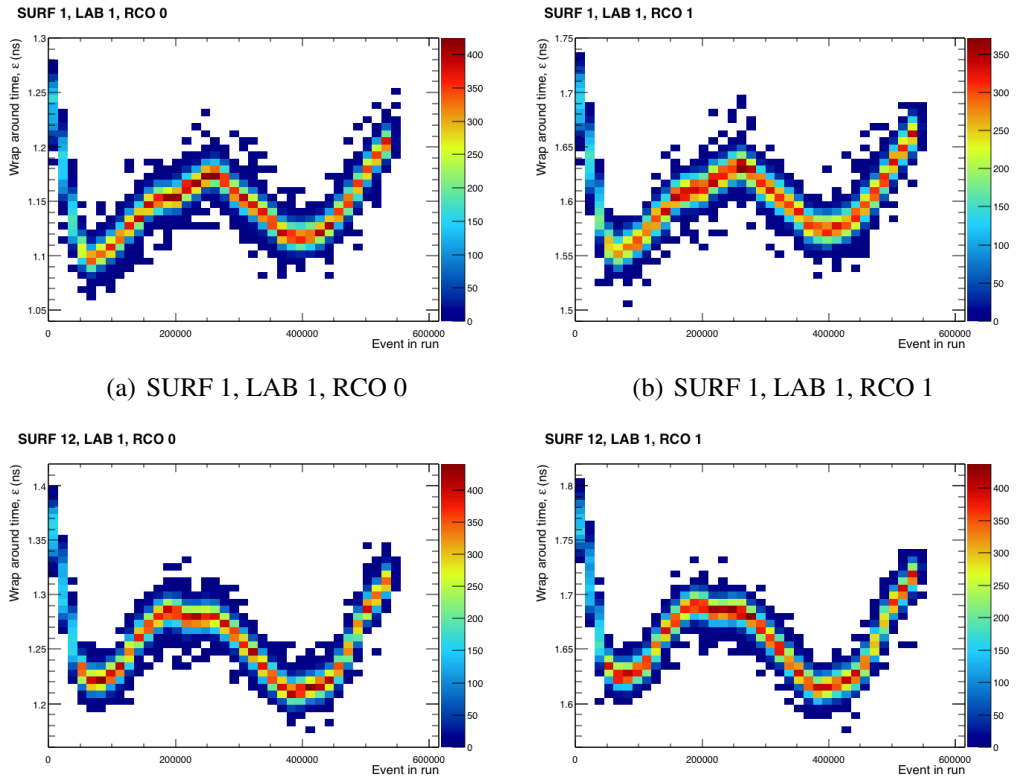

(a) SURF 1, LAB 1, RCO 0

(b) SURF 1, LAB 1, RCO 1

(c) SURF 12, LAB 1, RCO 0

(d) SURF 12, LAB 1, RCO 1

Figure 6.17: Distribution of ε as a function of event number for both RCO phases of LAB 1 on SURFs 1 and 12. Very similar patterns of variation were found for all LABs and SURFs.

The value of ε varies significantly with time. The oscillation causes double peak structure in Figure 6.16.

The calibration run took place over nearly 17 hours. The spectrum analyser that was monitoring the sine wave frequency indicated no change between when the run was started and stopped. Figure 6.18 shows a profile of the fractional variation of the cPCI clock and sine wave periods as a function of event number. The profiles are normalised by the means of the two distributions. The agreement is excellent, which suggests that this is caused temperature variation in the LAB chips, which is a known effect [12]. Over the range of temperatures in the LDB hanger during the calibration run, the mean δt sampling period varies by $O(0.1\%)$, an order of magnitude smaller than the difference in the RCO phase.

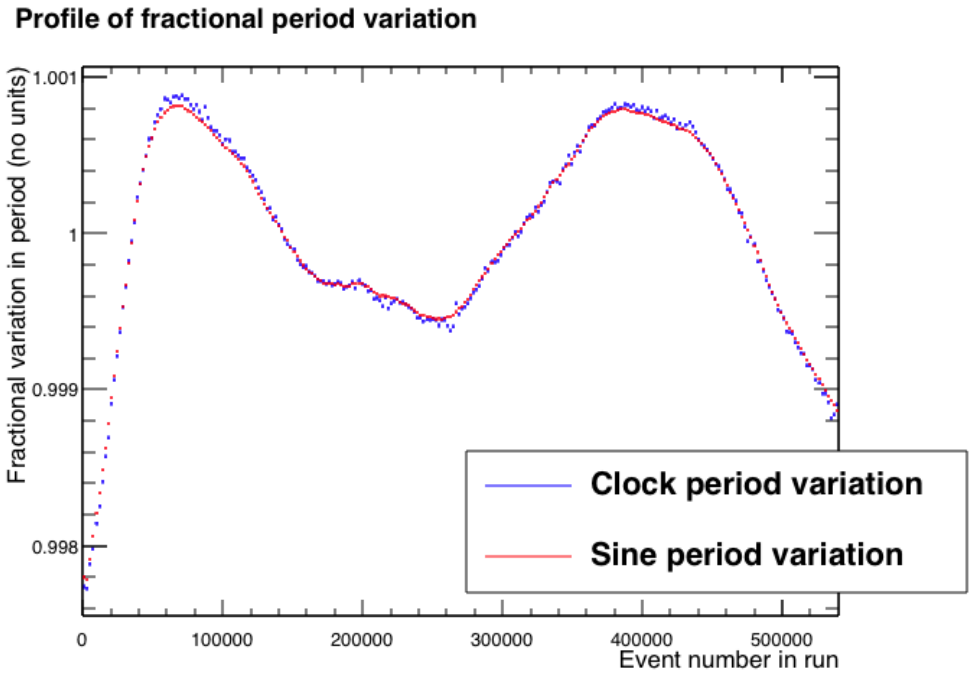

Figure 6.18: Normalised profiles of the clock period and sine wave periods as a function of event number in the sine wave calibration run.

This implies that the δts found in Section 6.2.1 were averaged over some temperature range. Knowing the true sine wave frequency as measured by the spectrum analyser, I made a temperature correction as a function of time to the calibration run. Applying this correction stabilised the variation as a function of time and allowed determination of the clock period. The results are shown in Figure 6.19. Once the mean cPCI clock period (corrected by the sine wave period) was established as 30 ns, this baseline was used to make corrections for all other runs.

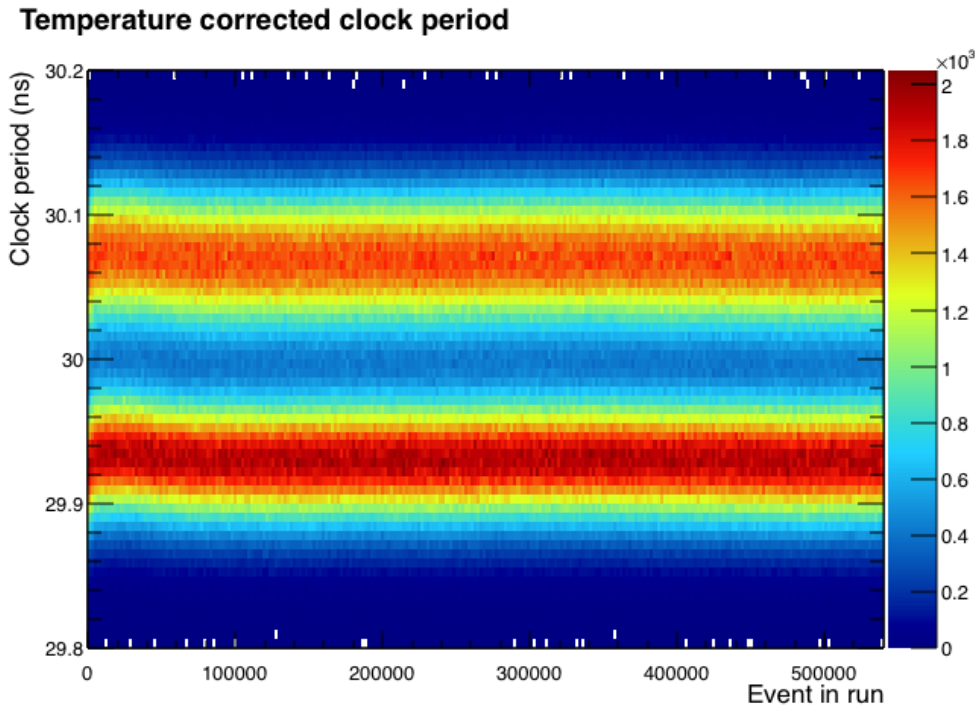

Figure 6.19: Clock period after being corrected by the variation in sine wave frequency. The clock period has a double peak structure that is not caused by temperature variation.

The scale of the temperature correction, as established in figure 6.18 is $O(0.1\%)$. However, Figure 6.17 shows that the fitted values of ε vary by $O(10\%)$. This is because the frequency parameter of the fit $f = 432.1\,\text{MHz}$ was fixed, whereas the apparent frequency varies as the δts change with temperature. This feature of the fit can be used as a tool to design a finely tuned temperature correction. The goal of the correction was to minimise variation in fitted ε. Figure 6.20 shows the very similar trends in ε vs. event number for all SURFs and LABs in both RCO phases.

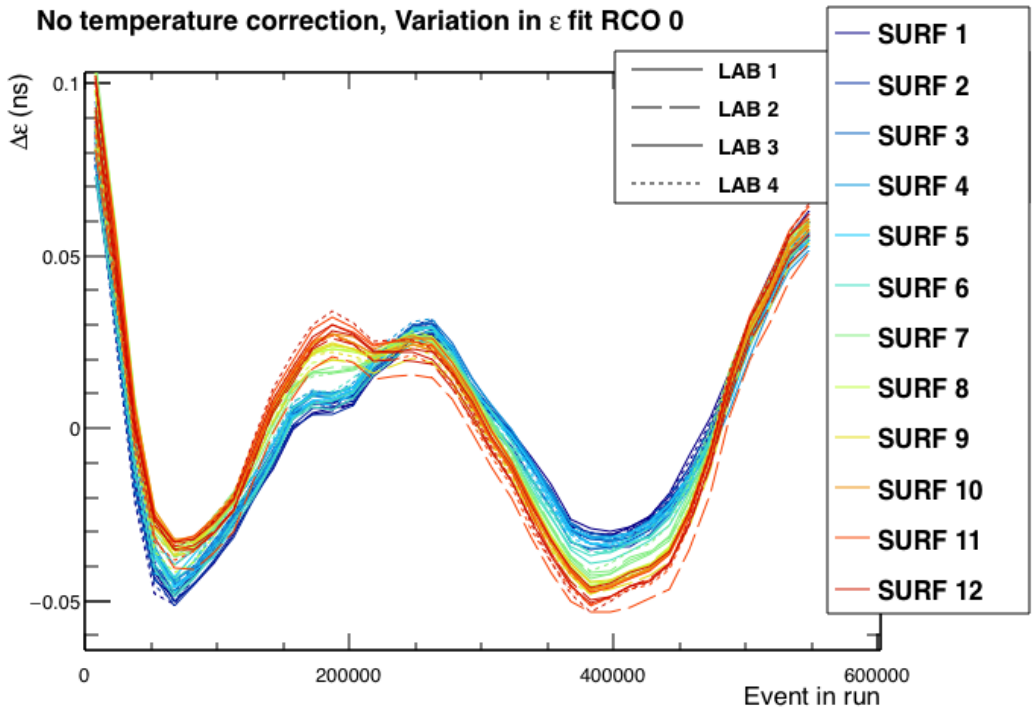

(a) Variation in fitted ε_0 during the calibration run.

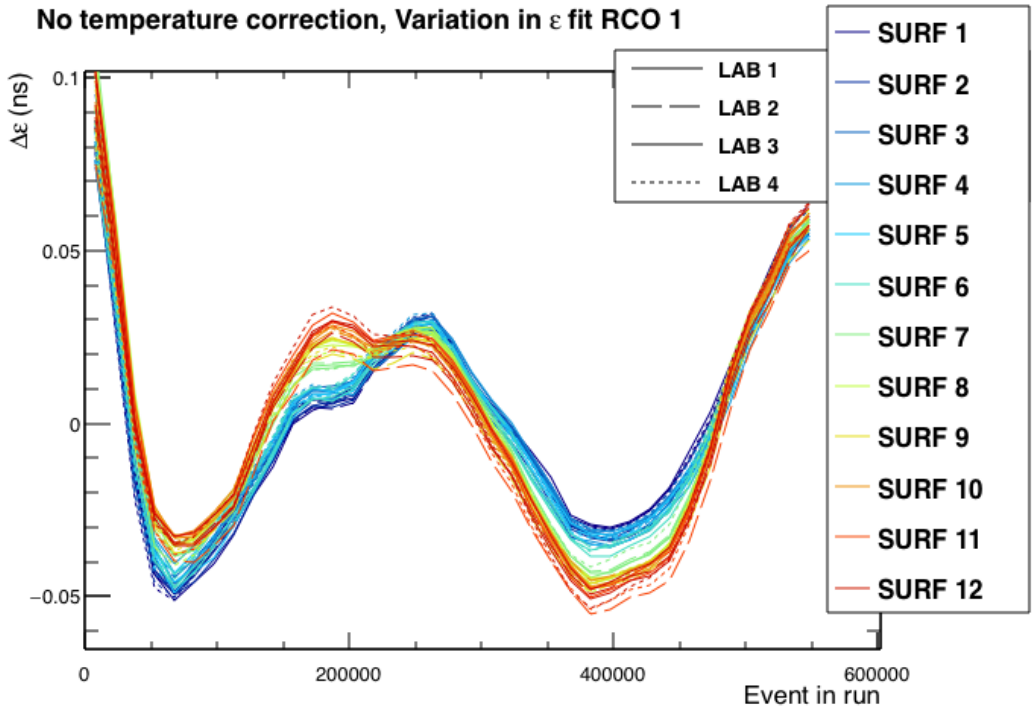

(b) Variation in fitted ε_1 during the calibration run.

Figure 6.20: Change of the fitted wrap around time during the sine wave calibration run.

While trying to achieve minimal variation ε as a function of time, I considered

three different ring buffer sizes. First, one ring buffer was assigned for the whole instrument, then one per SURF, and finally one per LAB. (Initially the periodic input under consideration was the sine wave, but this was switched to the clock during testing so the method could be applied to data sets other than the calibration run.) The temperature correction itself takes the form of a scale factor, f_{temp}, applied to the δts,

$$f_{\text{temp}} = \frac{T_{\text{true}}}{T_{\text{ring-buffer}}} \quad , \tag{6.5}$$

where

$$T_{\text{ring-buffer}} = \frac{1}{N}\sum_{i}^{N}\frac{1}{M}\sum_{j}^{M}T_{ij} \quad , \tag{6.6}$$

where f_{temp} is the temperature correction factor, N is the size of the ring buffer in events, where there are M periods per ring buffer per event, and T_{ij} is the period of the input. The number of periods, M, depends on the period and phase of the input and number of channels included in the ring buffer. During testing it was noted than the success of the different methods was fairly insensitive to the ring buffer size, N, which was reduced as the different methods were tried.

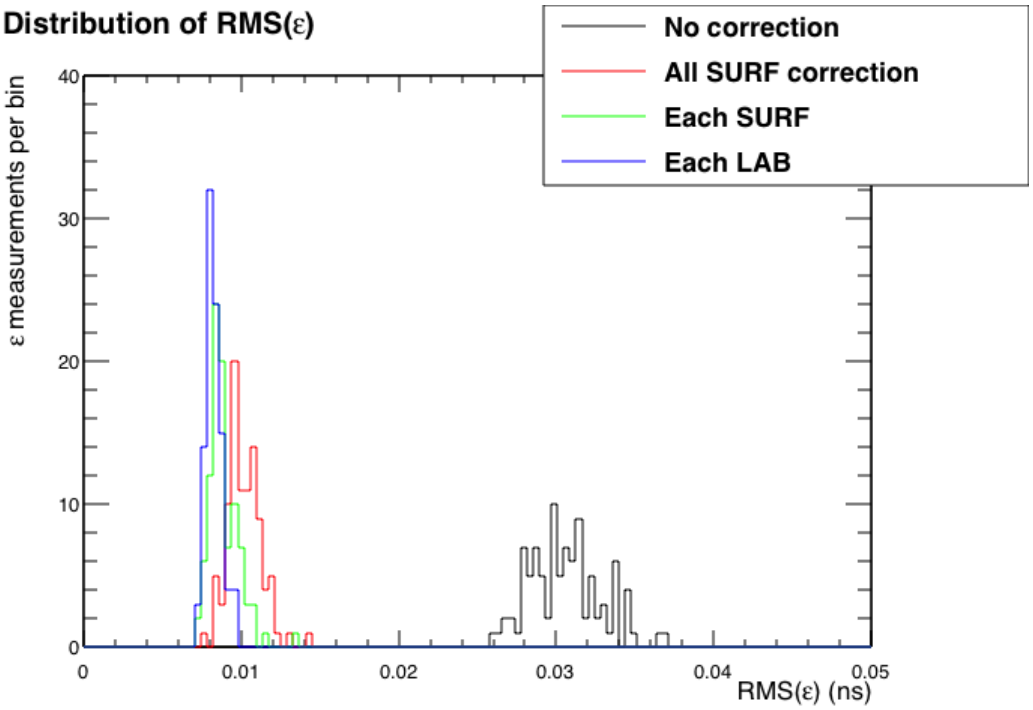

Figure 6.21: A comparison of the distribution of the ε RMS values for all SURFs, LABs and RCO phases for the different temperature correction methods.

Figure 6.21 shows a summary of the $RMS(\varepsilon)$ values for the different temperature correction methods. A mean instrument temperature correction is far superior to nothing, with small gains made for giving SURF, then each LAB an individual ring buffer.

A limitation of this temperature correction method is that it does not account for how the period of the clock itself changes with temperature. However, the identical behaviour of the apparent sine wave period and clock period, as shown in figure 6.18, indicates that it is a smaller effect than the temperature variation of the digitizers.

6.2.4 RCO phase determination in software

As discussed in Section 6.2.1 the RCO phase as reported by the LAB chips is reliable for `FirstHitBus` ≥ 40. However, calibration of all events requires an algorithm that can determine the RCO phase regardless of `HitBus` location.

An algorithm was developed that uses the 33 MHz cPCI clock to determine the RCO phase. The algorithm works by calibrating each SURF's clock channel in both possible RCO configurations. In the case that the `HitBus` is wrapped around the end of the SCA, the entire waveform is in RCO 0 or RCO 1. In the case that the `HitBus` is not wrapped around the end of the SCA then the section before the `HitBus` could be in RCO 1 or 0 with the section behind the `FirstHitBus` taking the other phase. In both cases there are only two possibilities.

During initial development only the case where `FirstHitBus` ≥ 40 is considered as the RCO phase is known from the SURF firmware. Figure 6.22 shows the measured clock period for RCO phases agreeing and flipped relative to the firmware reported value for SURF 1.

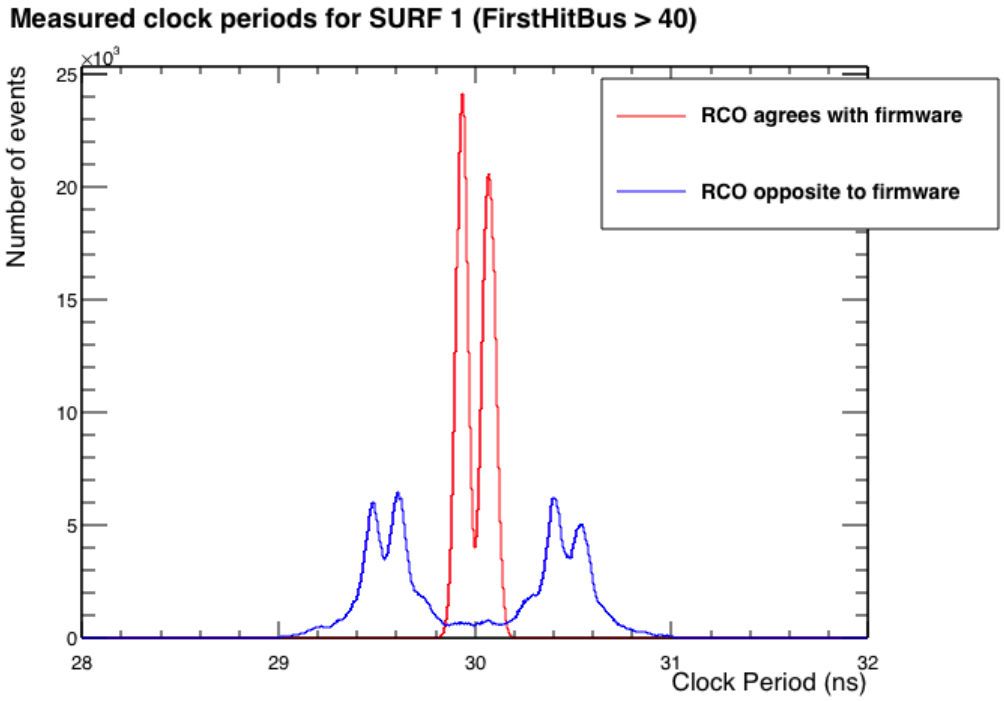

Figure 6.22: The measured clock period of SURF 1 with both configurations of RCO phases applied. A cut on `FirstHitBus` ≥ 40 has been applied.

When the wrong RCO phase is applied the clock periods usually appear too short or too long, however this is not always true. Figure 6.23 shows the measured clock periods plotted as a function of the SCA capacitor number, C_{zc}, of the upward zero crossing at the start of the clock period. Figure 6.24 shows the same distribution except that the clock channel was calibrated with the inverse RCO phase.

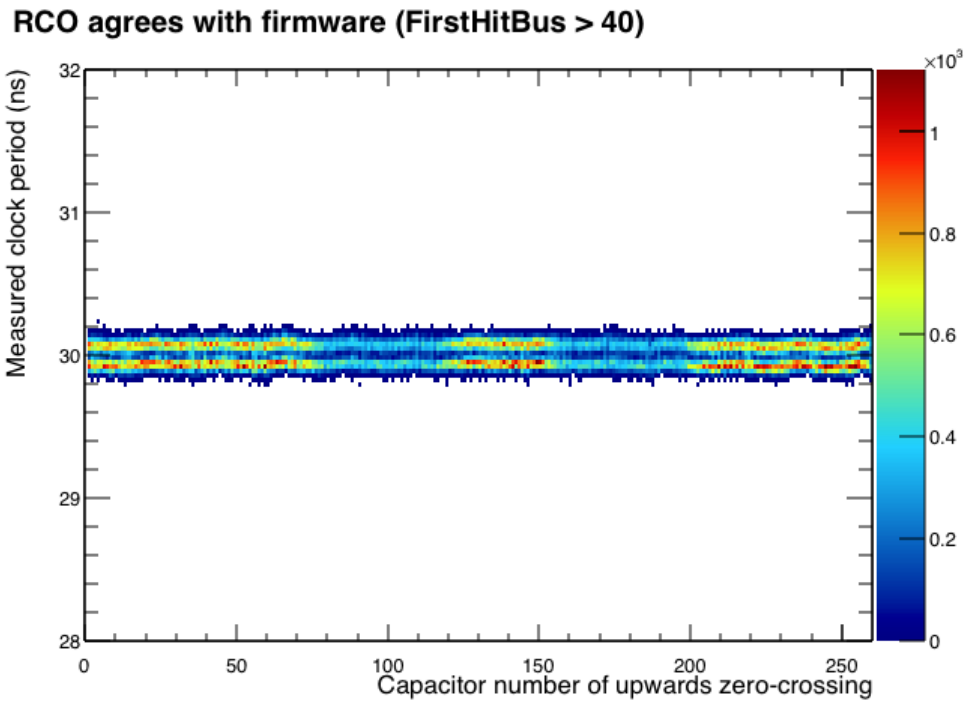

Figure 6.23: Measured clock periods in SURF 1 with δts and εs applied in agreement with firmware reported RCO phase.

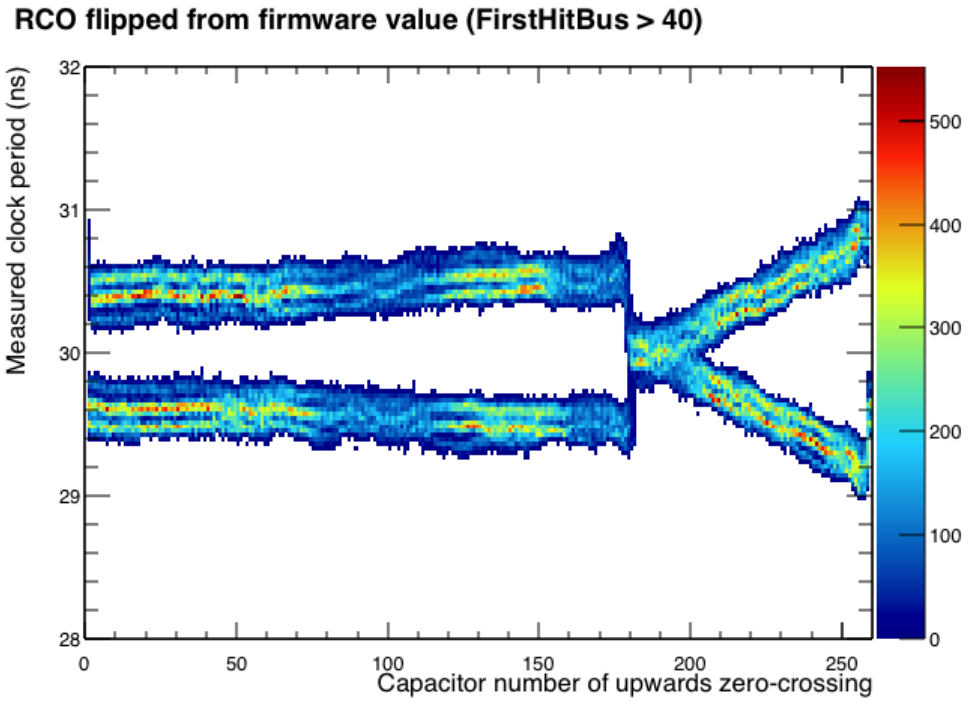

Figure 6.24: Measured clock periods in SURF 1 with δts and εs flipped relative to firmware reported RCO phase.

The firmware agreeing RCO configuration is consistent across the whole SCA. The inverted RCO distribution has an x-axis region where the measured clock period overlaps with true value in Figure 6.23. A rapid change occurs when $C_{zc} \approx 180$. This is approximately 29.2 ns before the wrap around time. A clock period measured with the inverted RCO phase δts is 0.45 ns (1.5% of 30 ns) longer or shorter than 30 ns. This happens to be the same magnitude, but opposite sign, to the difference between the ε values of the two RCO phases. The inverted ε value cancels out the inverted δts and the flipped RCO clock period starting around $C_{zc} \approx 180$ is equal to the true clock period.

After cutting on clock periods in which the C_{zc} lies in the range $170 < C_{zc} < 220$ the overlap between the correct and incorrect RCO clock periods is significantly reduced. This is shown in Figure 6.25.

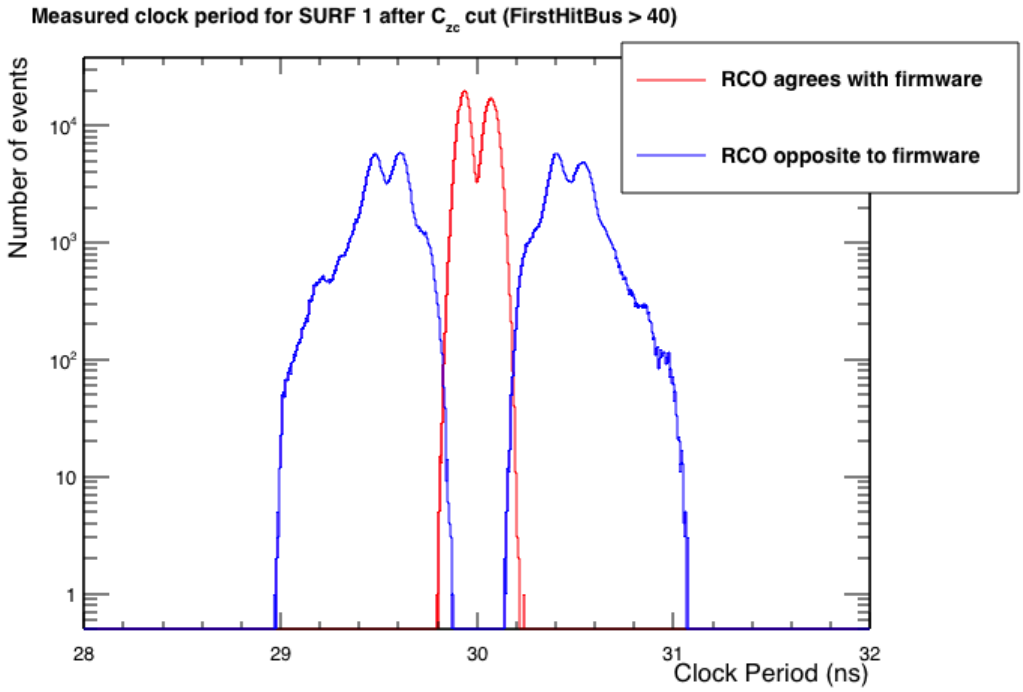

Figure 6.25: The measured clock period of SURF 1 with both configurations of RCO phases applied. A cut on `FirstHitBus` ≥ 40 has been applied. An additional requirement that C_{zc} does not lie in the range $170 < C_{zc} < 220$.

The cut on C_{zc} improves the separation of the two RCO phases, however there is a small residual overlap not localised to a region of SCA parameter space. Events lying in the overlapping regions of Figure 6.25 constitute a small fraction of the

total. In order to mitigate this small overlap one must combine the information from multiple clock crossings per event.

For each measured clock period, T_m, one calculates the absolute difference, ΔT_i, between T_m and the closest clock period mode (29.93 ns or 30.07 ns),

$$\Delta T_i = \min(|T_m - 29.93\,\text{ns}|, |T_m - 30.07\,\text{ns}|) \quad , \tag{6.7}$$

where i is the RCO phase. Then a figure of merit for the RCO phase discrimination, α, is assigned by finding the difference between the sum over ΔTs for both RCO phases.

$$\alpha = \left(\sum_N \Delta T_1\right) - \left(\sum_N \Delta T_0\right) \quad , \tag{6.8}$$

where N is the number of periods in the clock channel, excluding periods which begin with capacitor numbers, C_{zc}, in the range $170 < C_{zc} < 220$. The RCO value is assigned

$$\text{RCO} = \begin{cases} 1 & \text{if } \alpha < 0 \\ 0 & \text{otherwise.} \end{cases} \quad . \tag{6.9}$$

For the purposes of designing the algorithm, the RCO phases were not separated 1/0 but into agreement/disagreement with the firmware value. I have indicated this by renaming the α variable as β, and changing $\Delta T_{1/0}$ for $\Delta T_{a/d}$ (agreement/disagreement).

$$\beta = \left(\sum_N \Delta T_a\right) - \left(\sum_N \Delta T_d\right) \tag{6.10}$$

A plot of β for all SURFs and LABs in shown in Figure 6.26. A value $\beta < 0$ indicates that the algorithm agrees with the firmware reported RCO, $\beta > 0$ indicates the opposite. Figure 6.26 includes all values `FirstHitBus`, and the effects of the RCO latch delay become visible again.

The output of the algorithm is not 100% accurate. To reduce this error rate in the a second iteration is done, with the output of the first iteration used to modify the initial step (equation 6.12). The RCO phases assigned by the first iteration are assigned to the clock channels. The mode (29.93 ns or 30.07 ns) of each clock

period in all SURFs is estimated by taking the mean of the aligned[1] clock periods in each SURF, $\overline{T_m^i}$,

$$\overline{T_m^i} = \frac{1}{12} \sum_{\text{SURFs}} T_m^i \quad , \tag{6.11}$$

where i corresponds to the index of the aligned clock period, when averaged over SURFs. The peak value, $T_p = 29.93\,\text{ns}$ or $30.07\,\text{ns}$, closest to $\overline{T_m^i}$ replaces the right-hand side of equation (6.12). So ΔT_i is redefined as

$$\Delta T_i = |T_m - T_p| \quad , \tag{6.12}$$

where the other symbols retain their previous meeting. After redefining ΔT, the β distribution peaks are shifted away from each other, such that the gap straddles the zero value.

[1]There is significant clock delay as a function of SURF number, which must be accounted for. This is discussed in Section 6.3.1.

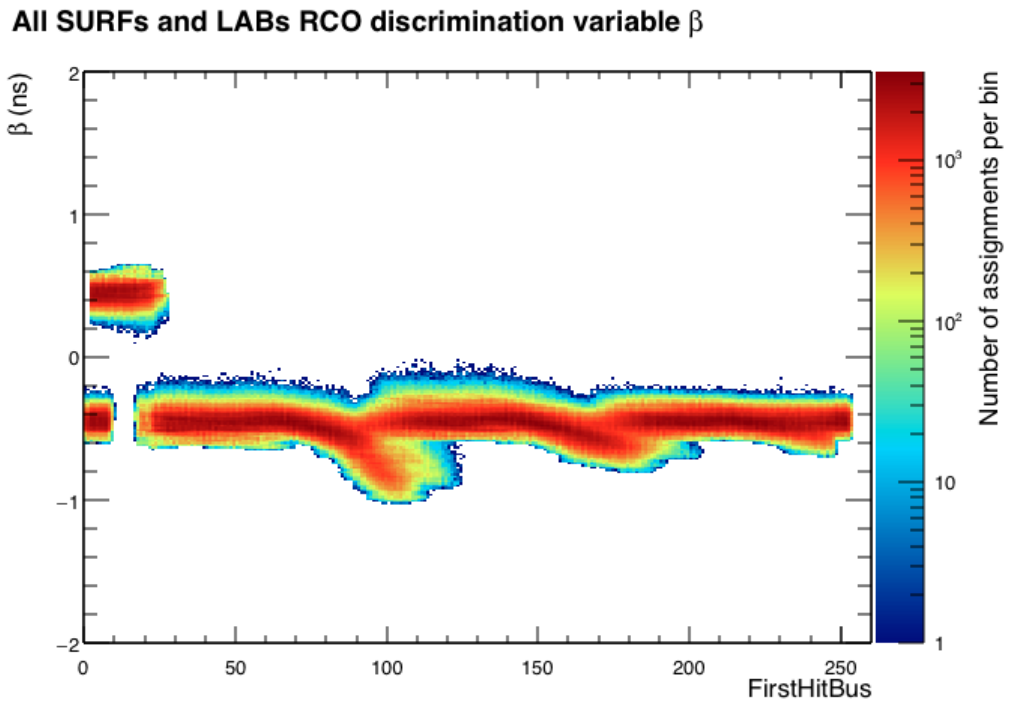

(a)

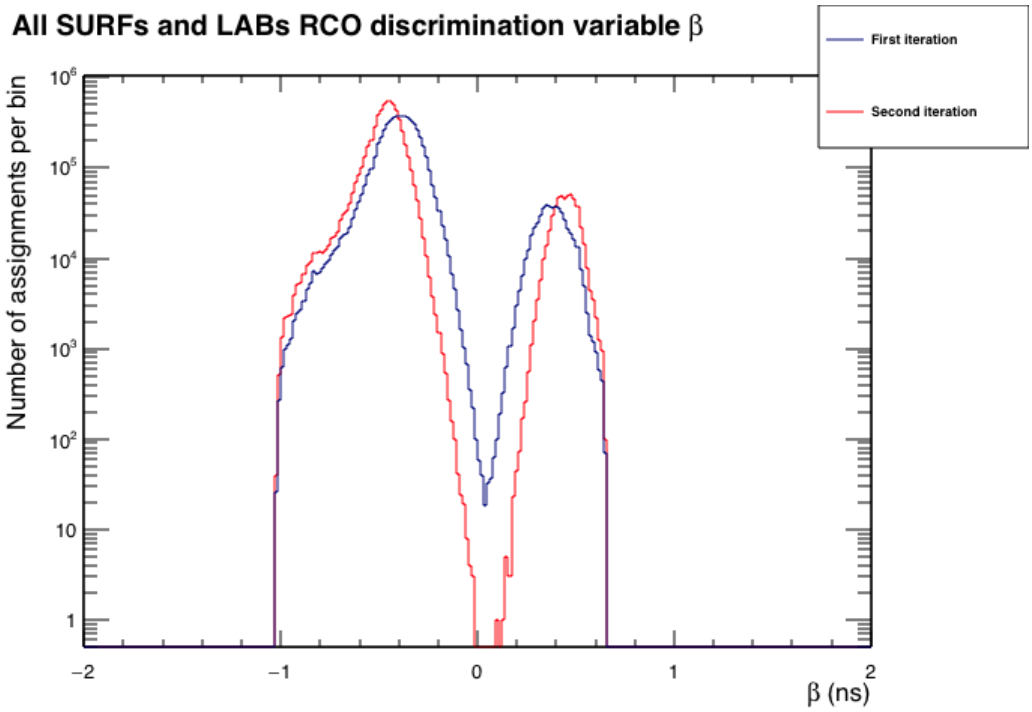

(b) Y-axis projection of (a). The two populations are separated with the β value now correctly predicting the RCO phase.

Figure 6.26: β plots for the second iteration of the RCO phase determination algorithm.

The β distribution separates the two populations, correctly predicting the RCO

phase. However, in a larger sample of events, the tail of the distribution will extend over $\beta > 0$. To counter this somewhat, the final RCO phase determination algorithm uses the firmware reported RCO values for LABs when the `FirstHitBus` ≥ 40. The RCO phases obtained by this algorithm are only used for LABs when the `FirstHitBus` < 40.

6.3 Inter-SURF timing

Once the timing inside a SURF was calibrated, the next task was to calibrate the relative timing between SURFs. When the TURF issues a trigger signal to the SURFs, the event is recorded on the next tick of the SURF's 250 MHz clock. This creates a delay of up to 4 ns in the recording of channels on different SURFs. This "trigger jitter" must be corrected for on an event by event basis. This is the reason the cPCI clock is broadcast to to all SURFs. The delay in a SURF digitising its channel will show up as a relative delay in the clock phase. By subtracting a delay, δt_{clock}, to each channel on a SURF such that the times of the rising clock edges are aligned the trigger jitter is removed.

In addition to this per-event correction, there are constant delays between channels through slight differences in signal chain components, such as differing cable lengths. This constant correction I call $\Delta t_{\text{channel-to-channel}}$.

A series of measurements were made to determine the set of $\Delta t_{\text{channel-to-channel}}$ values. A picosecond pulse generator was used to inject a pulse though the signal chain into two channels per measurement, a test channel and a reference channel. A diagram of the setup is shown in Figure 6.27.

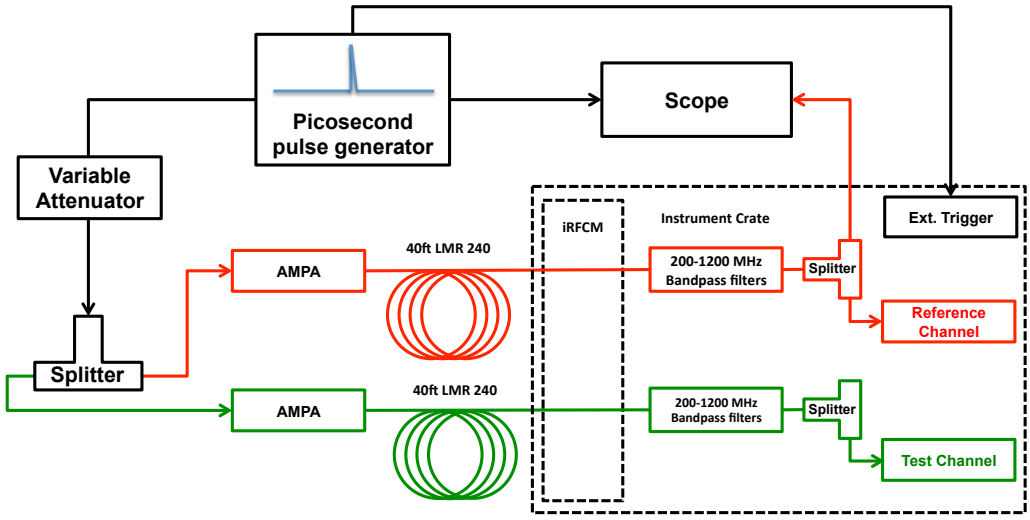

Figure 6.27: Test and reference pulses are injected into the AMPAs, directly behind the ANITA antennas. By finding the delay between the pulses one can calibrate out the differences in cable length, which causes relative delays between channels.

The reference channel, kept the same for all measurements, was (SURF 1 Channel 7). The test pulse input was moved around all other channels on the payload. Approximately 4000 pulses per channel, 1000 per LAB, were recorded for each test. As each LAB is in a different physical location on the SURF, the $\Delta t_{\text{channel-to-channel}}$ is slightly different.

After the signal from the picosecond pulser was split, it was injected into the test and reference channels at the AMPAs, which are directly behind the antennas. The time of maximum cross-correlation between the pulses, gives the relative delay between the two channels for each event. The cross-correlation, C_{12} of two regularly sampled signals, Φ_1, Φ_2, is defined as

$$C_{12}[\mathrm{j}] = \frac{1}{\sigma_1 \sigma_2} \sum_i \Phi_1[\mathrm{i}] \Phi_2[\mathrm{i+j}] \tag{6.13}$$

where N is the nnumber of points in the signal, i, j are the sample indices, and $\sigma_{1,2}$ is the RMS of $\Phi_{1,2}$. Akima interpolation was used to find the values of $\Phi_{1,2}$ at regular intervals.

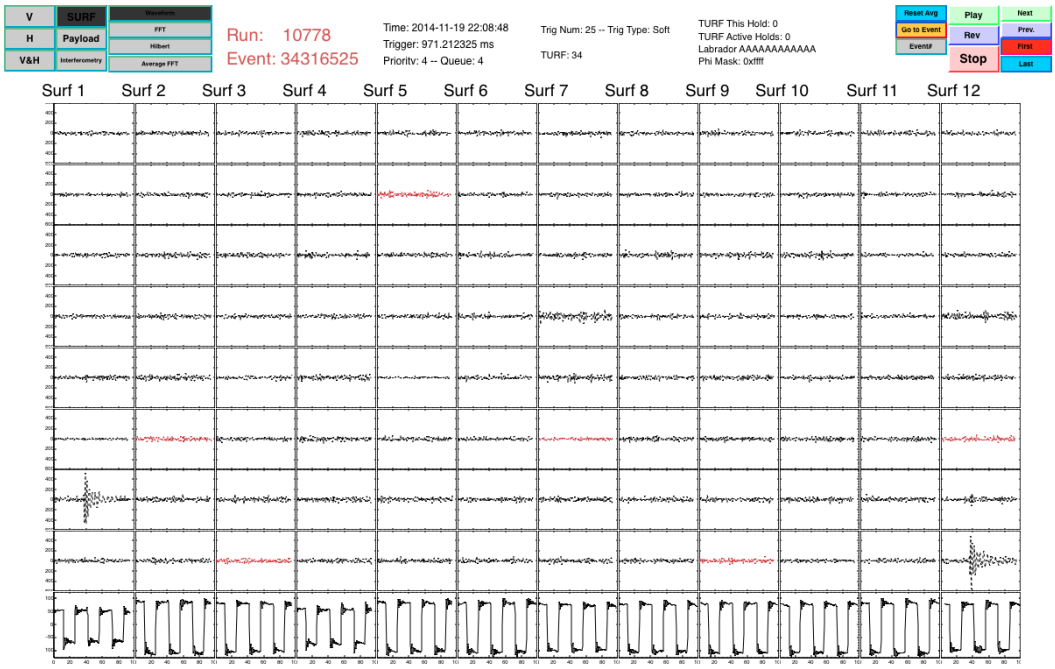

Figure 6.28: An event from the channel-to-channel delay calibration measurement as rendered in `MagicDisplay`. The reference pulse is in SURF 1 channel 7. In this case the test pulse is in SURF 12 Channel 8.

To find $\Delta t_{\text{channel-to-channel}}$ it is necessary to correct for the trigger jitter delay, Δt_{clock}

$$\Delta t_{\text{channel-to-channel}} = \Delta t_{\text{pulse}} - \Delta t_{\text{clock}} \quad , \tag{6.14}$$

where Δt_{pulse} is the time of maximum cross-correlation between the test and reference pulses. As the reference channel is in SURF 1, the Δt_{clock} is defined as the delay between the clock as recorded in SURF 1 and the clock on test channel's SURF. In the case that both channels are on SURF 1, then $\Delta t_{\text{clock}} = 0$.

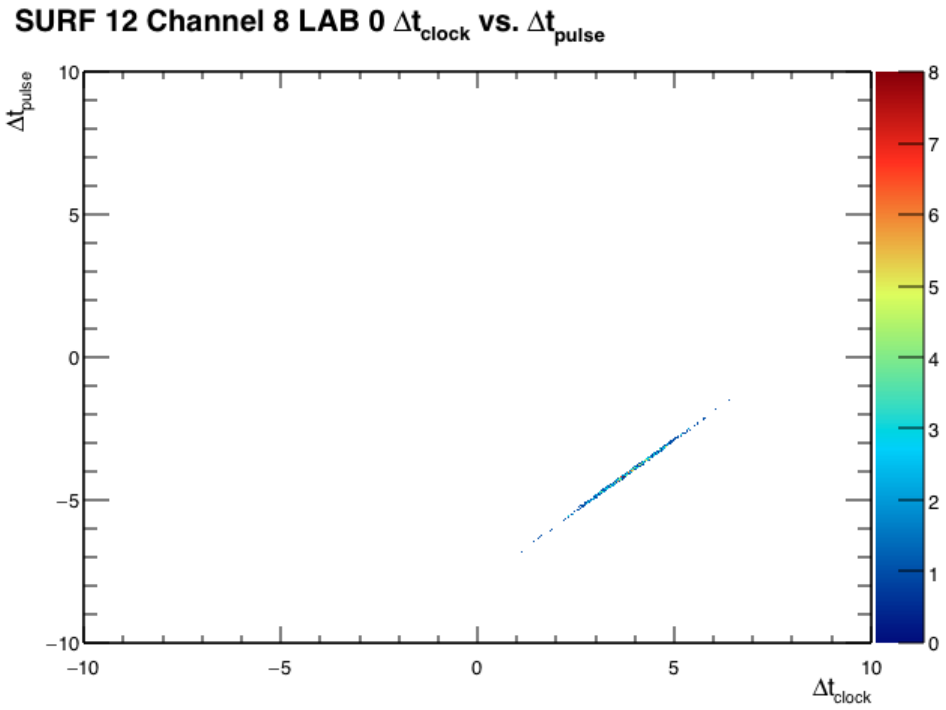

(a) The highly correlated Δt_{pulse} and Δt_{clock} distributions for SURF 12 Channel 8.

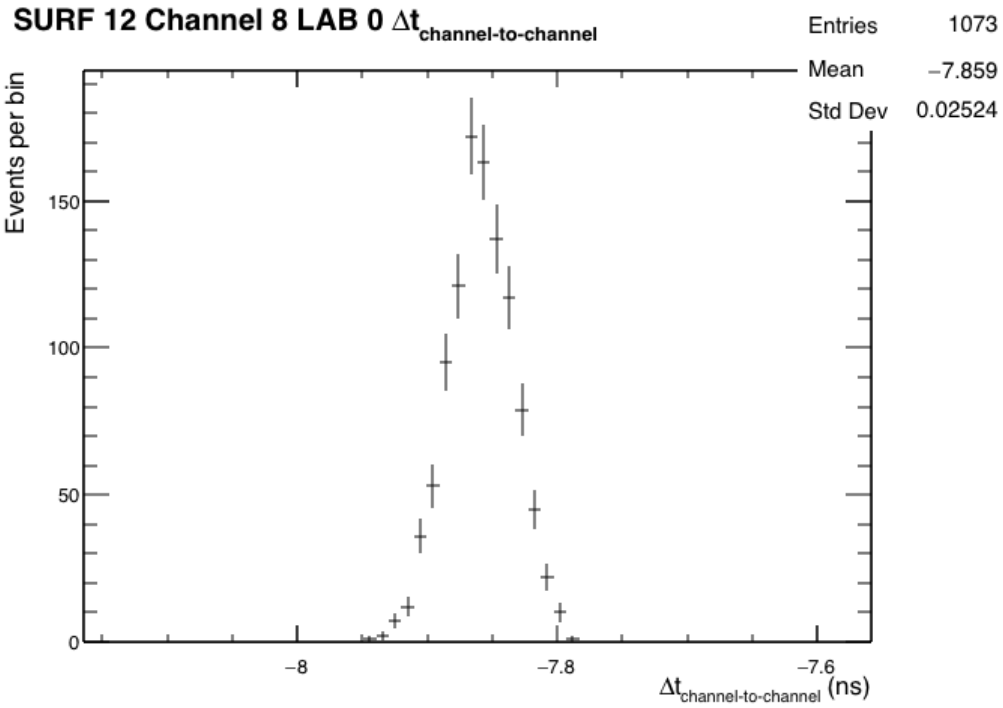

(b) The resultant $\Delta t_{\text{channel-to-channel}}$ distribution.

Figure 6.29: The Δt_{pulse}, Δt_{clock}, and $\Delta t_{\text{channel-to-channel}}$ for SURF 12 Channel 8.

6.3.1 Mean $\Delta t_{\text{channel-to-channel}}$ values

The mean values of the $\Delta t_{\text{channel-to-channel}}$ distributions for LAB 1 is shown in Figures 6.30 (the other LABs have nearly identical plots). The clock alignment algorithm used to find the Δt_{clock} is described in section 6.3.2. There are two distinct shifts in the mean channel distribution as SURF number increases, ~ 4 ns between SURFs 5-6, and SURFs 11-12.

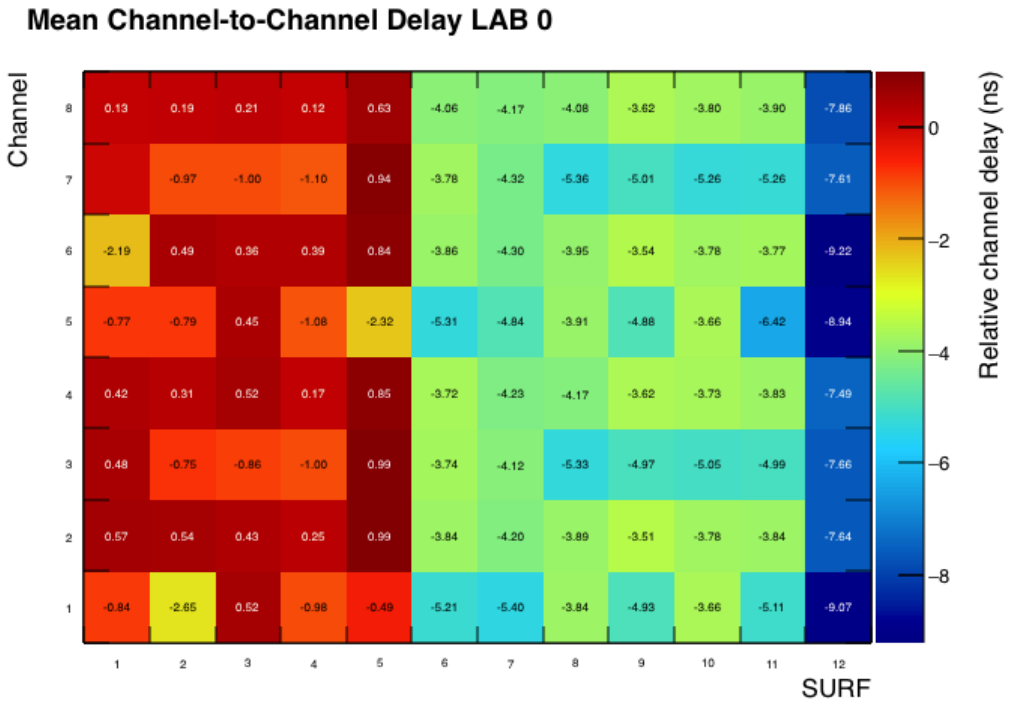

Figure 6.30: All SURFs and channels on LAB 0. The points for SURF 1 lie on top of one another as the other clocks are aligned to the clock in SURF 1.

The structure shown in Figure 6.30 was eventually understood in terms of the location of the SURFs in the cPCI crate. This is shown in Figure 6.31. The 4 ns transitions mark the boundaries of the cPCI buses, where bridge modules regenerate the clock. The regeneration delays the propagation of the clock along the cPCI backplane, which via equation (6.14) is absorbed into the $\Delta t_{\text{channel-to-channel}}$.

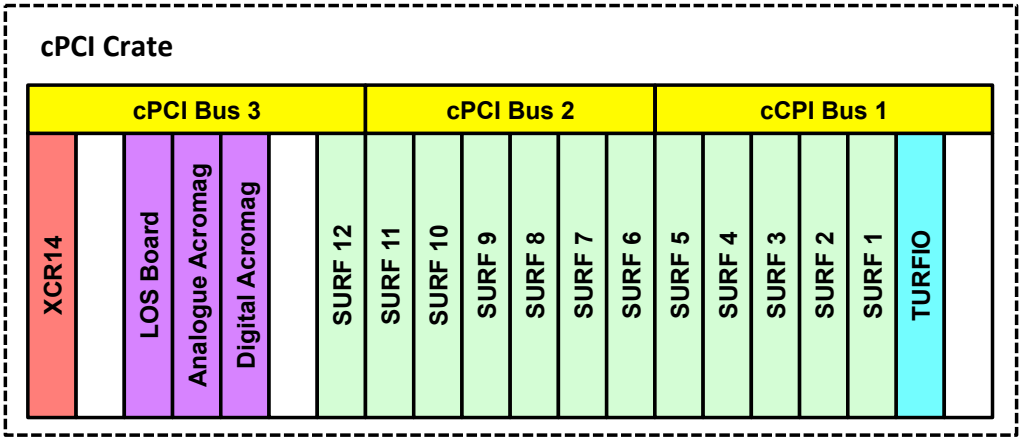

Figure 6.31: Board layout in the cPCI crate. The clock is generated in the cPCI crate next to the XCR14. Bridge modules sit between cPCI bus 3 and cPCI bus 2, and between cPCI bus 2 and cPCI bus 1.

6.3.2 cPCI Clock Alignment for Trigger Jitter Correction

The duty cycle of the cPCI clock was also found to vary as a function of SURF number. Figure 6.32 shows the clock in SURFs 10 and 12 with their rising edges aligned. Each rising edge is aligned because the periods are the same, but the falling edges are not because the duty cycle is different.

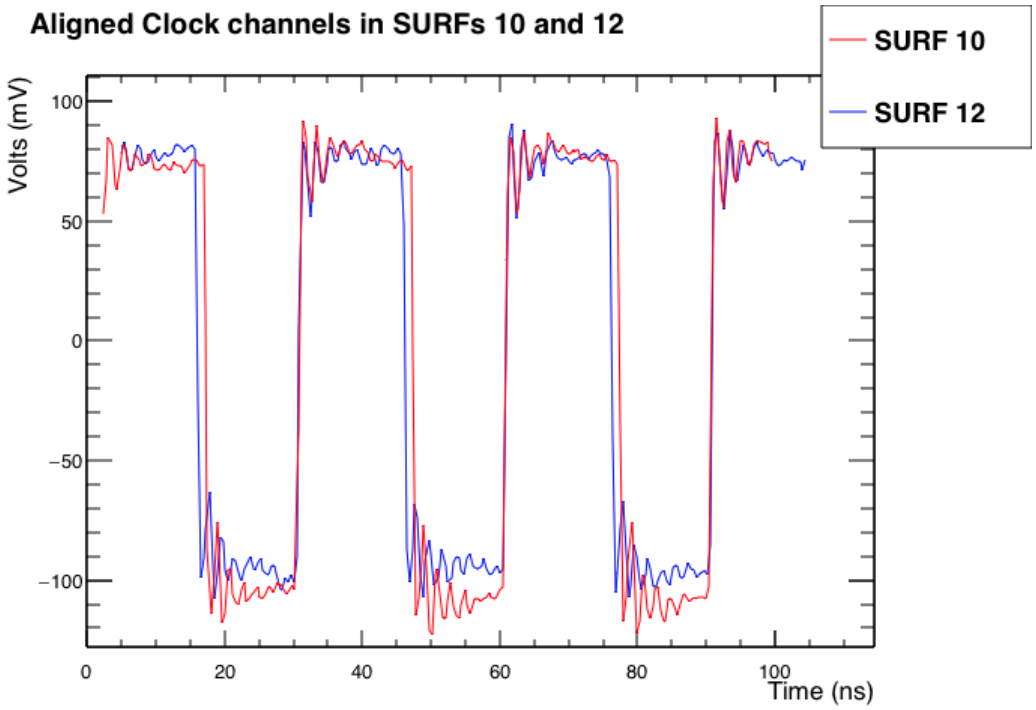

Figure 6.32: The clock channels in SURFs 10 and 12 with their rising edges aligned. Their falling edges are not aligned beacuse the duty cycle of the two channels is different.

Figure 6.33 is a histogram showing the clock duty cycle as a function of SURF. The y-axis is the time from the rising edge to the falling edge as a function of SURF number.

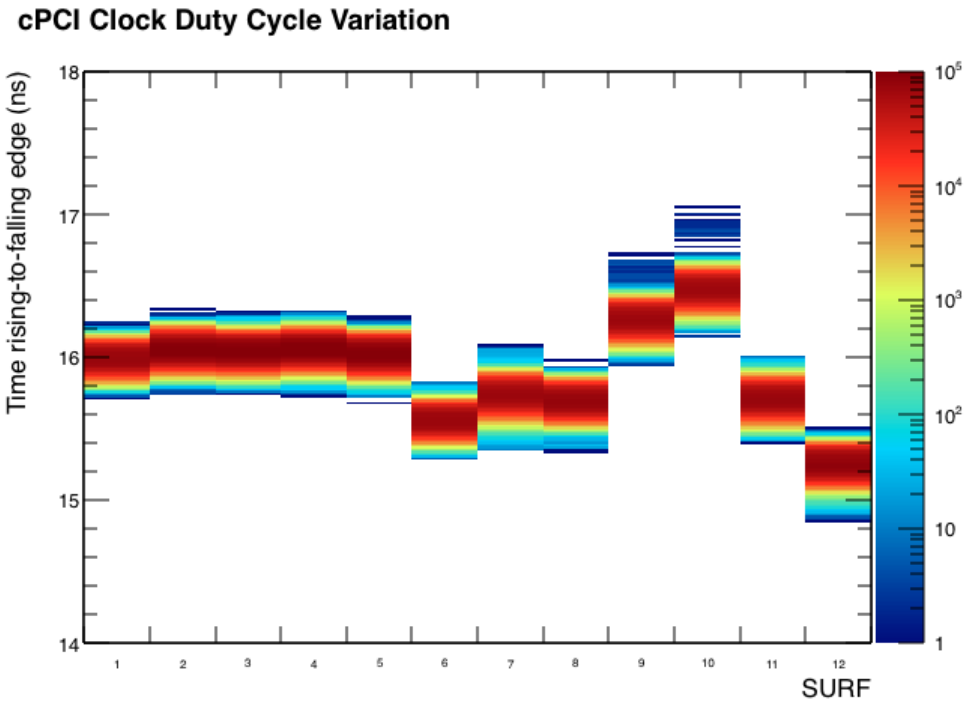

Figure 6.33: The duty cycle variation as a function of SURF. SURFs 10 and 12 were chosen for the example plot, figure 6.32, because they are the most extreme values.

In order to best align the rising edges of the clock windowing was applied following the rising edge of each clock period. Figure 6.34 shows the same clock channel from an event with two different window sizes.

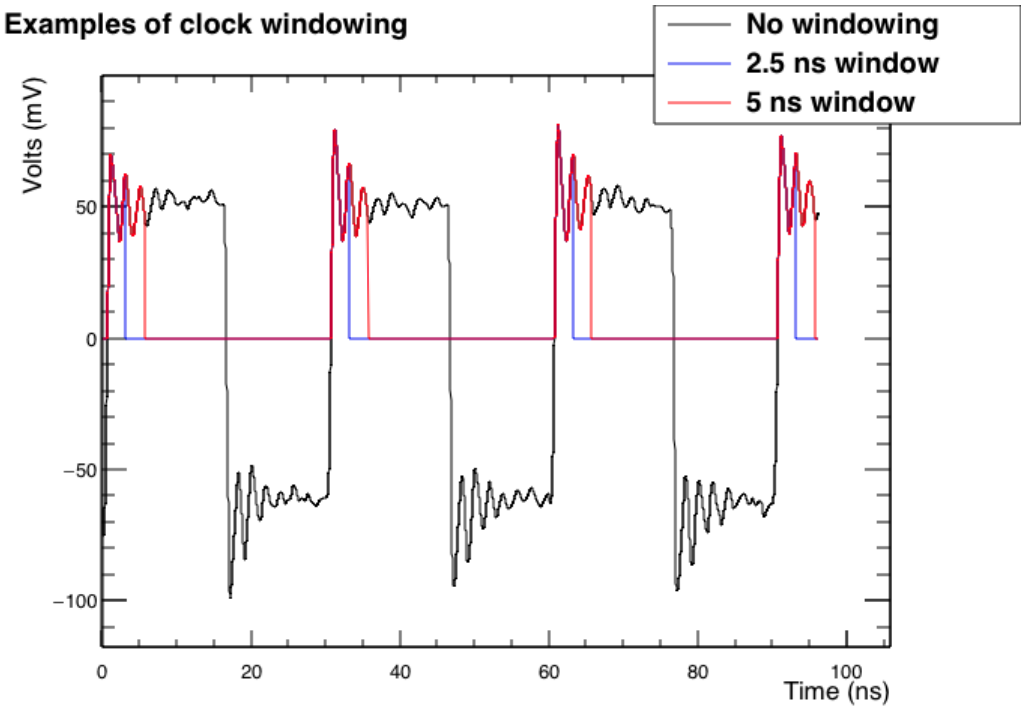

Figure 6.34: Example showing no windowing, 2.5 ns windowing and 5 ns windowing.

Multiple window lengths, 7.5 ns, 5 ns, 2.5 ns, and no windowing, were tested for each channel and LAB. The distribution of $\Delta t_{\text{channel-to-channel}}$ for channel 8 on SURFs 2 and 12 are shown in Figures 6.35 and 6.36. For SURF 12, the duty cycle variation causes the mean $\Delta t_{\text{channel-to-channel}}$ distribution to be shifted by 0.3 ns as the leading edges are better aligned by windowing. In the case of SURF 12, the windowing also reduces the width of the distribution. For SURF 2, where the duty cycle is more similar to SURF 1, the different windowing shifts the mean of the $\Delta t_{\text{channel-to-channel}}$ distribution around much less.

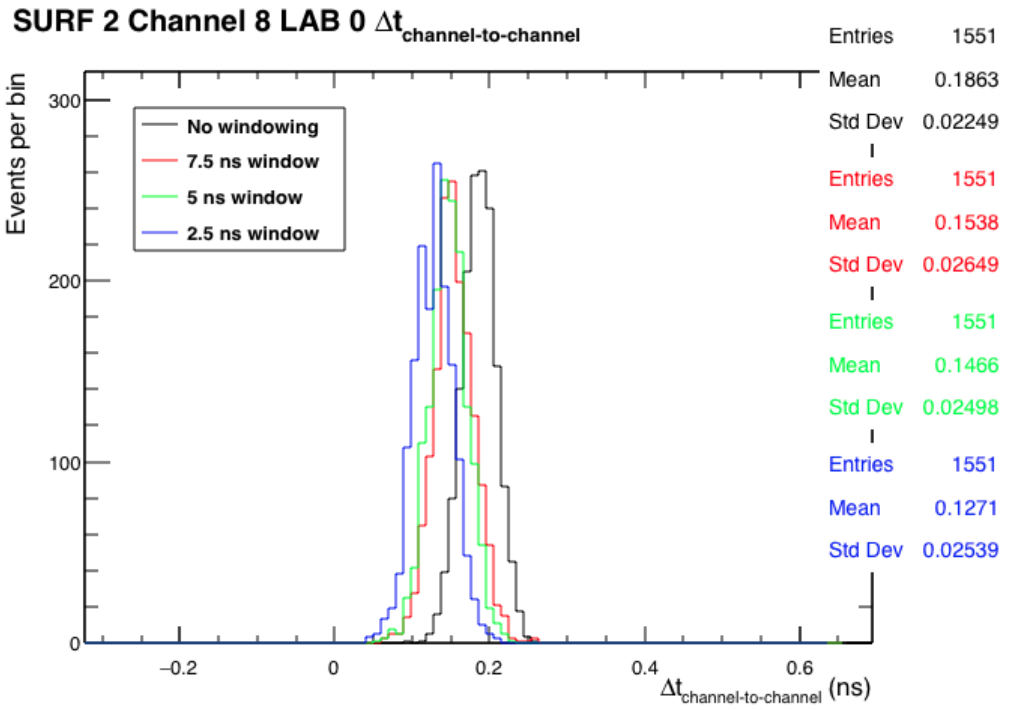

Figure 6.35: For SURF 2, with little duty cycle difference relative to SURF 1, no windowing gives the narrowest $\Delta t_{\text{channel-to-channel}}$ distribution.

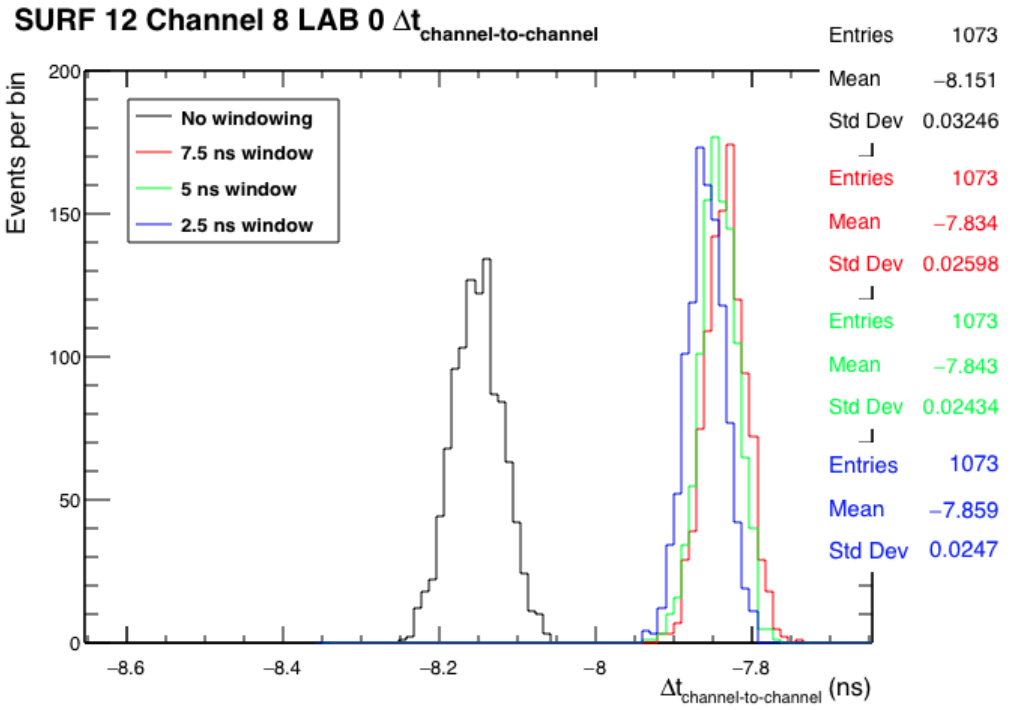

Figure 6.36: For SURF 12, the time the clock is high is almost 1 ns shorter than to SURF 1. In this instance the 5 ns window gives the narrowest $\Delta t_{\text{channel-to-channel}}$ distribution.

The RMS of the $\Delta t_{\text{channel-to-channel}}$ distributions for SURF 1 with different windowing lengths are plotted in Figure 6.37.The plots for the other SURFs are very similar.

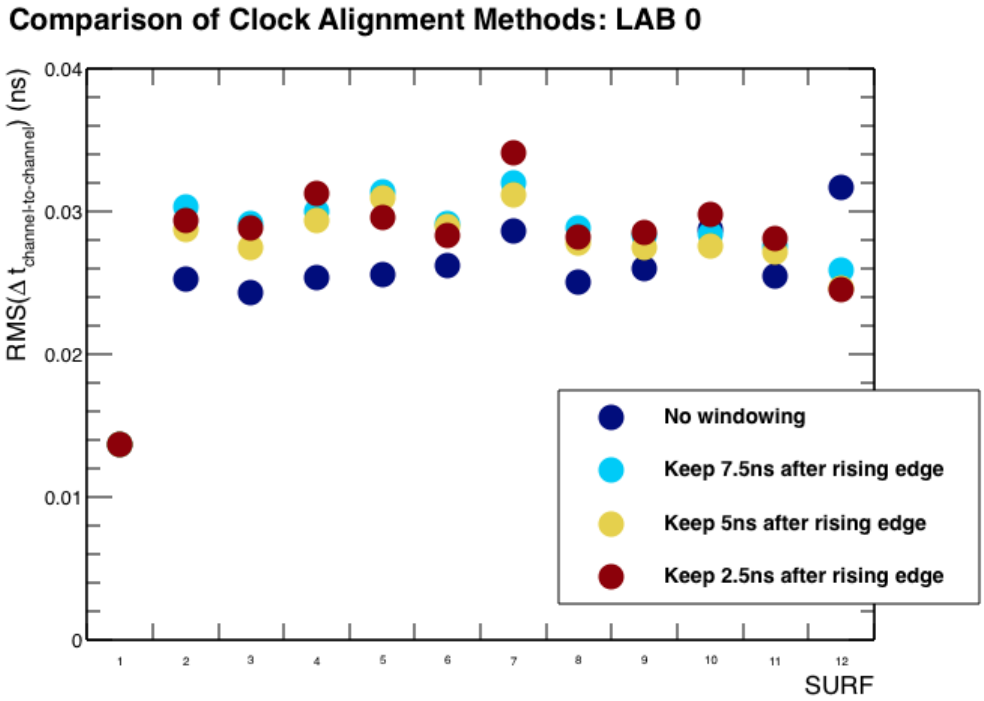

Figure 6.37: All SURFs and channels on LAB 0.

The windowing method that produced the minimum RMS was selected for each LAB and is used to calibrate all events in the ANITA-3 data set. This was used to derive the mean $\Delta t_{\text{channel-to-channel}}$ shown in Section 6.3.1. An estimate of the clock alignment resolution was made by subtracting the RMS of the $\Delta t_{\text{channel-to-channel}}$s in SURF 1 from the RMS of LABs greater than SURF 1.

$$\sigma^2_{\text{clock}} = \sigma^2_{\text{channel-to-channel}} - \sigma^2_{\text{channel-to-channel SURF 1}} \tag{6.15}$$

The resultant σ_{clock} distribution is shown in Figure 6.38. The average clock alignment resolution is just under 20 ps.

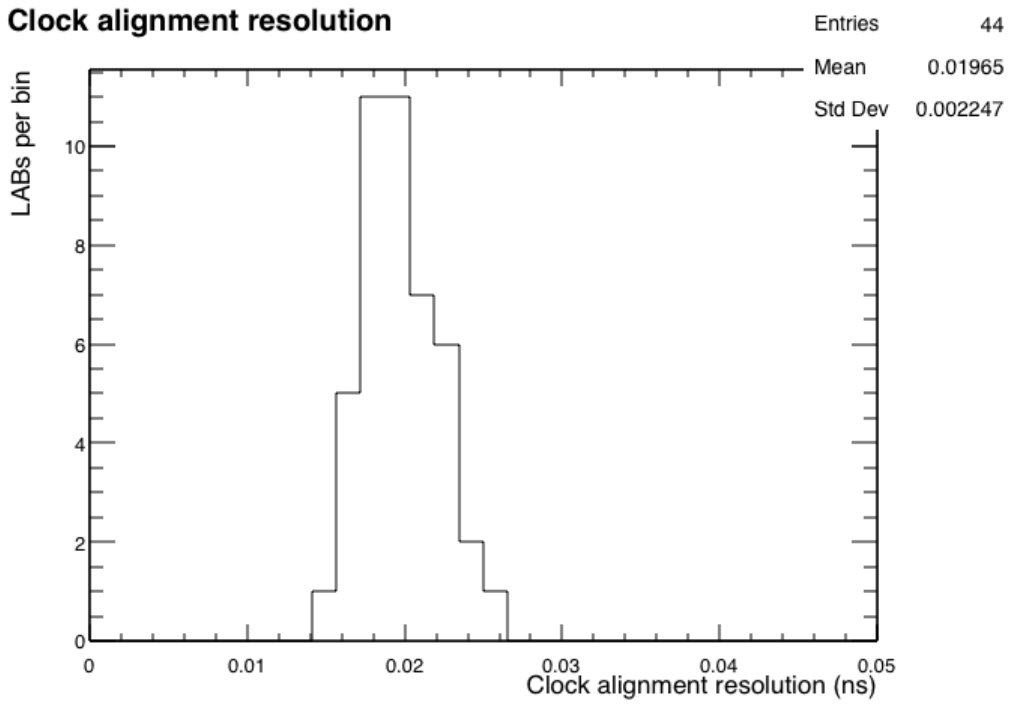

Figure 6.38: The σ_{clock} distribution.

6.3.3 Final Inter-SURF Timing Resolution from Efficiency Scan

A variation of the set up shown in Figure 6.27 was used to perform an efficiency scan of the trigger, where the pulse was split and injected into 6 channels over two Φ-sectors, rather than two channels. The variable attenuator was used to control the size of the pulse injected into the channels. This allowed for an estimate of the inter-SURF timing as a function of injected pulse SNR, as recorded in the SURF. The RMS, σ, was estimated from the last 20 ns of the digitised waveform, behind the pulse.

$$\sigma^2 = \frac{1}{N}\sum_N y_i^2 - \left(\frac{1}{N}\sum_N y_i\right)^2 \quad , \tag{6.16}$$

where y_i is the ith sample of the waveform, which has N samples in the last 20 ns. The SNR was estimated using the σ obtained from equation (6.16) and the maximum and minimum values of the pulse.

$$SNR = \frac{y_{\max} - y_{\min}}{2\sigma} \tag{6.17}$$

The RMS of the $\Delta t_{\text{channel-to-channel}}$ is shown in Figure 6.39 as a function of the SNR. This includes the resolutions of the pulse and clock alignment. Pulses with SNR < 3 were not consistently picked out by the finding the maximum of the channel cross-correlation. Using the calibration constants and methods described in this chapter, the ANITA timing resolution increases from around 65 ps at an SNR of 3 to around 30 ps at an SNR of 8.

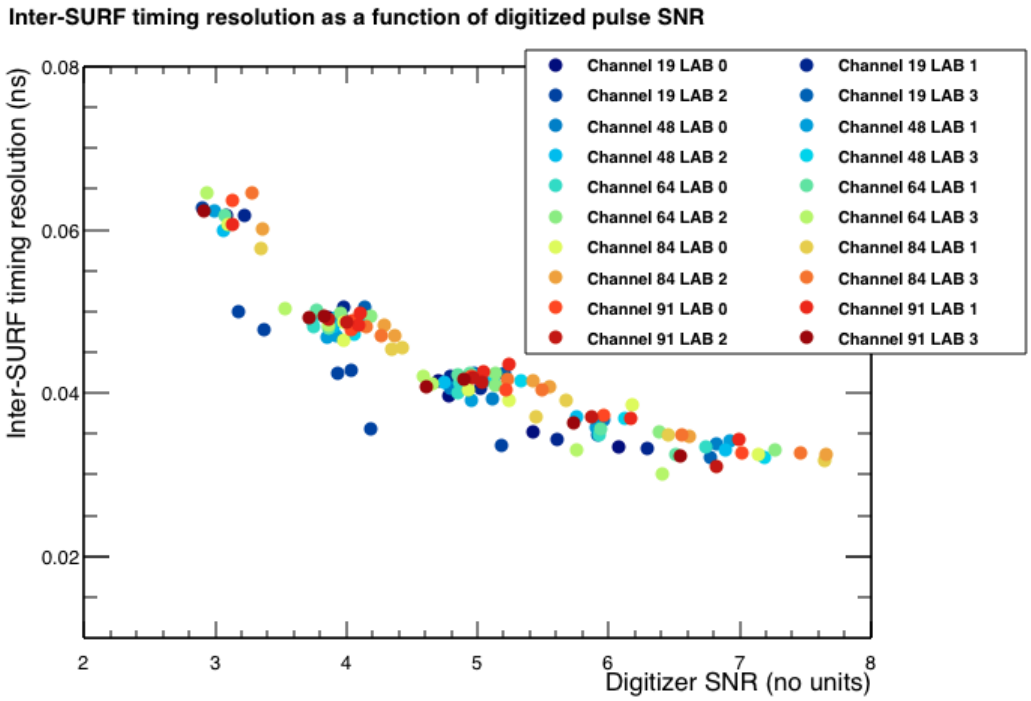

Figure 6.39: The inter-SURF timing resolution from the efficiency scan for each LAB on SURF 1, 3, 6, 8, 10, 11 for channels 1 or 3.

6.4 Summary

I calibrated the digitisation and relative channel timing in ANITA-3, a prerequisite of any analysis. I achieved a channel-to-channel timing in the range 65 ps to 30 ps after accounting for the uneven δts ($+\varepsilon$) in the digitizers, the RCO phase assignment, temperature correction, inter-SURF clock alignment, and cable delays.

Chapter 7

ANITA-3 Flight

Figure 7.1: ANITA-3 preparing for launch. Photograph courtesy of T.C Liu.

7.1 Flight Summary

ANITA-3 launched at 21:00 on the 16th December 2014 and, after 23 days and 10 hours, landed on the 9th January 2015 at 07:00. During the flight more than 78 million events were written to disk.

ANITA had some problems during the flight. Satellites just visible over the northern horizon emitted significant amounts of power in the ANITA band. In addition to this, the ϕ-masking and $L1$-masking, which are designed to prevent portions

of the payload triggering at a high rate, were partially broken. A channel (or Φ-sector) was masked when the L1 (L2) trigger rate exceeded a threshold for a given period and should have deactivated when the L1 (L2) rate went below a second threshold for a given period. However, the L1 (L2) triggers from the time when a channel (ϕ-sector) was masked were not recorded when the masking was active. This meant the channel or ϕ-sector was always deactivated after the low threshold time. This increased the experimental dead time for ANITA as the satellite noise quickly filled the digitizer event buffers when north facing channels were not masked. Figure 7.2 shows that the event rate was unstable during the entire flight. The event rate constantly jumps between a stable rate around 20 Hz, up to 80 Hz near the maximum possible, due to the broken ϕ-masking.

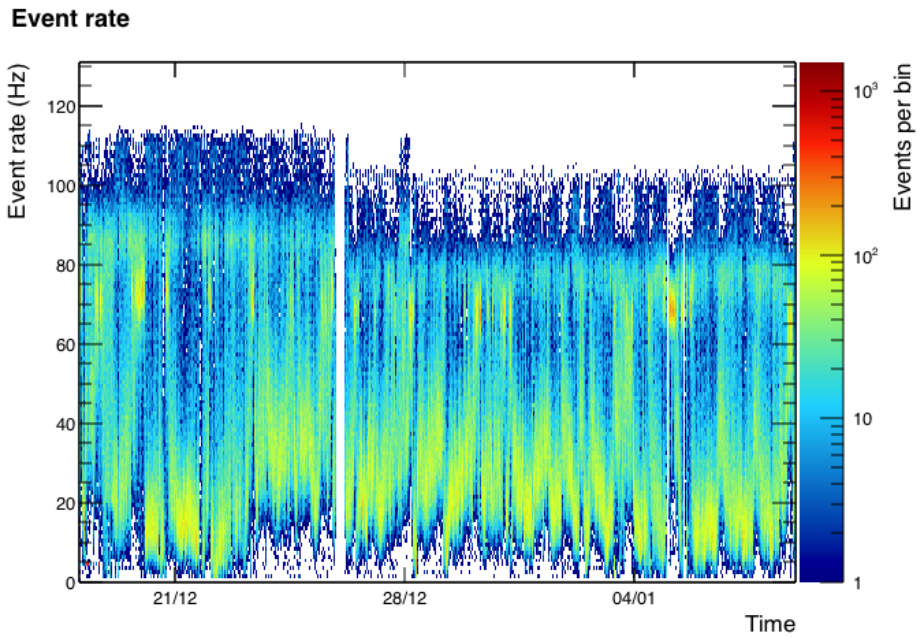

Figure 7.2: The event rate during the ANITA-3 flight. The event rate constantly jumps between a stable rate around 20 Hz to 80 Hz due to the broken ϕ-masking.

As a consequence ANITA-3 suffered constant dead time, when the event buffer was full and ANITA could not trigger. Figure 7.3 shows the number of seconds per hour ANITA was availble to trigger (the live time). The masking issue meant that the live time rarely went above 80%.

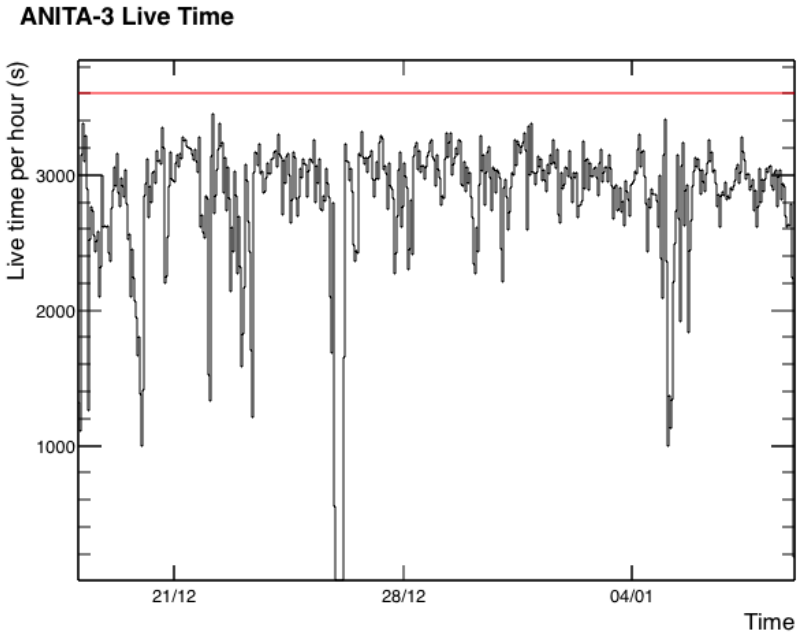

Figure 7.3: Seconds per hour that ANITA-3 was live. The red line indicates 3600 seconds.

Figures 7.3 and 7.2 show a portion of the flight that ANITA was completely inactive. The instrument went into an unresponsive state over Christmas day and was eventually brought back online with a remotely commanded power cycle. This shutdown is apparent in many other plots in this thesis, which show a gap in the data record around this time.

7.2 Flight Path and Calibration Pulser Stations

Figure 7.4 shows the flight path of ANITA-3 as recorded in the ADU5 GPS data.

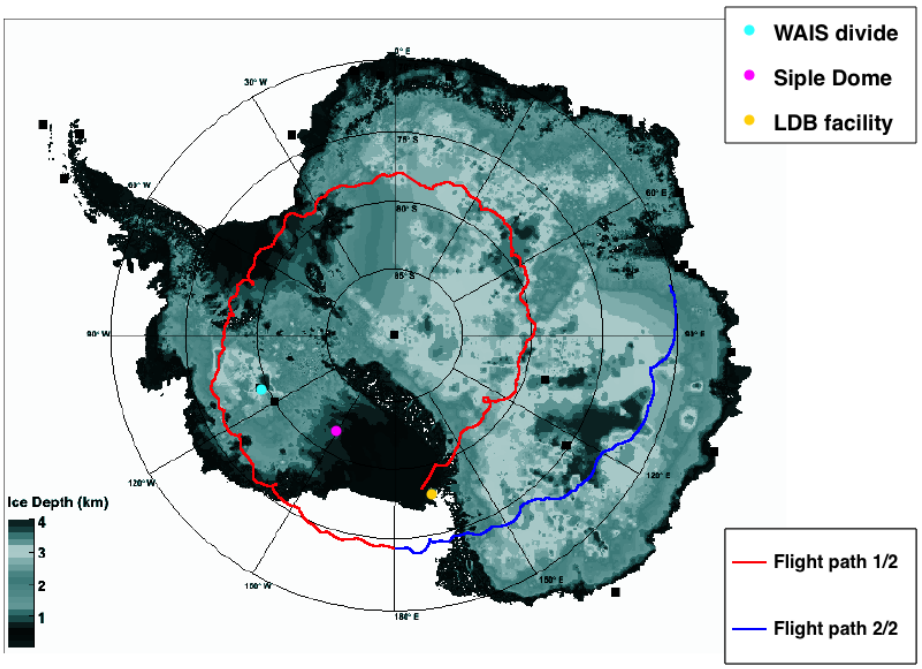

Figure 7.4: ANITA-3 flight path with markers added for pulser station locations. ANITA launched from the LDB facility, however the GPS data from ANITA's ascent to the float altitude have been omitted.

Three pulser stations were set up around the continent, at WAIS Divide, Siple Dome and the Long Duration Balloon (LDB) facility, from where ANITA was launched.

7.2.1 LDB Pulses

Immediately after launch, ANITA recorded calibration pulses from LDB. Both VPol and HPol pulses were fired at ANITA, the exact setup was varied to ensure a good sample calibration pulses were recorded[1]. The LDB station was set up to fire three pulses at 5 Hz. Because they fired relative to the GPS second, the pulses can be selected with timing information alone. Figure 7.5 shows the time after the time during each second that ANITA was triggered.

[1]The settings of the LDB pulser station are described here [65]

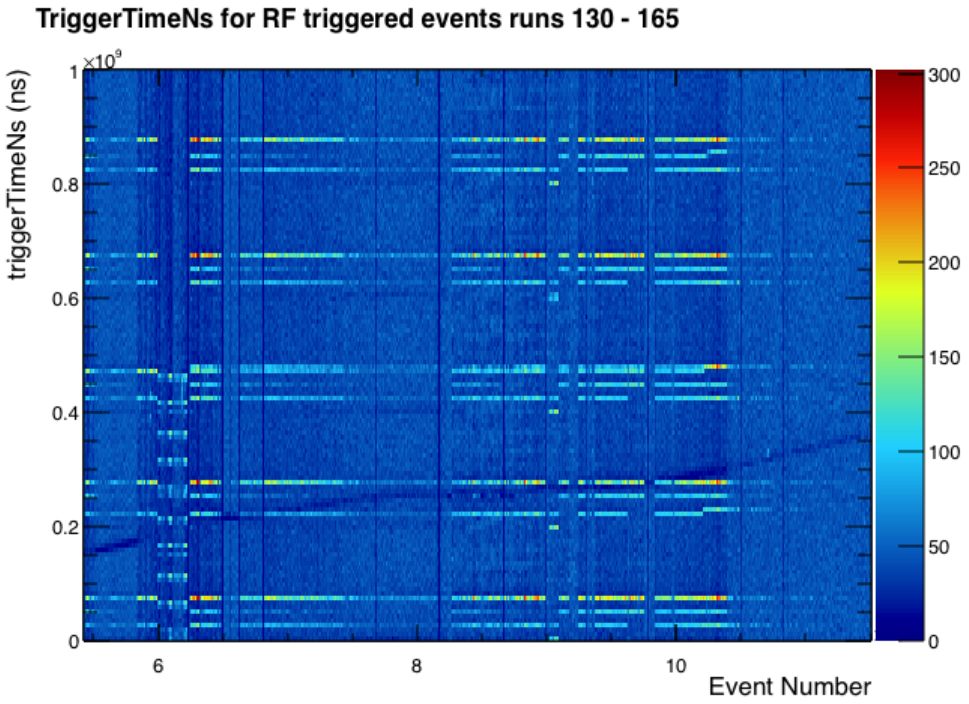

Figure 7.5: Plot of `triggerTimeNs` vs. event number for runs 130-165 over the whole 10^9 ns is shown. The distribution shows the 5 Hz pulsing with the three digital delays in 25 ms intervals.

A relatively high rate of pulses was necessary to try to counteract the high dead time that ANITA always experiences while large bases are within its field of view. Figure 7.6 shows a VPol calibration pulse from LDB selected with timing cuts relative to the GPS second.

Figure 7.6: One VPol pulser event from LDB as rendered in `MagicDisplay`. The red channels indicate L3 triggered Φ-sectors.

7.2.2 The WAIS Pulses

During the flight ANITA also came close enough to West Antarctic Ice Sheet (WAIS) Divide to record calibration pulses. A 2 kV pulse was emitted through a VPol discone antenna and a 6 kV pulser was a emitted through a miniature version of the ALFA (ANITA Low Frequency Antenna), emitting HPol pulses[2]. A picture of the setup is shown in Figure 7.7.

[2]The installation details are fully described in two internal ANITA notes [66, 14].

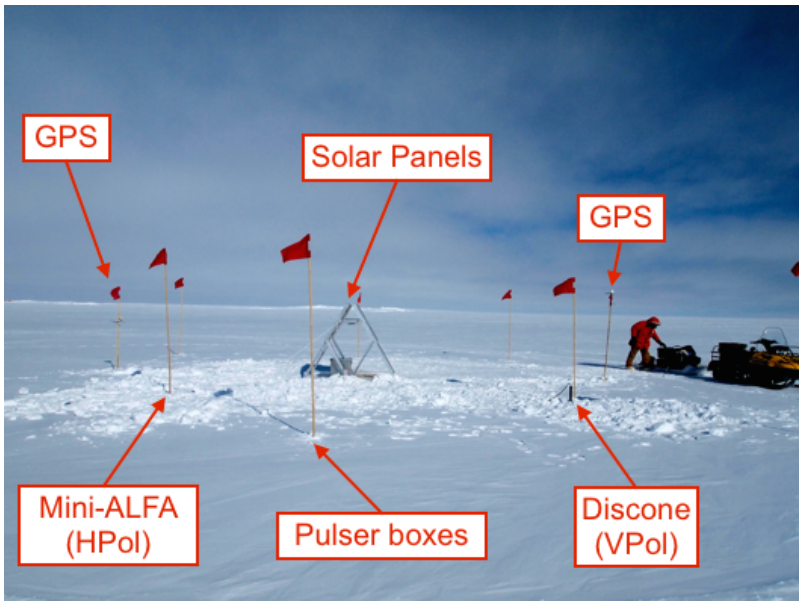

Figure 7.7: Photograph of the WAIS Field Pulser Station setup by Stephanie Wissel, taken from [14].

Both pulsers were configured to fire at 1 Hz at a constant offset from the GPS second. During the flight ANITA came close enough to trigger on the HPol pulser. Like the LDB sample, the WAIS pulses can be selected with timing information alone because the pulser was triggered by the GPS second signal, as shown in Figure 7.8.

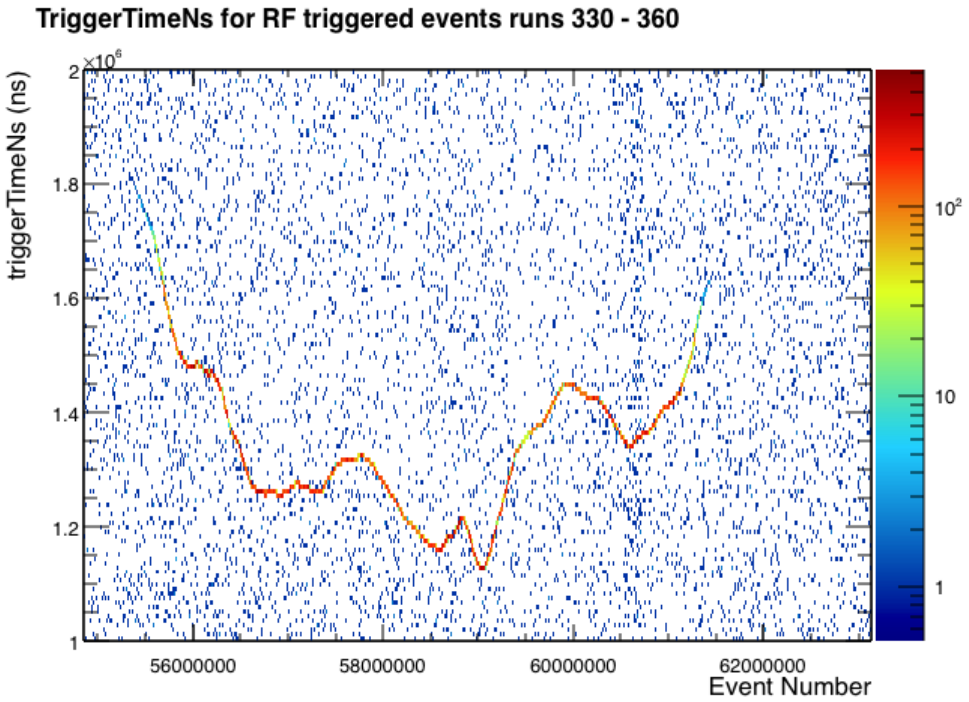

Figure 7.8: Time after the start of each second that ANITA was triggered while near WAIS divide (runs 330-360).

Over 118,000 HPol calibration pulses were recorded from WAIS divide. One is shown in Figure 7.9.

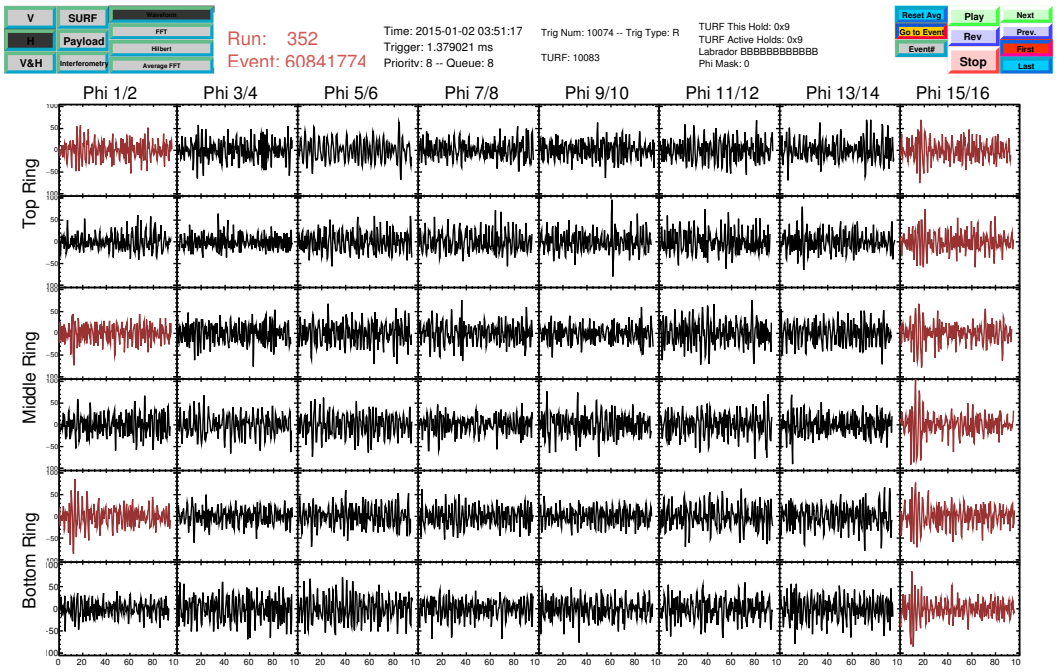

Figure 7.9: One HPol pulser event from WAIS Divide as rendered in `MagicDisplay`. The red channels indicate L3 triggered Φ-sectors.

7.3 Trigger Efficiency

The pulser stations allowed for a measurement of trigger efficiency when in flight. The WAIS pulses are used here as the environment is significantly quieter than around LDB and McMurdo Station. Since the WAIS pulses were fired once per second, the time between pulses implies the number pulses ANITA missed. Figure 7.10 shows the trigger efficiency as a function of Signal-to-Noise Ratio (SNR). Since the SNR of the pulses varied slowly as ANITA moved, I have assumed that missed pulses have the same SNR as the next pulse.

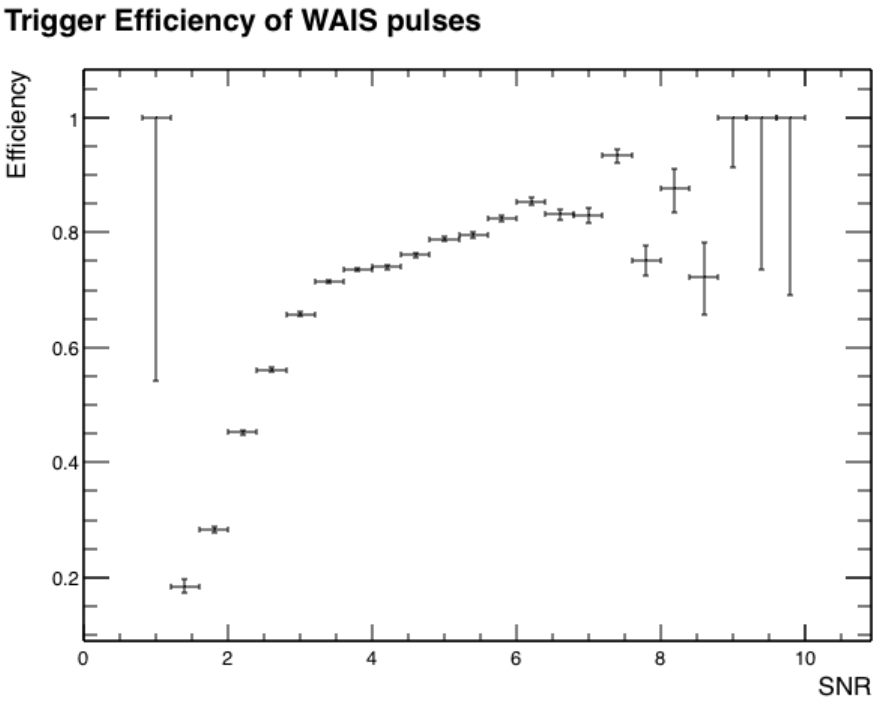

Figure 7.10: ANITA-3 trigger efficiency of WAIS pulser events as a function of SNR

The effects of the broken Φ-masking and high dead time are visible in figure 7.10, as the trigger efficiency does not reach 100% in any bins with high statistics. Figure 7.10 also shows that the 50% trigger efficiency was at an SNR of 2.2.

Chapter 8

Event Reconstruction

The ANITA event interferometric reconstruction methods use the time delay between a signal appearing in neighbouring channels to determine its arrival direction. This is important because human activity could produce impulsive signals that look like Askaryan radiation or a cosmic ray air shower. The only method to remove this artificial background is to be able to associate such events with localised regions of human activity. In this chapter I present the reconstruction software I wrote and summarise the angular resolution of ANITA-3 by reconstructing the calibration pulses collected during flight. The interferometric techniques described here were originally developed by Andres Romero-Wolf for ANITA-1 analysis [67].

8.1 Interferometic Method

The first step in the interferometric reconstruction is to remove the uneven time base caused by the LABRADOR digitizers. An Akima spline is used to interpolate the voltages so that every sample-to-sample $\delta t = (1/2.6)\,\text{ns}$, which is the average sampling rate of the digitizers. This is shown for a single channel in Figure 8.1.

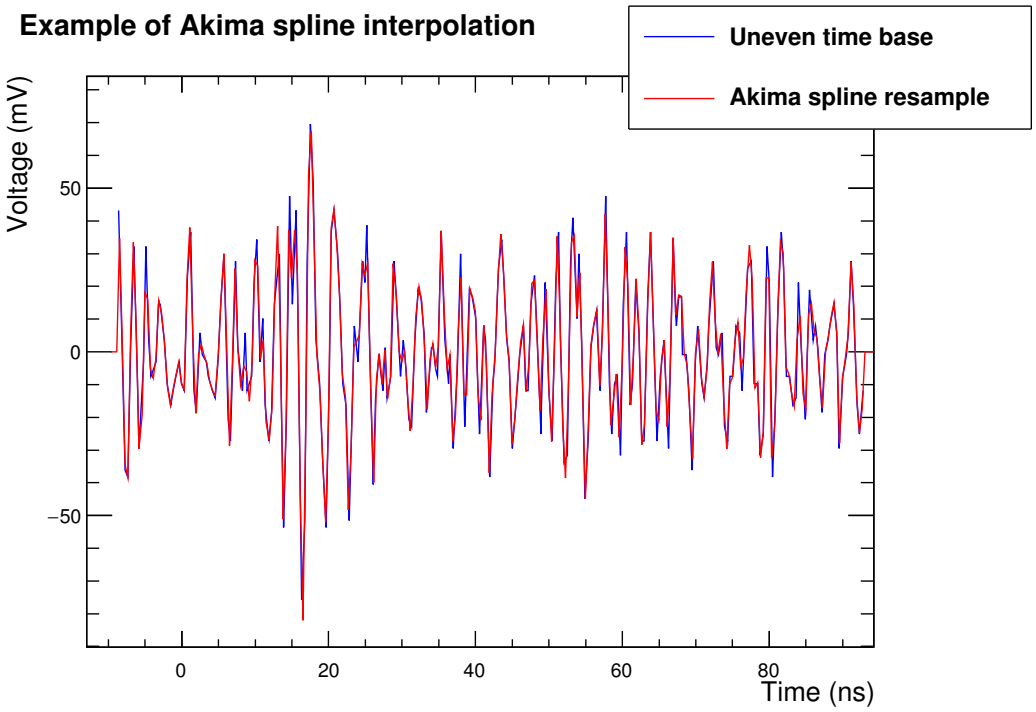

Figure 8.1: Interpolation of the uneven sample-to-sample δts so that $\delta t = (1/2.6)$ ns.

The second step in the reconstruction is to cross-correlate all channel pairs of the same polarisation within $\pm 2\Phi$-sectors. The cross-correlation, C_{ab}, is defined as

$$C_{ab}[\mathrm{j}] = \frac{1}{\sigma_a \sigma_b} \sum_i \Psi_a[\mathrm{i}] \Psi_b[\mathrm{i+j}] \quad , \tag{8.1}$$

where $\Psi_{a/b}$ is the amplitude of signal a/b, each with N samples and RMS $\sigma_{a/b}$. The $C_{ab}[j]$ is the correlation coefficient of the aligned voltages, Ψ_a and Ψ_b offset by j samples. The maximum value of C_{ab} is the time a signal took to travel between antennas a and b.

The cross-correlation, C_{ab} of two time series, Ψ_a, Ψ_b, can be obtained from a bin-by-bin multiplication in the Fourier domain, as shown in Equation (8.2).

$$\mathscr{F}\{C_{ab}\}[\mathrm{i}] = (\mathscr{F}\{\Psi_a\})^*[\mathrm{i}] \, (\mathscr{F}\{\Psi_b\})[\mathrm{i}] \quad , \tag{8.2}$$

where i is the sample, $\mathscr{F}$ is the Fourier transform and * is the complex conjugate. A naive implementation of the cross-correlation in equation (8.1) has $O(N^2)$ complexity due to the sum over N for each of the N samples. However, the Fast Fourier

Transform (FFT) algorithm has $O(N \log N)$ complexity, and so all cross-correlations are performed in the Fourier domain using equation (8.2), with two forward FFTs on the Ψs and an inverse FFT (iFFT) on the $\mathscr{F}\{C\}$. Figure 8.2 shows the antenna pairs that are cross-correlated.

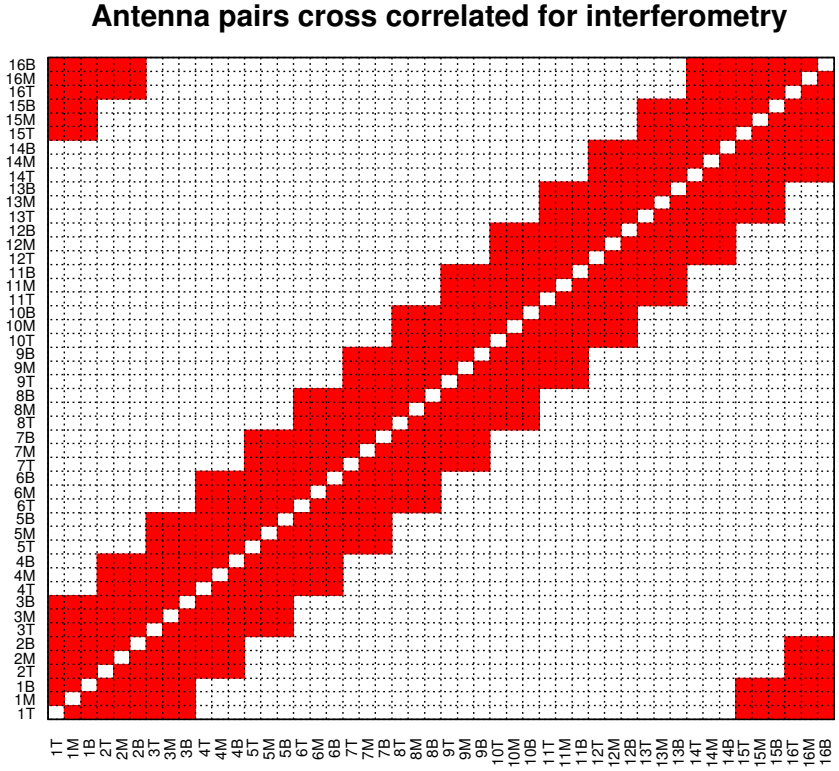

Figure 8.2: A red cell indicates channel pairs are cross correlated for interferometry, a white cell indicates they are not.

Figure 8.3 shows channels 15TH and 16MH from the example event (Figure 7.9) plotted on the same time axis. Both channels recorded the impulse from the WAIS Divide but with a time offset due to the physical separation of the antennas. The cross-correlation of 15TH and 16MH is shown in Figure 8.4. The two channels are maximally correlated at -5 ns, indicating that the pulse arrives in 15TH 5 ns after in 16MH.

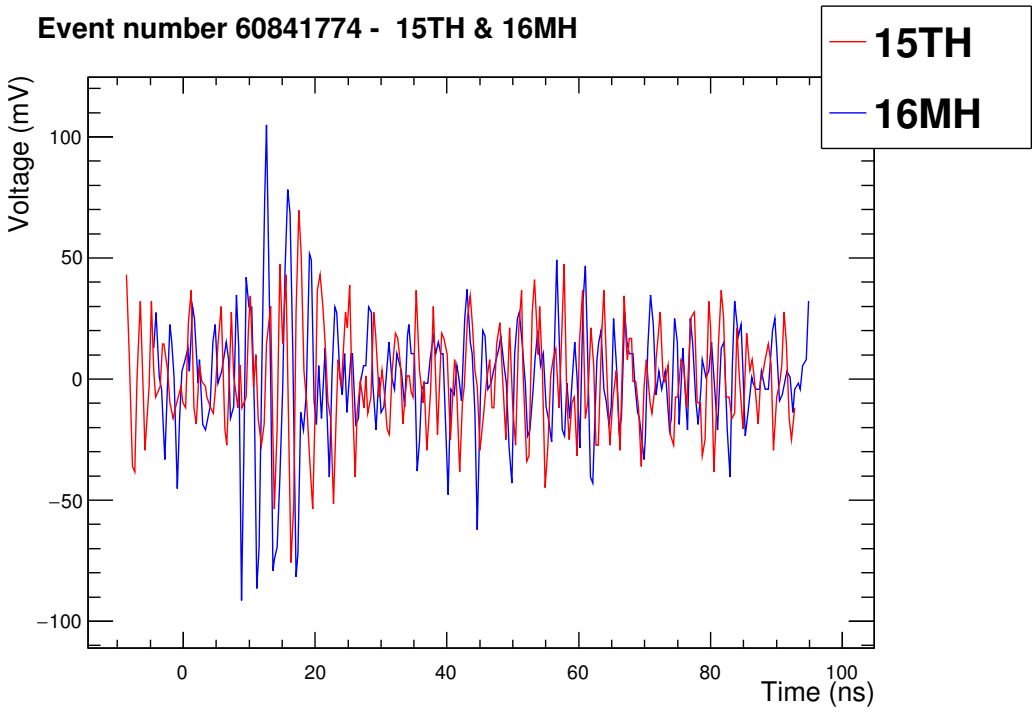

Figure 8.3: Event number 60841774, channels 15TH and 16MH.

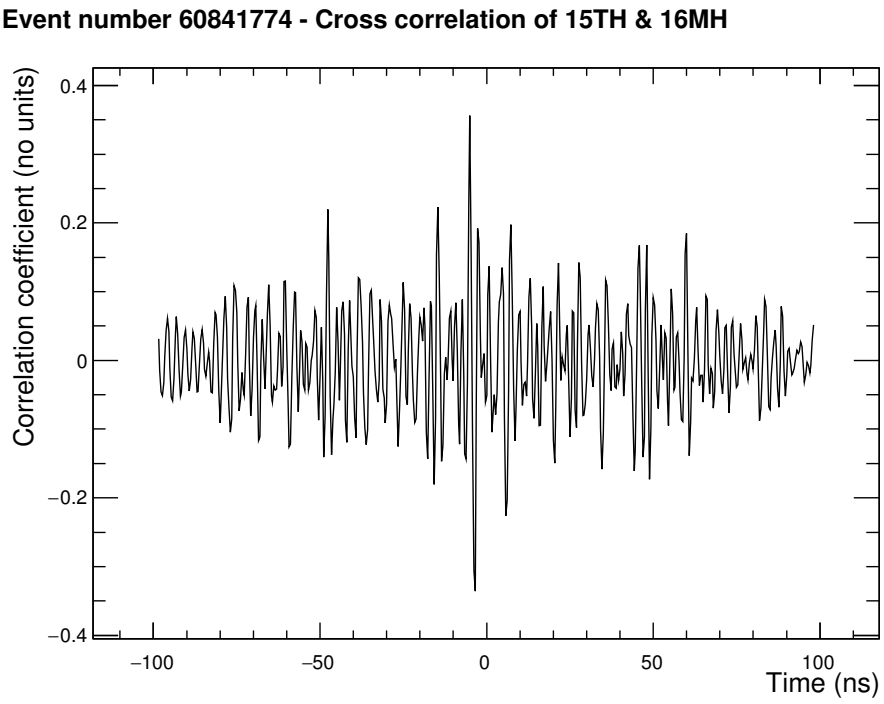

Figure 8.4: Event number 60841774, cross-correlation of 15TH and 16MH.

The third step in the reconstruction is to combine the delay information from the set of cross-correlations with the payload geometry to infer arrival direction.

As a plane wave passes the payload at the speed of light, c, the expected delay, $\delta t^{ij}_{\text{expected}}$, between antennas i, j is given by equation (8.3).

$$\delta t^{ij}_{\text{expected}} = \frac{1}{c}\cos(\theta)\left((z_j\tan(\theta) - r_j\cos\big(\phi - \phi_j\big) - \big(z_i\tan(\theta) - r_i\cos(\phi - \phi_i)\big)\right) \quad , \tag{8.3}$$

where the r_i, z_i, ϕ_i refer to the phase centre of the antenna i in cylindrical coordinates, the θ, ϕ are the incoming direction of the plane wave, and c is the speed of light in vacuum.

The $\delta t_{\text{expected}}$ distribution depends on the physical position of the antenna pairs and the arrival direction of the plane wave. The $\delta t_{\text{expected}}$ for 15TH and 16MH is shown in Figure 8.5.

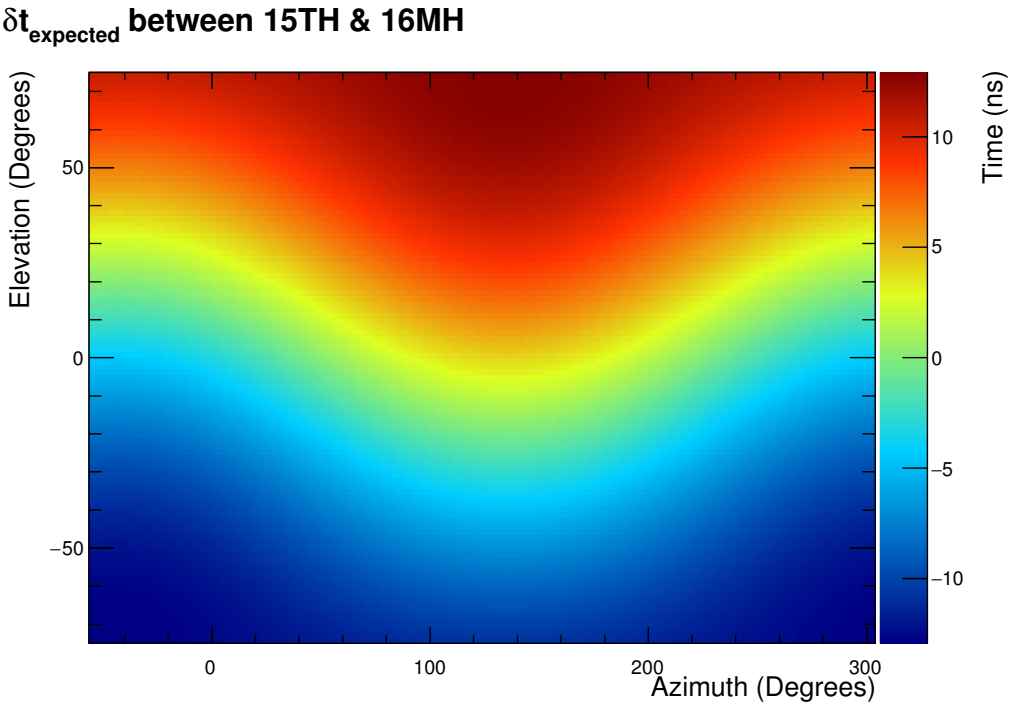

Figure 8.5: $\delta t_{\text{expected}}$ as a function of incoming signal direction in ANITA coordinates for antennas 15TH and 16MH.

For each antenna pair, i, j at bin in θ, ϕ, the cross-correlation is linearly interpolated at an offset $\delta t^{ij}_{\text{expected}}$. A correlation map is then filled with the linearly interpolated cross-correlation at θ, ϕ. Figure 8.6 shows the cross-correlation of 15TH and 16MH as a function of arrival direction, θ, ϕ.

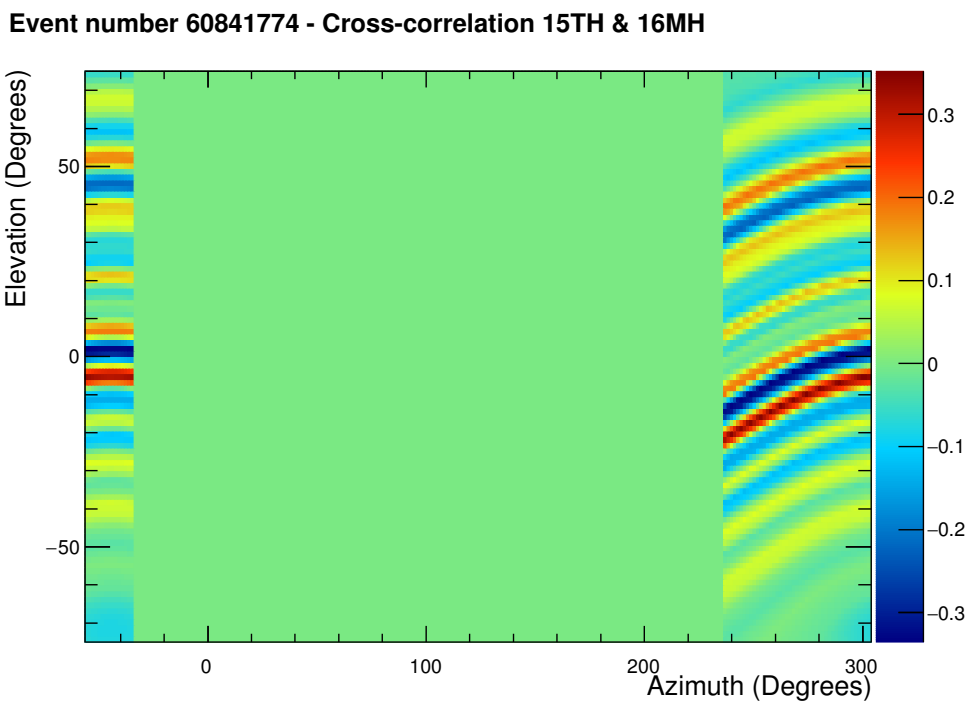

Figure 8.6: Cross-correlation of 15TH and 16MH as a function of arrival direction. The map is filled in for all values of azimuth that are within $\pm 2\Phi$-sectors of both antennas.

This is done for each antenna pair within $\pm 2\Phi$-sectors. The cross-correlation maps for 5 other pairs are shown in Figure 8.7. The bin-by-bin sum of the 6 maps (Figures 8.6 and 8.7) is shown in Figure 8.8.

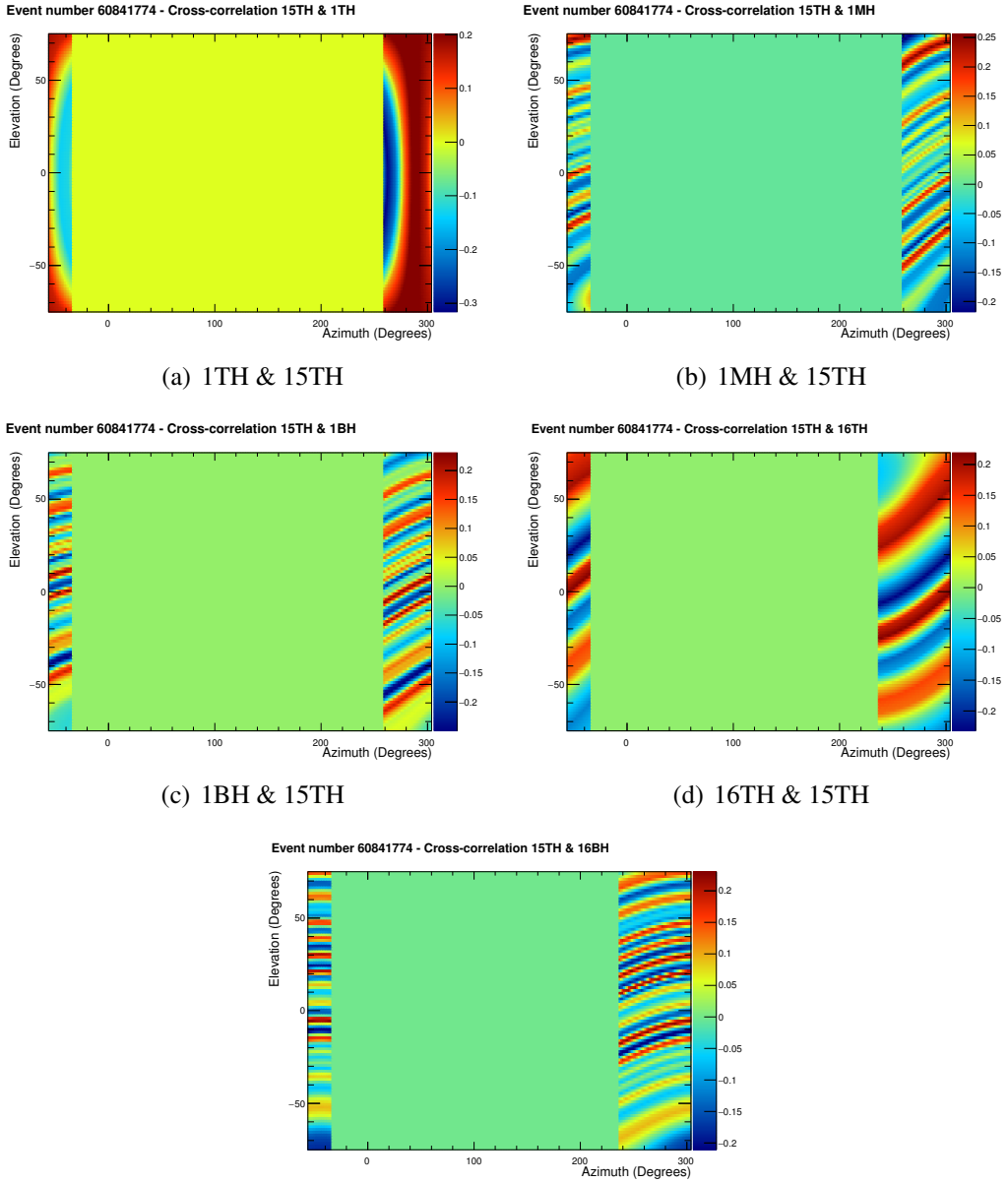

(a) 1TH & 15TH

(b) 1MH & 15TH

(c) 1BH & 15TH

(d) 16TH & 15TH

(e) 16BH & 15TH

Figure 8.7: The equivalent distributions for an additional 5 antenna pairs. The range of azimuth spanned by the sum is different for Φ-sector 1 and Φ-sector 16

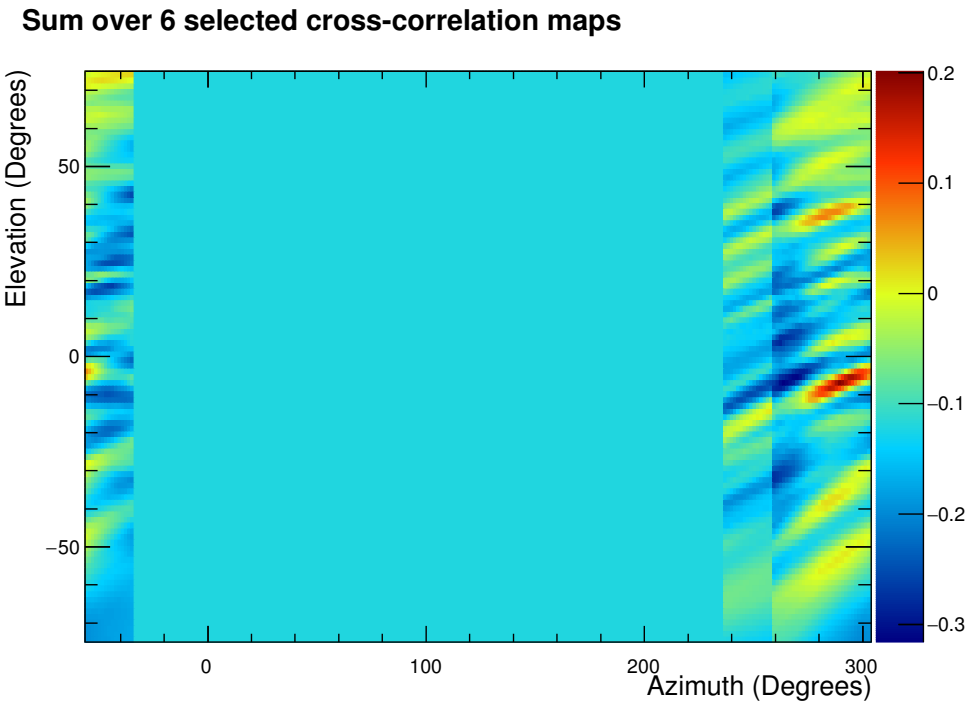

Figure 8.8: The sum of the correlation maps in Figures 8.5 and 8.6,

As cross-correlations for additional pairs are added together the stripes of positive correlation begin to overlap at a single point. In Figure 8.8 a unique peak is beginning to emerge around 290° in azimuth and −6° in elevation. The cross-correlation map after summing over all antenna pairs is shown in Figure 8.9, where a unique peak has emerged.

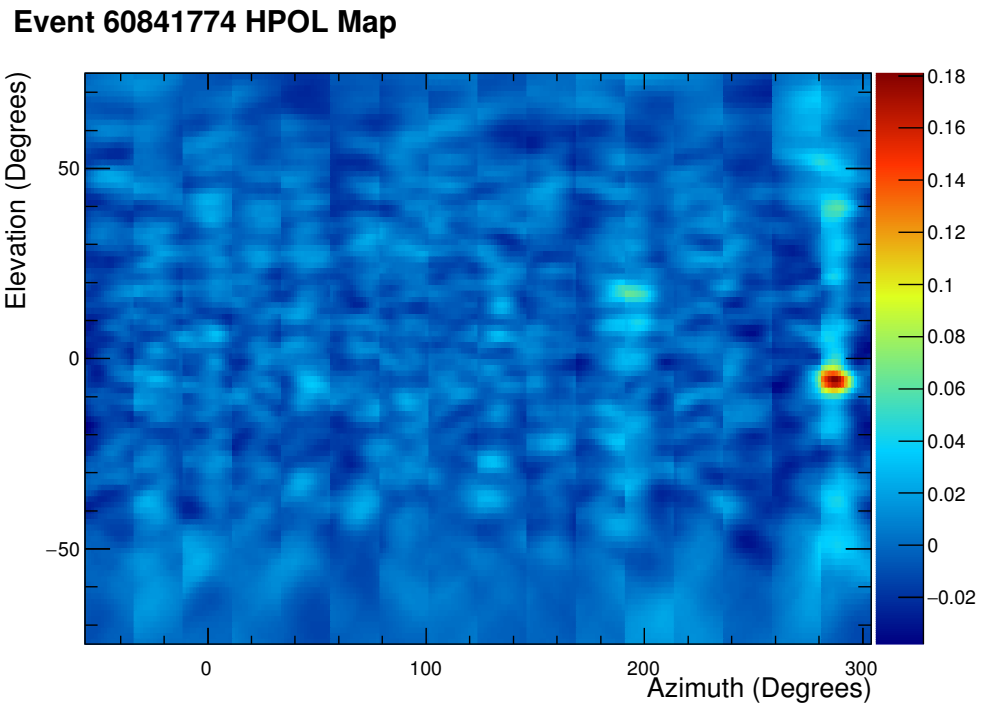

Figure 8.9: After summing the cross-correlation pairs for all the antenna pairs shown in Figure 8.2 a unique peak appears at 286° in azimuth and −7° in elevation.

The value of the peak is a useful discriminator against thermal noise, which is uncorrelated between channels. Figure 8.10 shows the interferometric map for a minimum bias triggered event. Since there is no coherence between the channels of neighbouring antennas, the peak value is much smaller.

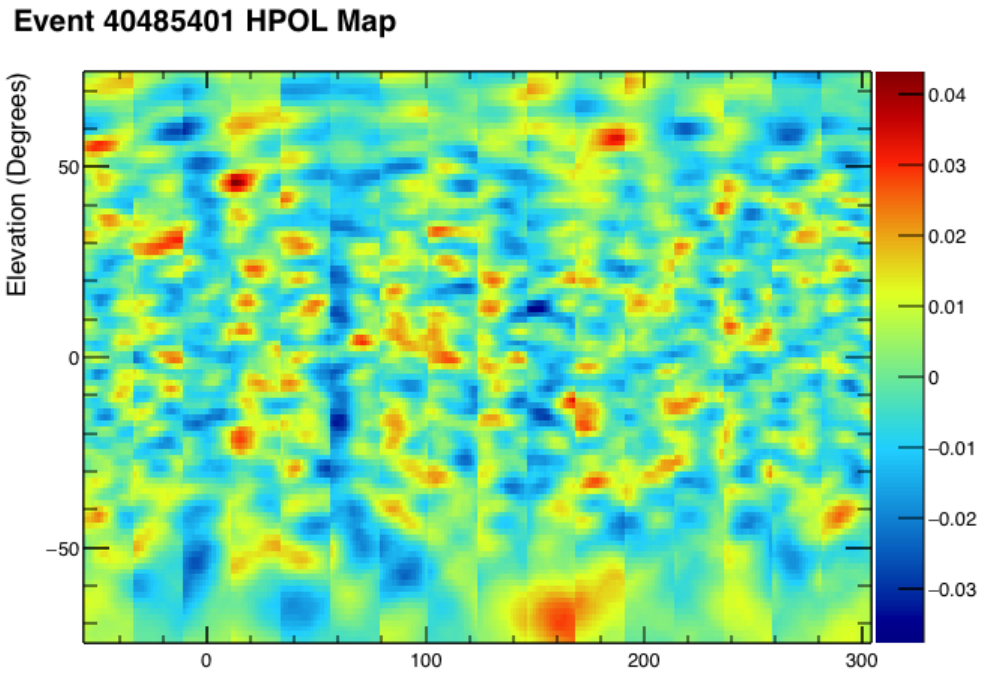

Figure 8.10: Interferometric reconstruction of a minimum bias event dominated by thermal noise. Because there is no coherence between channels the peak value of the map is much reduced.

The cross-correlation map in Figure 8.9 and Figure 8.10 are binned at 1.5° intervals in azimuth and elevation. To determine the arrival direction of an impulsive signal the next step in the reconstruction is to make a finely binned image centred on the peak in the first map. The azimuth of the peak is used to select all the channels contributing to this direction. The cross-correlations of these channels are interpolated by a factor of 40 to 10 ps, just less than the intra-SURF timing resolution (Section 6.3.3). Unlike the initial interpolation, which used an Akima spline, the second interpolation zero pads the Fourier transform of the evenly sampled waveforms and scales them such that the cross-correlation has a maximum possible value of 1. An example of this second interpolation is shown in Figure 8.11.

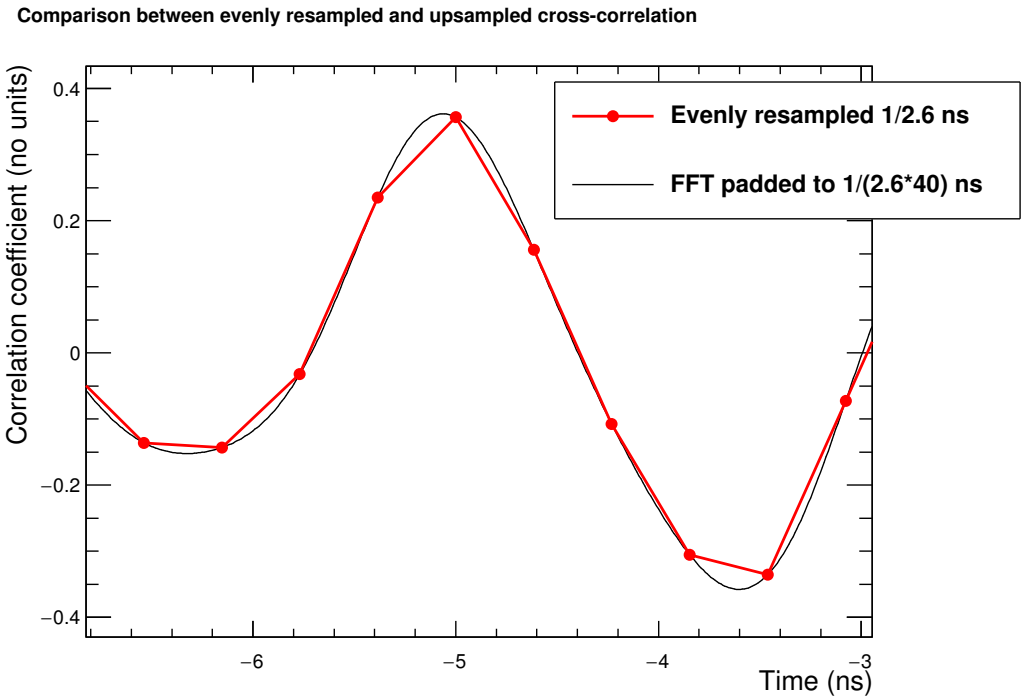

Figure 8.11: Close up on the peak of Figure 8.4. The first cross-correlation map uses the linearly interpolated values between the red points, as picked out by the red line. The second cross-correlation map uses linearly interpolated values between the sub10 ps interpolated points, as picked out by the black line.

The second cross-correlation map uses linearly interpolated values of the upsampled cross-correlation at each bin. The improvement in peak resolution can be seen in Figures 8.12 (first cross-correlation map) and 8.13 (second cross-correlation map). The azimuth and elevation values of the maximum peak are taken as the direction of origin of the plane wave.

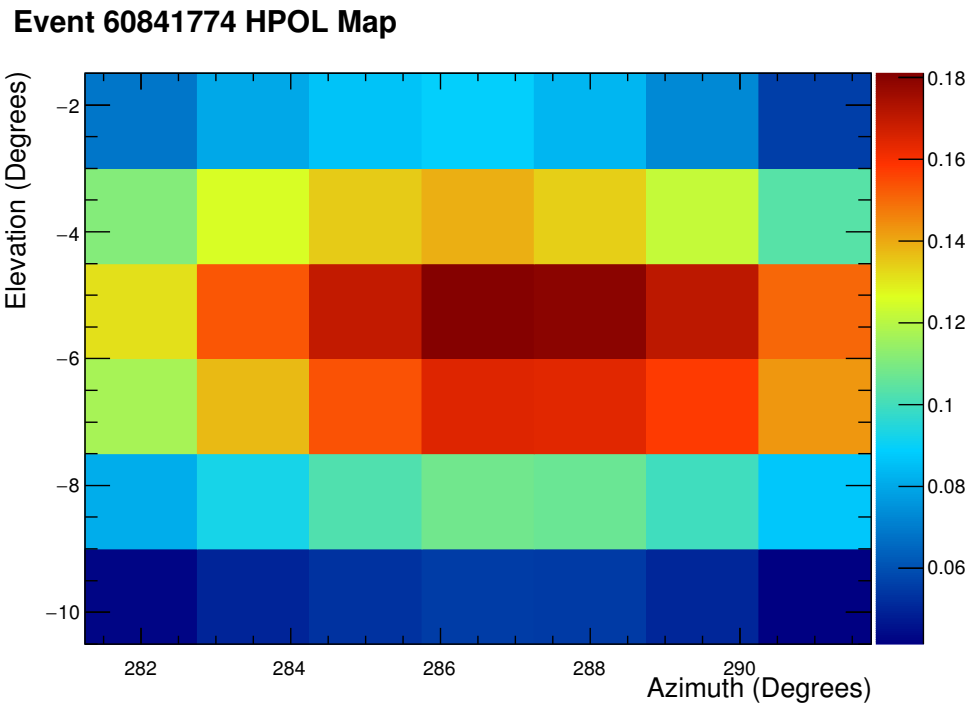

Figure 8.12: A close up of the peak in the cross-correlation map in Figure 8.9.

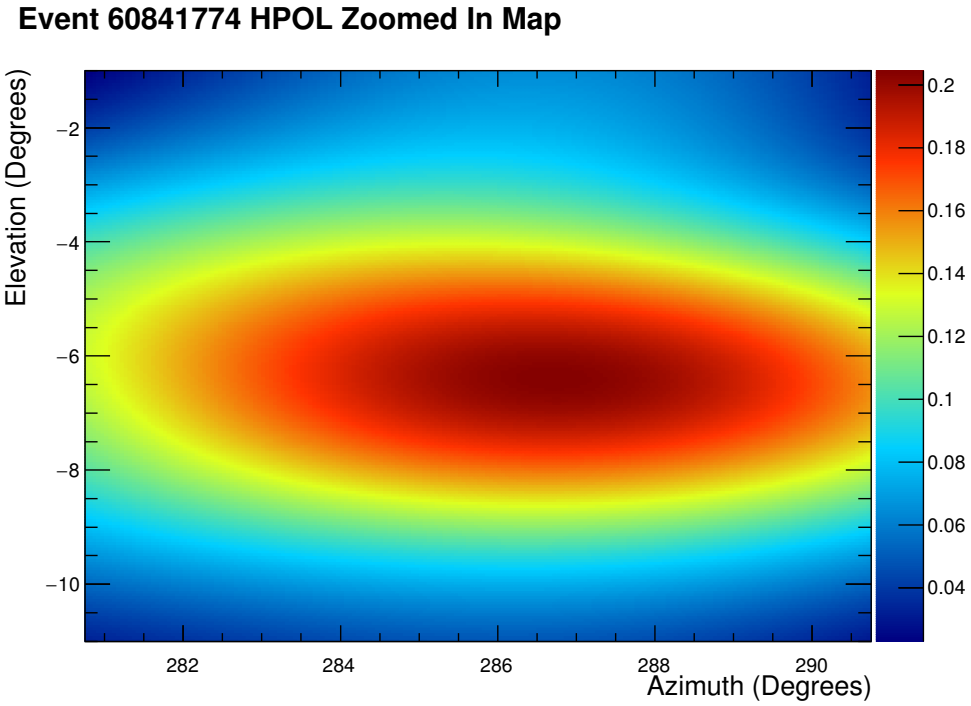

Figure 8.13: Finely binned cross-correlation map using the upsampled cross-correlations.

8.2 Coherently Summed Waveform and Hilbert Envelope

In addition to the peak direction and value of the interferometric map, another key variable in ANITA analysis is the peak value of the Hilbert envelope of the coherently summed waveform. The peak of the interferometric map implies a set of time offsets between neighbouring channels. The three FFT interpolated channels in the Φ-sector aligned closest with interferometric peak were summed withe relative delays applied to the channels. This reinforces the signal in the three channels by aligning the peaks and suppresses noise that will tend to cancel out as the waveforms are added together. An example of a coherently summed waveform for a particularly large SNR is shown in Figure 8.14a, and an example for a thermal noise dominated event is shown in Figure 8.14b.

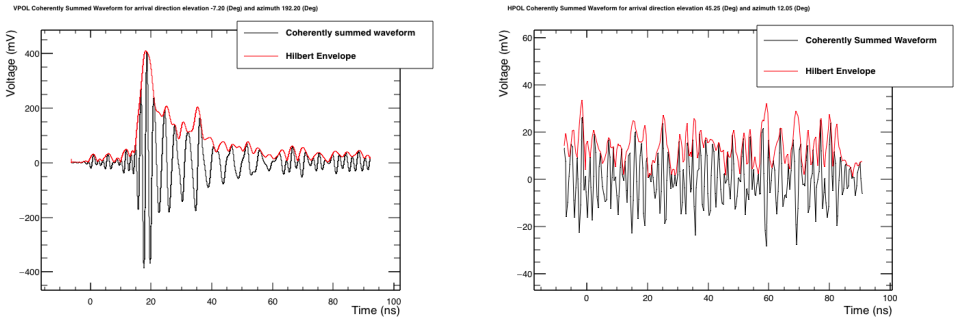

(a) Large impulsive event (b) Thermal noise event

Figure 8.14: Example of coherently summed waveforms and Hilbert envelope for a large VPol pulser event A large VPol pulser event (SNR > 20), and a thermal noise dominated event.

I have also plotted the Hilbert Envelope of the coherently summed waveform in Figure 8.14. The Hilbert Envelope is defined by

$$\Psi(t) = \sqrt{\psi^2(t) + H^2(t)} \tag{8.4}$$

Ψ is the coherently summed waveform, H is the Hilbert transform is the Fourier

transform $\mathscr{F}(h(f))$ and $h(f)$.

$$\mathscr{R}(h(f)) = \mathscr{I}(-\Psi(f))\mathscr{I}(h(f)) = \mathscr{R}(\Psi(f)) \tag{8.5}$$

where $\mathscr{R}$ and $\mathscr{I}$ denote the real and imaginary parts of h and Ψ. The peak of the Hilbert Envelope is a useful discriminating quantity for impulsive signal-like events.

8.3 Antenna Position Calibration

In addition to an accurate timing calibration, the interferometric method requires accurate knowledge of the positions of the antenna phase centres.

An initial estimate of the antenna phase centre positions was made using photogrammetry data taken in Antarctica [15]. Several photographs of ANITA were taken during its Antarctic pre-flight hang test and the vertices of the Seaveys were marked (Figure 8.15).

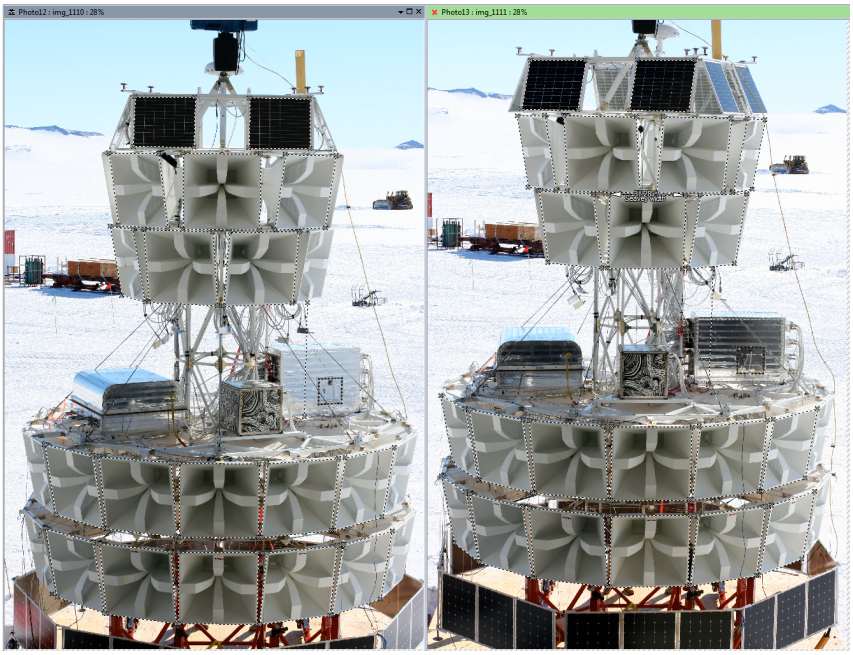

Figure 8.15: ANITA-3 taken during the Antarctic hang test. Vertices of antennas are marked in photographic input to photogrammetry software. Figure from [15].

The marked vertex positions were used with an antenna model to estimate the geometry of the payload. Initially the phase centre positions are estimated at 20 cm behind the centre of the face of the antennas. The results split the top ring into two

sub-rings as they are at different radii and heights. The relative results for the top sub-rings and the middle and bottom rings are shown as a function of Φ-sector in Figures 8.16, 8.17, 8.18.

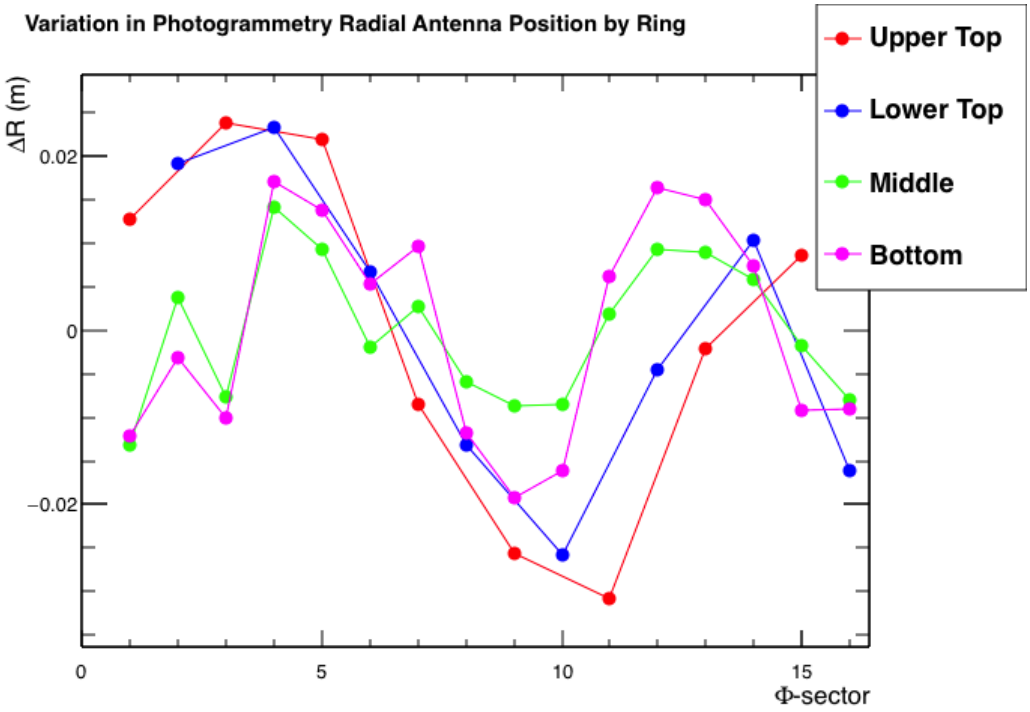

Figure 8.16: Distance from photogrammetry sub-ring mean radial position.

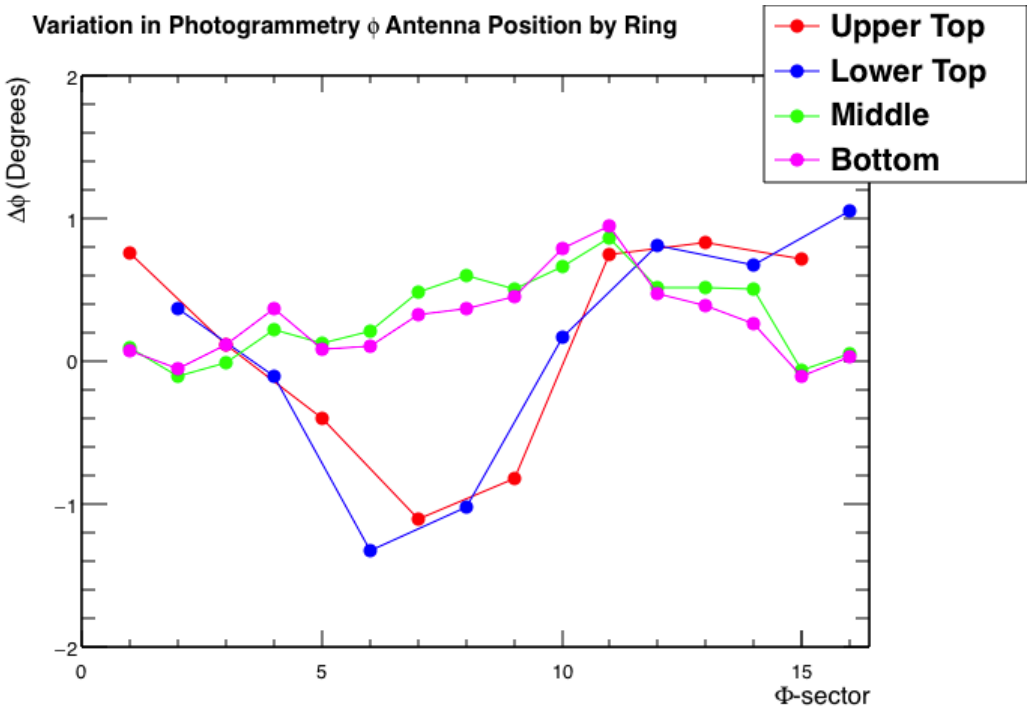

Figure 8.17: Angular shift from 22.5° separated Φ−sectors.

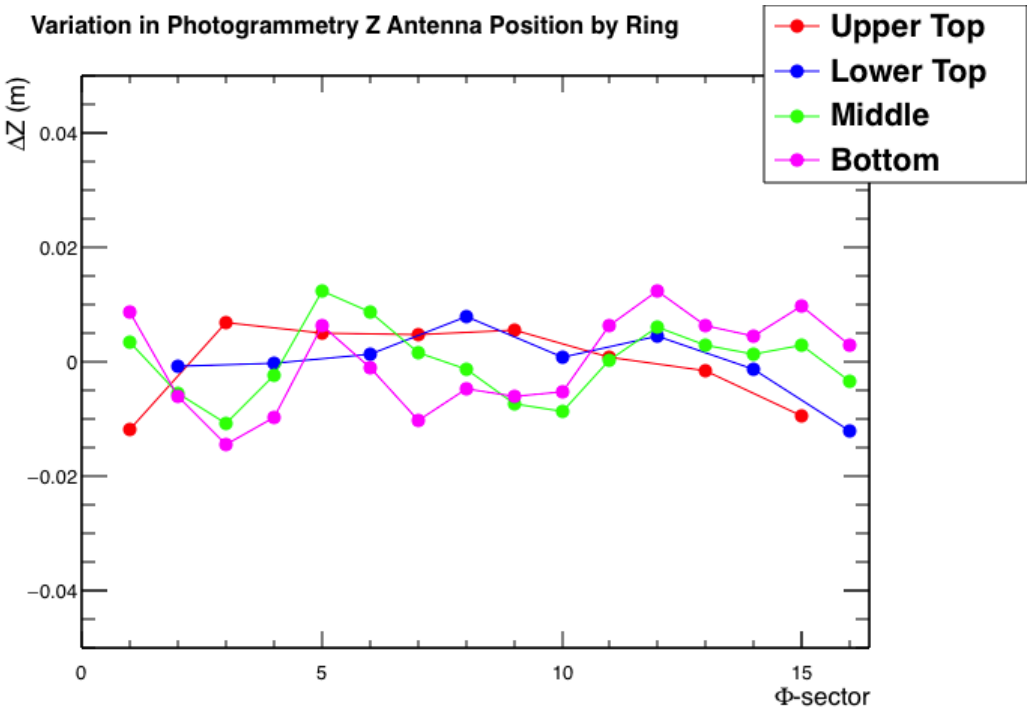

Figure 8.18: Distance from photogrammetry sub-ring mean height.

The photogrammetry indicates that the payload is not radially symmetrical

with some distortions as a function of Φ-sector, especially for the the r and ϕ positions.

8.3.1 ANITA Angular Resolution using Photogrammetry

The calibration pulses from WAIS Divide (Section 7.2.2) and LDB (Section 7.2.1) were reconstructed using the interferometry algorithm described in Section 8.1.

The ANITA GPS data gives position and heading information. I used the ANITA `EventCorrelator` library[68] and the GPS coordinates of the calibration pulsers to calculate the expected arrival direction (θ, ϕ) for every pulser event. Comparing the expected θ, ϕ with the position of the interferometric map peak gives an estimate of ANITA's angular resolution. In the following plots

$$\delta\phi = \phi_{\text{expected}} - \phi_{\text{measured}} \quad \text{and} \quad \delta\theta = \theta_{\text{expected}} - \theta_{\text{measured}} \quad . \tag{8.6}$$

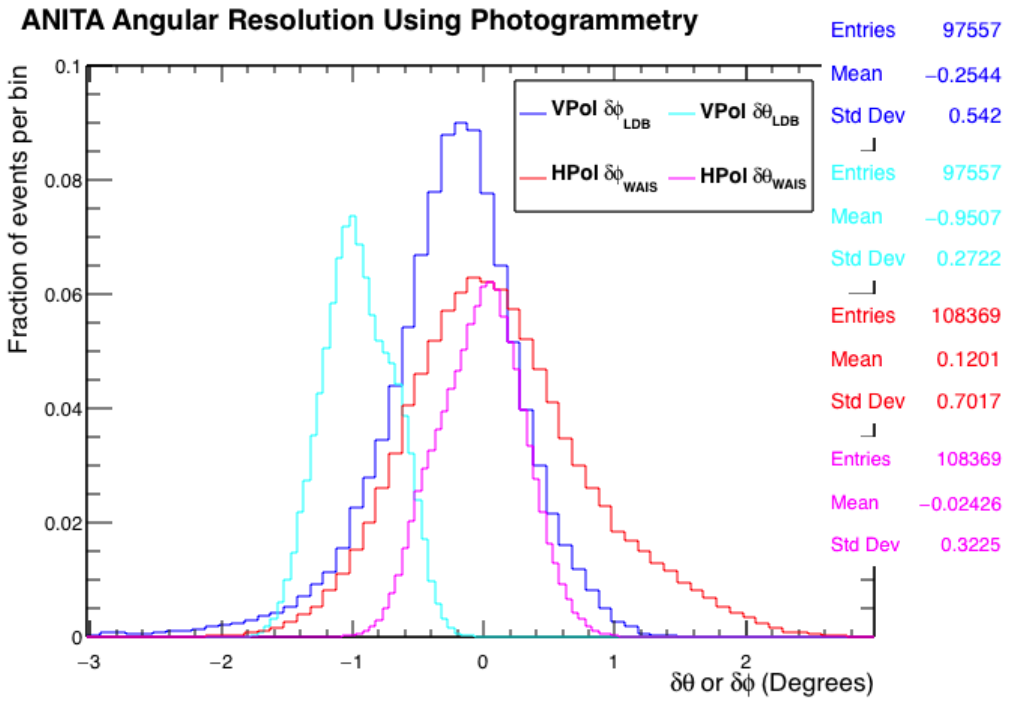

Figure 8.19: Angular resolution of the ANITA instrument in θ, ϕ for HPol and VPol using the phase centre positions obtained from the photogrammetry data. The red and magenta lines shows the HPol ϕ and *theta* resolutions respectively. The blue and cyan lines show the VPol ϕ and *theta* resolutions respectively.

A summary of the angular resolution of θ, ϕ for VPol and HPol is shown in

Figure 8.19. The VPol θ distribution is significantly offset from 0. Figures 8.20 and 8.21 show the angular resolution of ANITA in resconstructing the HPol pulser at WAIS Divide against the expected ϕ_{WAIS}. Figures 8.22 and 8.23 show the angular resolution of ANITA in resconstructing the VPol pulser at LDB against the expected ϕ_{LDB}. The mean of the resolution shifts as the payload rotates, adding to the width of the distributions.

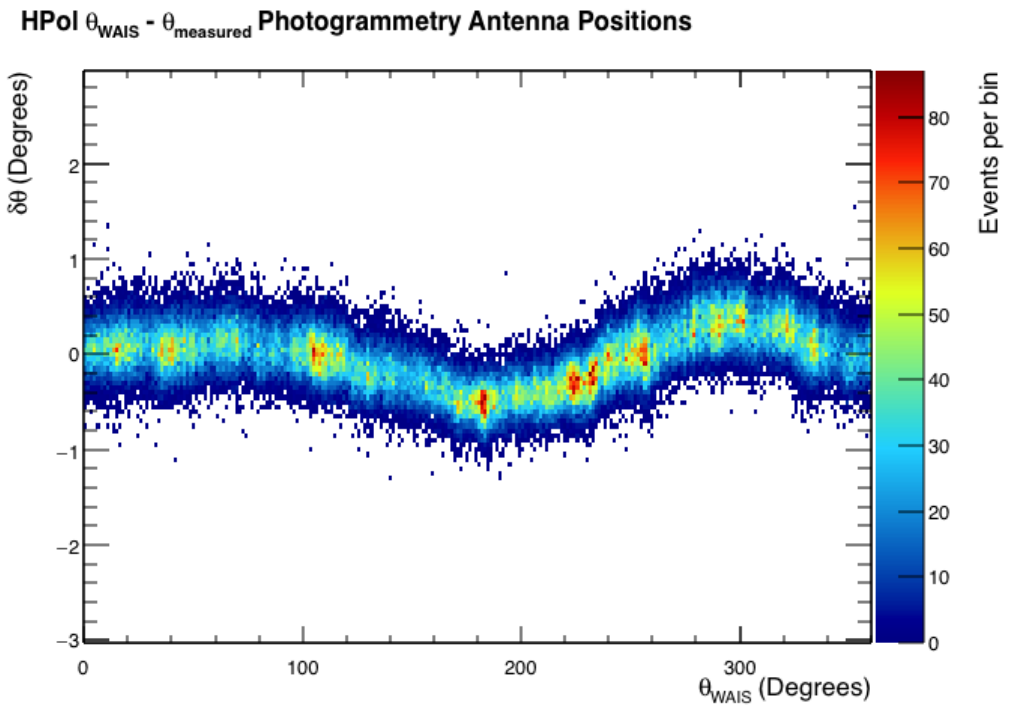

Figure 8.20: Difference between reconstructed θ and expected θ_{WAIS} plotted against ϕ_{WAIS}.

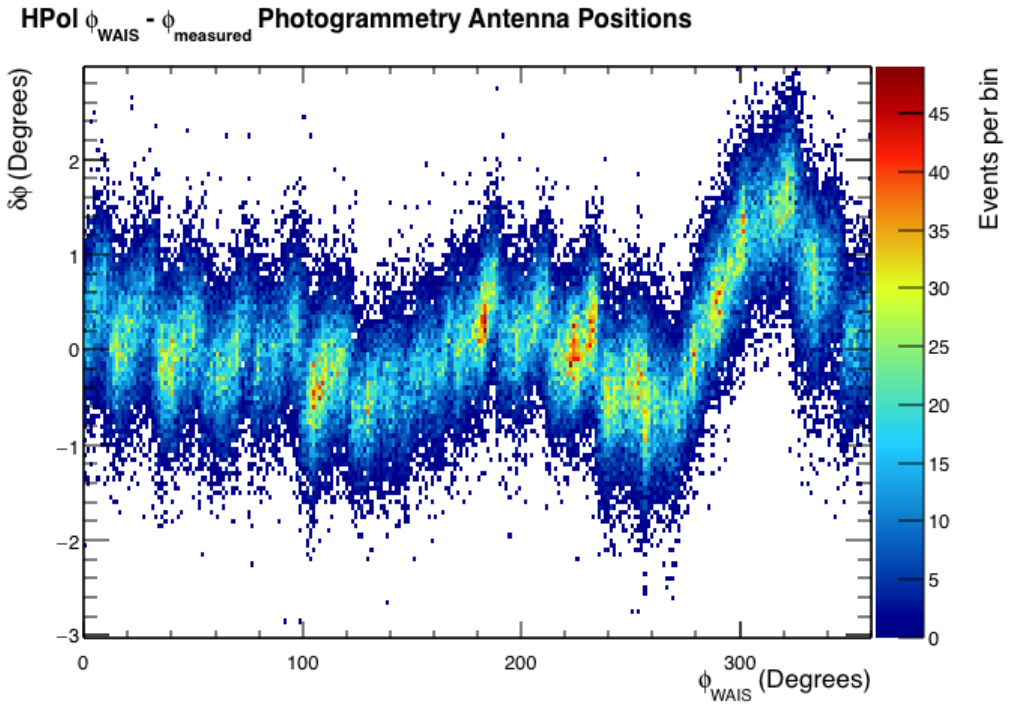

Figure 8.21: Difference between reconstructed ϕ and expected ϕ_{WAIS} plotted against ϕ_{WAIS}.

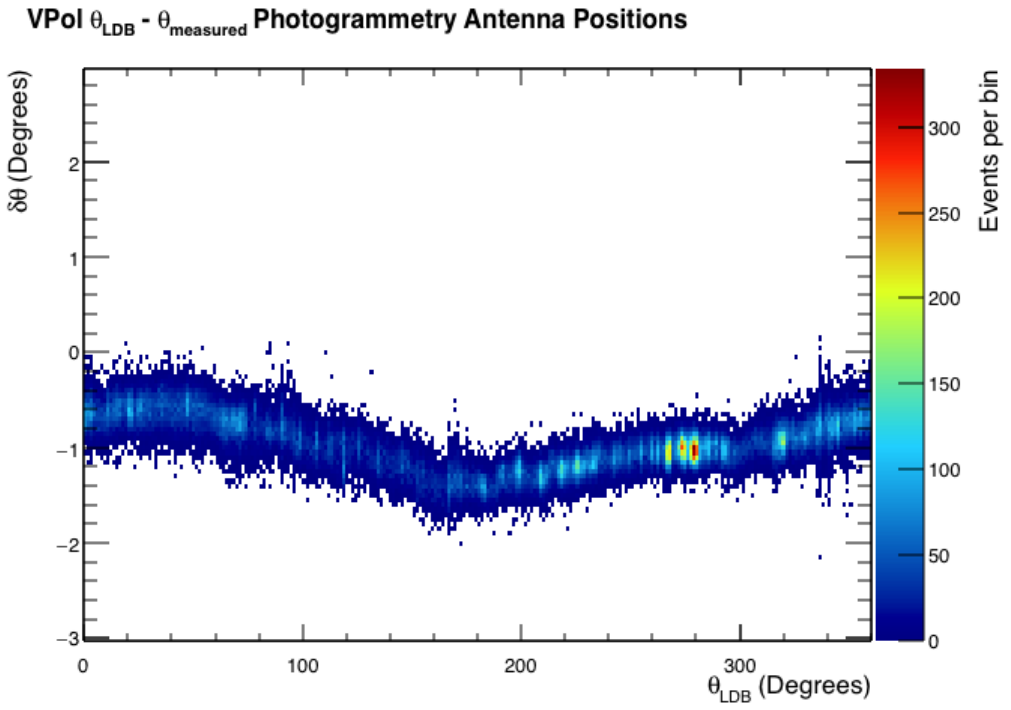

Figure 8.22: Difference between reconstructed θ and expected θ_{LDB} plotted against ϕ_{LDB}.

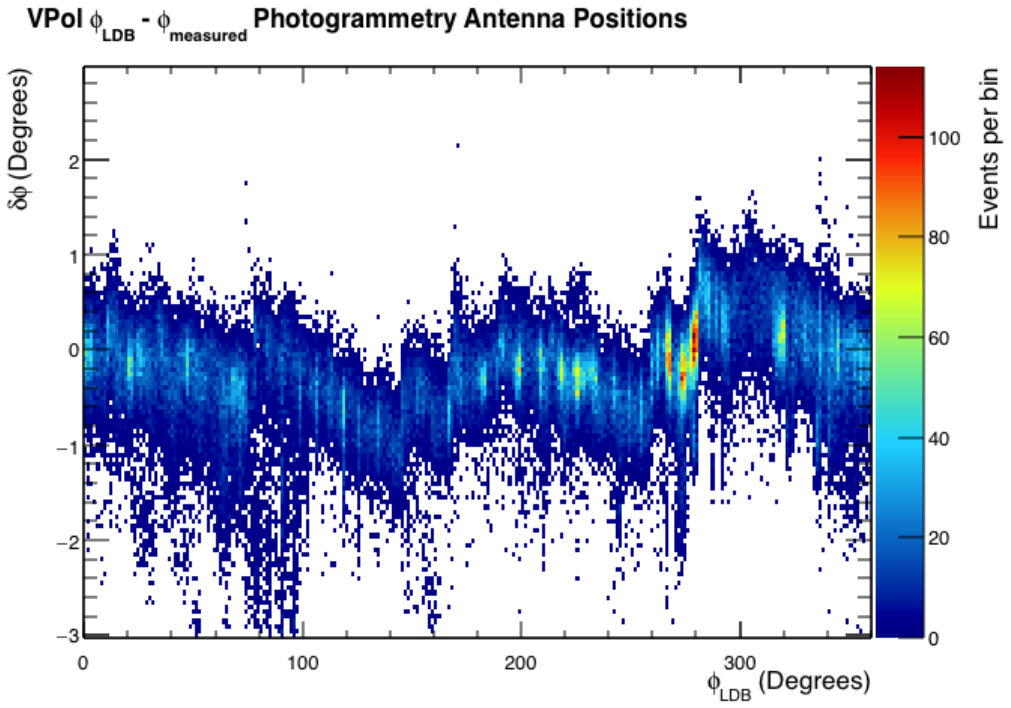

Figure 8.23: Difference between reconstructed ϕ and expected ϕ_{LDB} plotted against ϕ_{LDB}.

8.4 Phase Centre Fits

To improve the angular resolution distributions the pulser data from WAIS Divide and LDB was used as the input to a fitter for the phase centre positions. Linda Cremonesi cross-correlated the LDB and WAIS pulses in all nearest neighbour antennas and top-bottom pairs in each Φ-sector, i, j. The $\delta t^{ij}_{\mathrm{measured}}$ was compared with the $\delta t^{ij}_{\mathrm{expected}}$ on a channel-by-channel basis. Figure 8.24 shows a profile histogram of the distributions of $\delta t^{ij}_{\mathrm{measured}} - \delta t^{ij}_{\mathrm{expected}}$ for the top-bottom pair of antennas in each Φ-sector from the HPol WAIS pulser.

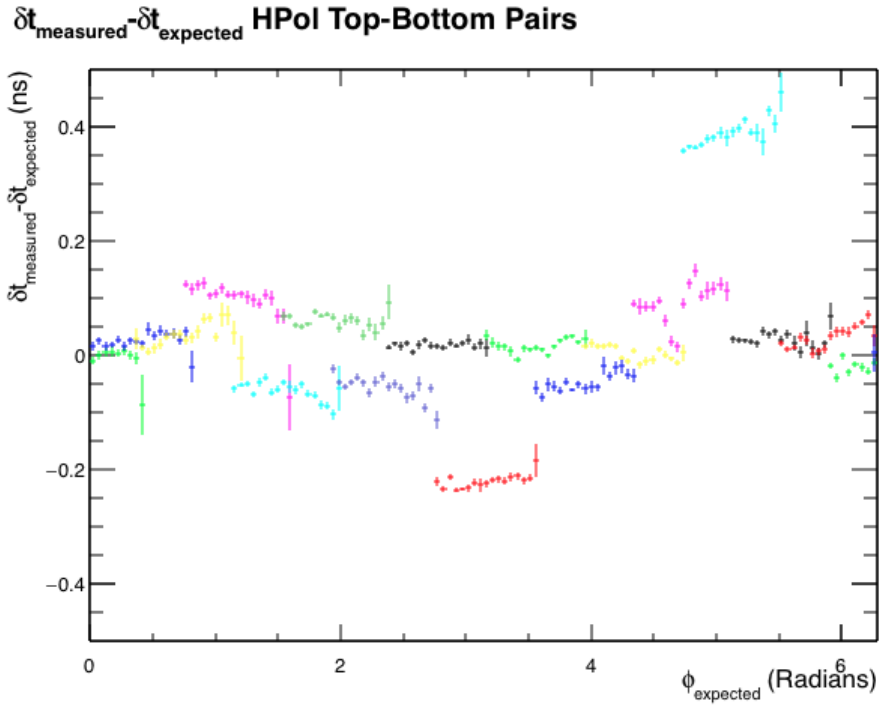

Figure 8.24: Distribution of $\delta t^{ij}_{\text{measured}} - \delta t^{ij}_{\text{expected}}$ for 16 antenna pairs. In this case, it is the top-bottom antenna pair in each Φ-sector. The original scatter plot was provided by Linda Cremonesi, which I have converted into a profile histogram to better show the structure as a function of ϕ_{expected}.

Figure 8.24 shows there are reasonably large mean offsets, and structure as a function of ϕ_{expected} for several channels. There are similar plots for the horizontal pairs and other vertical pairs in HPol and VPol.

To try and improve the distributions plotted in Figure 8.24, the phase centres of the antennas were varied in a fitter. For antenna i:

$$\begin{aligned} r_i &\rightarrow r_i + \Delta r_i \\ \phi_i &\rightarrow \phi_i + \Delta\phi_i \\ z_i &\rightarrow z_i + \Delta z_i \\ &\text{with an additional variable, } \Delta t_i \quad , \end{aligned} \tag{8.7}$$

where r_i, ϕ_i, z_i are the cylindrical coordinates of the phase centre. The relative channel-to-channel delay was calibrated from the AMPA input (see Section 6.3), so the Δt_i is an extra parameter to account for the delay between the antenna phase

centre and AMPA inputs. Figure 8.25 shows the $\delta t^{ij}_{\text{measured}} - \delta t^{ij}_{\text{expected}}$ vs. ϕ_{expected} distribution after the antenna have been shifted.

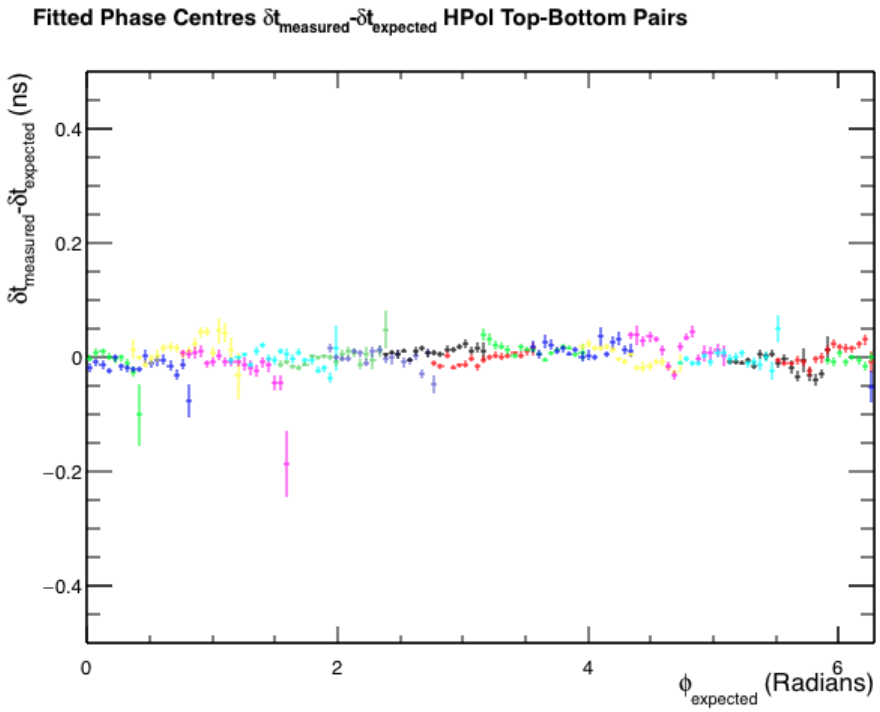

Figure 8.25: HPol top-bottom pairs after the fitted phase centre positions are used to calculate $\delta t_{\text{expected}}$. The original scatter plot was provided by Linda Cremonesi, which I have converted into a profile histogram to better show the structure as a function of ϕ_{WAIS}.

8.4.1 Off-Axis Delay

A higher order off-axis delay correction was applied in addition to the updated antenna positions from the phase centre fit. The interferometric reconstruction was updated to account for the off-axis delay of the antennas. Figure 8.26 shows the $\delta t^{ij}_{\text{measured}} - \delta t^{ij}_{\text{expected}}$ the results as a function of ϕ_{WAIS}. The distribution varies by ± 0.05 ns, which is within the inter-channel timing resolution at low SNR (Section 6.3.3). To account for this effect, the distribution was fitted with an anti-symmetric polynomial. The fit picks out the trend to within 0.01 ns, which is less than the inter-SURF channel-to-channel resolution.

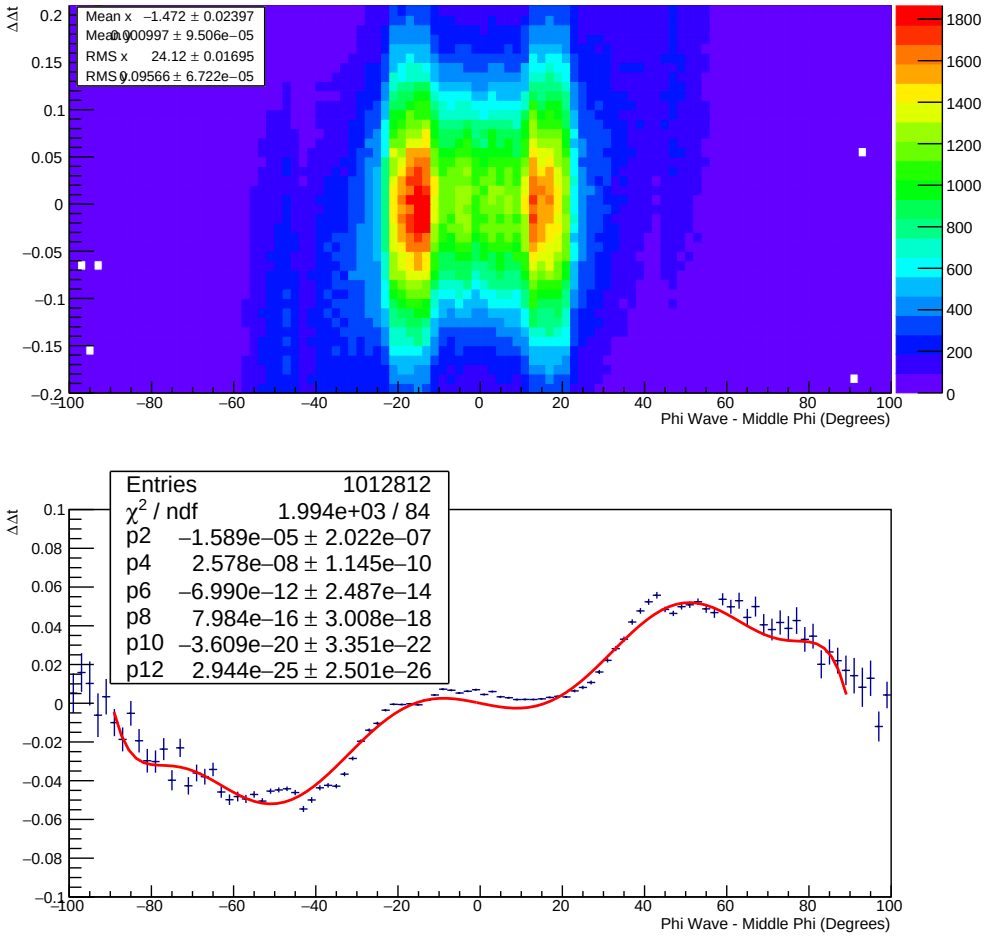

Figure 8.26: Off-axis delay averaged over all antennas. Figure produced by Linda Cremonesi.

This off-axis delay is accounted for in the reconstruction by adding a term to equation (8.3), which defines the expected travel time between antennas.

$$\delta t^{ij}_{\text{expected}}(\theta,\phi) \rightarrow \delta t^{ij}_{\text{expected}} + f(\phi-\phi_i) - f(\phi-\phi_j) \quad , \tag{8.8}$$

where ϕ is the direction of the incoming plane wave, $\phi_{i/j}$ is the antenna i/j azimuth, and $f(\phi-\phi_i)$ is fitted off-axis response function. This correction is included in the reconstruction when using the fitted phase centre positions.

8.5 Angular Resolution Using Fitted Phase Centre Antenna Positions

The angular resolution summary plot, Figure 8.19, was remade by reconstructing the pulser data using the phase centre antenna positions and extra cable delays obtained from the fit (Section 8.4). The updated ANITA-3 angular resolution is shown in Figure 8.27. The plot indicates an improvement over the results obtained using the photogrammetry alone (Figure 8.19). There is a notable improvement visible in the VPol $\delta\theta_{\mathrm{LDB}}$ distribution, as the extra 0.3 ns in the Δt distribution brings the mean value of $\delta\theta_{\mathrm{LDB}}$ much closer to zero. Previously this distribution was offset by around -1° (Figure 8.19). It is also notable that each of the distributions in Figure 8.27 is narrower than its photogrammetry equivalent (Figure 8.19). This reduced width is due to the removal of the large scale variation in resolution as a function $\phi_{\mathrm{WAIS/LDB}}$. This can be observed by comparing Figures 8.20, 8.21, 8.22 and 8.23 with Figures 8.28, 8.29, 8.30 and 8.31.

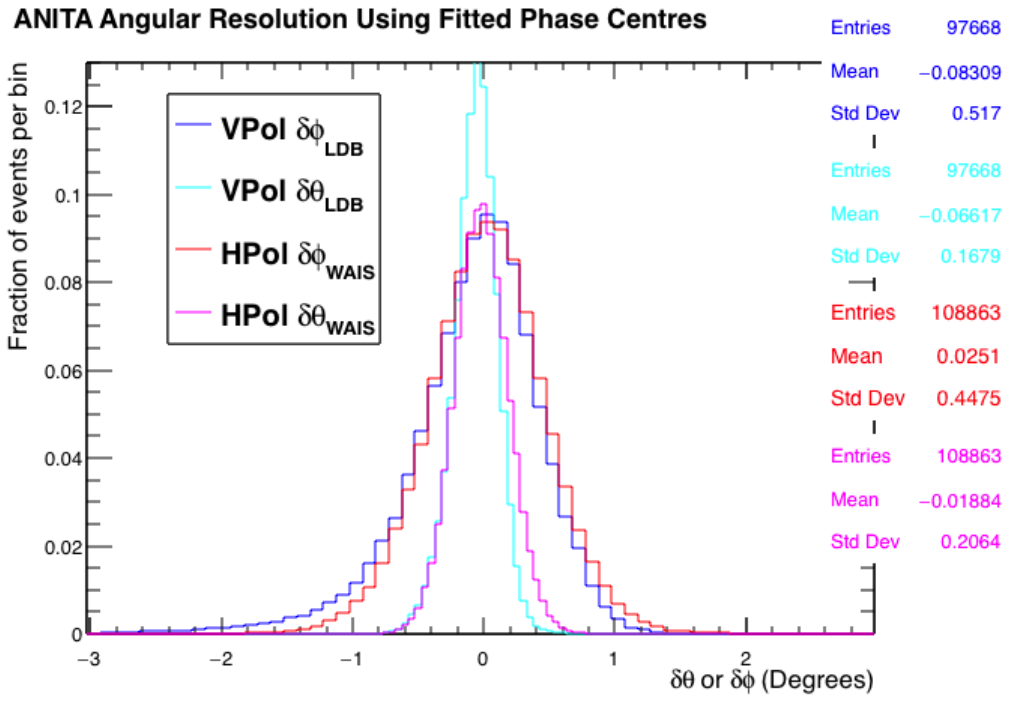

Figure 8.27: Summary of the angular resolution of the ANITA instrument using the phase centre positions obtained from the fit.

Table 8.1: Summary of angular resolutions before and after phase centre fits.

Polarisation	Direction	Photogrammetry		Fitted	
		Mean	Std. Dev	Mean	Std. Dev
Horizontal	Elevation (θ)	0.02°	0.32°	0.02°	0.21°
Horizontal	Azimuth (ϕ)	0.12°	0.70°	0.03°	0.45°
Vertical	Elevation (θ)	-0.95°	0.27°	-0.07°	0.17°
Vertical	Azimuth (ϕ)	0.25°	0.54°	-0.08°	0.52°

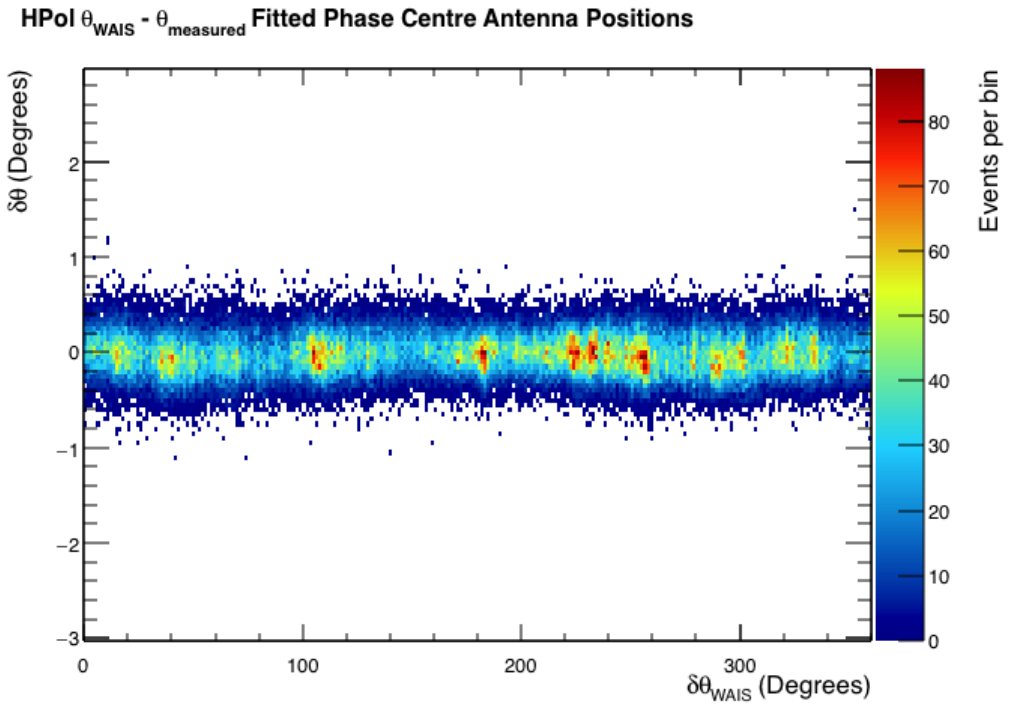

Figure 8.28: Difference between reconstructed θ and expected θ_{WAIS} plotted against ϕ_{WAIS}.

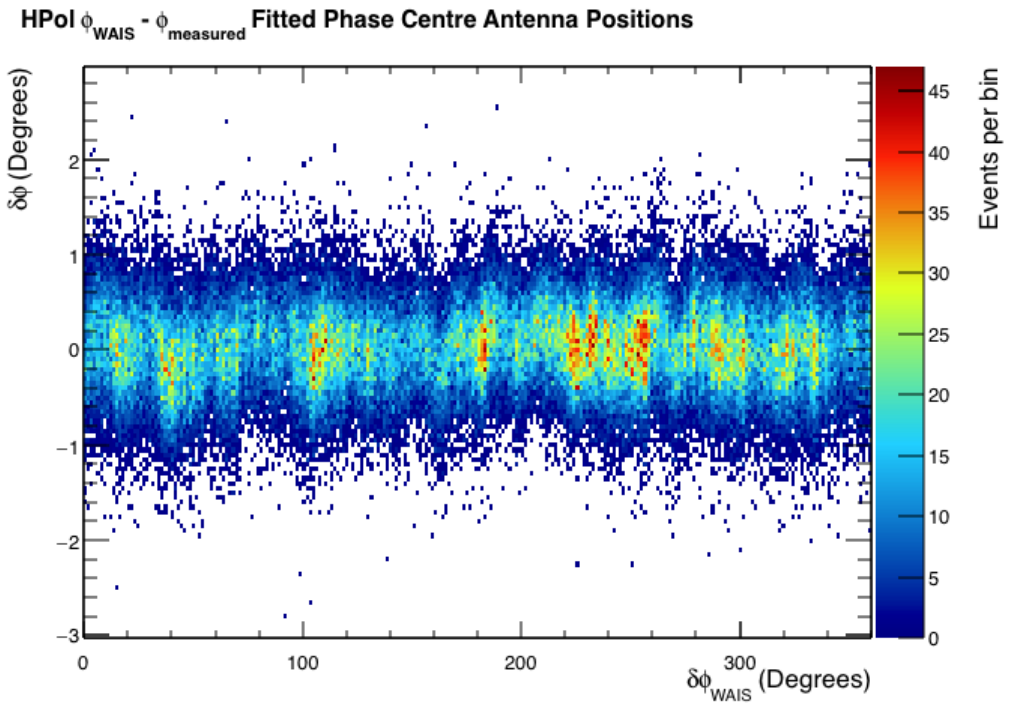

Figure 8.29: Difference between reconstructed ϕ and expected ϕ_{WAIS} plotted against ϕ_{WAIS}.

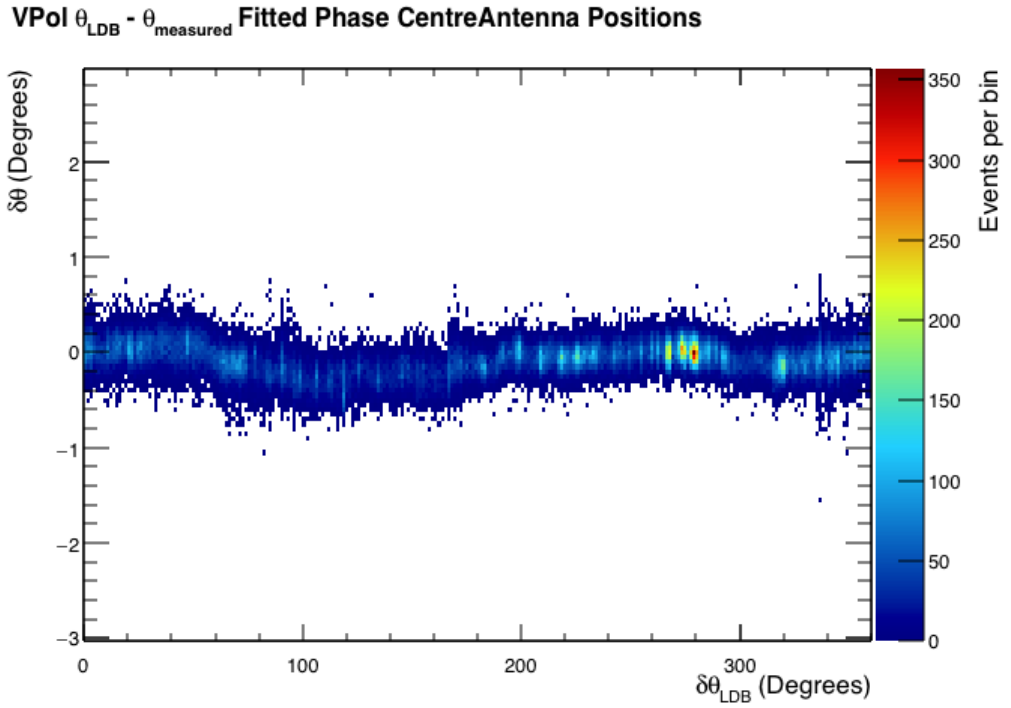

Figure 8.30: Difference between reconstructed θ and expected θ_{LDB} plotted against ϕ_{LDB}.

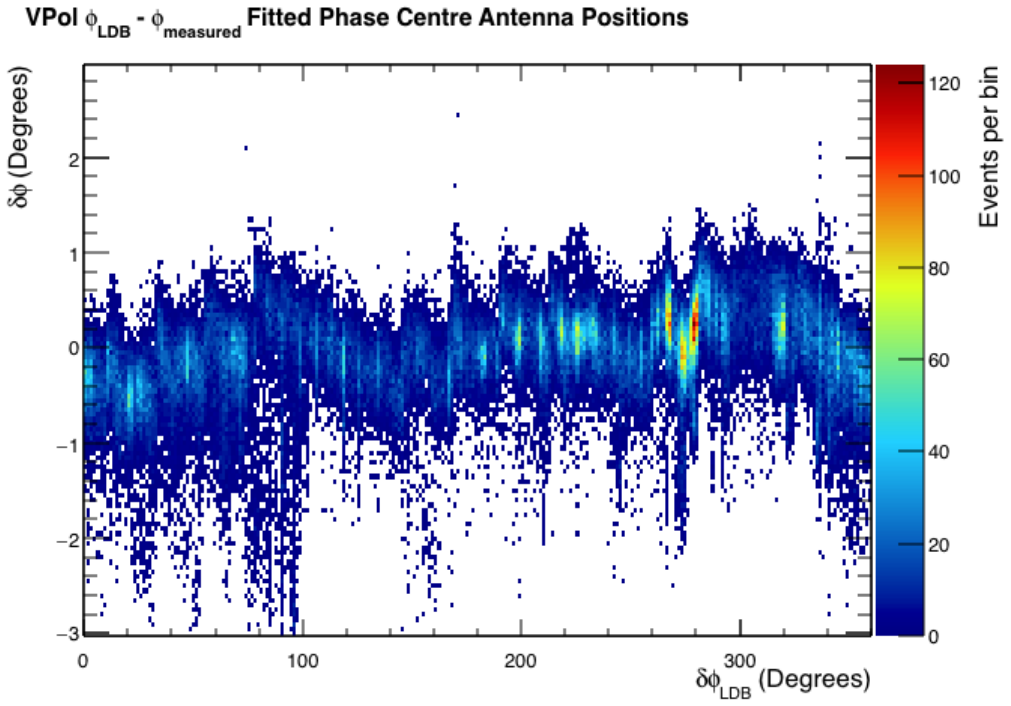

Figure 8.31: Difference between reconstructed ϕ and expected ϕ_{LDB} plotted against ϕ_{LDB}.

Although there was some improvement over the photogrammetry resolution, small scale structure as a function of ϕ is still present, especially for the VPol pulser data.

8.6 Cross Check With LDB HPol Pulser

The HPol pulser data from LDB was used to cross check the phase centres obtained fromby fitting the WAIS divide data. The WAIS and LDB HPol resolutions are plotted in Figure 8.32.

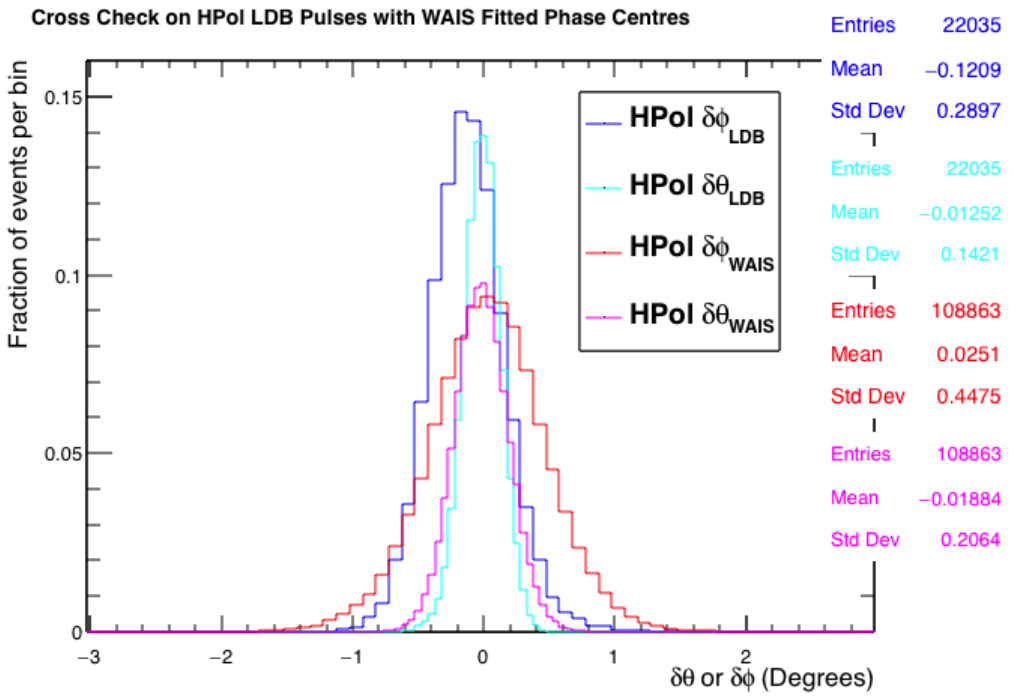

Figure 8.32: Comparison of the θ and ϕ resolutions for HPol reconstructing the WAIS divide and LDB HPol pulser.

Figure 8.32 shows an offset of $-0.12°$ in $\delta\phi$ although the $\delta\theta$ distributions agree well. This offset is smaller than the HPol resolution in ϕ but is systematic.

8.7 Angular Resolution as a function of SNR

The result from the timing calibration chapter (see Figure 6.39 in Section 6.3.3) indicated that the accuracy with which pulses can be aligned between channels depends on the Signal-to-Noise Ratio (SNR) of the pulse. To estimate the SNR of each pulser event, I find peak-to-peak voltage of the coherently summed waveform (Section 8.2), and the RMS voltage of the first 10 ns of each of the three waveforms. Then

$$\text{SNR} = \frac{y_{\text{max}} - y_{\text{min}}}{2 \text{ RMS}} \quad . \tag{8.9}$$

The θ and ϕ resolution plots for VPol and HPol were then binned in SNR. Figure 8.33 shows the VPol $\delta\theta$ resolution from LDB.

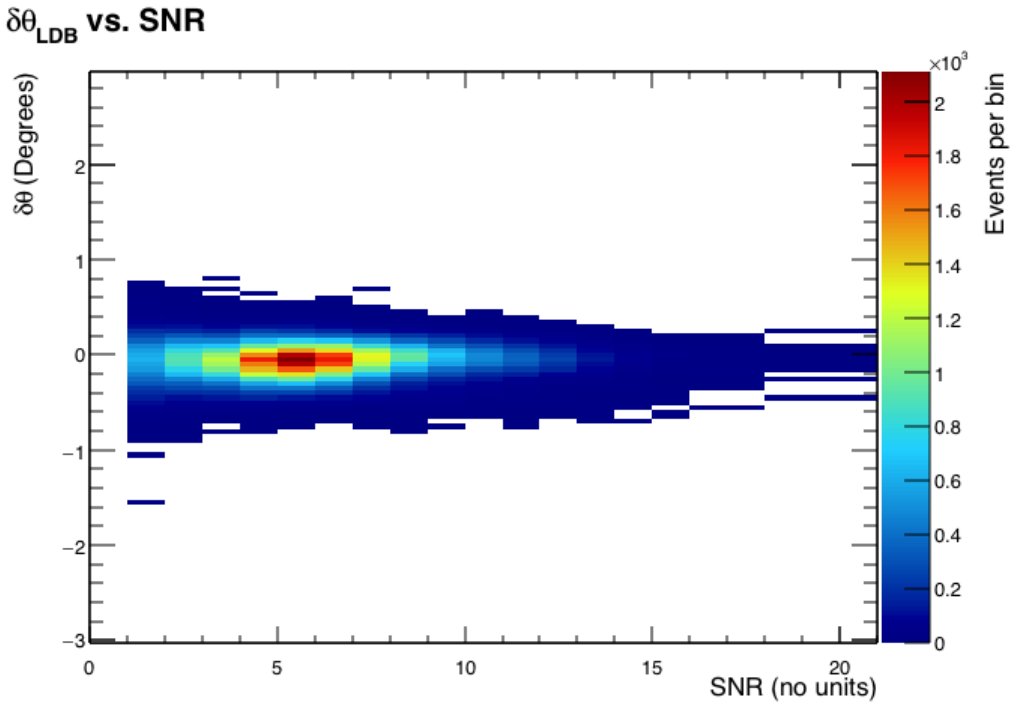

Figure 8.33: VPol $\delta\theta$ resolution binned in SNR, variable bin widths were used at the tail of the distribution when statistics are low.

A Gaussian was fitted to each bin in SNR, as described by equation (8.10), where σ_x is the width of the Gaussian for that bin.

$$y = A\exp\left(\frac{(x-\mu)^2}{\sigma_x^2}\right) \tag{8.10}$$

Figure 8.34 shows the σ_x distributions for VPol and HPol $\delta\theta$ and $\delta\phi$.

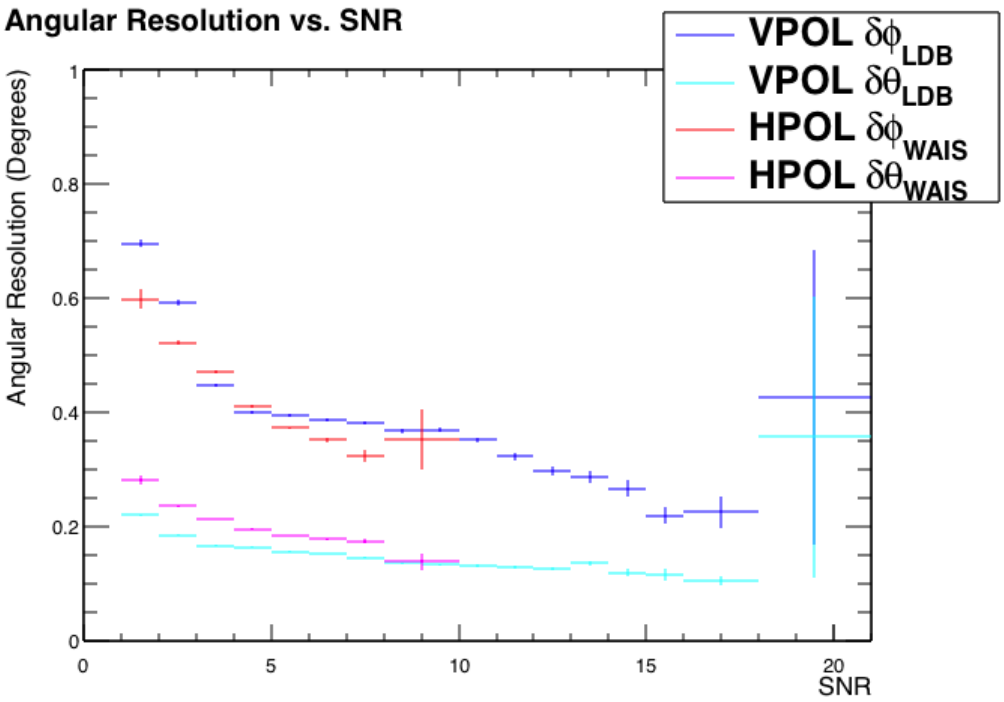

Figure 8.34: ANITA angular resolution using the fitted phase centre antenna positions as a function of Signal-to-Noise Ratio.

Figure 8.34 shows that the combined timing and antenna position calibrations gave ANITA-3 better than 0.7° angular resolution in azimuth (ϕ) for the smallest detectable pulses, increasing to sub-0.5° for larger pulse sizes (even in the relatively noisy environment of LDB and McMurdo base in the case of VPol). In the case of elevation (θ), the longer baseline of the antennas resulted in sub-0.3° resolution for the smallest detectable pulses, increasing to sub-0.2° with larger SNR. The apparent improvement in $\delta\phi$ at $SNR > 10$ is due to an uneven spread of received pulses around the payload. Some of the remaining width in the distribution is due to the small remaining antenna misalignment as a function of payload ϕ. By not sampling around the whole payload, this source of resolution is artificially removed.

8.8 Summary of Angular Resolution

I have described the ANITA reconstruction methods, in particular the interferometric map, and peak of the Hilbert envelope of the coherently summed waveform (called peak Hilbert for short). This reconstruction method gives ANITA sub-degree

resolution in azimuth and elevation. Specifically, after an antenna position calibration ANITA-3 has sub-0.8° resolution in azimuth and sub-0.3° is elevation for both polarisations. The fitted phase centres and off-axis response make a significant to the resolution over the photogrammetry estimated phase centre positions. Figures 8.35 and 8.36 show an example event before and after the calibrations are applied.

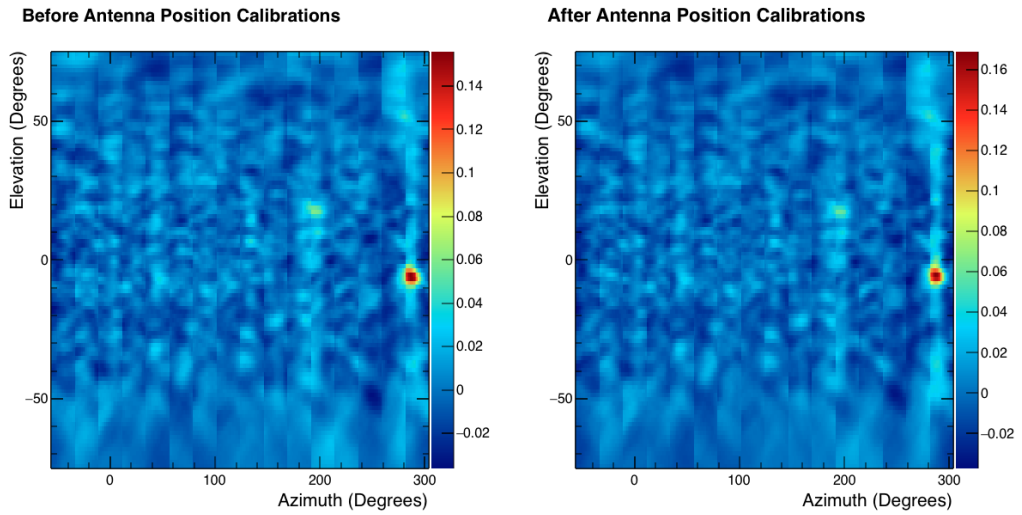

Figure 8.35: Example event reconstruction, before and after antenna calibration. The peak of the inteferometric map is larger after the calibration.

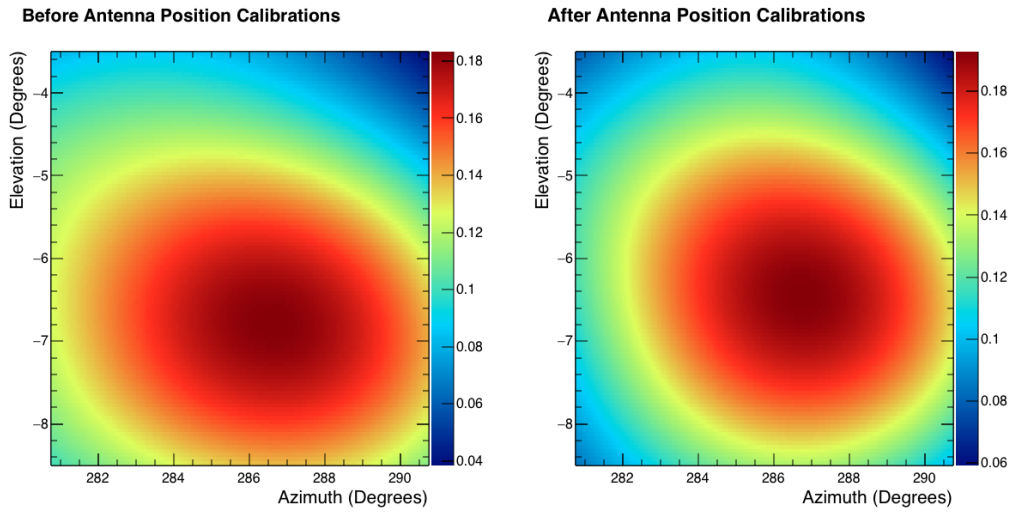

Figure 8.36: Example event reconstruction, before and after antenna calibration. The zoomed in interferometric map around the peaks in Figure 8.35 is larger after the calibration. The peak position has shifted slightly after the calibration is applied.

Chapter 9

Design of the ANITA-3 Event Prioritizer

Due to the limited satellite bandwidth in Antarctica, ANITA can only transmit around 0.1% of events to the ground during its flight. This limited bandwidth is best spent transmitting neutrino-like events in case the hard disks cannot be recovered. This is a real risk for scientific ballooning missions in Antarctica as the specific trajectory of the balloon is at the mercy of the elements, and access to the payload after the landing is not guaranteed.

A dedicated flight software program, the Event Prioritizer, was designed to select neutrino candidate events for transmission. One of the upgrades between ANITA-2 and ANITA-3 was incorporating a Graphics Processing Unit (GPU) into the flight computer. I wrote the ANITA-3 Event Prioritizer, which used the GPU to perform an interferometric analysis on each triggered event. This chapter describes the design of the ANITA-3 Prioritizer and gives an overview of its performance.

9.1 The Graphical Processing Unit

ANITA-3 flew a "ruggedised" GPU designed for operation in extreme environments, the Condor 3000x manufactured by Tech Source [69]. The GPU consists of multiple cores, each of which functions somewhat like a regular Central Processing Unit (CPU). The cores contain memory registers, which they can access almost instantaneously and the facility to perform mathematical operations on the

data they contain. The cores are connected to on-chip memory with a hierarchy of caches, from small, low latency caches to larger higher latency caches. Beyond the caches lies the global GPU memory, the largest and slowest memory available to the GPU. These similarities mean many of the strategies for writing fast GPU code are the same as writing fast CPU code.

I used of the `OpenCL` Application Programmer Interface (API) to write the Prioritizer GPU code, and to interface the flight CPU and GPU operations (e.g. transfer data from CPU to GPU and back again). In `OpenCL` the GPU code is contained in functions called kernels. Each line of kernel code is executed by the GPU a predetermined number of times in quick succession, and is divided up amongst the GPU cores in an assignable way. Because each line of code is executed in parallel, the GPU makes for fast computing when the operations on data are highly vectorized.

9.2 ANITA-3 Prioritizer Algorithm

The ANITA-3 Prioritizer was designed to apply the ANITA analysis methods to incoming events in real time. The reconstruction methods described here are very similar to those used in the Angular Resolution calibration in Chapter 8. The workload was split between the CPU and GPU with all the interferometry done by the GPU.

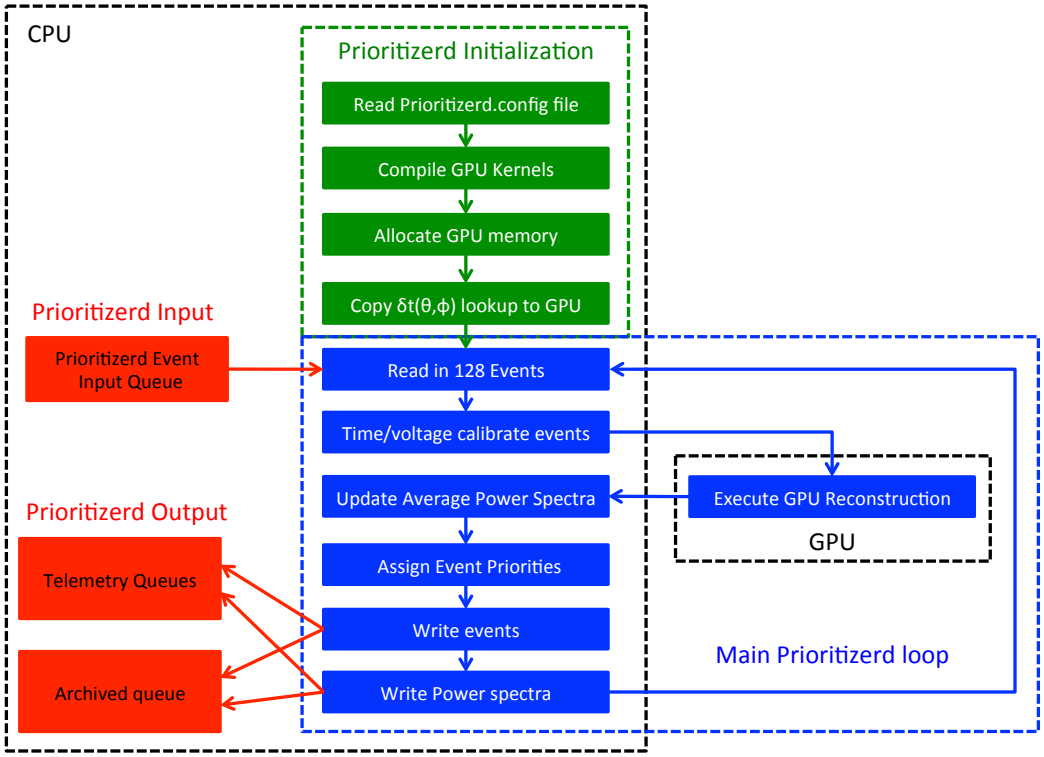

Figure 9.1: Flow chart showing the Prioritizer functionality. The GPU reconstruction is described in Section 9.2.1.

Figure 9.1 shows the division of labour between the CPU and GPU in Prioritizer. On startup, Prioritizer read in configuration files, compiled the GPU kernels, allocated regions of GPU memory, and copied a set constants (the δts between antennas as a function of Azimuth and Elevation) onto the GPU memory.

Some of the constants used to prioritise events could be set remotely. Settings changes would take effect when Prioritizer was restarted (the process could be remotely killed).

Once inside its main loop, the Prioritizer waited for at least 128 events in its input queue and read those events into memory. It then applied timing and voltage calibrations to the data. The calibrated event data were then copied to the GPU, which calculated power average power spectra and performed an interferometric reconstruction.

Data from the event reconstruction, the image peak value, Azimuth, Elevation, and Hilbert Peak were recorded for each event. The image peak and Hilbert en-

velope peaks were used to assign the event priority (Section 9.3). The Prioritizer also made power spectra for each channel to search for spikes indicative of radio communication Carrier Waves (CW). The spectra were averaged over one minute and transmitted to the ground.

9.2.1 GPU Reconstruction

The GPU made an interferometric map of the triggered Φ-sectors for each event and recorded the peak value and direction. The time offsets implied by the peak direction were then used to create a coherently summed waveform from neighbouring Φ-sectors. The Hilbert envelope of the coherently summed waveform then was found and its peak value recorded.

This process was divided amongst a series of GPU kernels and `OpenCL` functions to transfer data between the CPU and GPU. The `OpenCL` API puts the GPU kernels and data copying operations in a in a First-In-First-Out (FIFO) command queue. Dependencies of commands on one another can be encoded into the queue so that every compute units on the GPU is in use at all times, unless every commands in the queue is waiting for a currently running or queued command. The kernels and copy steps for the Prioritizer GPU reconstruction are shown in Figure 9.2.

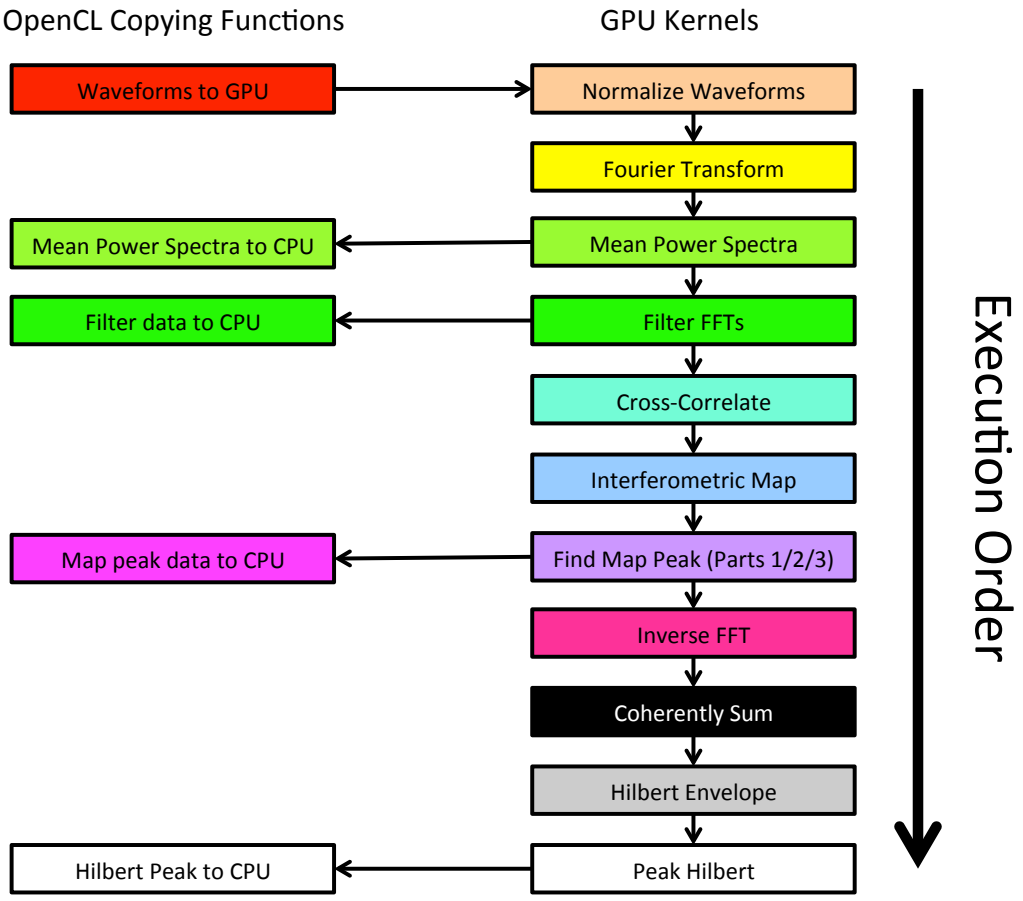

Figure 9.2: GPU kernel execution order, lines indicates order of execution.

9.2.2 GPU Event Rate

Prior to the hardware integration of ANITA-3, there was the possibility that new electronics could result in a multi-hundred Hz trigger rate. Once the functionality of each kernel was confirmed, significant effort went into making sure that the GPU code would be able to keep up with that event rate. A low overhead C profiling library was used to record time stamps between each step in the reconstruction. Figure 9.3 shows the evolution of the time required for each of the GPU operations over a few months in mid-2014. These steps do not exactly match the algorithm used in flight, shown in Figure 9.2.

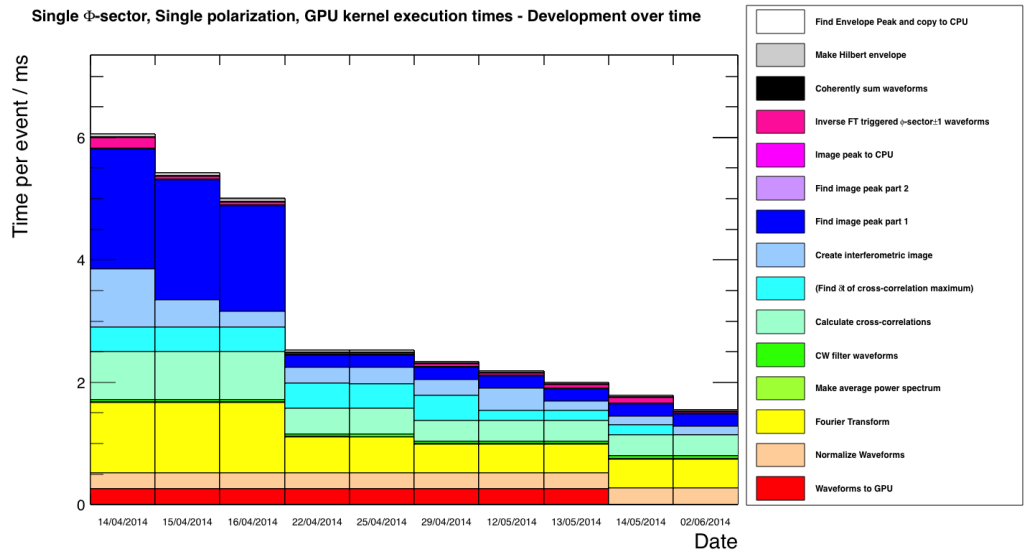

Figure 9.3: Stacked histogram of the time required to perform each step of the GPU calculation during a particular development window when functionality changed little.

Typically development work was focused on one operation at a time, for example, the improvements made between the first three columns in Figure 9.3 come from the "make image" kernel. Similar to CPU code optimisation, the strategy for GPU code optimisation lies in organising the code and data so that the sequentially executed instructions access sequential elements of memory. This maximises cache coherence and enables burst reading and writing from memory. This was the strategy used for almost all the gains shown in Figure 9.3.

The apparent delay from data transfer from CPU to GPU was hidden with asynchronous memory transfers (columns 8-9 in Figure 9.3). This was done by doubling the event data regions of GPU memory. The CPU copied the event data into region 1 while the GPU did the reconstruction on the event data in region 2, and vice versa. At other stages in improvement functionality changes allowed entire kernels to be removed.

Unlike the offline analysis which reconstructs 360° in azimuth, the GPU only reconstructed the L3 triggered Φ-sectors. Figure 9.3 shows the GPU reconstruction time required per event (per polarisation) for a single Φ-sector. Figure 9.4 shows that the GPU execution time scaled linearly with the number adjacent L3 Φ-sectors.

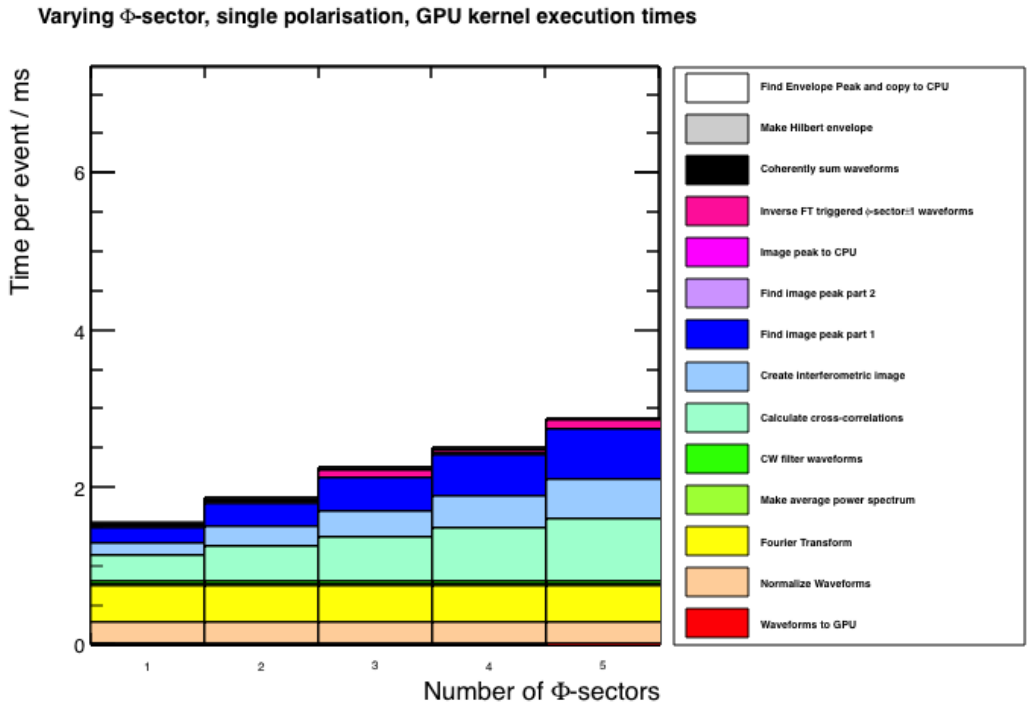

Figure 9.4: Time required to do the GPU interferometric reconstruction as a function of number of L3 triggered *phi*-sectors.

Since the initial steps in the reconstruction used all channels per polarisation, the time required for these steps do not change. However, the later kernels, starting with the cross-correlation kernel, required a linearly increasing time with the number of Φ-sectors in the reconstruction. The rate per polarisation per Φ-sector goes from 1 to 5, the rate reduces from 645 Hz down to 347 Hz per polarisation. The design of the ANITA-3 trigger meant that two neighbouring Φ-sectors were always present in an RF trigger. For a typical event with two L3 triggered Φ-sectors, the GPU interferometry rate was 536 Hz per polarisation.

9.3 Priority Determination

The Prioritizer assigned a number from 1 to 9 to each event. For RF triggered events priorities 1-6 were assigned using the peak of the interferometric map and the peak of the Hilbert envelope of the coherently summed waveform. This is described in Section 9.3.1. The other priorities, 7-9, have special meanings explained in Section 9.3.2, 9.3.3 and 10.5.2.

Table 9.1: Priority meanings.

Priority	Meaning
1 - 6	Mapped from Image Peak & Hilbert Peak
7	Prioritizer queue too long
8	Strong CW flag raised
9	Surf Saturation flag

9.3.1 Priorities 1-6

Priorities 1-6 were determined with a series of nested ellipses in Image Peak / Hilbert Peak parameter space. The ellipses were centred at the origin with the major axes aligned with the Image Peak / Hilbert Peak parameter space. Priority 1 was for any event outside the outermost ellipse. Priority 2 was for any event outside second outermost ellipse, but inside the Priority 1 ellipse. This nesting continued down to priority 6 which was assigned to any event inside the innermost ellipse. The default mapping is shown in Figure 9.5.

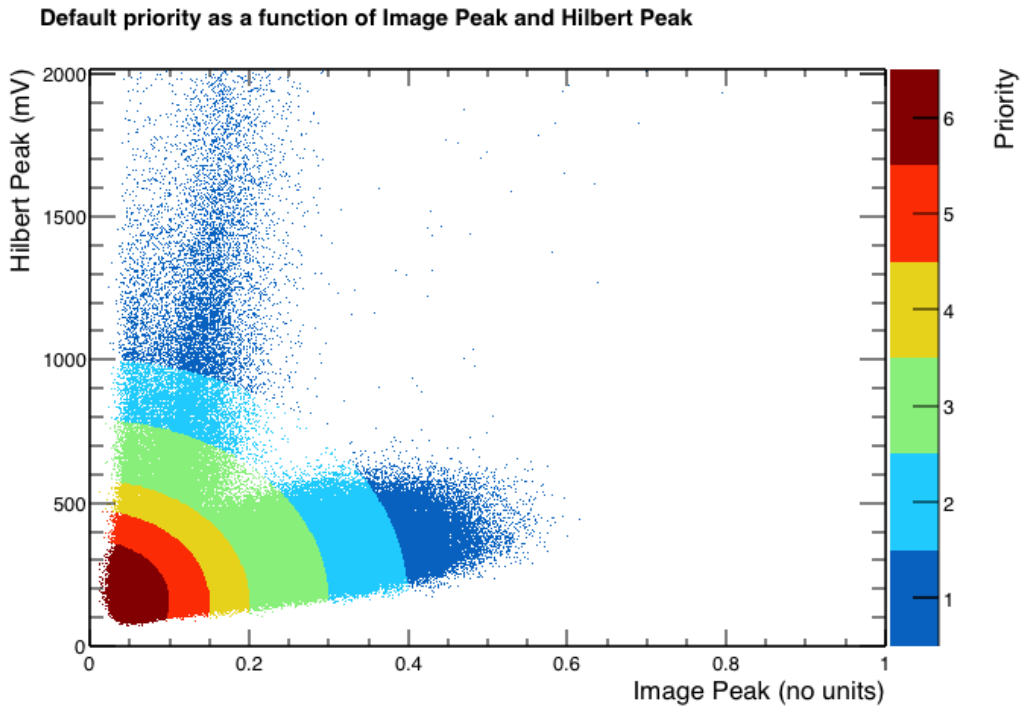

Figure 9.5: Events from a portion of the flight showing the initial Prioritizer settings.

The initial settings were tuned using an efficiency scan during the pre-flight calibration. The mapping of these variables to priority was set up to be remotely

configurable in flight, and they were altered in response to the environment. The population of events extending along the y-axis in Figure 9.5 are a category of payload noise events called self triggered blasts. An example self triggered blast is shown in Figure 9.6.

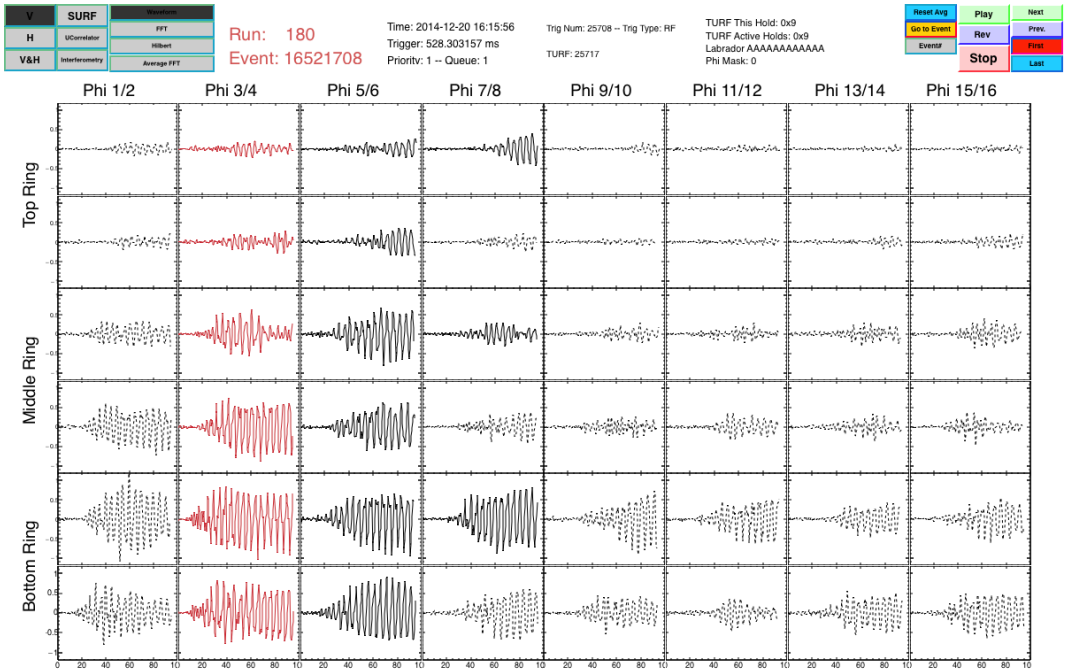

Figure 9.6: Example of a self triggered blast event, which received priority 1.

These are triggered by something on the lower part of the payload, as can be seen by the large difference in amplitude between the bottom and top rings. These events contain a lot of power but do not look very coherent to the interferometric method, which delays between channels from a plane wave passing the antennas.

In response to this class of background receiving high priority the priority boundary ellipses were reassigned. The priority of some events in the second half of the as a function of Image Peak and Hilbert envelope are shown in figure 9.7.

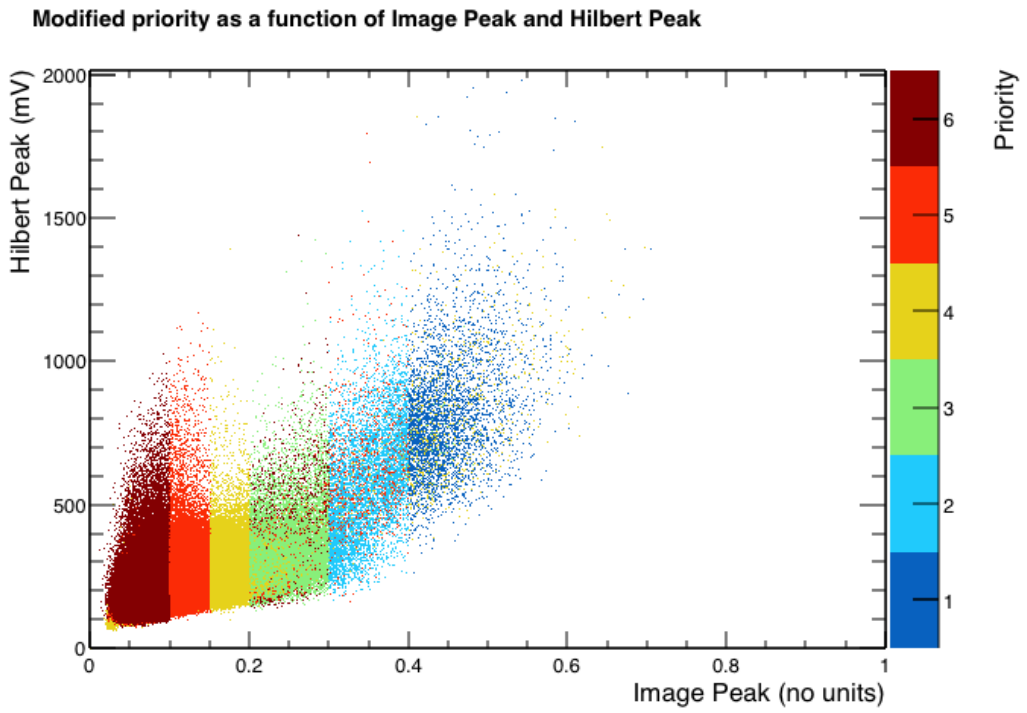

Figure 9.7: The priority of a sub-sample of events from the second half of the flight. Additional parameters were also used to reduce the number of high priority events causing the overlap in the priority values in the parameter space. See text for details.

As shown in Figure 9.7, the priority boundaries were set almost parallel to the Hilbert Peak axis. This meant that events with a high Hilbert envelope peak, but low coherence were assigned a low priority. The Prioritizer also had the facility to promote or demote events between priority groups based on the elevation of the interferometric map. Later in the flight, the Prioritizer was configured to demote events coming from very high or low elevations. This is described in more detail in Section 9.4.1.

9.3.2 Priority 7 - Prioritizer Queue Too Long

If the queue of events waiting to be reconstructed by the Prioritizer was above a threshold queue length, then the Prioritizer skipped the reconstruction and gave all events in the queue priority 7. At the beginning of the ANITA-3 flight the proximity to McMurdo base, a very noisy radio source, created large fluctuations in event rate. These conditions allowed a measurement of the speed of the Prioritizer in flight.

Figure 9.8 shows the event rate and rate of Priority 7 events as a function

of time in the vicinity of McMurdo. Although the GPU throughput calculated in Section 9.2.2 was approximately 250 Hz, Figure 9.8 shows that the total Prioritizer throughput is significantly lower.

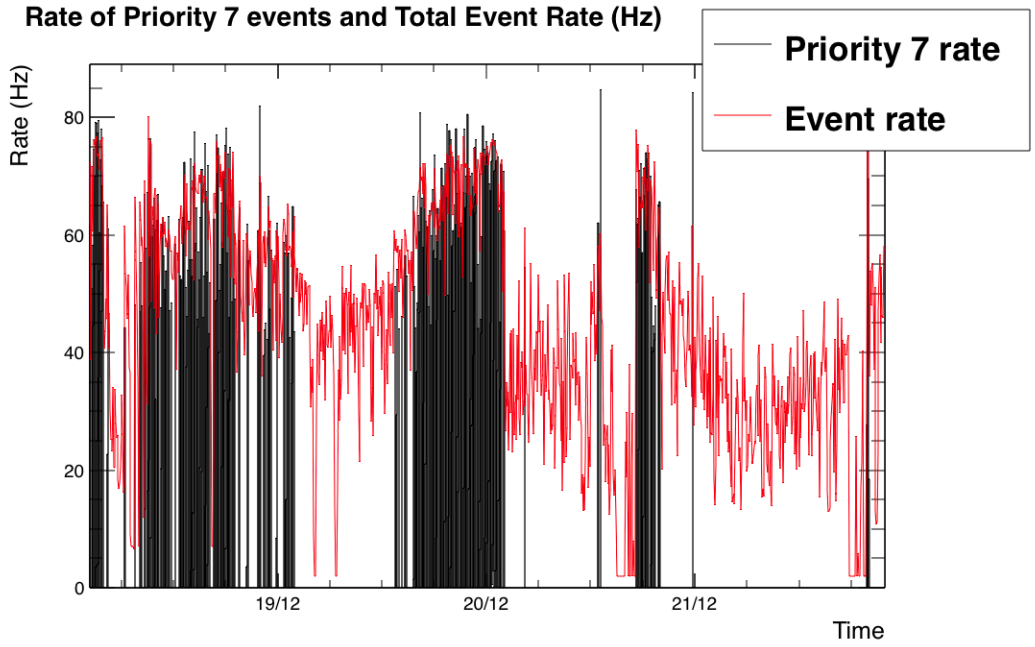

Figure 9.8: `Prioritizerd` was unable to keep up when the event rate above $\sim$ 60 Hz for extended periods.

Figure 9.9 shows a close up of one of regions with many priority 7 events.

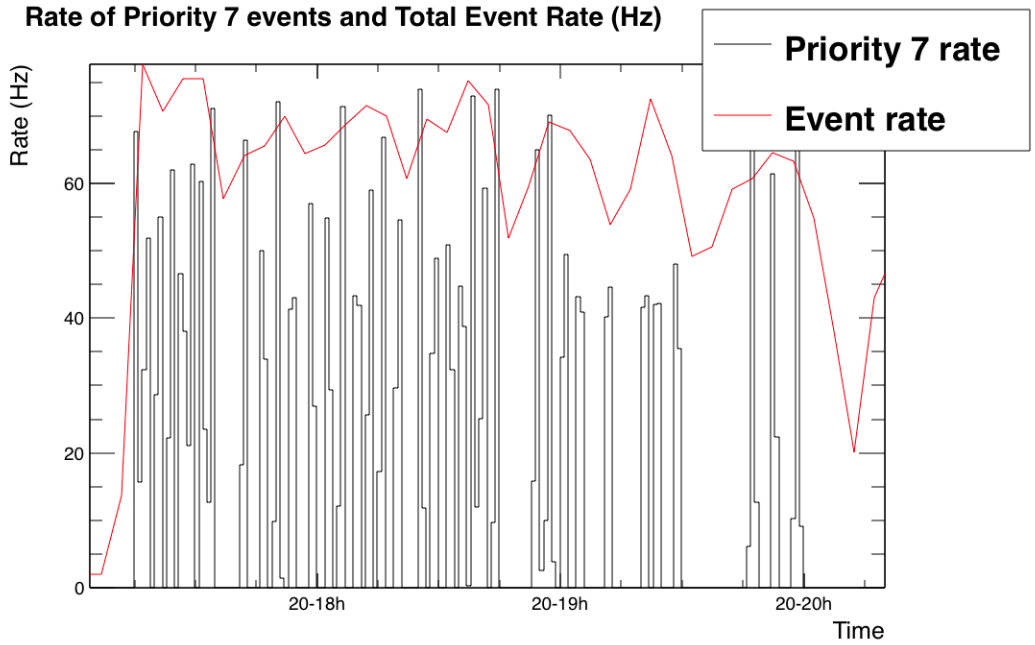

Figure 9.9: Over short timescales the spikes in Priority 7 events are caused by the queue being emptied completely and the delay required to fill it up beyond the Priority 7 threshold.

At 60 Hz the Prioritizer struggled to keep up with the event rate. This was not much of an issue for ANITA-3 since the nominal event rate during the flight was lower than 50 Hz.

The Prioritizer reconstruction used the CPU to perform the timing calibration of the waveforms before sending to the GPU to do the interferometry. This implies that the CPU based portion of the Prioritizer is a bottleneck. In future versions of the Prioritizer, the throughput rate could be increased by doing the various steps in the event timing calibration on the GPU rather than the CPU.

9.3.3 Priority 8 - Strong CW

Satellite communication with narrow band Carrier Waves (CW), is a coherent source of power, which can create large peaks in an interferometric map. The Prioritizer kept track of the power spectrum in each channel. Although the functionality to filter channels in the Fourier domain was present (Figure 9.2), the algorithm to assign which frequencies should be filtered was not finished prior to flight. The CW handling functionality present in the flight was much more basic. If the power

spectral density of any channel was above a (configurable) threshold, the event was assigned priority 8. This approach to CW handling was too simplistic to handle the near constant CW background from satellites (and from bases when nearby) during the flight.

Figure 9.10 shows the average power spectral density in channel 1TH for a portion of the flight.

The two large spikes at 260 MHz and 370 MHz are from geo-synchronous satellites which appear just above the horizon to the north of ANITA.

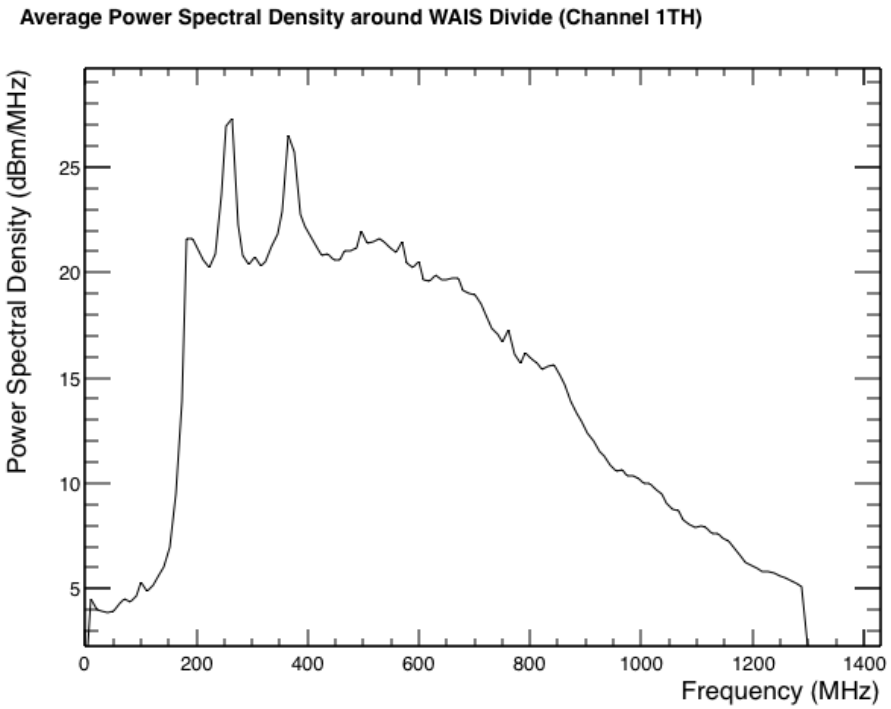

Figure 9.10: Single channel average power spectral density from around WAIS divide showing peaks from two separate satellites.

Because some sources of CW, such as the 260 MHz peak, were omnipresent during the flight, the CW filtering flag would assign almost any event a priority of 8 if it was set too low. During the flight the CW filter threshold had to be set very high to allow a reasonable number of events to receive priorities other than 8. This meant that only very strong upward fluctuations in CW presence were caught by the CW filter. This also meant that events that were full of CW received high priorities. Figure 9.11 shows an example of a priority 1 CW event triggered by a satellite.

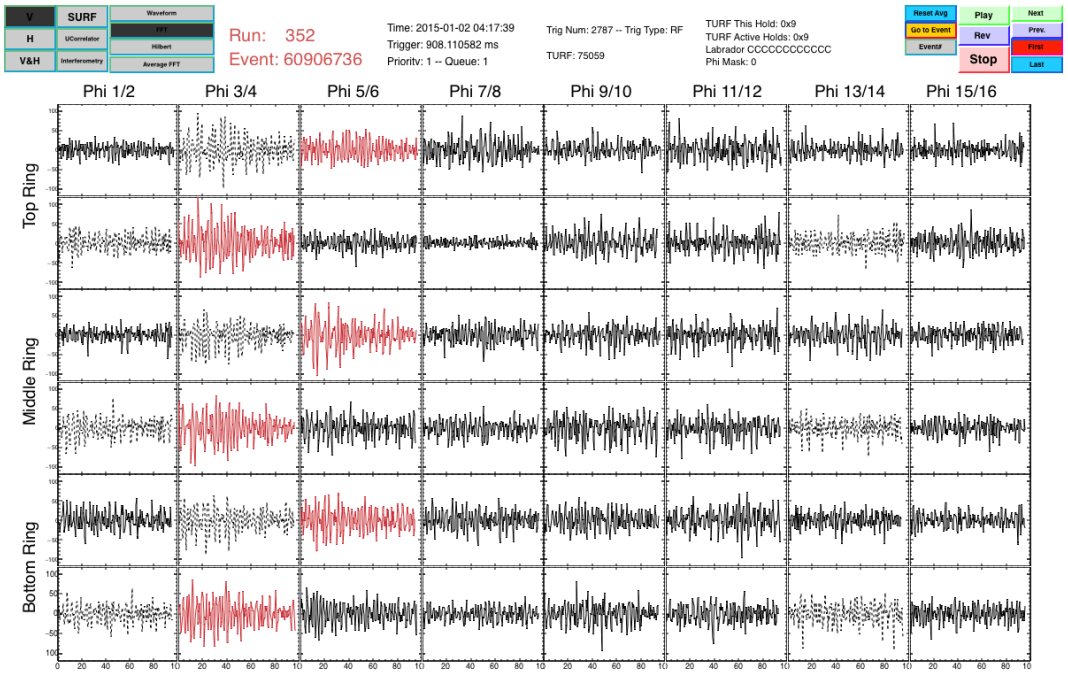

Figure 9.11: Example of a priority 1 event from around WAIS divide triggered by a satellite.

Future versions of the Prioritizer will need improved CW handling. This should be simple to achieve using functionality already present in the GPU code. Continually notching the satellite frequencies in the Fourier transforms of the waveforms at common satellite frequencies prior to interferometry would remove the corresponding peaks in the interferometric map. These notches could be configured remotely in a similar manner to the priority mappings described in Section 9.3.1.

9.3.4 Priority 9 - SURF saturation

Another class of background events occurs when the input voltage goes beyond the linear range of the LABRADOR digitizers. This class of bad events, which would seem to contain a lot of impulsive power in one channel were selected by the Prioritizer using a simple check on the maximum or minimum voltage. Events with a maximum absolute voltage greater than 1000 mV were assigned priority 9.

9.4 WAIS Pulse Priority

The Prioritizer classification of WAIS pulses gives an indication of its treatment of impulsive signals. The environment around WAIS divide was much quieter in terms

of radio noise than the pulser at LDB, which is close to McMurdo.

9.4.1 Reconstruction accuracy

Figure 9.12 shows the resolution of the WAIS pulser events in payload azimuth, when combining the Prioritizer map peak ϕ direction with the GPS information.

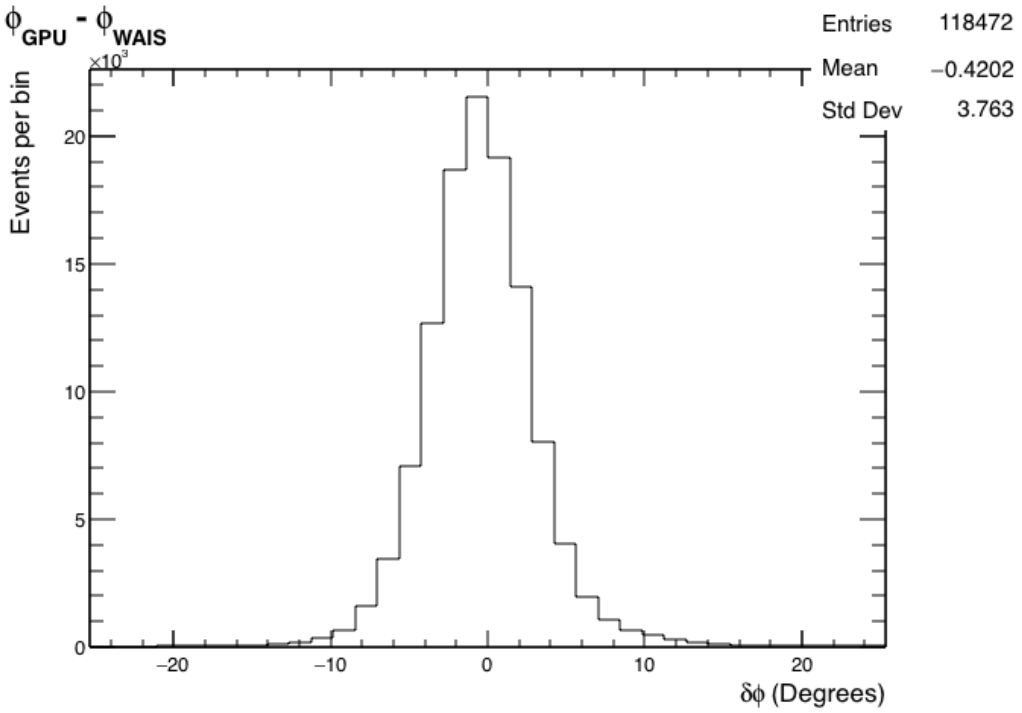

Figure 9.12: The Prioritizer picks out the WAIS pulser azimuth with an angular resolution of a few degrees.

Figure 9.12 shows that the GPU successfully picked out the source location for almost all WAIS events. The resolution is less good than the offline reconstruction, since the timing and antenna phase centre position calibrations were not finalised prior to flight. The feed positions from the ANITA design documents were taken as the antenna phase centre positions. This is the reason for the lower resolution than obtained with the offline software.

Figure 9.13 shows Prioritizer elevation resolution for the WAIS divide pulser.

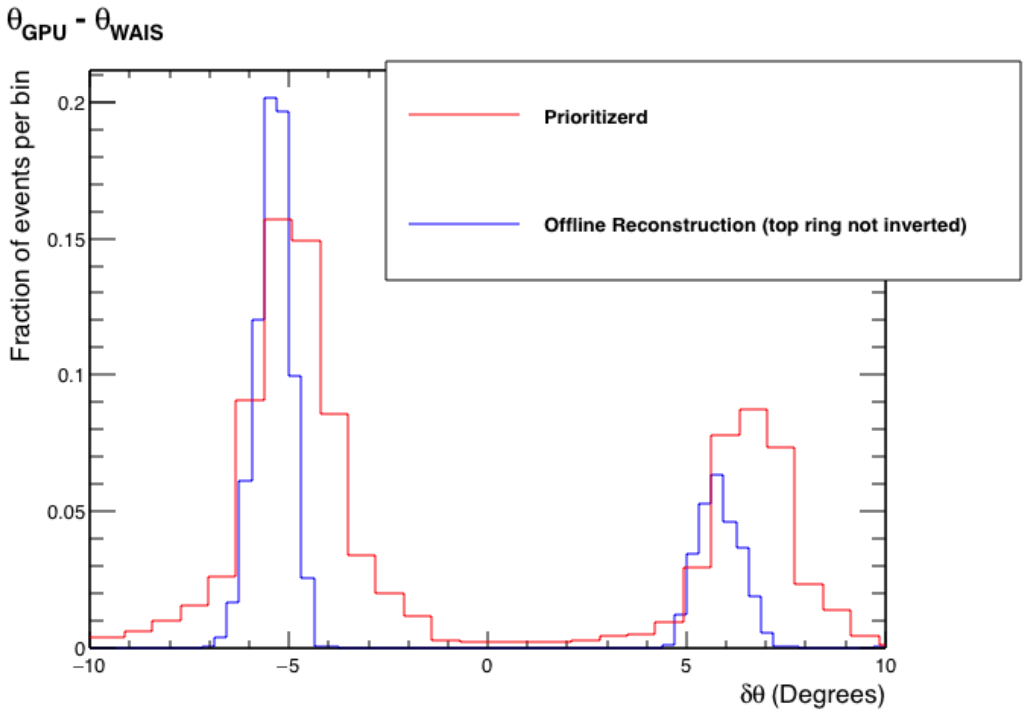

Figure 9.13: The Prioritizer has a varying offset in elevation from the true WAIS position. This is discussed in the text.

As mentioned in chapter 5, the top ring of antennas was installed upside down relative to the middle and bottom rings. This means that during analysis, the waveforms from the top and bottom rings must be inverted in software. The Prioritizer was tested in the lab prior to flight using data from pulses injected into the amplifiers directly behind the antennas. For this data set, the top ring channels should not be inverted. There was a compile time flag to enable the inversion which I forgot to turn on prior to flight. This caused a double peak in elevation resolution for all sources, including the WAIS pulser, which was rather confusing when looking at telemetry during flight. Figure 9.13 also shows a subset of the pulses reconstructed offline with the top ring software inversion disabled, showing the same trend as the Prioritizer reconstruction. An example of a single event with and without the top ring inversion is shown in Figure 9.14.

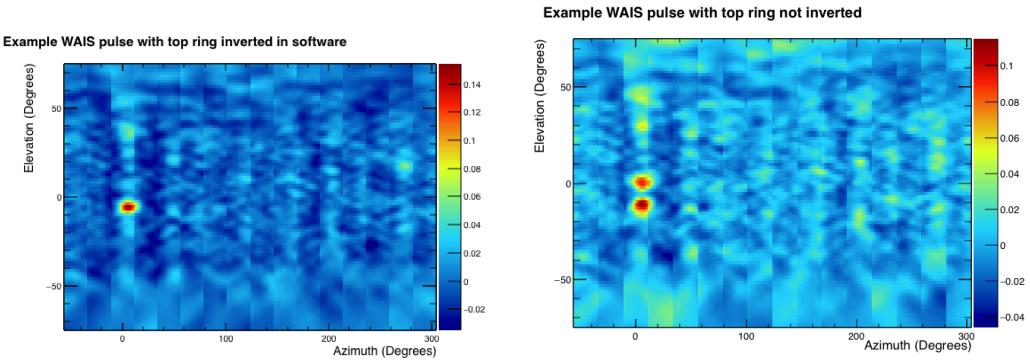

(a) Top ring channels inverted

(b) Top ring channels not-inverted

Figure 9.14: An example WAIS pulser event reconstructed with and without the top rings inverted. Thermal noise on top of the double peak in the right plot created causes the double peak in the $\delta\theta$ distribution (Figure 9.13).

The Prioritizer had a setting to allow promotion or demotion of events based on elevation angle. The design idea was to reduce the priority of events which can't be neutrinos as they reconstruct above the horizon. This bug caused the elevation angles assigned to all events to be distributed either side of the true value, making this shift of event priorities unreliable when near the horizon. In future versions of the Prioritizer, the compile time switch that allowed this failure mode will be altered to be remotely configurable, like many of the other Prioritizer settings.

9.5 Comparative Priority of WAIS Pulses

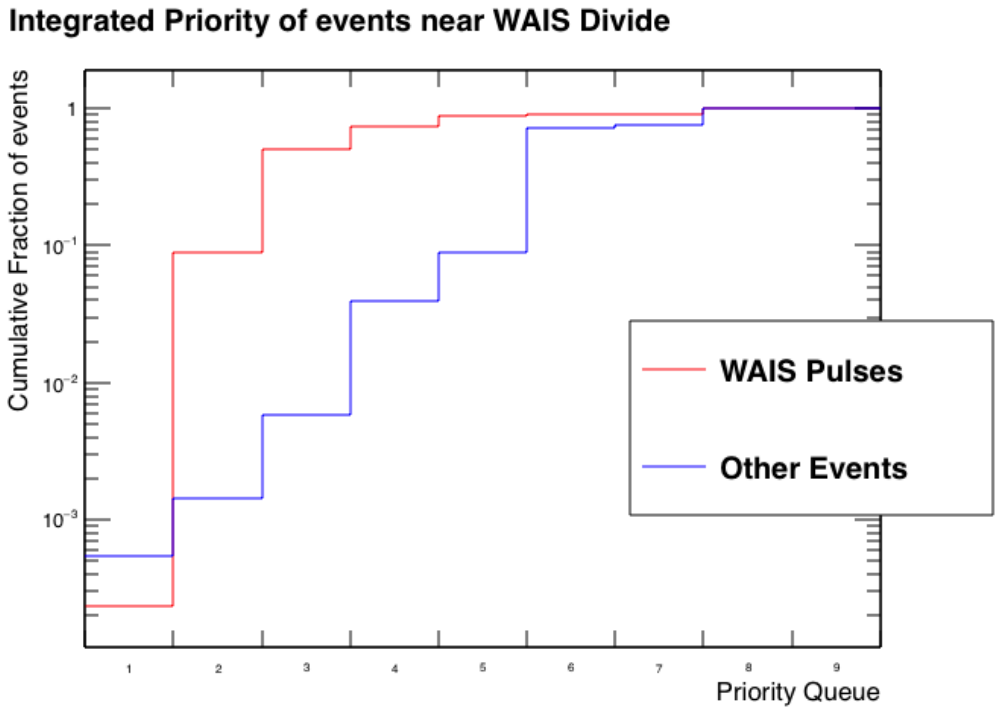

Figure 9.15: Comparison of the priority of WAIS pulses and other events around WAIS divide.

Figure 9.15 shows the how the WAIS divide pulser events and all other events from that region were classified. There are around 120,000 WAIS pulser events and 7 million non-pulser events. The value in each bin is the fraction of events assigned to that queue number or lower (which is a higher priority). The pulser distribution rises much earlier for the WAIS pulses compared to the background, more than half of the pulser events in priority queues three or lower. Unfortunately, this success did not extend to priority 1 bin. Other than about 30 WAIS pulses, everything in the priority 1 bin contained satellite CW noise events.

9.6 Summary

ANITA-3 was the first iteration of ANITA to use a GPU to perform real time analysis on the incoming data stream. The Prioritizer was flown with a bug, as it did not invert channels in the top ring. This caused the elevation angles of detected events to be incorrect. (This problem is easy to fix before ANITA-4.)

The functionality could be improved a lot with relatively little effort by adding remotely configurable notches to be applied prior to interferometry, and removing the simple CW threshold flag. A dedicated set triggered blast removal algorithm would also allow both Image Peak and Hilbert Peak parameters to contribute to the priority assignment.

Despite these flaws, the Prioritizer was successful in a number of ways. Firstly, high bandwidth priority was given to WAIS pulser events that background events in that region of Antarctica for two of the three highest priority bins. Secondly, enough of the parameters were remotely configurable to allow the priority mapping to adapted to noisy environment around McMurdo. Thirdly, the Prioritizer gave an azimuth resolution of 3.7°, which is significantly higher resolution directional information than anything available else during the flight. Similarly good elevation will be available in elevation after a simple bug fix. An additional possibility for ANITA-4 would be possible to combine the map peak ϕ position with heading information to raise or lower priorities of events based on source position in azimuth. For example, this could be used to reduce the priority of all events coming from a base as ANITA passes by.

Chapter 10

A Search for Ultra-High Energy Neutrinos and Cosmic Rays in the ANITA-3 data set

This chapter presents my search for ultra-high energy cosmic rays and ultra-high energy neutrinos in the ANITA-3 data set.

As discussed in Chapters 4 and 5, neutrino signals are expected to be impulsive and mostly vertically polarised. Cosmic ray events are impulsive and primarily horizontally polarised (the exact polarisation angle depends on the angle of the geomagnetic field).

The strategy for the analysis is to remove the two major sources of background, which are thermal noise events and anthropogenic signals. Thermal noise events are characterised by low power and coherence between channels. Anthropogenic events come from a relatively small regions of human activity since Antarctica is mostly desolate. First I develop data and event quality cuts to remove known types of bad events. Then I develop cuts to remove thermal noise events. Finally I develop cuts to remove the anthropogenic sources of background by grouping surviving events together on the continent. Isolated events that are sufficiently separate from sources of man-made noise are considered in the signal box.

10.1 Training Data

To develop cuts I created three sub-samples of the ANITA-3 data.

- The set of Minimum Bias (MB) triggers. The flight computer and GPS unit were set to issue a MB trigger at a rate of 1 Hz during the flight. These events contain no impulsive physics data, but they do provide information about the constant backgrounds from thermal and man-made noise.
- A sub-sample was constructed from 10% of the ANITA data set. Groups of 500 consecutive events were selected in each run, with a Poisson distribution gap with mean 4500 between each group. This sub-sample contains information about upwards fluctuations in backgrounds that trigger the instrument.
- The set of WAIS pulses. I used these events as a signal-like sample to train cuts.

10.2 Blinding

A decision was made by the collaboration to blind the neutrino search channel (impulsive vertically polarised (VPol) events) but not the cosmic ray search channel (impulsive horizontally polarised (HPol) events), as any measurement of cosmic rays is unlikely to contain new physics.

I blinded the VPol search by inserting some "fake" VPol impulsive events into the data set. I decided to use pulser events from WAIS divide with the polarisations swapped, rather than the VPol pulses from LDB because of the potential for CW contamination from McMurdo and other nearby bases. The total number of inserted events was between 10-15, selected by a random number generator and unknown to me.

To insert the pulses, the remaining 90% of the data not used for training cuts was divided into N segments. A Minimum Bias event chosen at random from each segment was overwritten with a inserted event. Not adding extra impulsive events to the 10% data set ensures that any cuts developed to remove background are not trained on any inserted signal events.

10.3 Software Frequency Notches and Band-Pass Filters

Human radio communication Carrier Wave (CW) frequencies are a major source of background for ANITA. CW creates peaks in the interferometric map that dominate over the thermal background. CW is narrow band and can be removed by adding notches in the frequency domain. Neutrino and cosmic ray signals are expected to be impulsive, and therefore broadband, and so will still point in the arrival direction after some amount of power is removed.

To select the frequencies to notch I reconstructed the sub-samples of the ANITA data and looked for structure in the distribution of directions from the interferometric reconstruction. If dominated by pure thermal noise, then the Minimum Bias sub-sample should point in all directions.

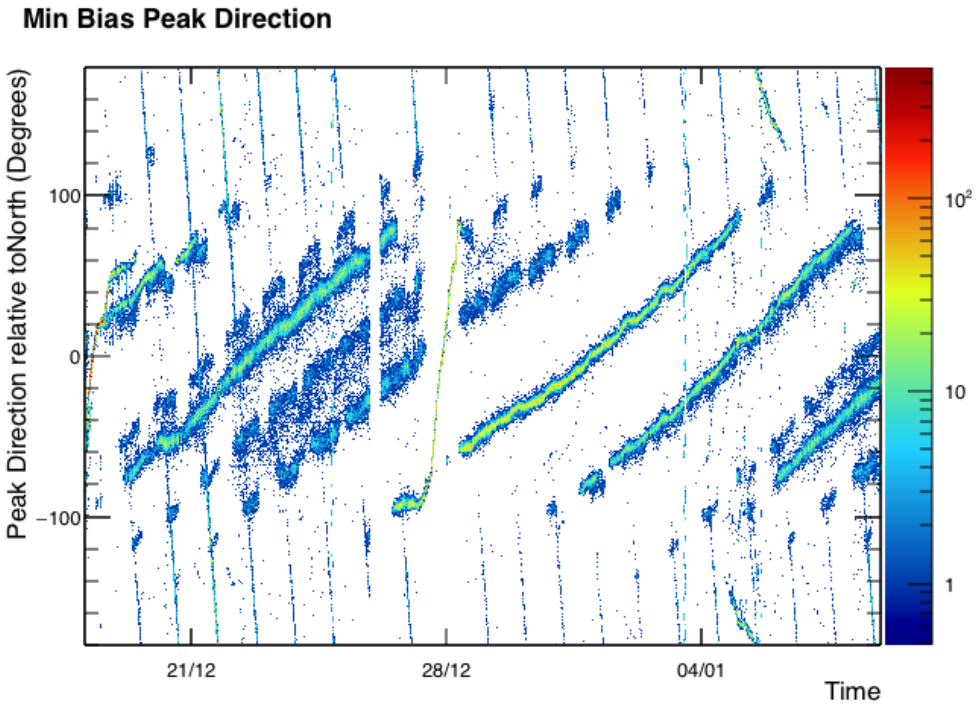

(a) Distribution of ϕ of interferometric reconstruction relative to north, $-90°$ is west,, $90°$ is east. No filtering is applied prior to reconstruction.

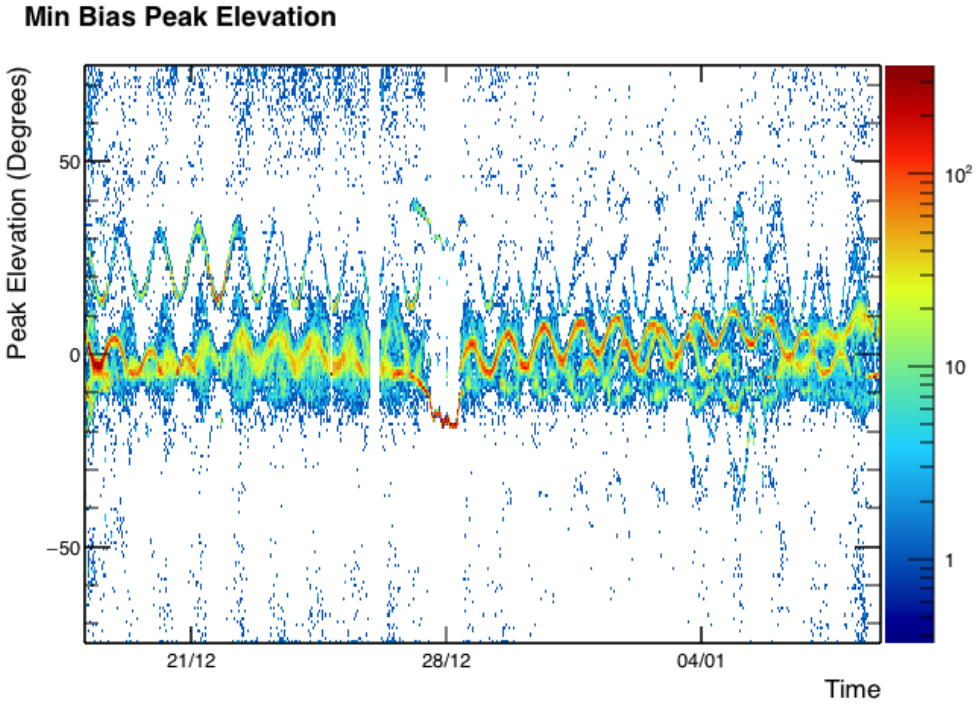

(b) Distribution of θ of interferometric. Positive θ values are above the payload, negative θ is below. At the ANITA float altitude the horizon is at $-6°$, which means that most events are above the horizon.

Figure 10.1: With no filtering applied the brightest point in the interferometric map for each event comes from satellites just above the horizon, which are present during the whole flight.

Figure 10.1 shows the direction of the interferometric map peak of MB events as a function of time during the flight. With no frequencies filtered, long streaks appear from West to East, centred around peak heading of 0 in Figure 10.1a. These are due to satellites to the north of ANITA. These streaks match up with the oscillations in the θ distribution (Figure 10.1b) just above the horizon. Figure 10.2 shows the power spectral density for a single channel for a single run during the flight. As the payload rotates each channel is exposed to the satellite CW at 260 MHz and 370 MHz. I removed all power in these frequencies before cross-correlating the channels to remove these large spikes in the power spectrum.

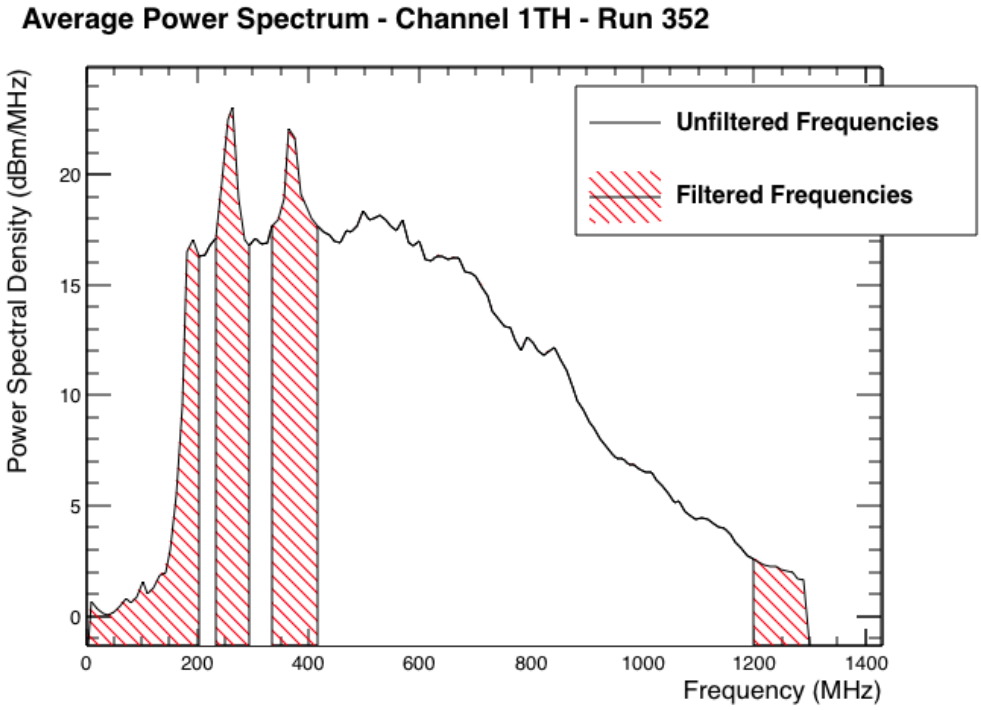

Figure 10.2: Notches and band passes applied to remove satellite background. Slashed red lines indicated filtered frequency bins.

.

I applied a notch from 234 MHz to 286 MHz to remove the peak centred on 260 MHz. I applied a notch from 344 MHz to 410 MHz to remove the peak centred on 370 MHz. I extended this second notch up to 410 MHz to catch intermittent satellite CW around 400 MHz. Finally, I added a band-pass filter around the ANITA frequency band from 200 MHz to 1200 MHz to suppress out of band noise. These bands removed all power in the given frequency ranges.

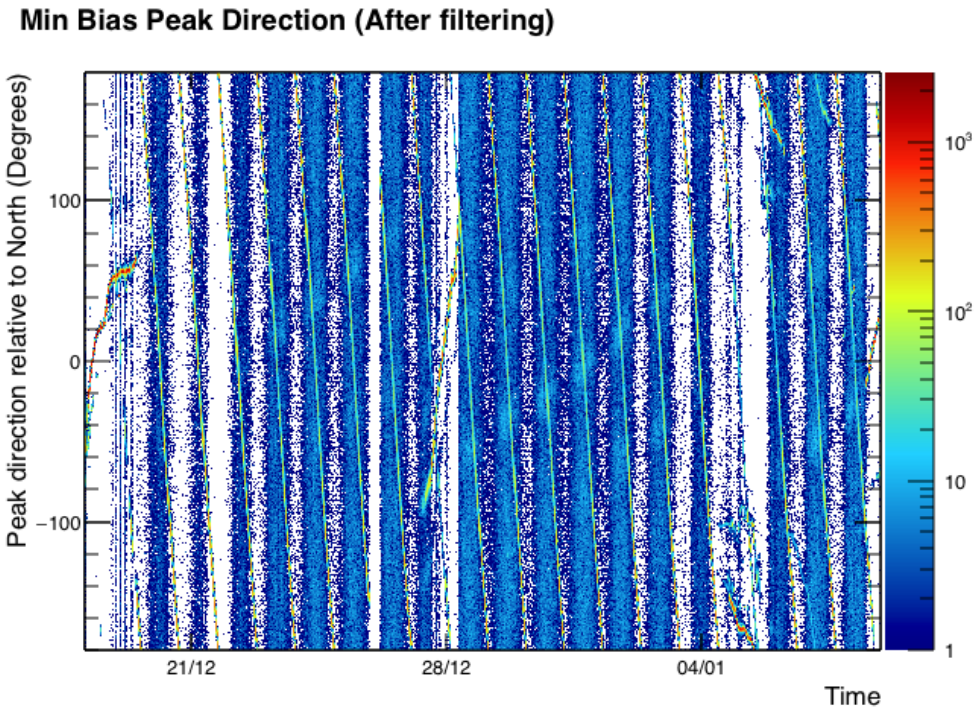

(a) Distribution of ϕ of interferometric reconstruction relative to north, $-90°$ is west, $90°$ is east. The frequency filtering described in the text is applied prior to reconstruction

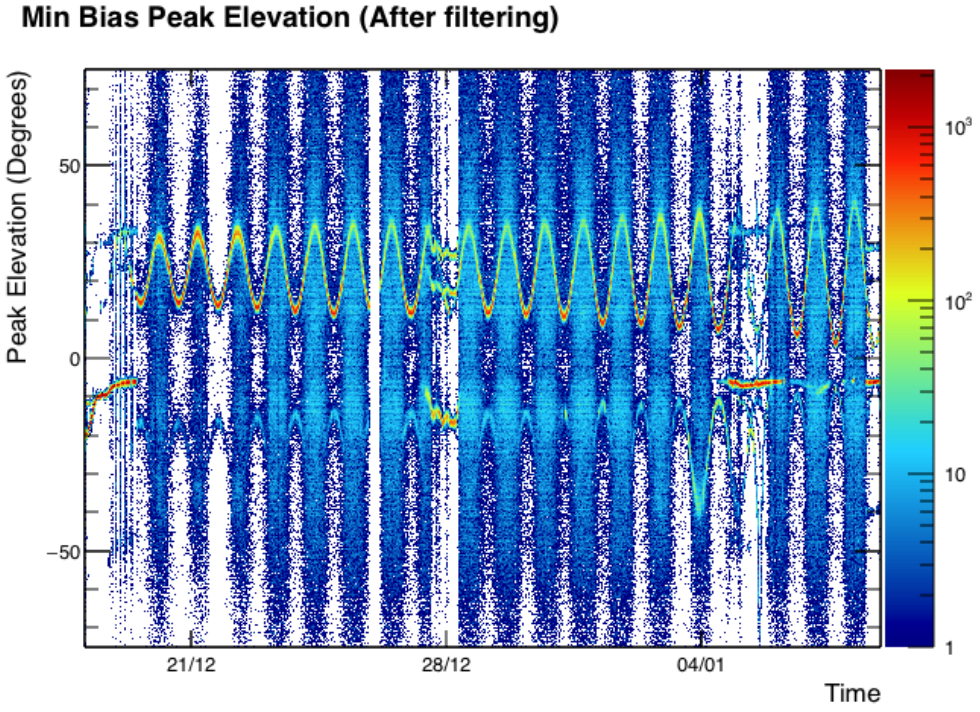

(b) Distribution of θ of interferometric reconstruction as a function of time. Positive θ values are above the payload, negative θ is below. At the ANITA float altitude the horizon is at $-6°$, which means that most events are above the horizon.

Figure 10.3: (a) and (b) show the ϕ relative to north and θ respectively, with the filtering described the text applied. The remaining structure in the θ, ϕ distributions comes from the Sun, which does not dip below the horizon in the Antarctic summer.

Figure 10.3a and Figure 10.3b show the ϕ relative to north and θ respectively for the Minimum Bias sample of events with the frequency bins highlighted in Figure 10.2 filtered before reconstruction. The only source of structure throughout the whole flight (there is short timescale structure when ANITA passes bases) is the Sun, which can be seen moving at a constant rate in ϕ relative to the payload (a). The Sun and its reflection on the ice can also be seen in the θ (b) distribution.

10.4 Quiet Time

Figure 10.4 shows the interferometric image peak as a function of time during the flight from the 10% data set. Periods when ANITA had bases within its field of view are marked by large increases in the interferometric image peak. In order to develop cuts to remove thermal noise I selected a period of quiet time marked by the box in Figure 10.4.

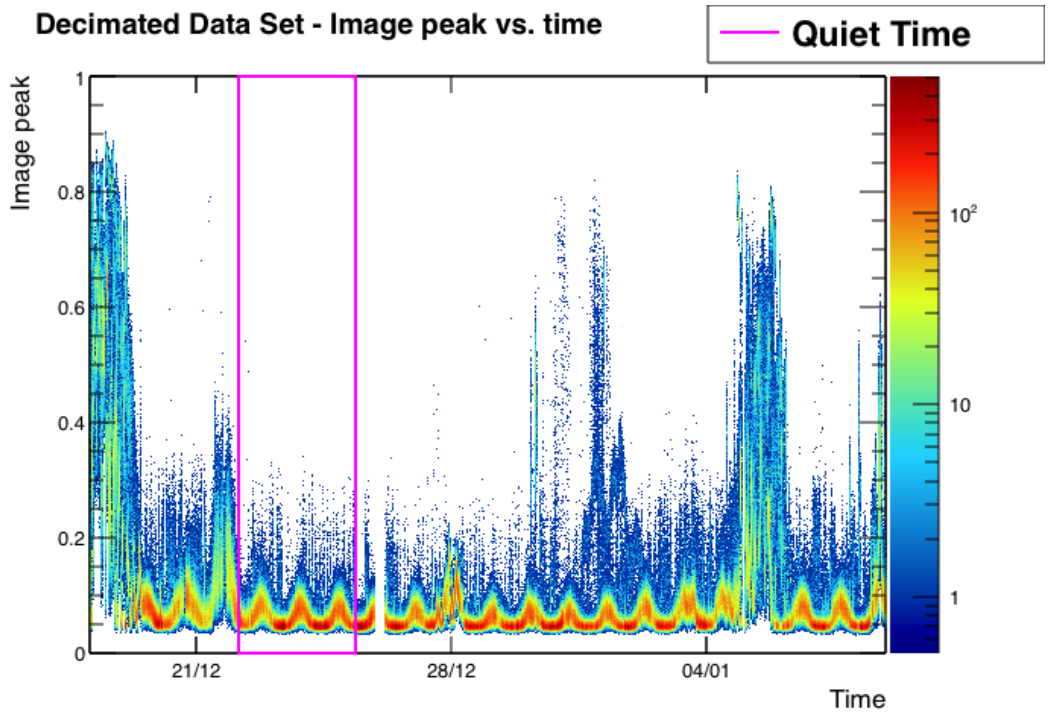

Figure 10.4: Selection of a period of quiet(er) time during the flight, corresponding to 3.25 days.

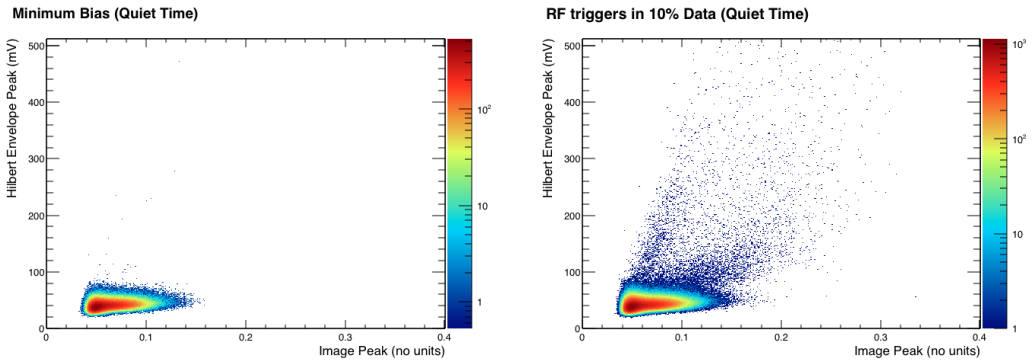

(a) MB events (b) RF triggers in 10% data set

Figure 10.5: Image peak vs. Hilbert Envelope Peak distributions of RF triggers in the 10% data set and MB triggers in the selected quiet time

.

Figure 10.5 shows the image peak vs. Hilbert envelope peak distributions for the MB events and decimated RF triggers during the selected quiet time. The Minimum Bias triggers (Figure 10.5a) from this period are an almost pure sample of thermal noise events. There are a small number of events in the MB sample from this quiet period, which match conditions for an RF trigger but are incorrectly tagged as MB events. These show up as outliers in the Figure 10.5a distribution. This is likely due to trigger bit latching error in the underlying trigger hardware during a high trigger rate.

10.5 Event Quality Cuts

10.5.1 Self-triggered blasts

The majority of events in the 10% data sub-sample (Figure 10.5b) are in the thermal region of the image peak / Hilbert peak parameter space. However, there is an additional population of events with higher Hilbert Peak that extend away from the thermal noise region of the distribution. A population of such events has been found in previous ANITA analyses [63, 10]. These are a type of event called self-triggered blasts. An example of a self-triggered blast is shown in Figure 10.6. For pulser events, like those discussed in Chapter 8, have approximately equal amplitude in all channels as the plane wave passes the payload. The large variation in amplitude the of the events, such as Figure 10.6 suggests the source of these events is near

the bottom of the payload. However, the exact location of the source is difficult to determine as the far-field approximation used in the interferometric reconstruction is not met.

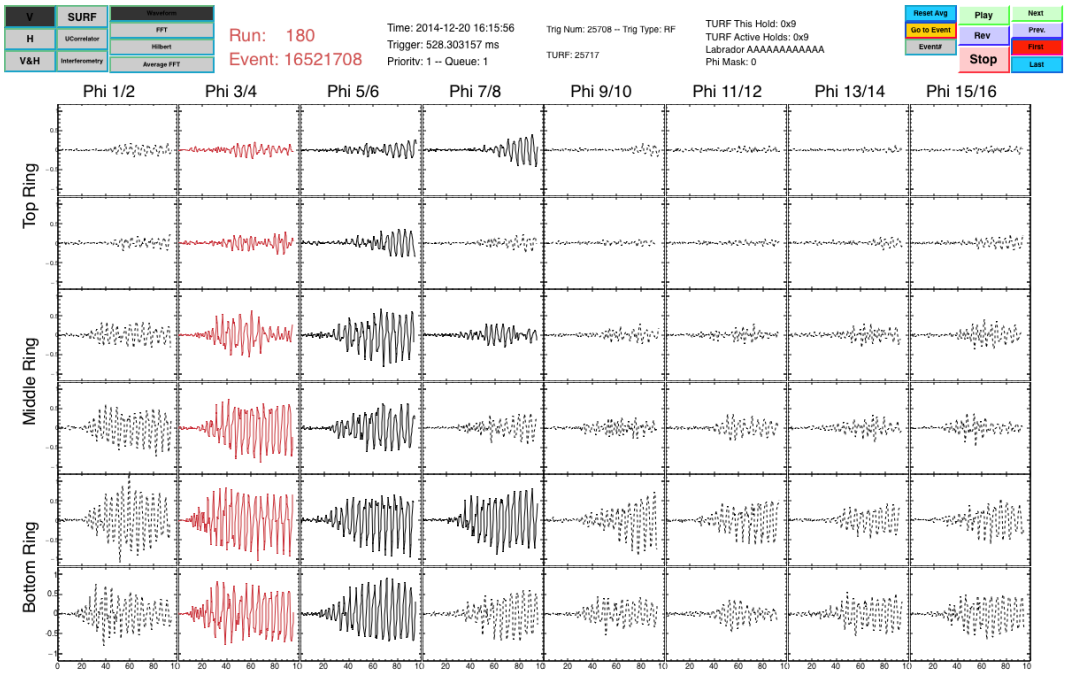

Figure 10.6: Example of a self triggered blast event rendered in `MagicDisplay`.

In order to remove these events I cut on the ratio of the peak-to-peak amplitude in the bottom and top rings,

$$R_{\text{self-triggered blast}} = \max\left(\frac{V^{\phi B}_{\max} - V^{\phi B}_{\min}}{V^{\phi T}_{\max} - V^{\phi T}_{\min}}\right) \tag{10.1}$$

While comparing the peak-to-peak ratios, I exclude channels 8TV, which had an intermittently broken amplifier, and 5TH which had the ANITA Low Frequency Antenna (ALFA) was mixed into it (Section 5.13).

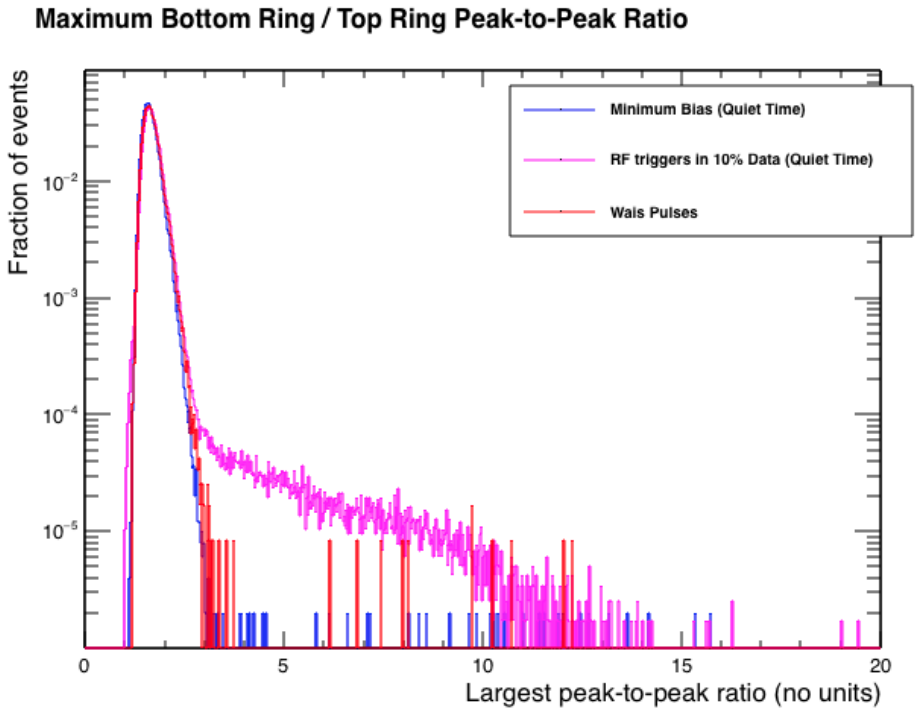

Figure 10.7: Distribution of $R_{\text{self-triggered blast}}$ for the three training data sub-samples.

While examining the low end of Figure 10.7 I noted that there is a shoulder in the RF triggers not present in the minimum bias or WAIS pulses. These are a different class of self triggering where the amplitude of the top ring is always larger than the bottom ring. An example event is shown in Figure 10.8

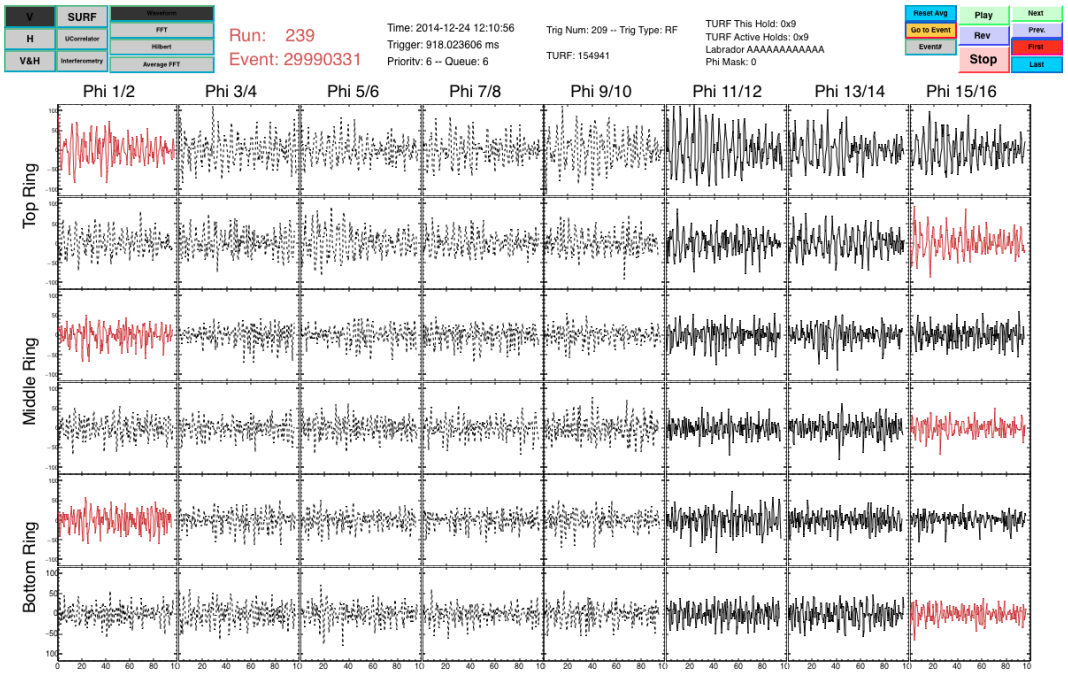

Figure 10.8: Example of an RF triggered with a power excess in the top ring.

In order to remove both these classes of background I remove events with

$$R_{\text{self-triggered blast}} < 1.1 \tag{10.2}$$

$$R_{\text{self-triggered blast}} > 2.8 \tag{10.3}$$

This cut is 99.9% efficient for WAIS pulses and quiet time minimum bias events, 99.1% efficient for the 10% data set in the quiet time.

10.5.2 SURF Saturation

Another class of bad event occurs when the voltage at a particular sample goes beyond the dynamic range of the LABRADOR digitisers in the SURF, called SURF saturation. This leads to apparent spikes in the waveform, which have the potential to add a lot of power to the Hilbert Peak value or distort the interferometric map. (The few WAIS pulse events which fail the self triggered blast cut exhibit this problem). An example is shown in Figure 10.9.

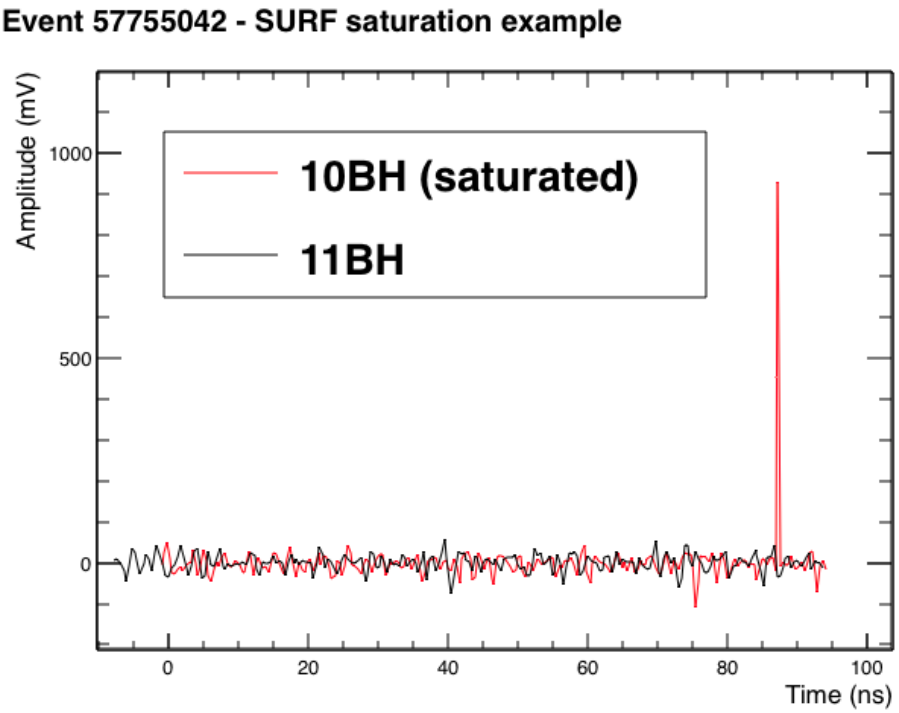

Figure 10.9: Two channels in neighbouring antennas. 10BH exhibits SURF saturation, while 11BH does not. This example shows SURF saturation causing an upward spike, it can also cause negative spikes.

I cut on three variables to remove these events. I find the maximum and minimum voltages ($V_{\max}, V_{\max}$) across all channels. The $V_{\max}$ and $-1 \times V_{\min}$ distributions for the three training data sub-samples are shown in figure 10.10.

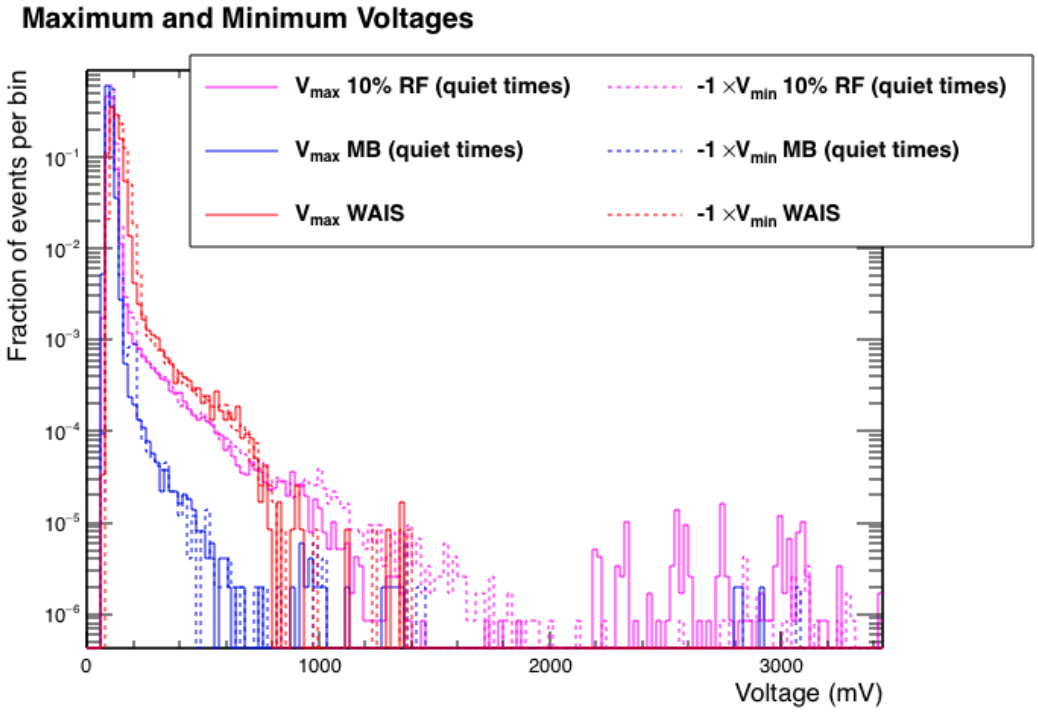

Figure 10.10: $V_{\max}$and $-1 \times V_{\min}$ for each event in the three training data sub-samples.

Since the maximum and minimum voltages follow very similar distributions I also cut on the asymmetry of the maximum and minimum voltages, as described by equation (10.4).

$$A_V = |V_{\max} - |V_{\min}|| \tag{10.4}$$

Figure 10.11 shows the voltage asymmetry for all events in the training data subset.

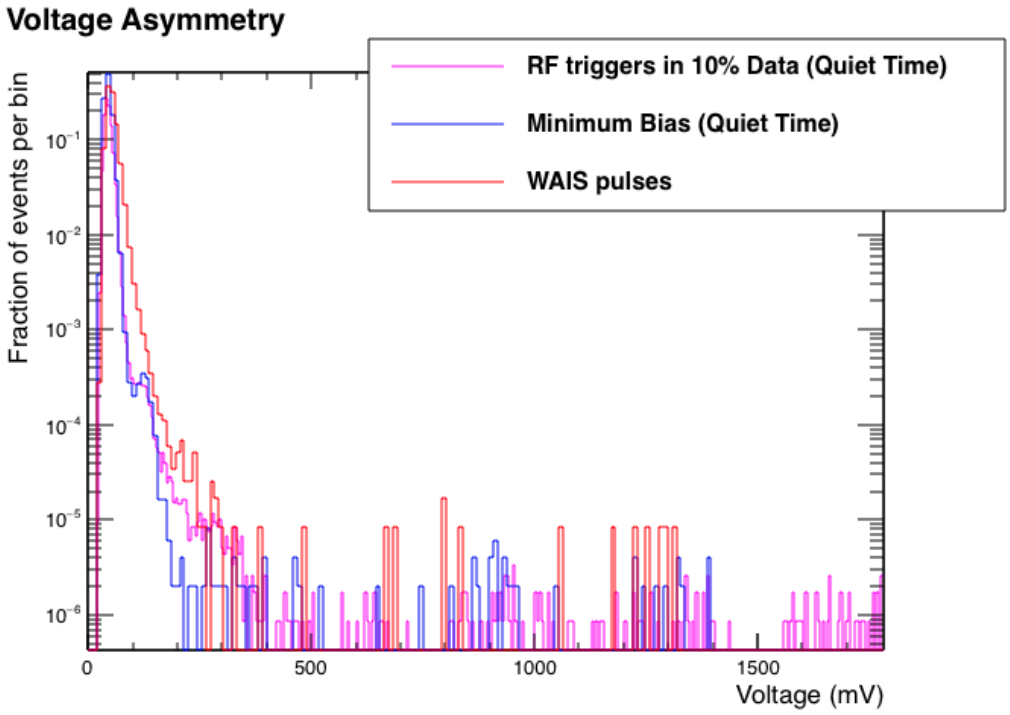

Figure 10.11: Largest value of $|V_{\max} + V_{\min}|$ from all channels in each event.

To remove SURF saturation events from the analysis data set I cut events with

$$V_{\max} > 2000\,\mathrm{mV} \tag{10.5}$$

$$V_{\min} > -2000\,\mathrm{mV} \tag{10.6}$$

$$A_V > 500\,\mathrm{mV} \tag{10.7}$$

This cut 99.9% efficient for the WAIS pulses, the quiet time minimum bias events, and the quiet time 10% data set.

10.6 Thermal Background Cuts

Once the self triggered blast and SURF saturation cuts were applied to the training data sub-samples from the quiet time, the RF triggers in the 10% data set closely resemble the minimum bias triggers. These two distributions after data quality cuts are shown in Figure 10.12.

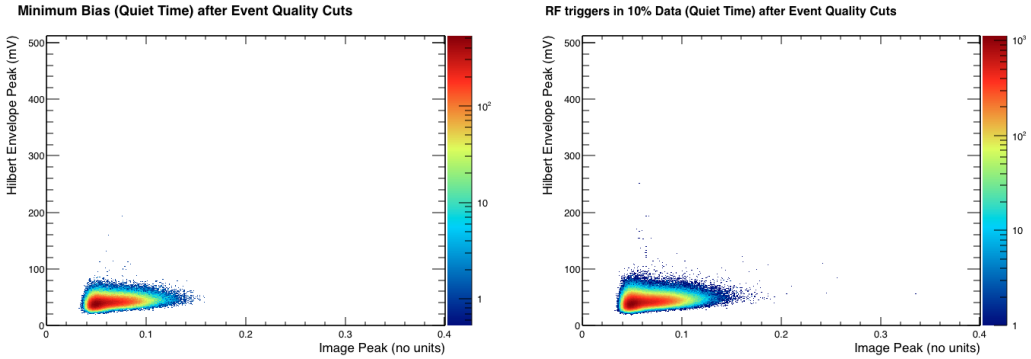

(a) MB events (b) RF triggers in 10% data set

Figure 10.12: Image peak vs. Hilbert Envelope Peak distributions of RF triggers in the 10% data set and MB triggers in the selected quiet time after data quality cuts.

To reject events triggered by thermal fluctuations I apply three cuts. The first cut requires coincidence between the peak in the interferometric image and the L3 trigger direction. Figure 10.13 shows the number of Φ-sectors between the nearest L3 trigger and the peak of the interferometric map for the three training data sub-samples.

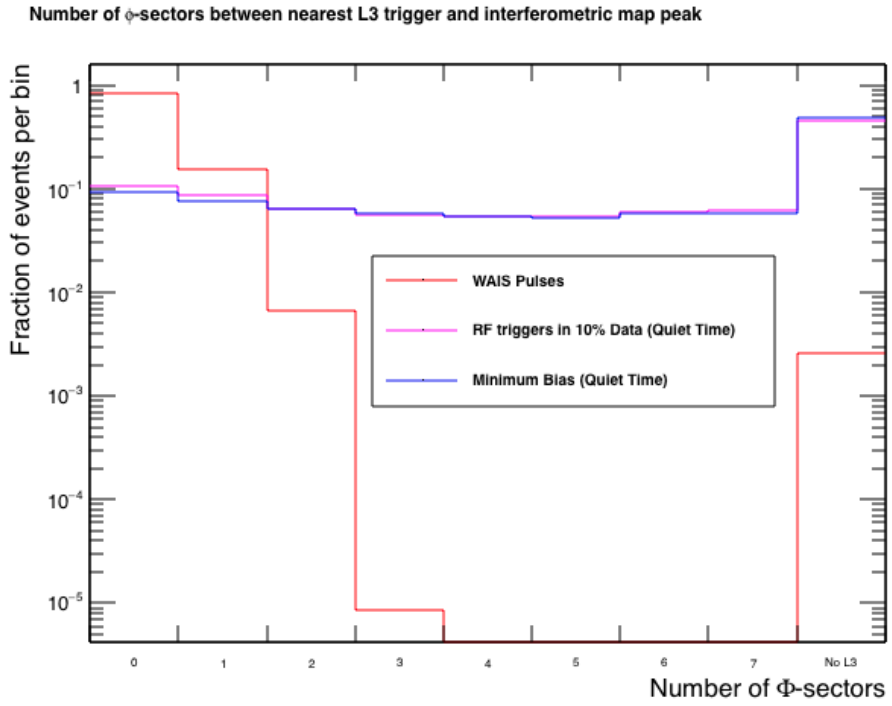

Figure 10.13: Number of ϕ-sectors between the nearest L3 triggered ϕ-sector and the peak of the interferometric map for the three training data sub-samples

The impulsive WAIS signals align well with the trigger. Triggers dominated by thermal noise fluctuations do not because thermal noise is not coherent between channels. I remove events with

$$\delta\phi\text{-sector} \geq 2 \tag{10.8}$$

During the ANITA-3 flight the L1 and L3 trigger masking was partially broken (see Section 7.1). A new offline ϕ-masking variable was constructed by looking for periods that a payload ϕ-sector was unmasked that were very close to the time required for a high trigger rate to trigger the ϕ-mask. I used this offline ϕ-masking variable to remove events if there was an L3 trigger in a ϕ-sector considered masked by the offline masking variable in either polarisation.

This cut is 92.2% efficient for WAIS pulses, 20.3% efficient for the 10% data sample, 63.2% efficient for the minim bias sample. For the minimum bias sample, this cut only removes events if the peak in the image aligns with an offline-masked Φ-sector as there are not necessarily any L3 triggers in the event.

10.6.1 Sun pointing events

The Sun is a source of coherence between channels and was visible in the reconstruction directions in the Minimum Bias sub-sample from the entire flight (Figure 10.3). Figure 10.14 shows the average image peak value as a function of angle to the sun during the quiet time.

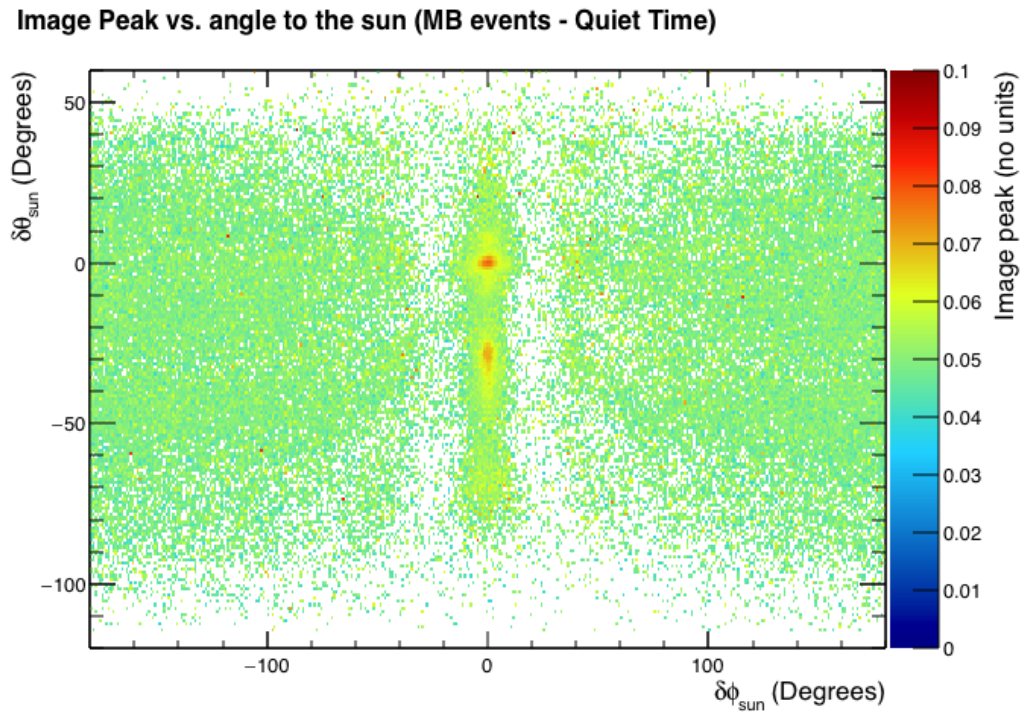

Figure 10.14: Image peak as a function of angle to the sun of the MB sub-sample during the quiet time.

Figure 10.15 shows the distribution of events as a function of angle from the sun in azimuth (ϕ) and elevation (θ).

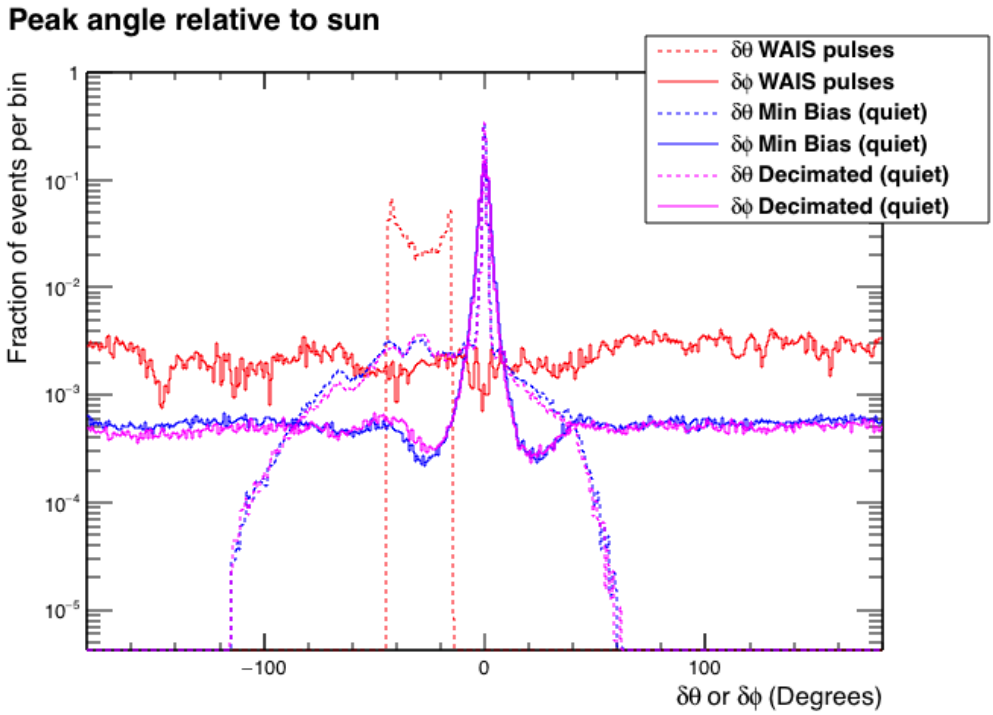

Figure 10.15: Fraction of events as a function of angle to the sun. The solid lines show Azimuth ($\delta\phi$) dotted lines show elevation ($\delta\theta$).

To reduce the coherence of the thermal background, I cut all events which point towards the sun in Azimuth. This removes the sun and its reflection. I remove events with

$$|\delta\phi_{\text{sun}}| < 20^{\circ} \quad . \tag{10.9}$$

as they fall inside the peak in Figure 10.15. This cut is 90% efficient for the WAIS pulses, 21.8% efficient for the quiet time 10% data set, and 25.0% efficient for the quiet minimum bias sample.

10.6.2 Extrapolated Fisher Discriminant

The combined effects of the cuts described so far reject 95% of the minimum bias sample. ANITA-3 has a data set of 78 million events. In order to have less than 0.5 thermal events passing cuts I designed a cut which would accept 5×10^{-9} thermal background events. A further factor of 10^{-7} reduction in acceptance is required to achieve this. I trained a Fisher discriminant in the interferometric image peak vs. Hilbert peak parameter space using the WAIS divide pulses and minimum bias quiet

time sub-sample passing all cuts listed so far. The two populations are plotted as a function of the discriminant variable are shown in Figure 10.16.

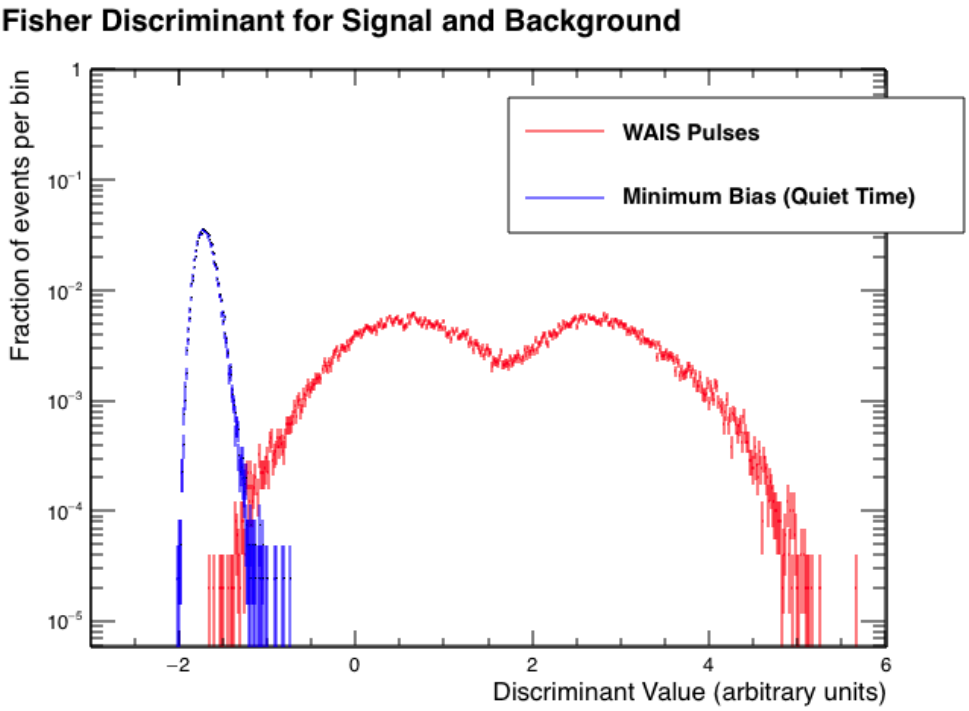

Figure 10.16: Output of the Fisher Discriminant

Figure 10.17 shows the acceptance as a function of the discriminant variable w_0. The thermal background follows an exponential distribution with a non-thermal tail.

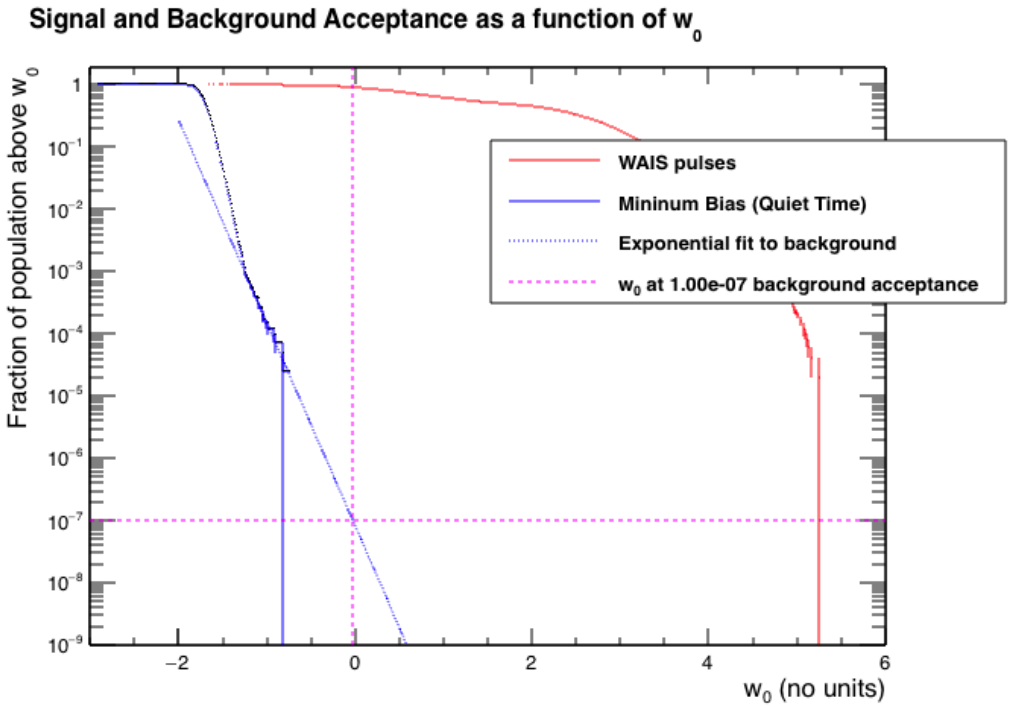

Figure 10.17: Event acceptance of WAIS pulses and minimum bias events as a function of Fisher discriminant, w_0. The non-thermal tail of the MB distribution has been fitted with an exponential and extrapolated to the point where the acceptance is a factor of 10^{-7} lower.

Since the extrapolation is over three orders of magnitude I fit an exponential to the non-thermal tail of the minimum bias distribution. This cut functions as a joint cut for the thermal background and weak CW contaminating the minimum bias quiet time sub-sample. After extrapolating the tail of the minimum bias distribution to an acceptance of 10^{-7}, I remove events with

$$w_0 < -0.0270745 \tag{10.10}$$

Figure 10.18 shows the cut from the extrapolated fisher discriminant in the image peak vs. Hilbert peak parameter space.

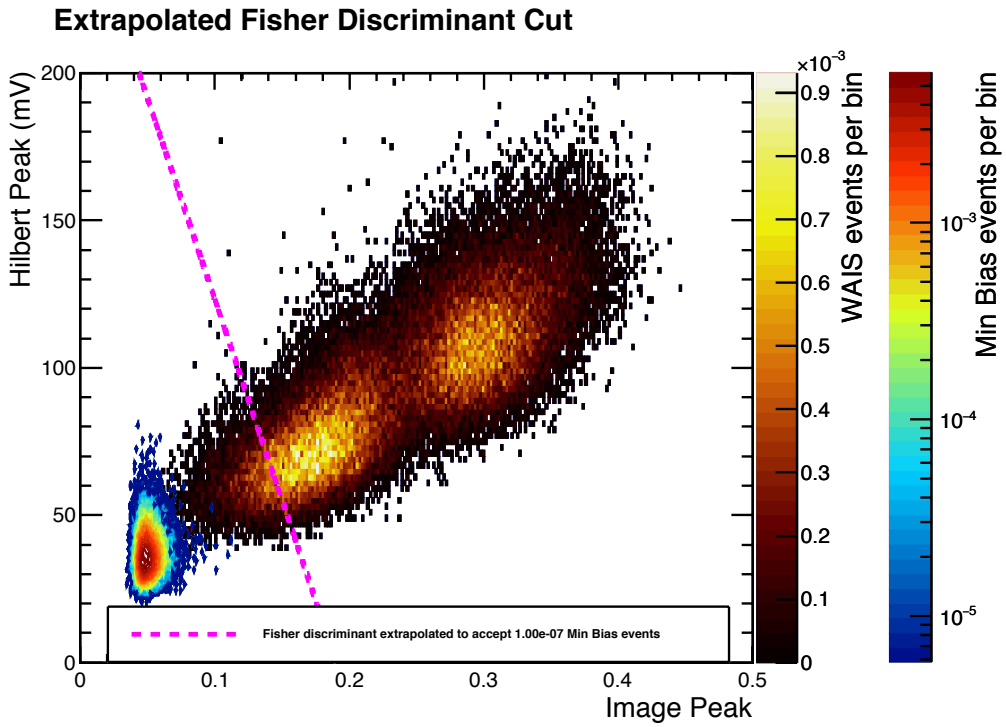

Figure 10.18: Extrapolated Fisher Discriminant cut as a function of image peak and Hilbert peak.

This cut is 90.7% efficient for the WAIS pulses, 0.02% efficient for the quiet time minimum bias data, and 0% efficient for the minimum bias data. The extrapolation from the distribution tail removes all minimum bias events from the quiet time minimum bias sample.

10.7 CW reduction and Elevation Cuts

The vast majority of events that pass the thermal cut will be man-made noise from bases. With no dynamic frequency filtering I add two additional cuts to events with strong CW contamination. Figure 10.19 shows an example of an interferometric map with strong CW. There are multiple large peaks because there are many time offsets that the CW waveforms correlate well.

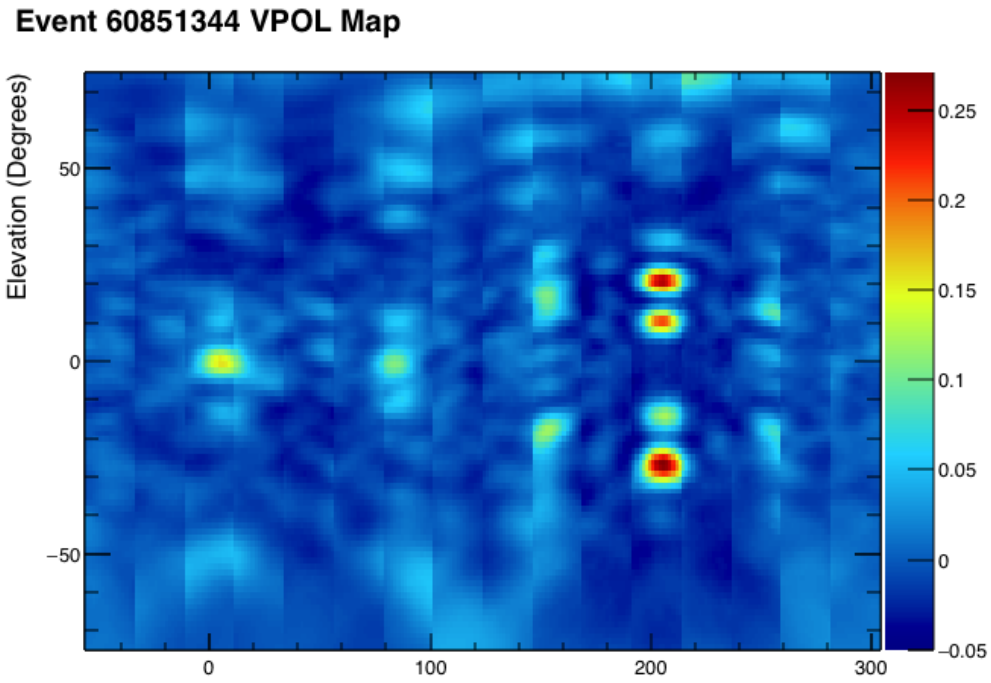

Figure 10.19: Example interferometric map from an event with strong unfiltered CW. The image has multiple peaks.

Since the thermal cut is finalised, I plot the 10% data set from the entire flight against the remaining WAIS pulses.

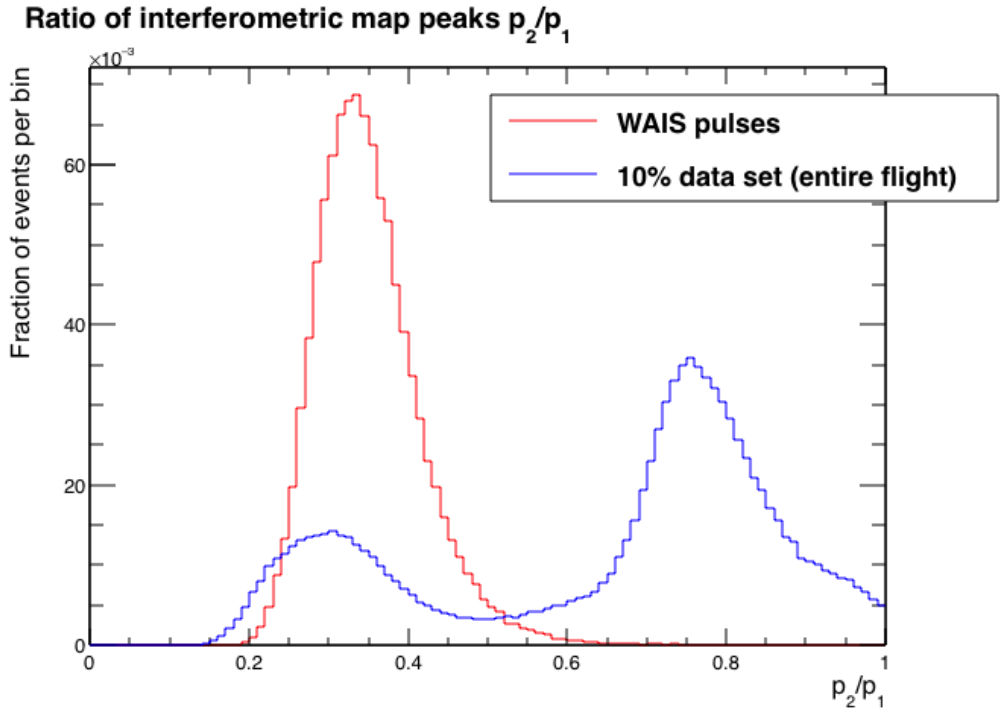

Figure 10.20: Ratio of second to first peak in the interferometric map for WAIS pulses and all decimated data surviving the cuts described so far.

Figure 10.20 shows the ratio of the second largest interferometric map peak, p_2, to the first peak, p_1. I remove events with

$$\frac{p_2}{p_1} > 0.5 \tag{10.11}$$

This cut is more than 97% efficient for WAIS divide pulses that survive the event quality and thermal cuts. This reduces the size of the decimated data set by 72%. Finally, I require that the event reconstruct at a reasonable angle of θ.

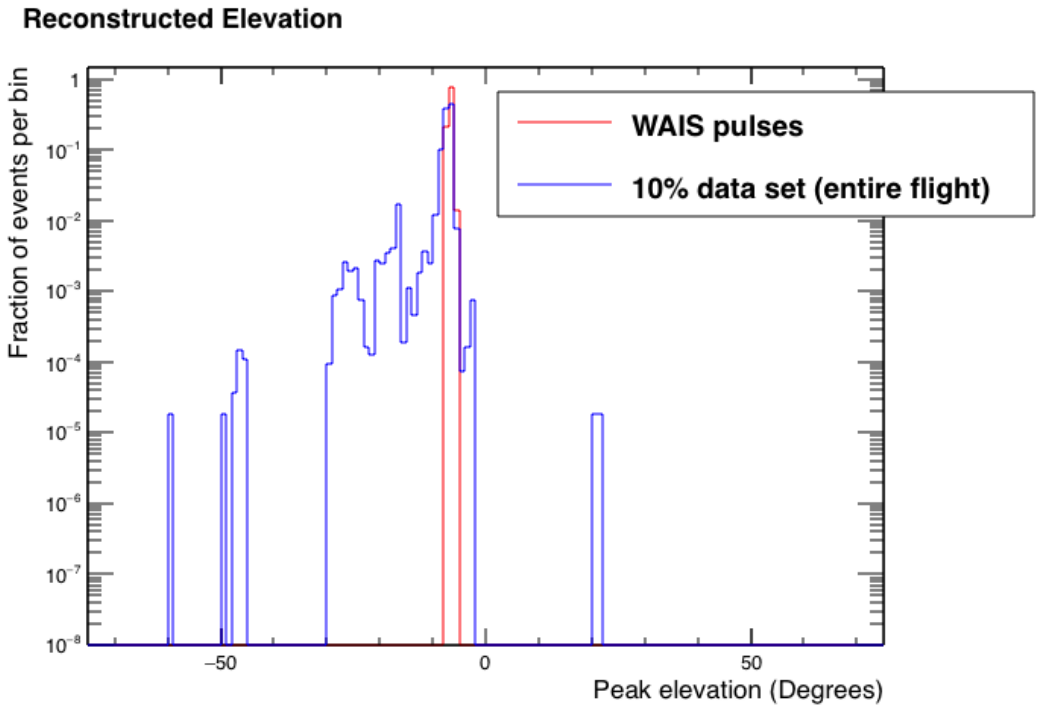

Figure 10.21: Distribution of elevations of WAIS pulses and 10% data passing all cuts described so far.

Neutrino signals are expected to come from the ice only. Previous analyses have detected direct and reflected cosmic ray events. I limit my cosmic ray search to reflected events only. Based on Figure 10.21 I remove events with

$$\theta > -6^\circ \tag{10.12}$$

$$\theta < -35^\circ \tag{10.13}$$

This cut is 100% efficient for the remaining WAIS pulses and 99.9% efficient for the remaining 10% data set.

10.8 Pre-clustering Cut Summary

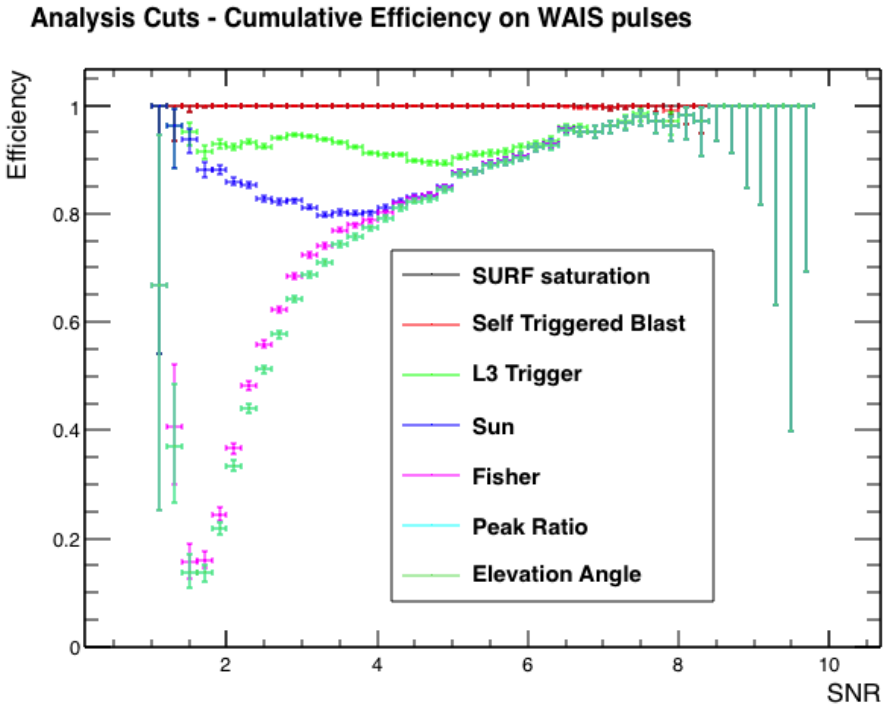

Figure 10.22: The cumulative effect on the WAIS pulse efficiency when applying the analysis cuts in sequence. (Note that since the elevation angle cut is 100% efficient for WAIS pulses, the Peak Ratio points are directly under the Elevation Angle points.)

Figure 10.22 shows the cumulative effects on the WAIS pulses applied in sequence. The SNR of the WAIS pulses varies with the payload position relative to WAIS. The sun cut affects the WAIS pulses for the couple of hours that the sun lines up with WAIS divide. This causes the dip in analysis efficiency in a particular position. The combined efficiency of all cuts on the WAIS pulses is 73.7%.

Table 10.1: Fraction of training data set events passing developed cuts

Cut	Pass in sequence	Pass if only
None	77651892	100%
SURF saturation	76482742	98.5%
Self Triggered Blast	76463089	98.5%
L3 trigger + masking cut	15842154	20.4%
Points to sun	6311650	8.1%
Fisher Discriminant	2066363	2.6%
Interferometry Peak Ratio	526254	0.7%
Elevation angle cut	526254	0.7%

10.9 Application of Cuts to Entire Data Set

I applied the analysis cuts to the entire data set. Table 10.2 shows the effects of the cuts as applied to the entire data set. The combined effect of the cuts is to remove 99.3% of the data.

Table 10.2: Number of events passing the analysis cuts

Cut	Pass - In Sequence	Pass - If only	Pass - If not applied
None	77651892 (100%)	77651892 (100%)	77651892 (100%)
SURF saturation	76482742 (98.5%)	76482742 (98.5%)	50348 (0.06%)
Self Triggered Blast	76463089 (98.5%)	77568755 (99.9%)	50345 (0.06%)
L3 trigger + masking cut	15842154 (20.4%)	3612561 (4.7%)	765359 (1.0%)
Points to sun	6311650 (8.1%)	30510028 (39.3%)	57328 (0.07%)
Fisher Discriminant	2066363 (2.6%)	10231319 (13.2%)	54509 (0.07%)
Interferometry Peak Ratio	526254 (0.7%)	5035284 (6.5%)	427705 (0.6%)
Elevation angle cut	526254 (0.7%)	20529936 (26.4%)	50367 (0.06%)

Since the thermal noise events follow a well behaved distribution, the vast majority of events remaining after these cuts are applied are anthropogenic signals. A different approach is taken to removing them.

10.10 Clustering

Neutrinos and cosmic ray signals from diffuse sources should be uncorrelated in arrival direction, whereas human activity is localised to particular regions on the continent. To remove the man-made background, I group events together in clusters.

For each event passing the cuts listed in Table 10.2, I project the interferometric peak direction θ, ϕ to the surface of the continent. The utilities to do this are contained in the ANITA `EventCorrelator` library [68], which uses data from the Radarsat Antarctic Mapping Project Digital Elevation Model (RAMP/DEM [70]) and BEDMAP [71] as a model for the Antarctic surface.

While developing clustering cuts I keep the number of isolated events (not clustered to a known base) hidden. Events that are isolated from all other events and known sources of human activity are considered inside signal box, which is hidden. I opened this hidden signal box after the clustering cuts were finalised, just before unblinding the neutrino search by removing the inserted events. Figure 10.23

shows all events passing pre-clustering cuts projected onto the continent.

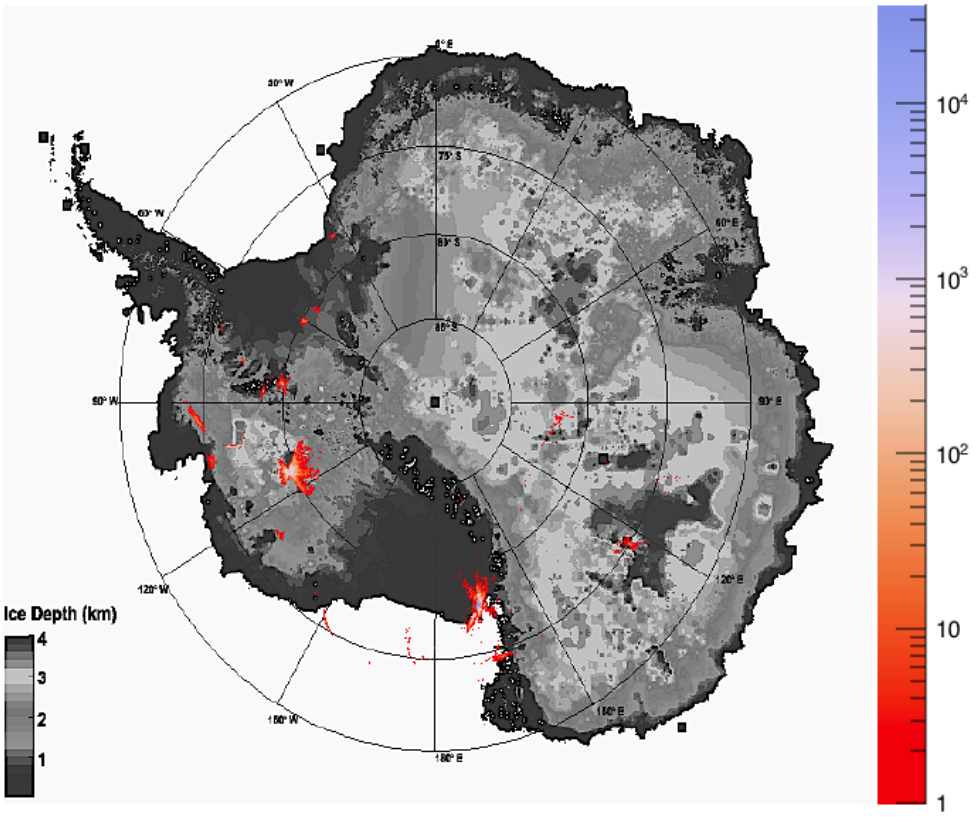

Figure 10.23: Histogram of events passing pre-clustering cuts projected onto the continent. (Isolated events in the hidden signal box are not plotted).

Initially, I clustered events to the location of Antarctic bases. The ANITA collaboration maintains a list of known bases in Antarctica. All 360 are plotted on a map of the continent in Figure 10.24.

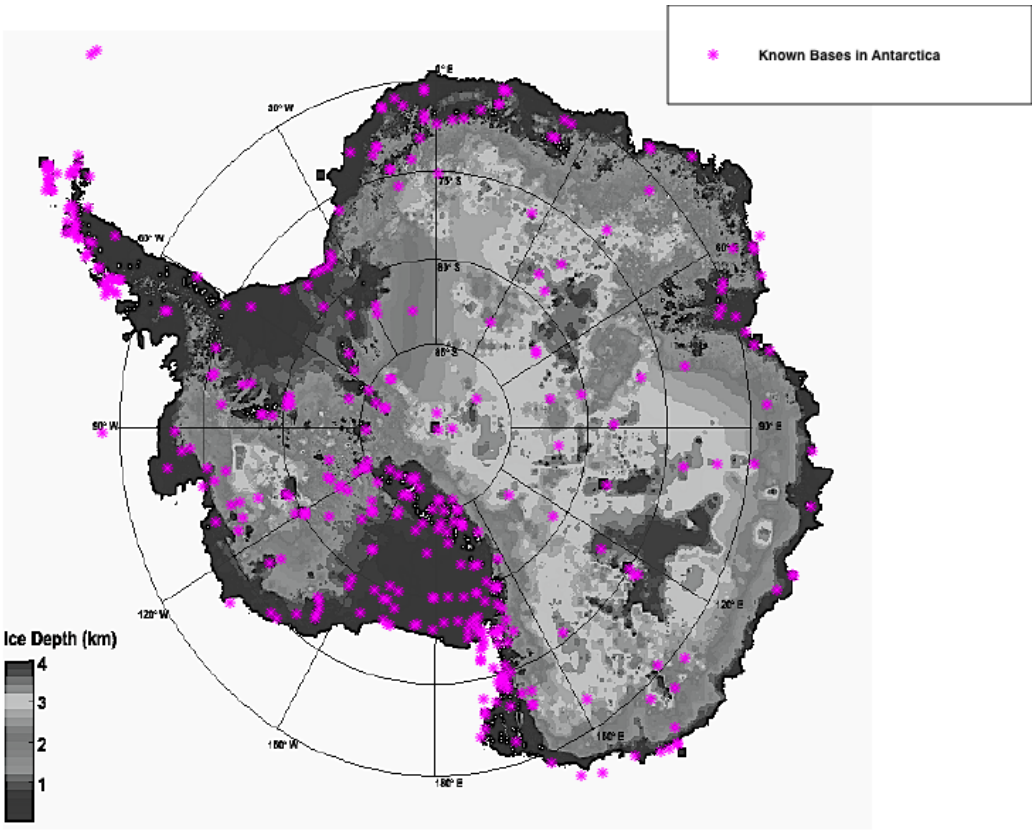

Figure 10.24: Position of known bases in Antarctica

For a base, b, I used the ANITA `EventCorrelator` library to predict the arrival direction of a signal from that base in payload coordinates (θ_b, ϕ_b). This can be compared with the direction of an interferometric map peak, θ_p, ϕ_p, to determine whether that base was the source of the signal.

To assess this on an event-by-event basis, I fitted the polarisation of the angular resolutions from Chapter 8.8 with a falling exponential plus constant term as a function of SNR.

$$\delta\theta = \exp(A_\theta + B_\theta SNR) + C_\theta \tag{10.14}$$

$$\delta\phi = \exp\left(A_\phi + B_\phi SNR\right) + C_\phi \tag{10.15}$$

For simplicity, and since the two distributions are very similar, I used a single fit to the broader of polarisation in azimuth and elevation in θ and ϕ. This is shown in Figure 10.25.

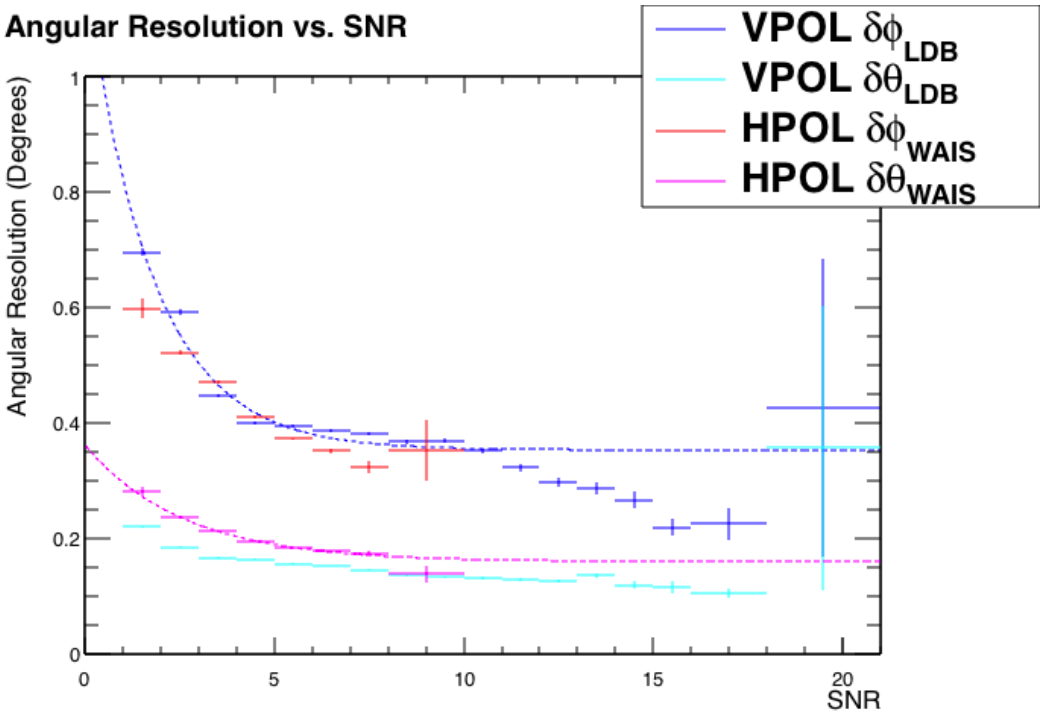

Figure 10.25: Angular resolution of calibration pulses by ANITA vs. SNR. The functions were fitted with an exponentially falling distribution plus a constant.

Table 10.3: Fitted parameters from equation (10.14) to the distribution in Figure 10.25.

Fit Parameter	Value
A_θ	-1.605 ± 0.059
B_θ	-0.3832 ± 0.0404
C_θ	0.16 ± 0.00
A_ϕ	-1.605 ± 0.059
B_ϕ	-0.3832 ± 0.0404
C_ϕ	0.16 ± 0.00

I used the fits to the angular resolution distributions in Figure 10.25 to translate the event SNR into reconstruction uncertainties $\sigma_\theta, \sigma_\phi$. Following the methods used in previous ANITA analyses [67, 10, 63], these two angular uncertainties were combined with the angular separation between a base and interferometric map peak location to form a log likelihood ratio, as shown in Equation (10.16).

$$-2\log(L) = \left(\frac{\phi_b - \phi_p}{\sigma_\phi}\right)^2 + \left(\frac{\theta_b - \theta_p}{\sigma_\theta}\right)^2 \tag{10.16}$$

10.10.1 Clustering Algorithm

For each event passing pre-clustering cuts, I computed $-2\log(L)$ from equation (10.16) for each base within 800 km. I associate events with a base if

$$-2\log(L) < 100 \quad . \tag{10.17}$$

The motivation for this value is described in Section 10.10.2. After events have been associated with known bases I cluster the remaining events into pseudo-bases with the following algorithm.

1. Fill the antarctic histogram of projected events (like Figure 10.23) with events not clustered to known bases or pseudo-bases.
2. Find the peak bin, and create a pseudo-base at the average location of all projected events in that bin.
3. Re-cluster all events with the new pseudo-base in the list of clustering centres.
4. If there are any remaining events not clustered to a base or pseudo-base, go to step 1.

This procedure assigns every point to a cluster.

The final step in the clustering algorithm is to allow events in small clusters ($N_{\text{events}} < 10$) to move to larger clusters. If the nearest point associated with a different cluster is within $-2\log(L) < 100$, then the point from the smaller cluster is moved into the larger cluster containing the other point. This final step was designed to reduce the number of small clusters at the periphery of large base clusters.

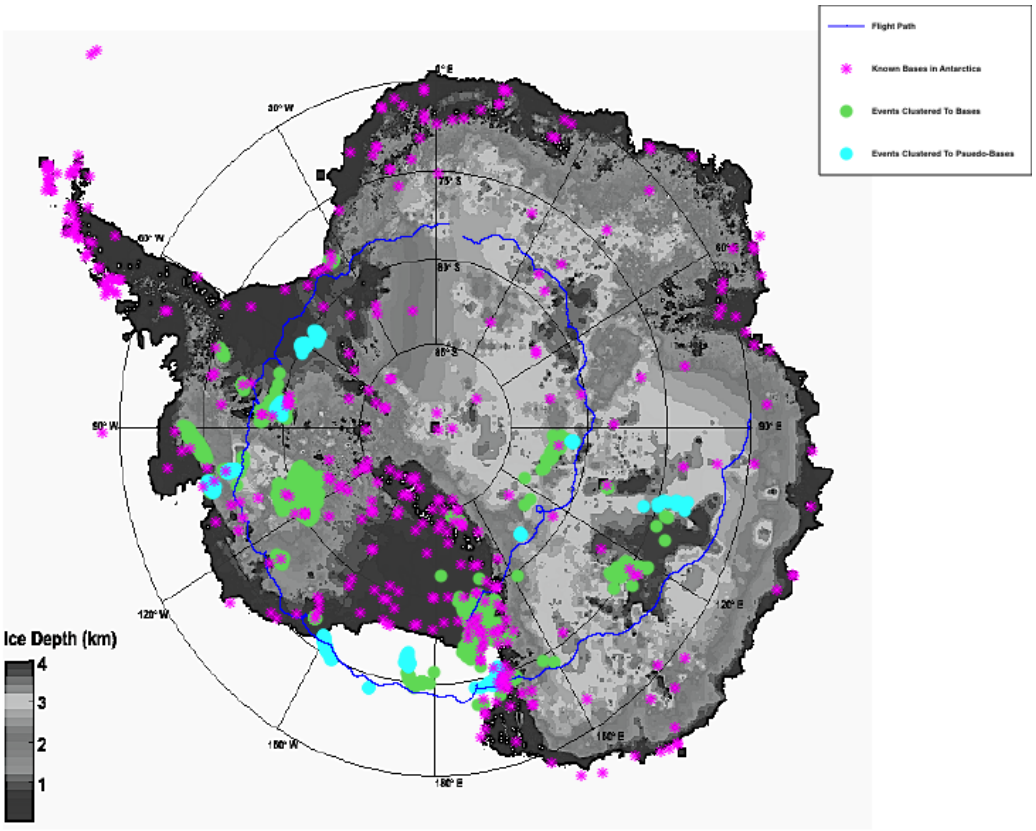

Figure 10.26: Events clustered to bases and pseudo-bases. Note that by eye it is not always obvious which events are associated with which base, as near the horizon small differences in angle correspond to large separations on the continent.

Figure 10.26 shows the post-clustering events excluding pseudo-base clusters containing one event (which are in the hidden signal box).

10.10.2 Clustering Background Estimate

In equation (10.17) I assign the clustering cut off log-likelihood at 100. This choice was motivated by two factors. Firstly, the value must be at least as wide as the distribution for large bases. Figure 10.27 shows the $-2\log(L)$ distribution for the WAIS divide base (not the pulser reconstructing to the pulser location). The cutoff is well below the value of 100.

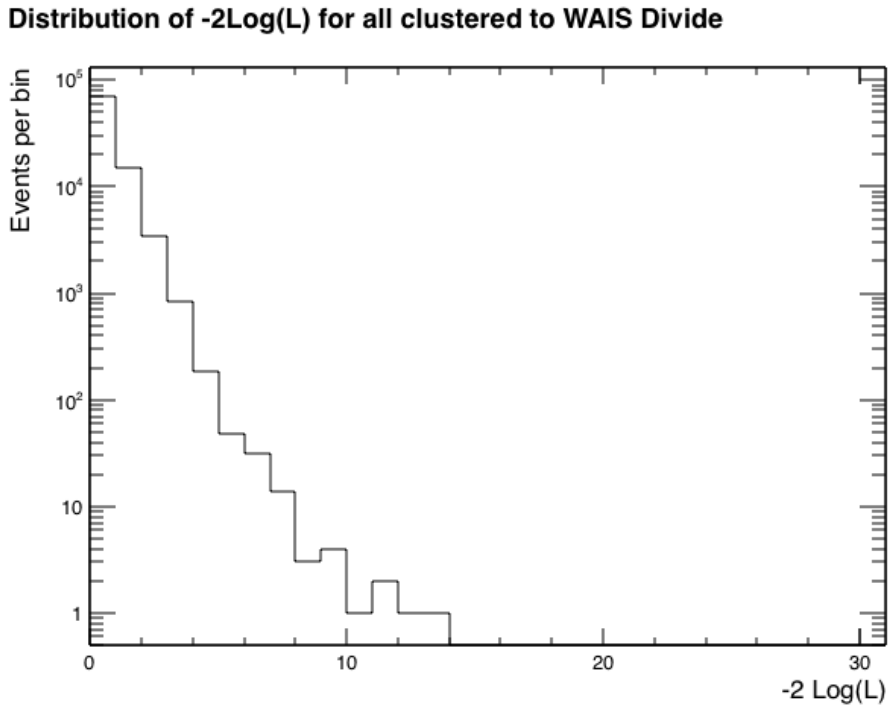

Figure 10.27: $-2\log(L)$ distribution for events reconstructing to WAIS divide (not the pulser events).

The second motivating factor was to choose a value $-2\log(L)$ such that the background estimate for events in the hidden signal box was small. As has been done in previous ANITA analyses [10, 63], to estimate the number of isolated signals I assume that the distribution of clusters sizes from known pseudo-bases, N^p, is the same as known bases N^k, as shown in Equation (10.18).

$$\frac{N_1^p}{N_{\text{small}}^p} \sim \frac{N_1^k}{N_{\text{small}}^k} \tag{10.18}$$

From this I infer the number of unknown pseduo-bases with one event, N_1^p,

$$N_1^p \sim N_{\text{small}}^p \frac{N_1^k}{N_{\text{small}}^k} \quad . \tag{10.19}$$

Figure 10.28 shows the distribution of small event clusters ($N \leq 4$) for known bases and pseudo-bases as I vary the $-2\log(L)$ clustering threshold.

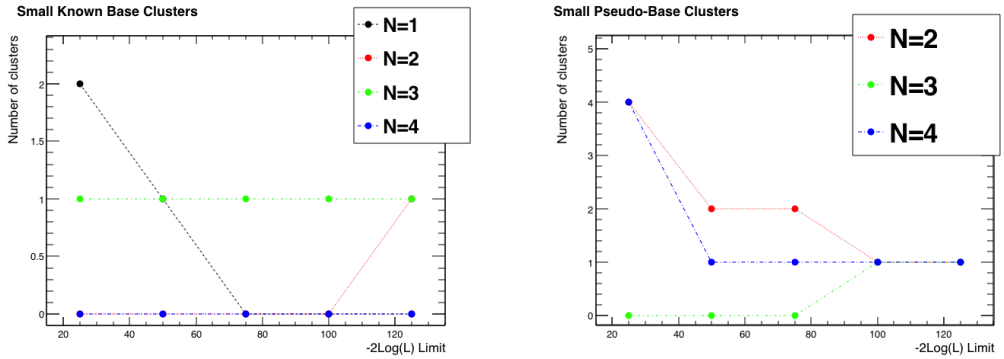

(a) Small Known Base Clusters (b) Small Pseudo-base Clusters

Figure 10.28: How the sizes of the small pseudo-base clusters and known base clusters varied with different choices of $-2\log(L)$ cut. The hidden signal box (pseudo-base clusters of size $N = 1$) is not shown.

I chose the cut $(-2\log(L) < 100)$ as this is the first point where all the N^k values are either 0 or 1. This indicates that the clustering method should produce a small anthropogenic background.

At $-2\log(L) = 100$ the known base clusters of size 1, $N_1^k = 0$. In order for the background estimate (equation (10.19)) to be not be trivially 0, I assigned $N_1^k = 1$. The value of N_1^p is either 0 or 1 depending on whether $N_{\text{small}}^{p/k} = 2,3,4$. Averaging over the three values, I estimate a background of

$$N_1^p = 0.33 \pm 0.22 \tag{10.20}$$

I break this down into a separate polarisation for the horizontal and vertical polarisation by looking at the polarisation content of all the small bases (known and pseudo). Figure 10.29 shows the polarisations of events in the small clusters.

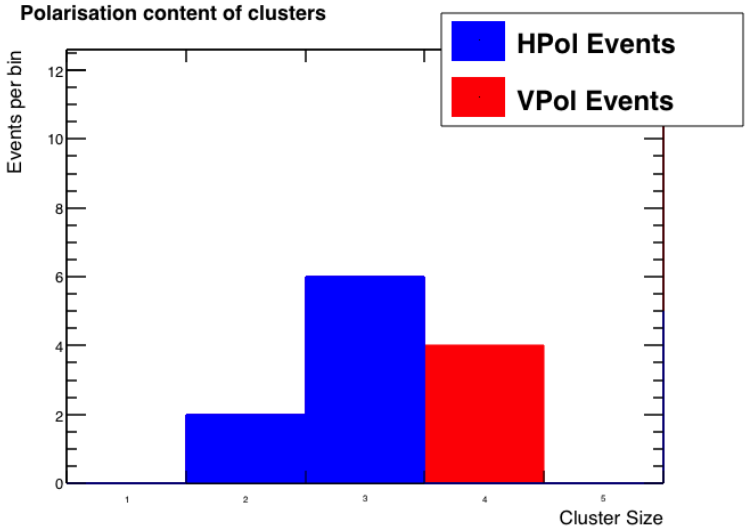

Figure 10.29: Polarisation content of small known base and pseudo-base clusters (excluding the hidden signal box).

I weight the anthropogenic background estimate of the two polarisations by the polarisation contents of the small clusters.

$$N_1^p(V) = 0.11 \pm 0.07 \tag{10.21}$$

$$N_1^p(H) = 0.22 \pm 0.15 \tag{10.22}$$

$$\tag{10.23}$$

10.11 Opening the Signal Box and Unblinding

After opening the base hidden signal box (N_1^p) I found 11 events. Of these 11, 2 were vertically polarised and 9 were horizontally polarised. After unblinding I found that both vertically polarised events were inserted events.

Table 10.4: Events in the hidden signal box.

Run	Event Number	Polarisation	Comment
248	32907848	H	Impulsive
250	33484995	H	Impulsive
255	35573717	V	Inserted event
284	41529195	H	Impulsive
307	47652140	H	CW Event
343	58592863	H	Impulsive
348	59669787	V	Inserted event (reconstructs to the ocean)
370	66132615	H	CW Event (reconstructs to the ocean)
371	66353449	H	CW Event (reconstructs to the ocean)
405	75543698	H	CW Event
434	83670528	H	CW Event

10.12 Post Unblinding discussion

After unblinding I discovered two issues in my analysis. Both issues made the analysis less sensitive that it could otherwise have been.

The first issue was discovered in the $\sigma_\theta, \sigma_\phi$ lookup described in Section 10.10.1, which always returned the maximum angular uncertainty (as if every event had $SNR = 0$). This corresponds to assigning all events the largest possible angular uncertainty. This makes more likely that a cosmic ray or neutrino signal event is clustered into a group of background events, making it harder to produce a false positive signal.

The second issue was that the sun cut was not applied prior to clustering. This meant that events that failed the sun cut were projected onto the continent to be clustered into bases and pseudo-bases. This feature also makes it more likely to cluster signal events into anthropogenic background events, making it harder to produce a false positive signal. A future version of this analysis will have greater sensitivity by correcting these issues.

I applied the sun cut to the final candidate list. One of the inserted VPol events and the final four CW events in table 10.4 were removed. Cutting events which point to the sun removes 40° in azimuth, around 11% of ANITA solid angle. Applying this cut to the candidate list in table 10.4 removed 80% of the CW events. However, this is not unexpected as the fisher discriminant cut (Section 10.6.2) was trained to

remove CW without the extra coherence from the sun present in the same part of the interferometric map. A revised candidate event list, with the sun cut applied post-clustering, is presented in table 10.5.

Table 10.5: Events in the hidden signal box after applying the sun cut post clustering.

Run	Event Number	Polarisation	Comment
248	32907848	H	Impulsive
250	33484995	H	Impulsive
255	35573717	V	Inserted event
284	41529195	H	Impulsive
307	47652140	H	CW Event
343	58592863	H	Impulsive

10.12.1 Additional Waveform Shape Cuts

The interferometric map and unfiltered waveforms (unmodified and deconvolved) are shown in Figures 10.30, 10.31, 10.32, 10.33 and 10.34.

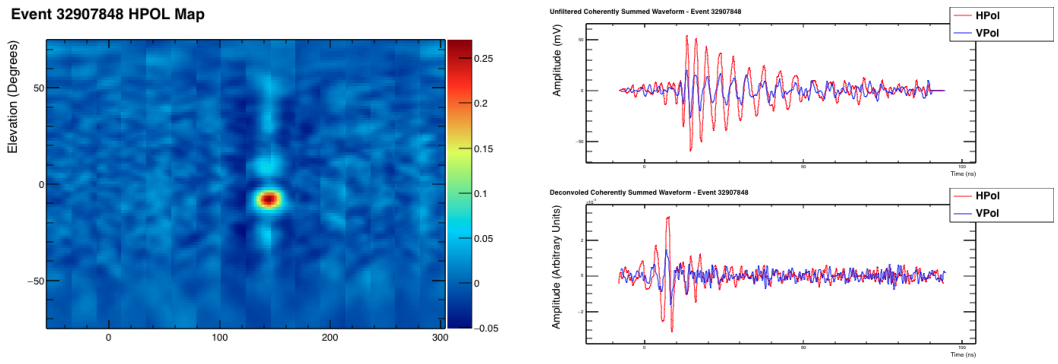

(a) Interferometric Map (b) Coherently Summed Waveform

Figure 10.30: Interferometric map and coherently summed waveform for event number 32907848

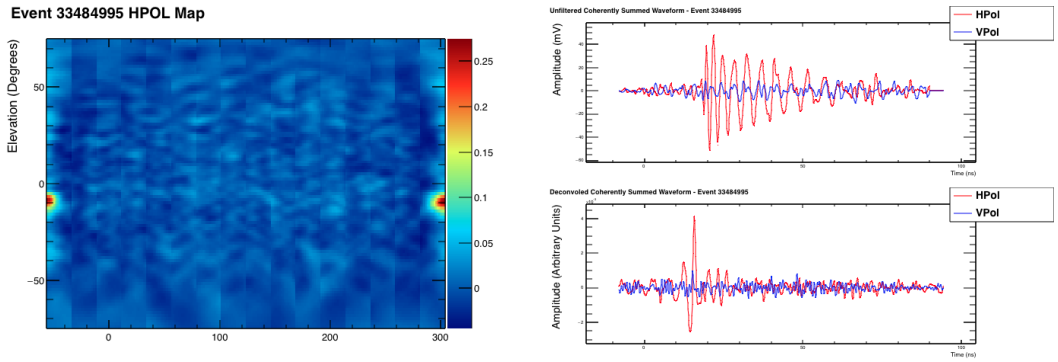

(a) Interferometric Map (b) Coherently Summed Waveform

Figure 10.31: Interferometric map and coherently summed waveform for event number 33484995

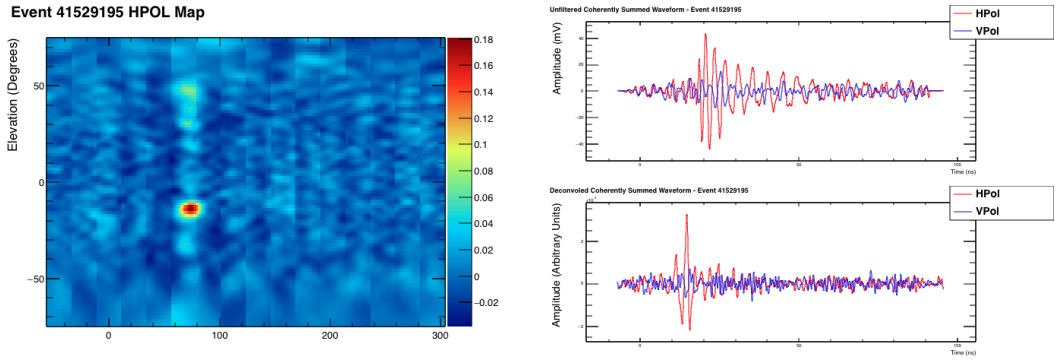

(a) Interferometric Map (b) Coherently Summed Waveform

Figure 10.32: Interferometric map and coherently summed waveform for event number 41529195

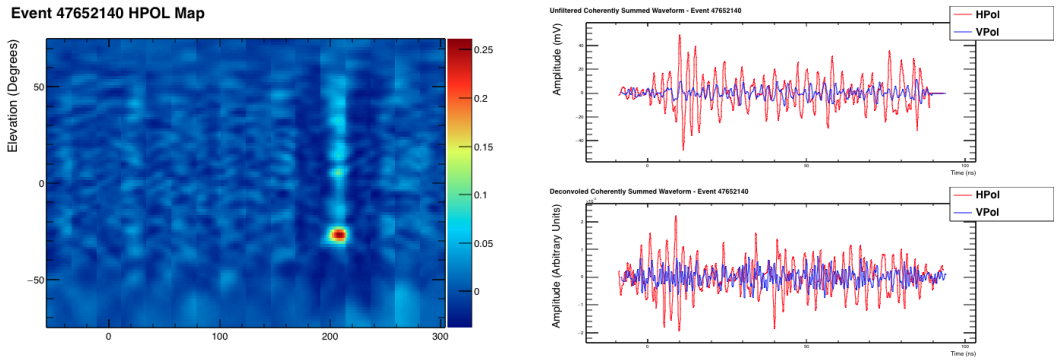

(a) Interferometric Map (b) Coherently Summed Waveform

Figure 10.33: Interferometric map and coherently summed waveform for event number 47652140

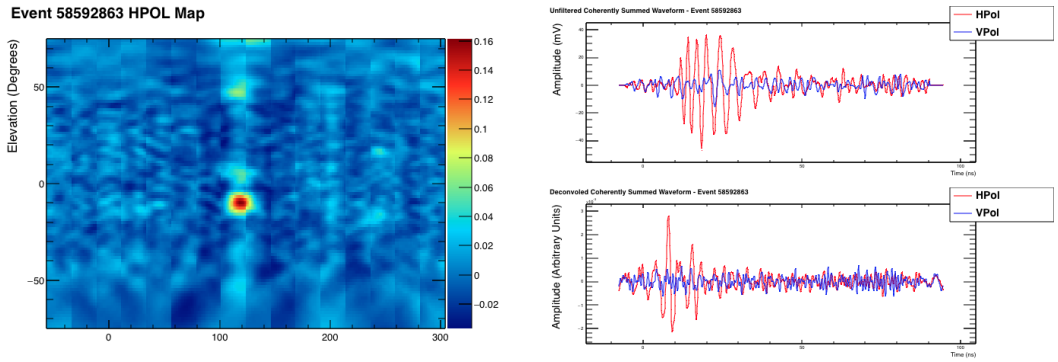

(a) Interferometric Map (b) Coherently Summed Waveform

Figure 10.34: Interferometric map and coherently summed waveform for event number 58592863

Figure 10.35 shows the candidate events with the effects of the system response removed. The impulsive events are aligned by peak location.

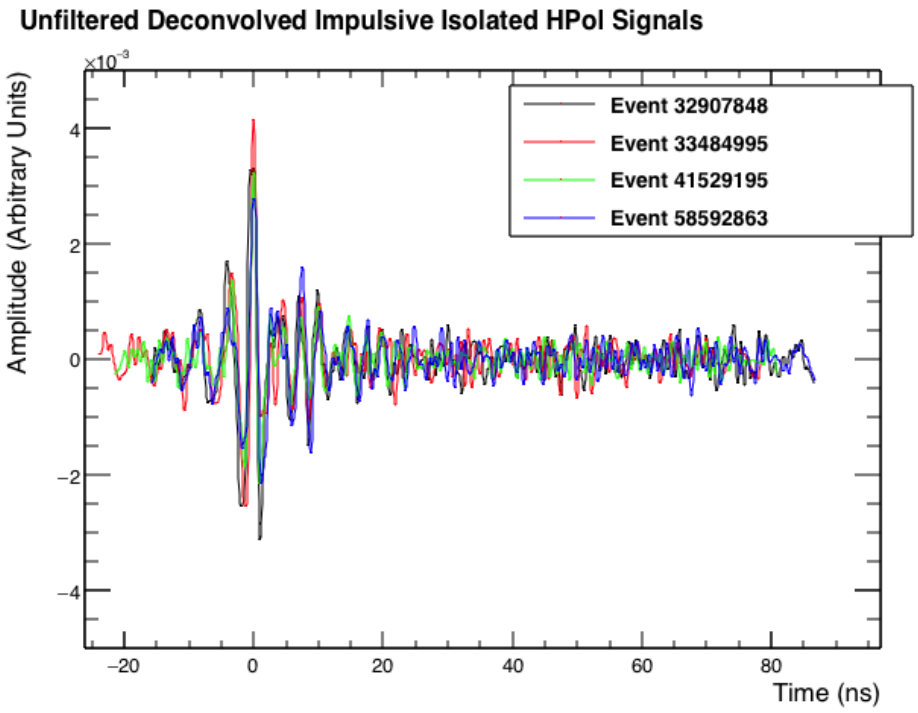

(a) Deconvolved Impulsive Events Aligned

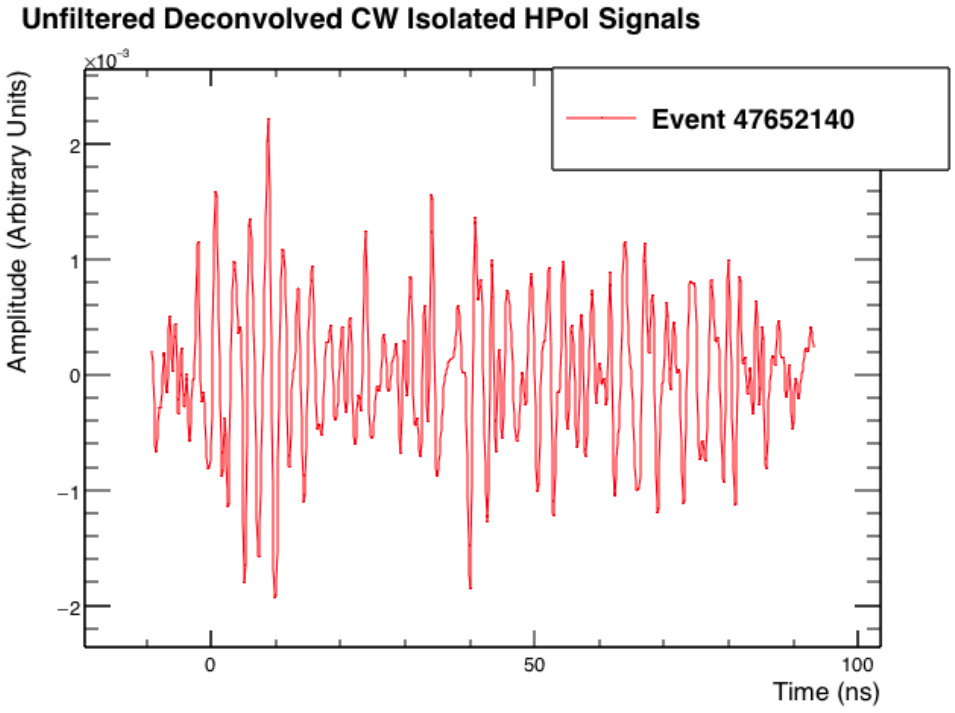

(b) Deconvolved CW Event

Figure 10.35: Isolated HPol events. The waveforms have been deconvolved to remove the effects of the system response. The impulsive aligned waveforms are very consistent with each other.

To remove the obviously non-impulsive signal that leaked into the final candidate lists I apply some "by hand" waveform shape cuts. I require that a significant fraction of the power be contained in a short time around the peak voltage. This is true of the impulsive events in Figure 10.35a, but not surviving the CW event in Figure 10.35b.

10.13 List of blinded events

There were 11 events inserted into my analysis data set. Table 10.7 lists the events along with which cuts they failed. Of the events that surviving pre-clustering cuts, two were clustered into large (> 100) event clusters.

Table 10.6: Cut labels for table 10.7.

Label	Cut	Number of failed inserted
Cut 1	SURF saturation	0
Cut 2	Self-triggered Blast	0
Cut 3	L3 Trigger + offline Φ-sector masking	3
Cut 4	Sun	2
Cut 5	Fisher Discriminant	2
Cut 6	Elevation Angle	0
Cut 7	Map Peak Ratio	3
Cut 8	Clustering	2

Table 10.7: Which cuts removed the inserted events. I have marked 59669787 with an asterisk to indicate that it passed clustering but failed the sun cut post clustering.

Event Number	SNR	1	2	3	4	5	6	7	8
6246129	5.48	pass	pass	fail	pass	pass	pass	pass	N/A
18157703	4.80	pass	pass	pass	pass	pass	pass	pass	fail
23218582	3.59	pass	pass	fail	pass	pass	pass	pass	N/A
27293573	3.24	pass	pass	fail	pass	pass	pass	pass	N/A
35573717	4.17	pass	pass	pass	pass	pass	pass	pass	pass
41177605	3.36	pass	pass	pass	pass	pass	pass	fail	N/A
53554633	3.18	pass	pass	pass	pass	fail	pass	fail	N/A
59669787	5.62	pass	pass	pass	fail	pass	pass	pass	(pass*)
62579341	2.13	pass	pass	pass	pass	fail	pass	fail	N/A
72645879	2.93	pass	pass	pass	fail	pass	pass	pass	N/A
75455288	3.86	pass	pass	pass	pass	pass	pass	pass	fail

Tables 10.6 and 10.7 show that a 3/11 of the inserted events failed the offline ϕ-

masking cut (cut 3). These events passed all other cuts, which implies that are good impulsive events. If a reblinding is performed for further analysis of the ANITA-3 data set, I will check for events failing this cut prior to insertion. Of the remaining eight inserted events, two failed the sun cut, which is consistent with the angular width of the cut, $40°/360° \approx 11\%$. Of the remaining six events, three failed three failed the peak ratio cut, and two of those three failed the thermal cut. These are weak impulsive events. An enhanced CW filtering algorithm that enabled tighter thermal cut may be able to recover these events. Finally, two of the three (or four) surviving events cluster to bases or other clusters. The event insertion distributed the events evenly in event number, not time. This increases the probability of events to be inserted near bases when the event rate was high. This in turn, makes these events more likely to cluster to a base than an event from a quieter period of the flight.

10.14 Monte Carlo Simulation of the ANITA-3 Flight

10.14.1 Introducing `IceMC`

`IceMC` is a Monte Carlo (MC) simulation program [20] maintained by the ANITA collaboration. It throws tens of millions of neutrinos at the Antarctic continent, models the Askaryan radiation generated, and propagates it through the ice and air to a simulation of the ANITA instrument. The simulation accounts for the effects of components in the trigger and digitizer paths on the RF signal as it travels through ANITA and the trigger logic described in Section 5.7. `IceMC` outputs data in the ANITA-3 format and so can be analysed in an identical fashion to the real ANITA-3 flight data.

Figure 10.36 shows a simulated neutrino event in ANITA-3 rendered in `MagicDisplay`.

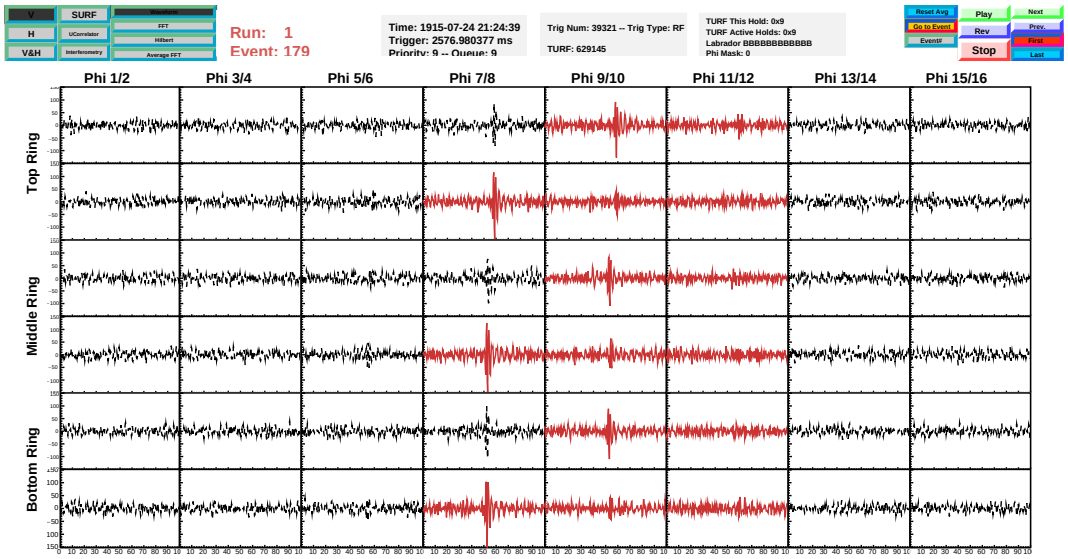

Figure 10.36: Monte Carlo neutrino event rendered in `MagicDisplay`.

The flight path of the instrument is modelled using the GPS data, the trigger thresholds of each channels, Φ-sector and channel masking are also used in the `IceMC` simulation. This allows us to reproduce the conditions of the flight in a fully controlled simulation, estimating the instrument's exposure to ultra-high energy neutrinos. Linda Cremonesi generated samples of Monte Carlo neutrinos at decades of energy between 10^{19} eV and 10^{21} eV with a simulation of the ANITA-3 flight. Figure 10.37 shows the population of 10^{20} eV MC neutrinos that triggered the payload.

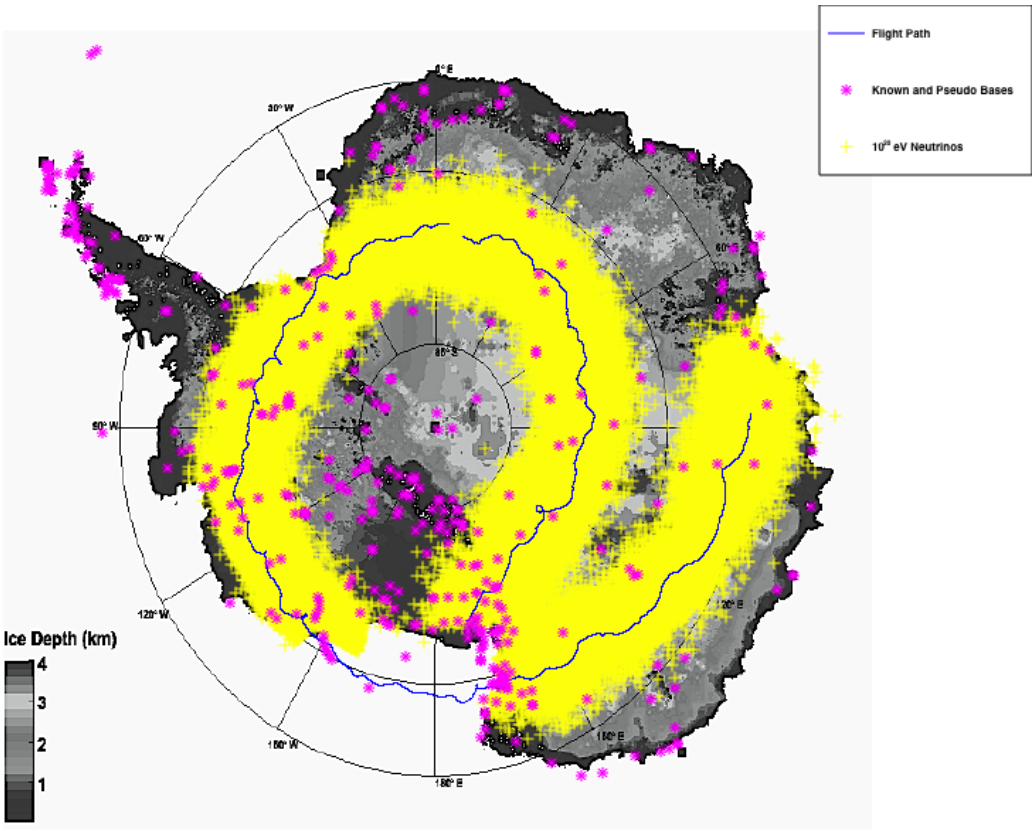

Figure 10.37: Positions of 10^{20} eV MC neutrinos that triggered the instrument.

10.14.2 Monte Carlo Validation

The noise in the Monte Carlo is not currently set correctly for the conditions of the ANITA-3 flight.

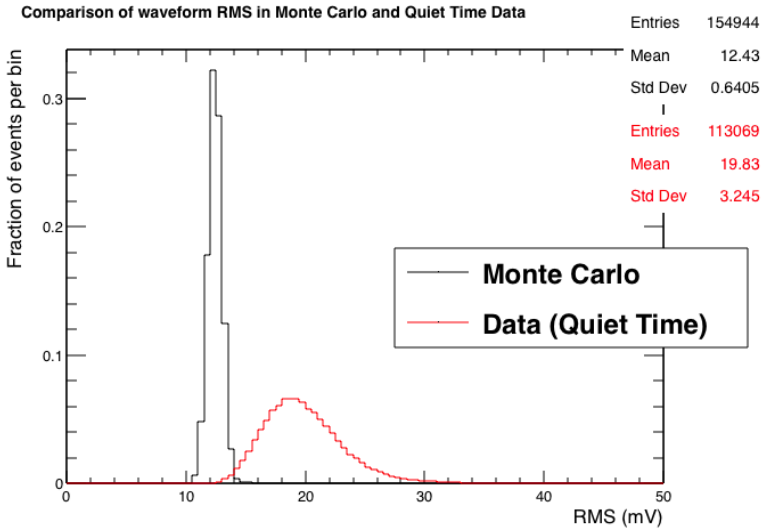

Figure 10.38: Comparison of minimum bias non-sun pointing events from a run in the quiet time data (Section 10.4) with the Monte Carlo. Satellite frequencies have been notched in the data.

Figure 10.38 shows that the noise level is not in the Monte Carlo. From the means of the distribution in Figure 10.38, I derive an RMS scaling factor

$$f_{RMS} = \frac{RMS_{Data}}{RMS_{MC}} \tag{10.24}$$

Figure 10.39 shows the interferometric figures of merit for the WAIS pulses, and MC neutrinos before and after scaling the MC SNR by $1/f_{RMS}$.

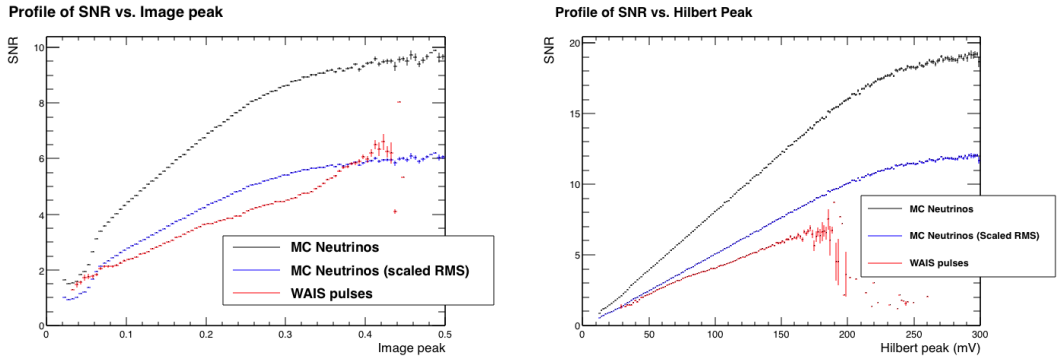

(a) Profile of Image Peak vs. SNR

(b) Profile of Hilbert Peak vs. SNR

Figure 10.39: The agreement between Image peak and Hilbert Peak in Data and Monte Carlo is significantly improved by scaling the MC SNR by $1/f_{RMS}$.

Figure 10.39 shows that some (much smaller) disagreement in the analysis

figures of merit remains after scaling the RMS alone. None of the analysis variables rely on SNR directly, and the agreement between the Image Peak and Hilbert Peak variables is reasonable.

10.14.3 Monte Carlo Trigger Efficiency

An accurate estimate of the trigger efficiency is critical to estimating ANITA's exposure to ultra-high energy neutrinos. A sample of Monte Carlo neutrinos was generated where neutrino events that did not trigger the instrument were saved. Figure 10.40 shows the efficiency of simulated neutrinos and the WAIS divide calibration pulser efficiency plotted against function of corrected SNR.

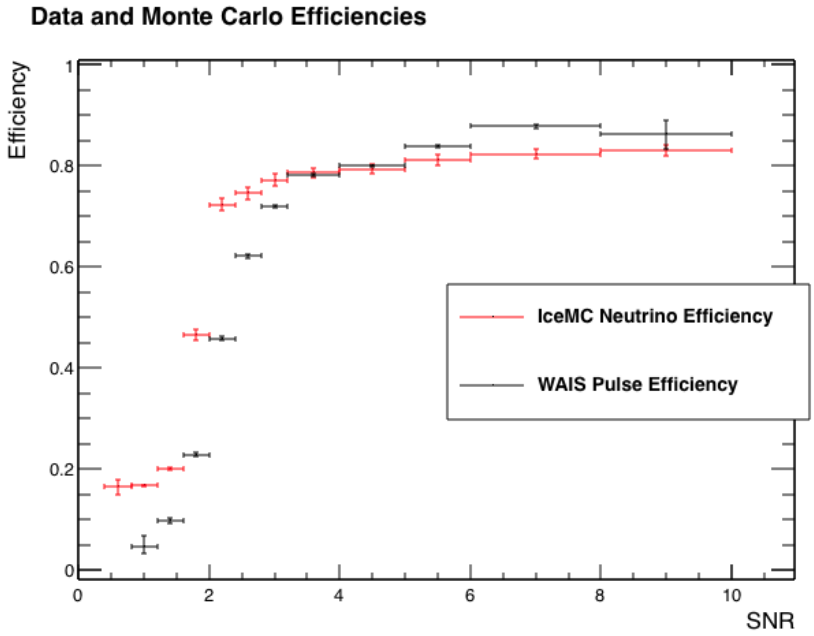

Figure 10.40: Comparison of calibration pulser efficiency and Monte Carlo neutrino efficiency as a function of SNR.

`IceMC` takes account of the conditions of the flight, including the ϕ-masking. The effects of Φ-masking prevent the Monte Carlo efficiency reaching 1. At large SNR this agrees well with the WAIS divide efficiency. At lower values of SNR, the MC efficiency curve before the WAIS divide curve. To address this inconsistency, I apply a re-weighting to the Monte Carlo neutrino sample, derived from the ratio of the two efficiency histograms in Figure 10.40, with the additional requirement that the re-weighting for any bin cannot exceed 1.

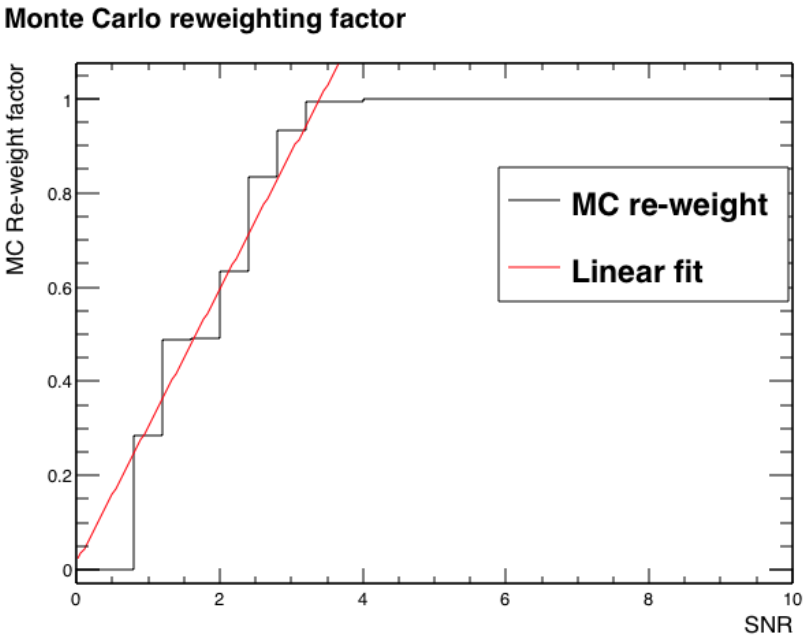

Figure 10.41: Monte Carlo re-weighting factor, with a linear fit to the leading edge of the slope.

A linear fit is applied to the leading edge of the histogram in Figure 10.41. During analysis of the Monte Carlo neutrino sample, the weights of neutrinos passing the simulated trigger will multiplied by a weight, $w_r(SNR)$, such that when $0 \leq w_r \leq 1$,

$$w_r = a \times SNR + b \quad , \tag{10.25}$$

where $a = 0.289692$, and $b = 0.0158606$.

10.14.4 Monte Carlo Analysis Efficiency

I applied my analysis to the Monte Carlo neutrino sample. The pre-clustering analysis efficiency of the MC energy samples vs. SNR is shown in Figure 10.42. The analysis efficiency of the WAIS pulses is plotted for comparison.

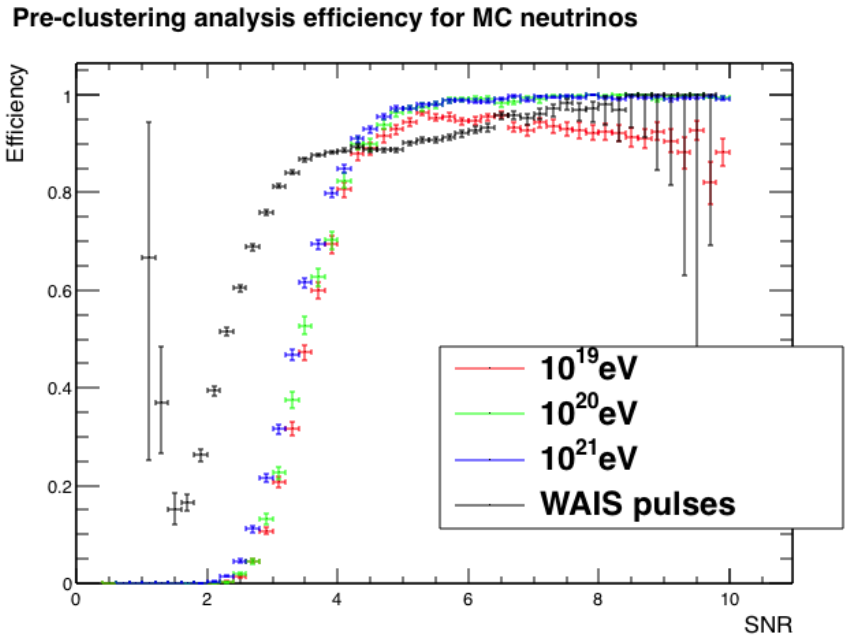

Figure 10.42: Pre-clustering Monte Carlo analysis efficiency. The SNR of the MC neutrinos is scaled by the factor derived in equation (10.24).

The correction factor applied in Section 10.14.2 improves the agreement between the data and MC curves, although there is still a discrepancy.

10.15 Flux Estimate

By applying my analysis to the Monte Carlo neutrino samples, I set a limit on the flux of ultra-high energy neutrinos arriving at the Earth. I set a limit on the differential flux, dN_ν/dE_ν, with

$$E_\nu \frac{dN_\nu}{dE_\nu} = \frac{N_{90}}{A_{eff}(E_\nu) T_{live} \varepsilon(E_\nu)} \quad . \tag{10.26}$$

E_ν is the neutrino energy, N_ν is the neutrino flux (number of neutrinos per unit, area per unit solid angle, per unit time) arriving at the Earth. N_{90} is the 90% upper confidence limit on the mean of a Poisson distribution given 0 observed events in the absence of background [4]. T_{live} is the live time of the experiment, which is obtained from Figure 7.3.

The parameters $\varepsilon(E_\nu)$ and $A_{eff}(E_\nu))$ come from `IceMC`. The efficiency, $\varepsilon(E_\nu)$, is the number of neutrinos that pass the MC trigger and all analysis cuts,

divided by the total number of neutrinos generated. $A_{eff}(E_\nu))$ is the aperture of the experiment with units km^2 sr. This number is estimated by `IceMC` from

$$A_{eff} = 4\pi N_{int} \frac{V_{ice}}{L_{int}} \tag{10.27}$$

where 4π is the total solid angle of the sky, V_{ice} is the volume of ice in Antarctica, L_{int} is the neutrino interaction length (using standard model neutrino cross-sections calculated in [72]). Figure 10.43 shows the limit curve obtained from Equation (10.26) applying my analysis to the `IceMC` neutrinos.

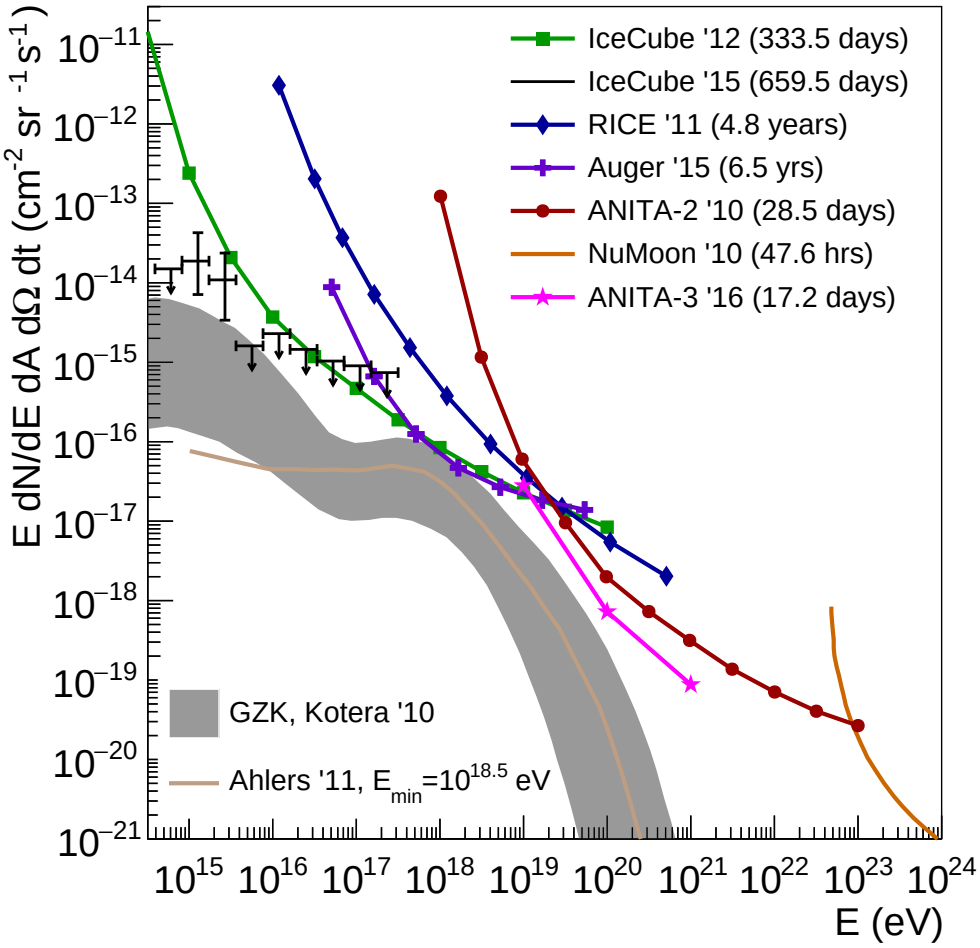

Figure 10.43: Limit curve obtained from equation (10.26) applying my analysis to the `IceMC` neutrino samples.

10.16 Summary

10.16.1 Neutrino Search

I performed an analysis on the ANITA-3 data set and found 0 isolated vertically polarised neutrino-like signals on an expected background of 0.11 ± 0.07 (Section 10.10.2). The limit from this analysis of the ANITA-3 data sets the world's most stringent limit in the $10^{19}\,\mathrm{eV} < E_\nu < 21\,\mathrm{eV}$ energy range.

10.16.2 Cosmic Ray Search

I identified 4 isolated impulsive events that are predominantly horizontally polarised. Further analysis of polarisation angle vs. geo-magnetic field is required to confirm that they match the expected properties of a radio pulse induced by a cosmic ray air shower.

10.16.3 Future Improvements to the Analysis

This analysis could be improved in several ways. A number of issues were present in the final analysis, which if removed have the potential to improve the sensitivity (see Section 10.12). Beyond those simple changes, the sensitivity could be improved with a better CW filtering algorithm. The non-thermal tail in the Fisher Discriminant distribution (Figure 10.17) is due to CW contamination in the minimum bias distribution. An adaptive filter that looks for peaks in the power spectrum and tries to remove power on an event-by-event basis could react to short timescale CW that does not show up in power spectra averaged over long timescales. This would allow the Fisher discriminant cut to be set closer to the thermal noise, improving the analysis efficiency at low SNR.

Chapter 11

Conclusions and Outlook for ANITA-4

The analysis presented in Chapter 10 sets the worlds best limit in the energy range 10^{19} eV to 10^{21} eV. Several improvements, stated in the chapter, could further strengthen that limit. The analysis also revealed four isolated impulsive horizontally polarised events. Further study of the polarisation angles are required to confirm that they are cosmic ray air shower induced radio pulses.

Figure 10.43 indicates that the measurements by ANITA are now approaching the sensitivity required to detect the cosmogenic neutrino flux in optimistic models. Models at the upper end of this range have proton dominated cosmic ray spectrum and sources with large maximum acceleration energies. Although a proton dominated cosmic ray spectrum is disfavoured by recent results from the Pierre Auger Observatory [50], iron rich models still predict significant fluxes for sources with large maximum acceleration energies [6].

ANITA-4 is scheduled to fly later this year. It has several upgrades from ANITA-3 including a new hybrid polarisation trigger, which should help reduce the satellite background. Instead of triggering on vertically polarised (VPol) and horizontally polarised (HPol) trigger separately, the signals are mixed into left-circular polarised (LCP) and right-circularly polarised (RCP) signals. The trigger will require coincidence between LCP and RCP, which have equal power for linearly polarised signals at any incoming angle. This maintains sensitivity to neutrino and

cosmic ray events. Satellite signals are entirely LCP and will be less able to trigger the instrument. Additionally, requiring a coincidence in LCP and RCP allows the threshold against thermal noise to be set lower as two coincident thermal fluctuations are required to create an antenna level trigger. This should improve the sensitivity of ANITA-4 over ANITA-3 making it the best probe of the high energy cosmogenic neutrino flux in the world.

In conclusion, the unexplored parameter space for cosmogenic neutrinos is shrinking, and the coming years may well see the first detection of cosmogenic neutrinos. New experiments with novel detection technologies are emerging to constrain the cosmogenic neutrino flux parameter space, while the ANITA experiment continues to set the world's best flux limit at high cosmogenic neutrino energies. It is an exciting time in the ultra-high energy neutrino Universe.

Bibliography

[1] M. M. Reynoso and O. A. Sampayo, Journal of Physics G: Nuclear and Particle Physics **40**, 055202 (2013).

[2] J. W. Cronin, T. K. Gaisser, and S. P. Swordy, Sci Am **276**, 44 (1997).

[3] W. F. Hanlon, *Updated Cosmic Ray Spectrum*, 2008 (accessed 2016).

[4] Particle Data Group, K. A. Olive *et al.*, Chin. Phys. **C38**, 090001 (2014).

[5] K. Kotera and A. V. Olinto, Annual Review of Astronomy and Astrophysics **49**, 119 (2011).

[6] K. Kotera, D. Allard, and A. Olinto, J. Cosmol. Astropart. Phys. **2010**, 013 (2010).

[7] H. Alaeian, An introduction to cherenkov radiation, `http://large.stanford.edu/courses/2014/ph241/alaeian2/`, 2014.

[8] P. W. Gorham *et al.*, Physical Review D **72**, 023002 (2005).

[9] P. W. Gorham *et al.*, Phys. Rev. Lett. **99**, 171101 (2007).

[10] M. J. Mottram, *A Search for Astrophysical Ultra-High Energy Neutrinos and Cosmic Rays with ANITA-2*, PhD thesis, University College London, 2011.

[11] H. Schoorlemmer *et al.*, Astroparticle Physics **77**, 32 (2016).

[12] G. Varner *et al.*, Nuclear Instruments and Methods in Physics Research Section A: Accelerators, Spectrometers, Detectors and Associated Equipment **583**, 447 (2007).

[13] H. Schoorlemmer and B. Strutt, SURFv3 firmware update - RCO accuracy, ANITA Internal Note https://www.phys.hawaii.edu/elog/anita_notes/571, 2014.

[14] S. Wissel and D. Saltzberg, Field pulser installation, ANITA Internal Note https://www.phys.hawaii.edu/elog/anita_notes/595, 2014.

[15] K. L. Konstantin Belov and A. Romero-Wolf, Anita iii payload geometry, ANITA Internal Note https://www.phys.hawaii.edu/elog/anita_notes/622, 2014.

[16] R. Aloisio, (2012), 1211.2004.

[17] K. Greisen, Phys. Rev. Lett. **16**, 748 (1966).

[18] V. Beresinsky and G. Zatsepin, Physics Letters B **28**, 423 (1969).

[19] P. W. Gorham *et al.*, Phys. Rev. Lett. **103**, 051103 (2009).

[20] P. W. Gorham *et al.*, Physical Review D **82**, 022004 (2010).

[21] P. W. Gorham *et al.*, Physical Review D **85**, 049901 (2012).

[22] W. Pauli, Neutrino hypothesis letter, CERN Pauli Archive https://cds.cern.ch/record/83282/files/meitner_0393.pdf, 2014.

[23] F. Reines and C. L. Cowan, Phys. Rev. **92**, 830 (1953).

[24] G. Danby *et al.*, Phys. Rev. Lett. **9**, 36 (1962).

[25] B. T. Cleveland *et al.*, The Astrophysical Journal **496**, 505 (1998).

[26] Q. R. Ahmad *et al.*, Phys. Rev. Lett. **87**, 071301 (2001).

[27] Y. Fukuda *et al.*, Phys. Rev. Lett. **81**, 1158 (1998).

[28] B. Pontecorvo, Soviet Journal of Experimental and Theoretical Physics **26**, 984 (1968).

[29] Z. Maki, M. Nakagawa, and S. Sakata, Prog. Theor. Phys. **28**, 870 (1962).

[30] B. Kayser, (2012), 1206.4325.

[31] SNO Collaboration, Q. R. Ahmad *et al.*, Phys. Rev. Lett. **89**, 011301 (2002).

[32] S. Fukuda *et al.*, Physics Letters B **539**, 179 (2002).

[33] Y. Ashie *et al.*, Phys. Rev. Lett. **93**, 101801 (2004).

[34] M. G. Aartsen *et al.*, Physical Review D **91**, 072004 (2015).

[35] T. Araki *et al.*, Phys. Rev. Lett. **94**, 081801 (2005).

[36] F. P. An *et al.*, Phys. Rev. Lett. **108**, 171803 (2012).

[37] J. K. Ahn *et al.*, Phys. Rev. Lett. **108**, 191802 (2012).

[38] P. Adamson *et al.*, Phys. Rev. Lett. **106**, 181801 (2011).

[39] P. Adamson *et al.*, Phys. Rev. Lett. **110**, 171801 (2013).

[40] K. Abe *et al.*, Physical Review D **91**, 072010 (2015).

[41] N. Agafonova *et al.*, Phys. Rev. Lett. **115**, 121802 (2015).

[42] V. Hess, Physikalische Zeitschrift **13**, 1084 (1912).

[43] P. Auger, P. Ehrenfest, R. Maze, J. Daudin, and R. A. Fréon, Rev. Mod. Phys. **11**, 288 (1939).

[44] L. O. Drury, Astroparticle Physics **39-40**, 52 (2012).

[45] A. M. Hillas, Annual Review of Astronomy and Astrophysics **22**, 425 (1984).

[46] T. Antoni *et al.*, Astroparticle Physics **24**, 1 (2005).

[47] W. D. Apel *et al.*, Physical Review D **87**, 081101 (2013).

[48] G. T. Zatsepin and V. A. Kuz'min, Soviet Journal of Experimental and Theoretical Physics Letters **4**, 78 (1966).

[49] A. A. Penzias and R. W. Wilson, ApJ **142**, 419 (1965).

[50] T. P. A. Collaboration *et al.*, (2015), 1509.03732.

[51] S. Barwick, D. Besson, P. Gorham, and D. Saltzberg, Journal of Glaciology **51**, 231 (2005).

[52] P. Allison *et al.*, Physical Review D **93**, 082003 (2016).

[53] S. R. Klein, IEEE Trans. Nucl. Sci. **60**, 637 (2013).

[54] G. A. Askar'yan, Soviet Journal of Experimental and Theoretical Physics **21**, 658 (1965).

[55] D. Saltzberg *et al.*, Phys. Rev. Lett. **86**, 2802 (2001).

[56] J. V. JELLEY *et al.*, Nature **205**, 327 (1965).

[57] H. R. ALLAN, R. W. CLAY, and J. K. JONES, Nature **227**, 1116 (1970).

[58] J. Alvarez-Muñiz, W. R. Carvalho, A. Romero-Wolf, M. Tueros, and E. Zas, Physical Review D **86**, 123007 (2012).

[59] K. D. de Vries, A. M. van den Berg, O. Scholten, and K. Werner, Phys. Rev. Lett. **107**, 061101 (2011).

[60] K. Belov *et al.*, Phys. Rev. Lett. **116**, 141103 (2016).

[61] S. Barwick *et al.*, Astroparticle Physics **70**, 12 (2015).

[62] P. Gorham *et al.*, Astroparticle Physics **32**, 10 (2009).

[63] A. G. Vieregg, *The Search for Astrophysical Ultra-High Energy Neutrinos Using Radio Detection Techniques*, PhD thesis, University of California Los Angeles, 2010.

[64] R. Gandhi, C. Quigg, M. H. Reno, and I. Sarcevic, Astroparticle Physics **5**, 81 (1996).

[65] S. Wissel and D. Saltzberg, Ldb pulser installation, ANITA Internal Note https://www.phys.hawaii.edu/elog/anita_notes/617, 2014.

[66] S. Wissel and D. Saltzberg, Recovery of femote field stations, ANITA Internal Note https://www.phys.hawaii.edu/elog/anita_notes/598, 2014.

[67] A. Romero-Wolf, S. Hoover, A. Vieregg, P. Gorham, and t. A. Collaboration, (2013), 1304.5663.

[68] T. A. Collaboration, The anita event correlator library, https://github.com/anitaNeutrino/anitaEventCorrelator, 2016.

[69] EIZO, Eizo rugged solutions (formerly tech source), www.eizorugged.com/, 2016.

[70] H. Liu, K. C. Jezek, B. Li, and Z. Zhao , Radarsat antarctic mapping project digital elevation model, version 2.0, 2015.

[71] P. Fretwell *et al.*, The Cryosphere **7**, 375 (2013).

[72] A. Connolly, R. S. Thorne, and D. Waters, Physical Review D **83**, 113009 (2011).